Lecture Notes

"HYDROELASTISITY"

By

Jan V. Aarsnes

15 October 2009

Table of content

1 INTRODUCTION 5

1.1 BACKGROUND 5
1.2 INTRODUCTION TO HYDROELASTICITY 5
1.3 MAIN TOPICS 5
1.3.1 Vortex Induced Oscillations 5
1.3.2 Whipping, Springing an Ringing 5
1.3.3 Hydroelastic slamming 6
1.3.4 Very Large Floating Structures 6
1.3.5 Membrane Structure 7
1.3.6 Aquaculture structure 7

2 VORTEX INDUCED VIBRATION 8

3 SPRINGING 9

3.1 DESCRIPTION OF LINEAR SPRINGING 9
3.2 SPRINGING RESPONSE CALCULATION – BEAM MODEL FOR ELASTIC HULL 11
3.2.1 General formulation 11
3.2.2 Free vibrations – natural frequencies and natural mode shapes 11
3.2.3 Forced oscillations 14
3.3 DISCUSSION OF SPRINGING RESPONSE 15
3.4 NONLINEAR SPRINGING 17

4 IMPACT LOADS AND TRANSIENT HULL VIBRATIONS - WHIPPING 21

4.1 GENERAL DESCRIPTION OF WHIPPING 21
4.2 WATER ENTRY AND SLAMMING LOADS 23
4.2.1 Description of slamming 23
4.2.2 Slamming pressure and slamming forces 26
4.2.3 Numerical calculation of Slamming pressure and slamming forces 30
4.2.4 Experimental Validation of Slamming Force calculation; "Slam2D" 32
4.3 DYNAMIC EFFECTS ON SLAMMING LOADS 36
4.3.1 Effect of dynamic response – Given Impact load 36
4.3.2 Measurements of slamming Loads 39
4.4 WHIPPING RESPONSE CALCULATION 41
4.5 DISCUSSION OF WHIPPING RESPONSE 42
4.5.1 Parameters governing the whipping response 42
4.5.2 Contribution from elastic response to fatigue damage 42
4.5.3 Contribution from elastic response to maximum values 46

5 RINGING REPONSE OF OFFSHORE PLATTFORMS 48

5.1 GENERAL 48
5.2 EXCITATION OF RINGING 49
5.3 DESCRIPTION OF RESULTS FOR RINGING RESPONSE OF TLP 51

6 NUMERICAL ANALYSIS - SPRINGING AND WHIPPING RESPONSE 55

6.1 GENERAL 55
6.2 EQUATION OF MOTION- STRUCTURAL FORMULATION 56
6.3 HYDRODYNAMIC FORCES 58
6.3.1 General formulation 58
6.3.2 Hydrodynamic Radiation forces 59

6.3.3 Excitation forces 60
6.4 RESPONSE CALCULATION. 61
6.4.1 Response due to General loading – Direct Method. 61
6.4.2 Response due to Linear Harmonic excitation – The Frequency Response Method. 62
6.4.3 General nonlinear loading - Convolution integral method 62
6.4.4 Frequency dependency of added mass and hydrodynamic damping 63

7 MODEL TEST – SPRINGING AND WHIPPING 65

7.1 GENERAL 65
7.2 SCALING LAWS 65
7.3 SHIP MODELING 67
7.3.1 Backbone model 67
7.3.2 Fully elastic model 68
7.3.3 Hinged Models 69
7.4 MEASUREMENTS/INSTRUMENTATION 72
7.5 TEST EXECUTION. 73
7.6 DECAY TEST 74
7.7 ANALYSIS OF RESULTS FROM WAVE TESTS – WHIPPING AND SPRINGING 75
7.7.1 General about test result analysis 75
7.7.2 Results for Springing Response. 75
7.7.3 Results for Whipping Response. 77
7.8 SCALING FROM MODEL TO FULL SCALE. 81

8 HYDROELASTIC SLAMMING 82

8.1 GENERAL 82
8.2 THEORETICAL DESCRIPTION – ONE ELASTIC BEAM 82
8.2.1 Structural modelling. 82
8.2.2 Impact Loads - Hydrodynamic Boundary Value Problem 85
8.2.3 Simplified Solution 87
8.3 MODEL TEST RESULTS - SINGLE BEAM 90
8.4 EFFECT OF AIR POCKET. 94
8.5 THREE BEAM MODEL 95
8.5.1 Theoretical formulation. 95
8.5.2 Model test results 96
8.6 3-D APPROACH 98

9 VERY LARGE LOATING STRUCTURES 102

9.1 GENERAL DESCRIPTION 102
9.2 HYDROELASTIC ANALYSIS 103
9.2.1 General description 103
9.2.2 Linear, Wave Frequency analysis 104
9.2.3 Non-Linear effects 107
9.3 CASE STUDY 107

10 MEMBRANE STRUCTURES 112

10.1 GENERAL 112
10.2 STATIC SHAPE OF MEMBRANE STRUCTURE 113
10.2.1 2-Dimesional membrane structure. 113
10.3 DYNAMIC TENSION IN WAVES – 2-DIMENSIONAL CASE. 118
10.3.1 Theoretical formulation. 118
10.3.2 Numerical results. 121
10.4 3-DIMENSIONAL SOLUTION FOR HEAD SEA. 123
10.4.1 Theoretical formulation. 123

10.4.2 Hydrodynamic coefficients 126
10.4.3 Numerical results for Membrane responses..... 129
10.5 COMPARISON WITH EXPERIMENT. 131

11 AQUACULTURE STRUCTURES 133

11.1 DESCRIPTION OF AQUACULTURE STRUCTURES 133
11.2 NUMERICAL SIMULATION OF RESPONSE IN WAVE AND CURRENT 135
11.2.1 Hydrodynamic forces on Nets 135
11.2.2 Hydrodynamic forces on the floater collar..... 138
11.2.3 Structural modelling of floating collar. 140
11.2.4 Mooring Forces..... 140
11.2.5 Equation of motion – Time integration 140
11.2.6 Approach time integration of net structure dynamic..... 141
11.3 COMPARISON WITH MODEL TEST RESULTS 144
11.3.1 Net cage in uniform Current..... 144
11.3.2 Flexible PEH cage with net in wave and current..... 146

12 REFERENCES 148

A1 GENERAL 152
A2 GENERAL FORMULATION 152
A3 FREE OSCILLATION..... 152
A3.1 Undamped Case..... 152
A3.2 Damped Case..... 153
A4 LINEAR, HARMONIC EXCITATION CASE..... 154
A5 NON-HARMONIC LOADING - TRANSIENT RESPONSE 156

1 INTRODUCTION

1.1 Background

This compendium has been prepared for the Course "Hydroelasticity". Parts of the notes are based on earlier lecture notes and "Power Point" presentations within this Filed. This includes contributions from the following;

- Rong Zhao (in general)
- Ole Hermundstad (Springing and whipping)
- Ole David Økland (Springing and whipping)
- Pål Lader (Aquaculture structures)
- Reza Taghipour (VLFS)

1.2 Introduction to hydroelasticity

Different definitions of the term "hydroelasticity" have been use;

- Hydroelasticity is the branch of science which is concerned with the motion of deformable bodies through liquids
- Study of marine structures when fluid flow and the structural elastic reactions must be considered simultaneously and that we have mutual interactions
- For a hydrodynamics the term hydroelasticity refers to the satisfaction of the deformable body surface boundary conditions of the boundary value problem for the velocity potential mathematical model.

Each of them are covering important aspect of the topic Hydroelasticity.

In this course different areas area within marine technology where there is a strong interaction between hydrodynamic loading and elastic structural response will be outlined and discussed.

1.3 Main topics

The main topics to be covered within this course in Hydroelasticity can be summarized as follows;

- Vortex Induced Oscillation
- Springing, whipping and ringing response of ships and offshore structures
- Hydroelastic Slamming
- Large Floating Structures
- Membrane structures
- Aquaculture structures
- Large Floating Structures

1.3.1 Vortex Induced Oscillations

See separate Presentation by Carl Martin Larsen

1.3.2 Whipping, Springing an Ringing

The ship hull can be regarded as an elastic structure with different natural modes and frequencies. As for rigid body motions resonance motions in the different modes can introduce large dynamic amplifications of the responses. It is therefore of fundamental importance to analyze the dynamic behavior of the ship structure also for the elastic modes of vibrations.

Dynamic response of an elastic structure may be generated either by steady state excitation or by impact loads of short duration. The elastic response of the hull girder is denoted as springing and whipping respectively, i.e;

- Springing Response; is steady state resonant hull girder vibrations due to wave loading.

- Whipping Response; is transient hull girder vibrations due to wave loads that increase rapidly and with short duration (i.e slamming loads).

The elastic hull structure vibrations may in principle occur both in the vertical and horizontal plan. For surface piercing ships the vertical forces will in general be dominating. This applies both to vertical wave loads and to slamming loads. We will therefore in this course limit our self to vibrations in the vertical plan.

Ringing Response; is the transient high frequency response at the natural frequency of an elastic mode typically occurring in extreme wave conditions with large and steep individual waves. Ringing has been observed for offshore structures as Gravity Base Structures (GBS) and Tension Leg Platforms (TLP). These concepts are characterised with some relatively high elastic natural frequencies, which are outside the range of normal (i.e. linear) wave loading. The ringing excitation occurs in sea states with wave periods well above the elastic natural periods.

Springing, whipping and Ringing responses in general are discussed in Chap 3, 4 and 5 respectively.

The springing, ringing and whipping responses can in principle be assessed by model tests and / or by theoretical methods. This is discussed in Chapter 6 and 7 respectively.

1.3.3 Hydroelastic slamming

A dynamic structural response will arise if the duration of the impact load is comparable to, or shorter than, the relevant natural period of the structure. For bow flare slamming on ships, the duration of the slamming load will often be long compared to the short natural period of the hull plating. Hence a quasi static approach is applicable. On the other hand slamming on the wetdeck of a catamaran may give rise to a dynamic structural response in the local plating since the rise time of the pressure is shorter than the plating natural period. Such cases where the duration of the slamming load is much shorter than the natural period of the structure is denoted *Hydroelastic slamming.*

Hydroelastic slamming is discussed in Chapter 8.

1.3.4 Very Large Floating Structures

Very Large Floating structures (VLFS) are characterized by it's huge dimensions. Typical dimensions can be Length x Breadth, LxB=5 km x 1 km. Design and construction of these structures are therefore associated with massive cost and labour. A key feature of VLFS's is their large horizontal extension relative to the vertical one. This leads to a significant elastic behaviour which is dominant relative to the rigid-body motions. Hence the flexibility and the coupling effect between structural deformation and hydrodynamic loads strongly affect the response. In this way the VLFS must be regarded as a hydroelastic structure.

VLFS is discussed in Chapter 9.

1.3.5 Membrane Structure

Applications of liquid filled membrane structures in the sea are restricted to liquids with density lighter than sea water. Examples of existing applications are storage container, transporting fresh water and collection of oil spill from a damaged tanker or from a blow out. Fabric structures have also been used as pens for fish farming, but then connected to a frame structure or to a floating flexible collar. The fabrication costs for flexible containers are much lower than for conventional structures used for sea-transportation as barges and ships.

The response of a membrane structure in waves is highly hydroelastic as the membrane structure follows the wave action to a large extent and the elasticity of the fabric govern the hydrodynamic loading

.

Application of Membrane structure is discussed in Chapter 10.

1.3.6 Aquaculture structure

The marine fish farms used for aquaculture purpose consist of highly flexible structural components such as fish nets, anchor lines and elastic or hinged floating collar structures in the free surface zone. The mooring lines and nets are connected to the floaters. The installations are exposed to loads from wind, waves and current and due to the dominating elastic behavior of the different components, a hydroelastic approach will be required for design and analysis.

Application of Aquaculture structures is discussed in Chapter 11.

2 VORTEX INDUCED VIBRATION

See separate Lecture Note from Carl Martin Larsen

3 SPRINGING

3.1 Description of Linear springing

Springing may be explained in the following way. The ship hull can be regarded as a flexible beam and will have resonant natural modes and frequencies. If the wave loading in a sea state excite in the same frequency range as the natural frequency of the elastic hull, resonant hull girder vibration will be generated. This is called springing.

Resonant vibrations implies that;

- The vibration sustain over a certain period (”steady-state” phenomenon)
- there are wave-forces that oscillate with the same frequency as one of the natural frequencies of the hull girder – usually the lowest frequency

For a monohull, the 2-node vertical vibration mode will normally have the lowest natural frequency. Typical natural period for this 2-node mode will be 1-2 s, depending on ship length. For a catamaran, the torsion (twisting) mode will often have the lowest frequency. Torsion vibrations may also be induced in monohuls with large deck openings (e.g. container ships).

For a ship with forward speed *U*, the wave encounter frequency is given from;

$$\omega_e = \omega_0 + \frac{\omega_0^{\,2}}{g} U \qquad (3.0)$$

where ω_0 is the incoming wave frequency. Linear springing occur when the encounter frequency approach the natural frequency of the lowest natural flexible mode. This is illustrated in Fig 3.1 which shows the wave spectrum based on encounter frequency for a ship in head sea waves at different speed. The natural frequency of the 2-node mode for different ship size is also shown.

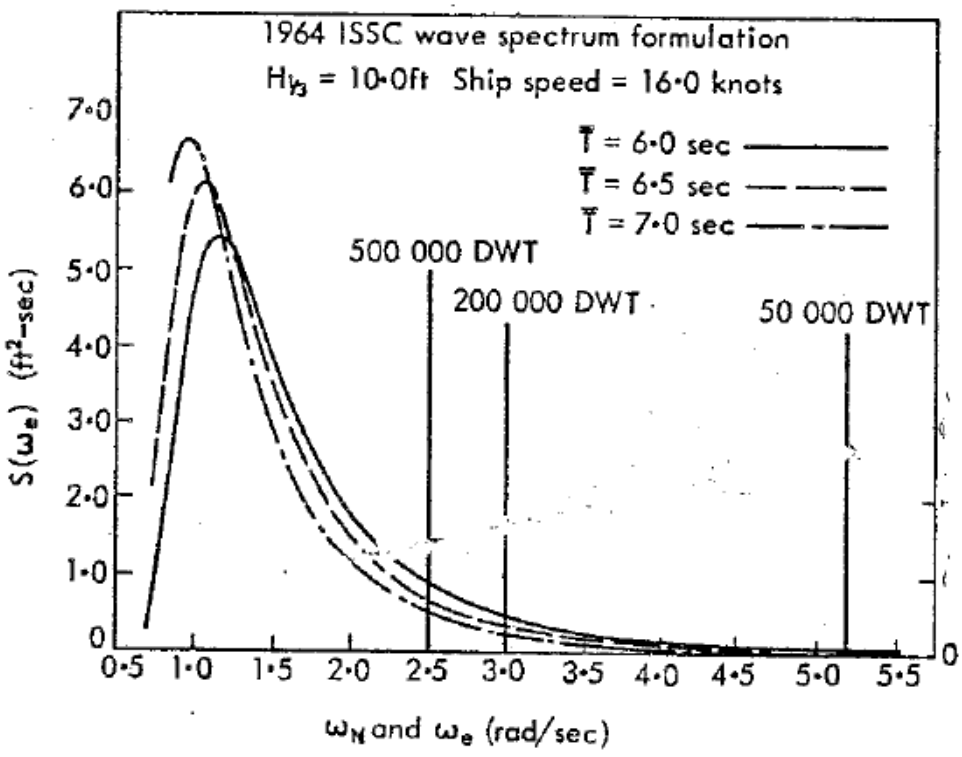

Figure 3.1 *Wave energy and natural frequency for 2 node mode of vibration for different size ships.*

.

It is seen that for the actual case the high frequency tail of the encounter wave spectrum has significant energy at the natural frequency range for the 2-node mode for the larges ship size.

The springing response is illustrated in Fig. 3.2 where transferfunction for vertical bending moment midship is shown. The large peak at the resonance frequency represent the springing effect. This will typically occur for relatively short waves. For short waves the excitation forces of the global 2-node mode is relative small, but as they occur at high frequencies, the hydrodynamic damping is very low and hence high resonance response peaks may occur.

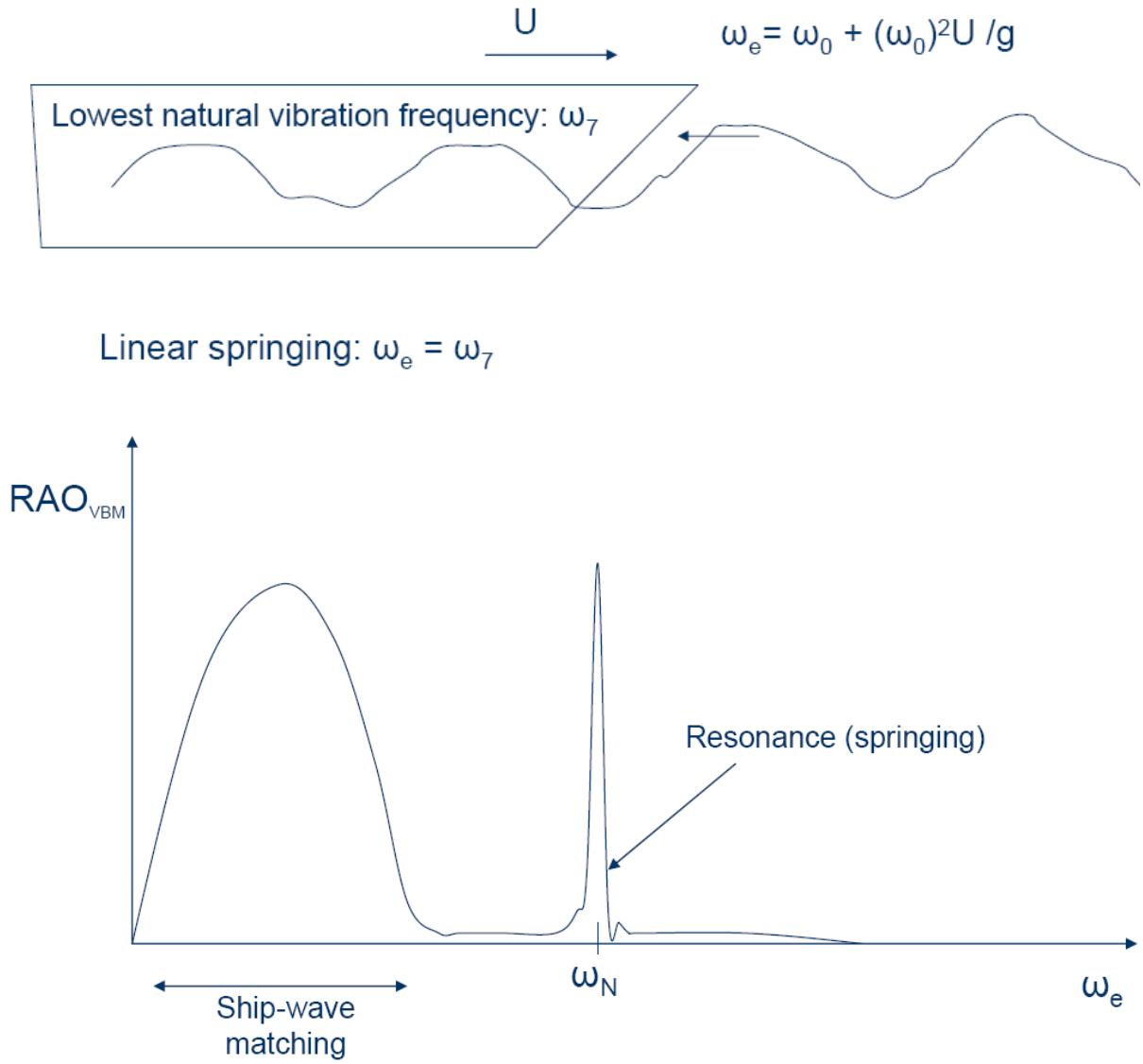

Figure 3.2 *Bending moment RAO (regular waves) Effect of Linear Springing.*

Calculations suggest that springing may give a significant contribution to the extreme response for some ships, but *springing* vibrations are generally more *important for fatigue*. It has been found, see Storhaug et al.(2006) for details, that springing may contribute to about 40% of the accumulated fatigue damage for long bulk carriers.

It is therefore important to include the effect of springing in the design and analysis of ship designs.

3.2 Springing response calculation – Beam Model for Elastic Hull

3.2.1 General formulation

A ship can be regarded as an elastic beam with variable mass and bending stiffness distribution along the length. The simplest approach to the beam theory is the classical Euler beam. This approach is based on the following assumptions;

- Shear deformation can be neglected.
- Effect of rotary inertia is neglected.
- Axial deformations is neglected

The first assumption imply that loading normal to the beam axis is carried by a pure bending behavior.

The differential equation for the vertical vibrations for an elastic beam can be derived by considering equilibrium in forces and moments acting on a small beam element. The results is the Beam Equation which applies for the vertical elastic deflection of the beam, $y(x,t)$ as function of longitudinal position, *x* and time *t*;

$$m(x)\frac{\partial^2 y(x,t)}{\partial t^2}+\frac{\partial^2}{\partial x^2}\left[EI(x)\frac{\partial^2 y(x,t)}{\partial x^2}\right]=q(x,t) \tag{3.1}$$

Where $m(x)$ is the structural mass pr length unit, E is the Young's module, $EI(x)$ is the bending stiffness and $q(x,t)$ is the total (hydrodynamic) force. The total hydrodynamic force includes both the wave excitation force (i.e the wave force acting on a fixed structure) and the hydrodynamic force due to forced oscillation in the elastic modes. This can be written on the following form;

$$q(x,t)=p(x.t)-\left[a(x)\frac{\partial^2 y}{\partial t^2}+b(x)\frac{\partial y}{\partial t}+c(x)y\right] \tag{3.2}$$

Where $p(x,t)$ is the wave excitation force , $a(x)$ is the added mass coefficient, $b(x)$ is the damping coefficient and $c(x)$ is the hydrostatic force coefficient. The damping coefficient includes both the hydrodynamic damping and the structural damping and the damping effect of the cargo.

Inserting eq. (3.2) into eq. (3.1) gives the following expression:

$$\left[m(x)+a(x)\right]\frac{\partial^2 y(x,t)}{\partial t^2}+b(x)\frac{\partial y}{\partial t}+\frac{\partial^2}{\partial x^2}\left[EI(x)\frac{\partial^2 y(x,t)}{dx^2}\right]+c(x)y=p(x,t) \tag{3.3}$$

The hydrostatic restoring term $c(x)y$, has normally very little effect on the springing response.

3.2.2 Free vibrations – natural frequencies and natural mode shapes

The solution of equation (3.3) is usually found by the "normal modes" approach. The basis for this approach is that any forced deformation of the elastic structure can be approximated by the sum of a limited number of normal modes of the system multiplied by the time dependent principal coordinate of the different modes. The normal modes are determined from the free vibration case, i.e using $q(x,t)=0$ and $b(x)=0$ in eq. (3.3). A

solution for the vertical beam deflection, $y(x,t)$, can now be assumed on the following form;

$$y(x,t) \propto e^{i\omega t}\psi(x) \tag{3.4}$$

which gives a harmonic oscillation in time and a time independent shape function (Normal Mode), $\psi(x)$.

As an example the simplified case with a uniform elastic beam is considered. Uniform beam assumption implies that all parameters in eq. (3.3) are constant along the ship length. The equation for free vibration can now be written;

$$-\omega^2 \frac{m+a}{EI}\psi(x) + \frac{\partial^4 \psi(x)}{\partial x^4} + \frac{c}{EI}\psi(x) = 0 \tag{3.5}$$

Introducing the parameter *β,* defined from;

$$\omega^2 \frac{m+a}{EI} - \frac{c}{EI} = \left(\frac{\beta}{L}\right)^4 \tag{3.6}$$

Gives the following equation for the free vibration;

$$\frac{\partial^4 \psi(x)}{\partial x^4} - \left(\frac{\beta}{L}\right)^4 \psi(x) = 0 \tag{3.5b}$$

the general solution of the differential equation given by eq (3.5b) can be written as (see e.g Thomsen (1993) for details);

$$\psi(x) = A\sin(\frac{\beta}{L}x) + B\cos(\frac{\beta}{L}x) + C\sinh(\frac{\beta}{L}x) + D\cosh(\frac{\beta}{L}x) \tag{3.7}$$

The unknowns in eq. (3.7) are determined from the actual boundary conditions. For the hull girder the boundary conditions are that the shear forces, *V(x)* and bending moment *M(x)* are zero at the ends of the ship, i.e. at $x = 0$ and $x = L$. This gives;

$$V(x) = 0 \Rightarrow \frac{\partial^3 \psi}{\partial x^3} = 0 \quad \text{for} \quad x = 0 \quad \text{and} \quad x = L \tag{3.8}$$

$$M(x) = 0 \Rightarrow \frac{\partial^2 \psi}{\partial x^2} = 0 \quad \text{for} \quad x = 0 \quad \text{and} \quad x = L \tag{3.9}$$

Substituting the 4 boundary conditions into the general solution given by (3.7) gives 4 linear equations, 2 for $\frac{\partial^2 \psi}{\partial x^2}$ and 2 for $\frac{\partial^3 \psi}{\partial x^3}$ as follows;

$$\begin{bmatrix} -1 & 0 & 1 & 0 \\ 0 & -1 & 0 & 1 \\ -\cos\beta & \sin\beta & \cosh\beta & \sinh\beta \\ -\sin\beta & -\cos\beta & \sinh\beta & \cosh\beta \end{bmatrix} \begin{bmatrix} A \\ B \\ C \\ D \end{bmatrix} = \begin{bmatrix} 0 \\ 0 \\ 0 \\ 0 \end{bmatrix}$$

The solution of these 4 equations can be shown to give the following equation;

$$\cos\beta \cdot \cosh\beta = 1 \tag{3.10}$$

This equation is satisfied for the following β values;

$$\beta_i = 0\text{, } 4.73,\ 7.853,\ 10.996\text{ , }\ \ldots \tag{3.11}$$

$$\beta_1 = 0\text{,}$$

$$\beta_i \approx \frac{\pi}{2}(2i-1)\text{, }\quad \text{i=2, 3, 4...}$$

Using equation (3.6) gives the following results for the natural frequencies:

$$\omega_i^{\,2} = \left(\frac{\beta_i}{L}\right)^4 \frac{EI}{m+a} + \frac{c}{m+a}$$

Which gives:

$$\omega_i = \sqrt{\left(\frac{\beta_i}{L}\right)^4 \frac{EI}{(m+a)} + \frac{c}{(m+a)}} \tag{3.12}$$

The mode shapes for the lowest mode shapes is shown in Fig 3.3 for the uniform beam case. It should be noted that from free vibrations only the shape of the modes is known. The actual amplitude of oscillations will depend on the imposed excitation force.

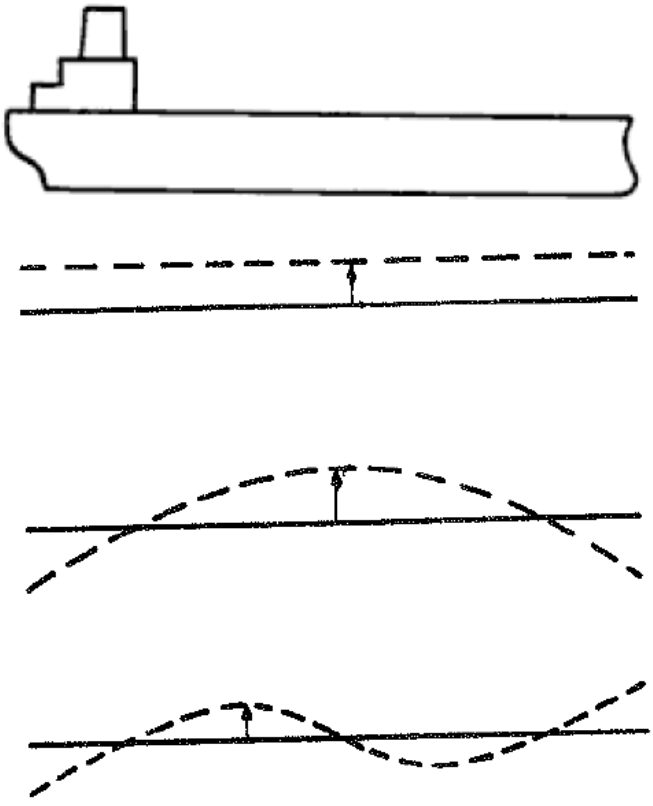

Mode 1:
Rigid Body Motion
i=1

Mode 2:
Fundamental Mode
i=2

Mode 3:
i=3

Figure 3.3 *Mode shapes for uniform beam*

Example of calculated mode shapes for a (storhaug and Moan (2006)

For Rigid body motion (heave);

$$\omega_1 = \sqrt{\frac{c}{m+a}} = \omega_0$$

The first elastic mode is for i=2 which gives:

$$\omega_2 = 22.5\sqrt{\frac{EI}{L^4(m+a)}} \tag{3.13}$$

The natural period for this fundamental mode will for a large monohull be typically 1-2 s.

3.2.3 Forced oscillations

One basic assumption is that the forced vertical elastic deflection of the beam, $y(x,t)$ can be written as a linear sum of the normal modes;

$$y(x,t) = \sum_{i=1}^{N} q_i(t)\psi_i(x) \tag{3.14}$$

Where $q_i(t)$ are the time dependent principal coordinates. The normal modes $\psi_i(x)$, have the important property of being orthogonal functions;

$$\int_0^L \psi_i(x)\psi_j(x)dx = 0 \quad \text{for} \quad i \neq j$$
$$\int_0^L \psi_i(x)\psi_j(x)dx \neq 0 \quad \text{for} \quad i = j \tag{3.15}$$

Inserting the assumed solution given by eq. (3.14) into the Beam equation (3.3) gives;

$$(m+a)\sum_{i=1}^{N}\ddot{q}_i(t)\psi_i(x) + b\sum_{i=1}^{N}\dot{q}_i(t)\psi(x) + EI\sum_{i=1}^{N}q_i(t)\frac{d^4\psi_i(x)}{dx^4} = p(x,t) \tag{3.16}$$

Where the assumptions of a uniform beam have been used. To establish an equation for each mode *i* separately, the orthogonal properties of the normal modes, see equation (3.15) is used by multiplying equation (3.16) with $\psi_j(x)$ and integrating over the length. This gives for mode *i*;

$$(m+a)\left[\int_0^L {\psi_i}^2(x)dx\right]\ddot{q}_i(t) + b\left[\int_0^L {\psi_i}^2(x)dx\right]\dot{q}_i(t) + EI\left[\int_0^L \frac{d^4\psi_i(x)}{dx^4}\psi_i(x)dx\right]q_i(t) = \int_0^L p(x,t)\psi_i(x)dx \tag{3.17}$$

By introducing generalized mass, added mass, damping, stiffness and load eq. (3.17) can be rewritten to the form;

$$\ddot{q}_i + \frac{\overline{b}_i}{\overline{m}_i + \overline{a}_i}\dot{q}_i + \omega_i{}^2 q_i = \frac{1}{\overline{m}_i + \overline{a}_i}\,\overline{f}_{A,i} e^{-i\omega_e t} \tag{3.18}$$

In the above equation it has been used that the excitation force is assumed to be a harmonic oscillating function, i.e;.

$$p(x,t) = \hat{p}(x)e^{-i\omega_e t}$$

Then generalized mass, stiffness and excitation terms are given by;

$$\overline{m} = m\int_0^L \psi_i{}^2(x)dx, \qquad \overline{k} = EI\int_0^L \left(\frac{\partial^2 \psi_i(x)}{\partial x^2}\right)^2 dx \qquad \overline{f} = \int_0^L \overline{p}(x)\psi_i(x)dx \quad \text{etc...}$$

In this way one has reduced the coupled system with infinite number of degree of freedom to an uncoupled system which can be solved independently. The solution of each of the equations is similar to the differential equations for a system with one degree of freedom, see Appendix A for details.

The bending moment and shear force are now obtained as;

$$M(x,t) = EI(x)\sum_{i=1}^{N}\frac{\partial^2 \psi_i(x)}{\partial x^2}q_i(t)$$

$$Q(x,t) = EI(x)\sum_{i=1}^{N}\frac{\partial^3 \psi_i(x)}{\partial x^3}q_i(t)$$

The "normal modes" solution used for equation (3.3) is valid only for the case $b(x) \to 0$, but it is also assumed to be a good approximation for a lightly damped system. The alternative to normal mode solution for forced oscillations is numerical integration.

The main assumption for the use of Beam Theory is that the length is significantly larger than the breadth and height. The length in this context is to be understood as the length between two nodes. This imply that for higher order mode shapes the use of beam theory will be questionable. However for the global elastic response of the ship hull girder the main interest will be for the lowest few modes.

Modal analysis require an linear system, i.e a system where there is a linear relation between load and structural responses. This is a reasonable assumption for global ship hull modeling.

3.3 Discussion of Springing response

An example of measured Bending moment stresses in full scale is shown in Fig. 3.4. Effect of springing with large peak at natural frequency of the first elastic mode is seen in the measured response. From the equation for encounter frequency, eq. (3.0) and the equation for the natural frequency for the first elastic mode, eq. (3.13) it is clear that it will be ships with high speed and/or low natural frequency for the first elastic mode which will be most exposed to springing. Springing may therefore give significant contributions to global response for;

- Ships with high forward speed (i.e. high encounter frequencies)
- Ships with low natural frequencies. I.e. relatively flexible hulls compared to the mass.

Practical examples of type of ships where spring can be important ;

- High speed vessels
- Vessels made of aluminum of fibre-reincorced plastics (low EI, ref eq. (3.13))
- Great-Lakes bulk carriers (shallow draft and with reduced scantlings give flexible ships with large excitation forces)

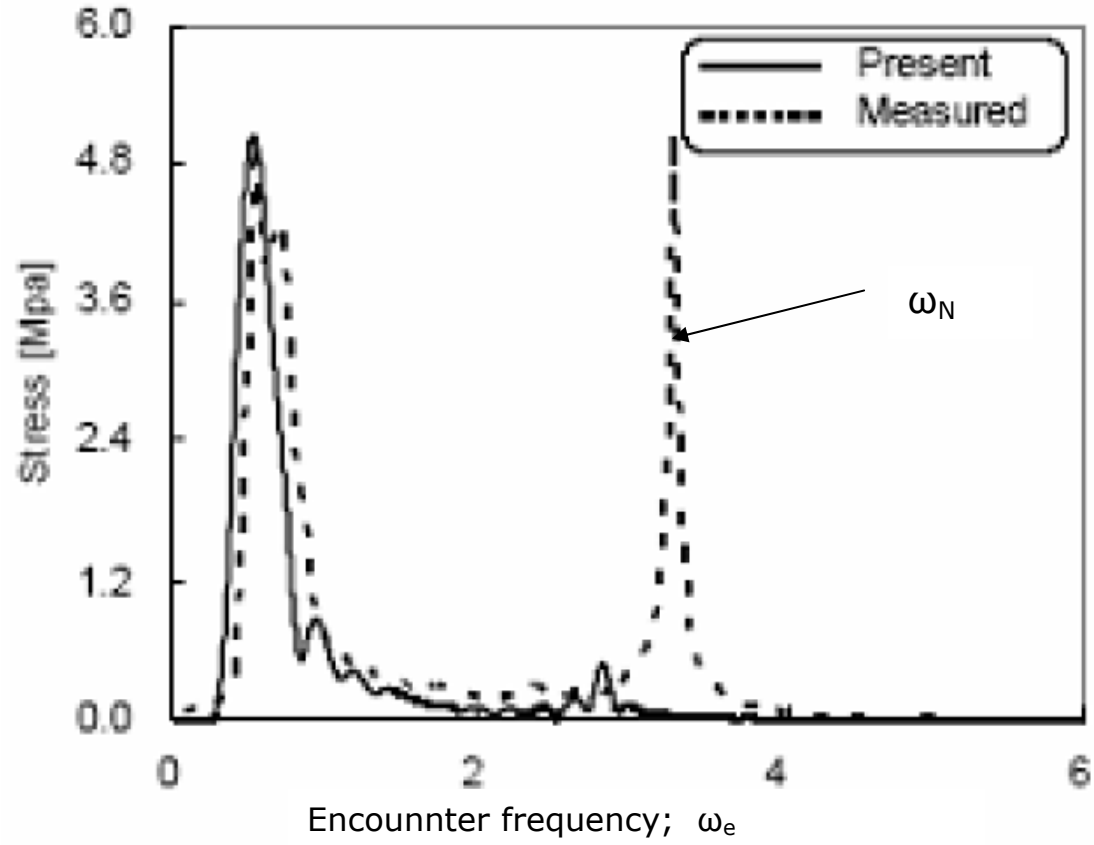

Figure 3.4 *Calculated and measured Bending moment stresses in full scale. Head sea. Effect of Springing with large peak at natural frequency first elastic mode.*

The physical parameters that govern the springing response can now be summarized as follows;

- Hull girder stiffness. Lower stiffness generally gives more springing, since resonance will occur for longer waves, which contains more energy and also give higher excitation per unit amplitude (higher RAO) due to less cancellation (ship-wave matching).

- Bow (and stern) geometry. Blunt bows seem to give more springing than slender bows. Bow stem slamming and wave reflection can contribute to the springing forces.

- Structural damping. Since springing occurs at relatively high frequencies, damping caused by wave generation is low. For high speed ships, however, hydrodynamic damping due to lift effects from the transom stern becomes important. For other ships, structural damping is important. Structural damping is very difficult to predict by theoretical methods. One needs to rely on measured data from the ship in question or from similar ships.

- Loading condition. More cargo gives higher mass and lower eigenfrequency (natural frequency) of the hull girder. A lower eigenfrequency will generally cause more springing. However, more cargo also gives a higher draft. Since most hydrodynamic

pressures decay rapidly with draft, this means that the pressure variation (i.e. springing excitation forces) under the forward part of the ship bottom becomes lower. This latter effect is normally stronger than the effect of a reduced eigenfrequency and springing is normally worse for ballast condition. A wide ship may also have a low draft even in loaded condition.

- Ship speed. A higher speed will give resonance for longer waves, which in turn will give more springing. Some studies indicate that the springing vibration amplitude increases with the square of the forward speed.

- Wave condition. Since relatively high encounter frequencies are needed to give springing, the phenomenon is most pronounced in moderate sea-states, where most of the wave energy is contained in relatively short waves. *Linear* springing forces normally come from very short waves, and they are therefore very sensitive to the high-frequency tail of the wave spectrum.

- *Nonlinear* springing forces get a contribution from the interaction between waves with different frequencies and different directions. This gives rise to forces that oscillate with the sum of the frequencies of the different waves. The total springing forces are therefore dependent not only on the frequency-distribution of the wave energy, but also on the directional distribution.

3.4 Nonlinear Springing

The linear excitation forces for springing are associated with waves of small wave length relative to the ship length. Non-linear springing is steady state response generated by higher order wave forces. The different possible excitation effects for non-linear springing can be summarized as follows;

- nonlinear excitation forces with frequency $N\omega_e$, where N=2,3,... .N=2 is the most important.

- Waves with frequency ω_{ej} and ω_{ek} give nonlinear excitation forces with frequencies: $2\omega_{ej}$, $2\omega_{ek}$, $\omega_{ej}+\omega_{ek}$, $\omega_{ej}-\omega_{ek}$, $\omega_{ek}-\omega_{ej}$

Is should be noted that Nonlinear springing occurs for much longer (and more energetic) waves. Nonlinear excitation forces increase with the square of the wave amplitude (2^{nd} order forces). In summary second order forces excite over a broad frequency range and also for frequencies much higher than for linear wave force excitation. The effect is illustrated in Figure 3.5 which shows RAO for the Vertical midship bending moment in regular waves. The peak at ω_N is excitated at encounter frequency $\omega_e = 0.5\omega_N$.

A typical example of nonlinear spring measured in model tests is shown in Figure 3.6. The ship is towed in head se waves in regular waves with encounter frequency $\omega_e \cong 0.5\omega_N$. From the time history plot of the measured midship vertical bending moment response at two different frequencies are clearly shown. This is also shown on the response spectrum plot with two pronounced peaks, one at the encounter frequency of 0.4 Hz and one at the natural frequency of the first elastic mode at 0.8 Hz. The filtered signals shows that the wave frequency amplitude (i.e. from low pass filtering) is significantly smaller than the springing frequency contribution (i.e. from the high pass filtered signal), 125 000 kNm and 175 000 kNm respectively for this case.

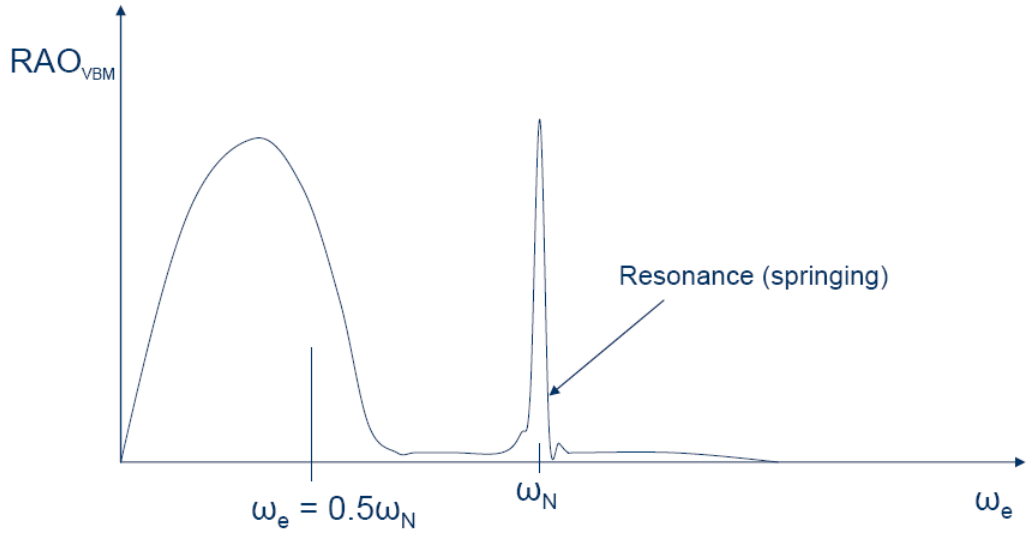

Figure 3.5 *Bending moment RAO (regular waves) Effect of Nonlinear Springing.*

This test results clearly illustrate that nonlinear forces can give a very significant contribution to the total global responses when the first flexible mode is excited.

The additional loading mechanisms which generate nonlinear springing (i.e additional force contributions relative to linear wave forces) can now be summarized as follow;

- Quadratic terms in the pressure (Bernoulli's equation). In linear theory these terms are neglected
- Pressure acts on the instantaneous position of the hull on the instantaneous wetted area. In linear theory the pressure is evaluated and integrated over the mean position of the hull below z=0.
- In the hydrodynamic boundary value problem, the body boundary condition should be satisfied on the instantaneous position of the hull on the instantaneous wetted area. In linear theory the body boundary condition is satisfied on the mean position of the hull below z=0.
- The free surface condition(s) should be satisfied on the instantaneous position of the free surface. In linear theory, the free surface condition is satisfied on z=0.
- Wave components with different directions will generate sum-frequency pressure oscillations (2nd order cross coupling terms). I.e. should not only consider long-crested waves in springing analyses.
- "Regular" slamming loads at the bow
- Nonlinear wave reflection at the bow (nonlinear 3D effect)

The two last points illustrates that there is not always a clear dividing line between whipping and nonlinear springing.

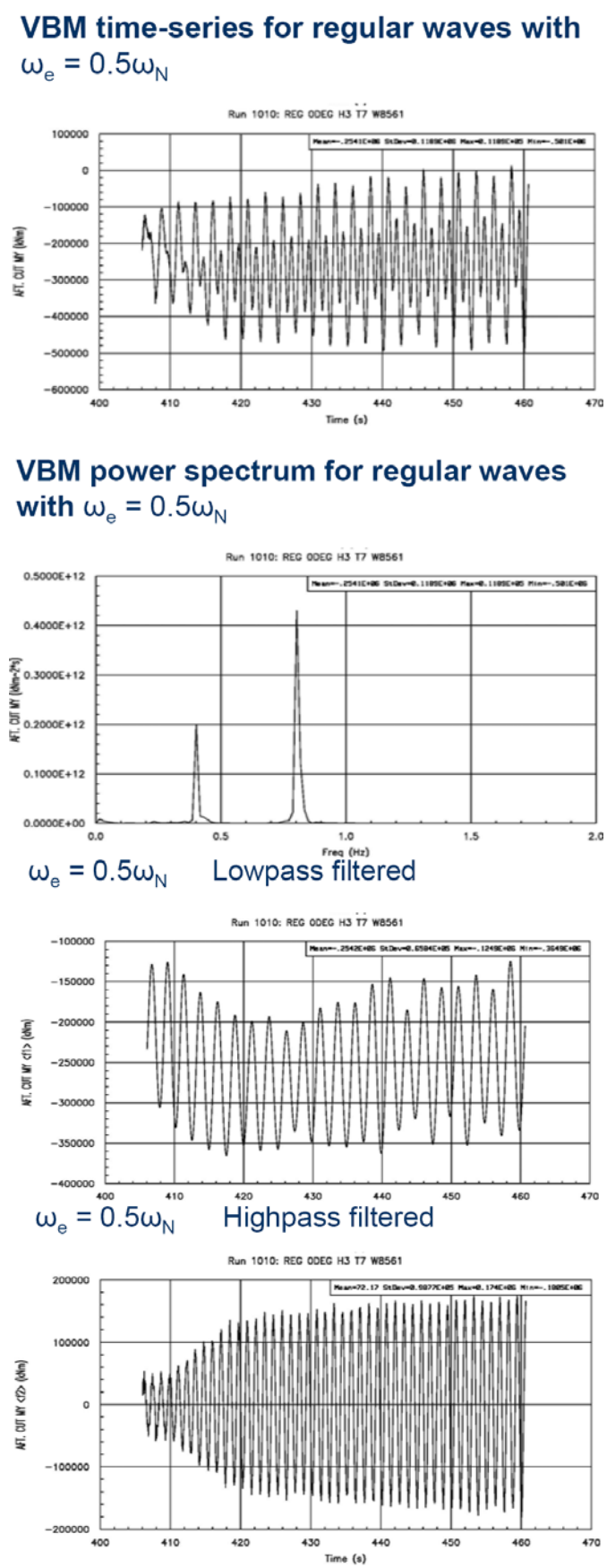

Figure 3.6 *Bending moment RAO (regular waves) Effect of Nonlinear Springing. Total time series, Power spectrum of total time series, Low pass filtered and High pass filtered response.*

Calculation methods for Non-Linear springing can be categorized as follows;

- Frequency-domain methods (2D or 3D)
  - Captures some of the nonlinear phenomena
- Time-domain methods (2D or 3D)
  - Captures more of the nonlinear phenomena
  - But no complete theory has yet been developed!

Numerical methods will be further discussed in Chap 6.

4 IMPACT LOADS AND TRANSIENT HULL VIBRATIONS - WHIPPING

4.1 General description of Whipping

Whipping is transient hull girder vibrations due to wave-loads that increase rapidly. This will normally be impact loads like those arising from bottom slamming or bow flare slamming as illustrated in Fig. 4.1. The 2-node and 3-node vertical vibration modes will normally be the most important. For catamarans, and for monohuls with large deck openings, torsion/twisting vibrations may also be important.

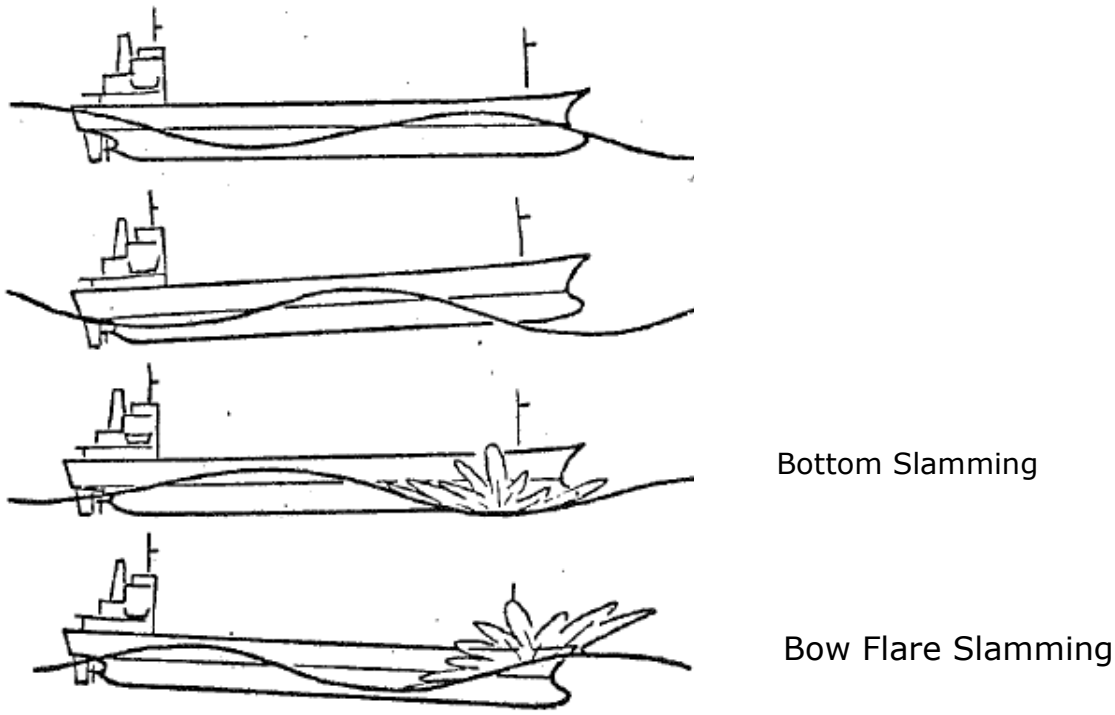

Figure 4.1 *Illustration of impact loads situation generating whipping response.*

Normally, whipping is associated with violent slamming loads in severe wave conditions. The highest hull girder responses are often associated with whipping events. Hence, whipping may contribute significantly to the design loads and are therefore important to assess. Another aspect of whipping response is that severe slamming/whipping will make the shipmaster slow down the speed.

An example of observed whipping response measured in model tests for a monohull in head sea regular waves is shown in Fig. 4.2. The Pitch motion, relative wave motion and vertical bending moment amidships is shown as function of time. Also impact forces measured at two force panels in the bow area is included. The high peaks in the vertical bending moment following the impact loads illustrate the whipping response behaviour.

In Fig. 4.2B measured vertical bending moment midship for a ridged and a elastic hull is shown, see Drummen et al. (2008). The results are from model tests with a container ship in head sea waves. Tests were carried out both with a ridged hull and an elastic modeled hull. Both were tested in the same wave condition. The trigging of the elastic hull girder vibration after hit by a large wave is clearly seen.

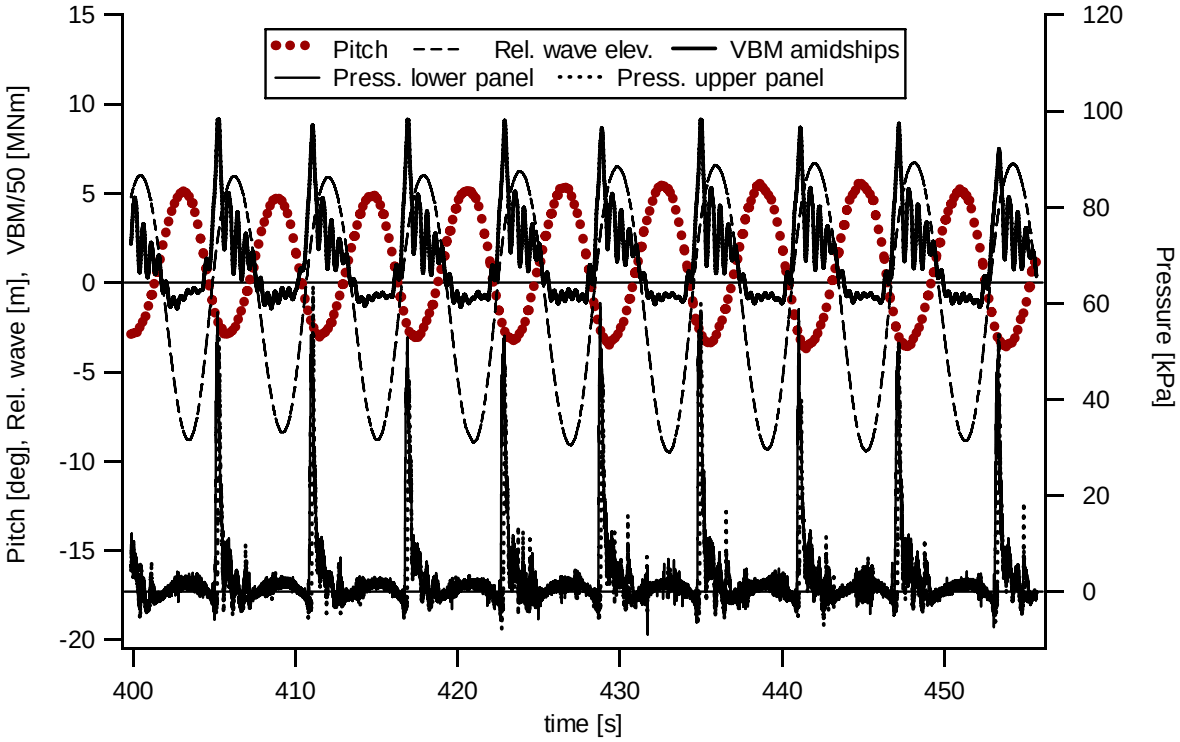

Figure 4.2 *Example of measured whipping response in mode with a monohull in regular head sea waves.*

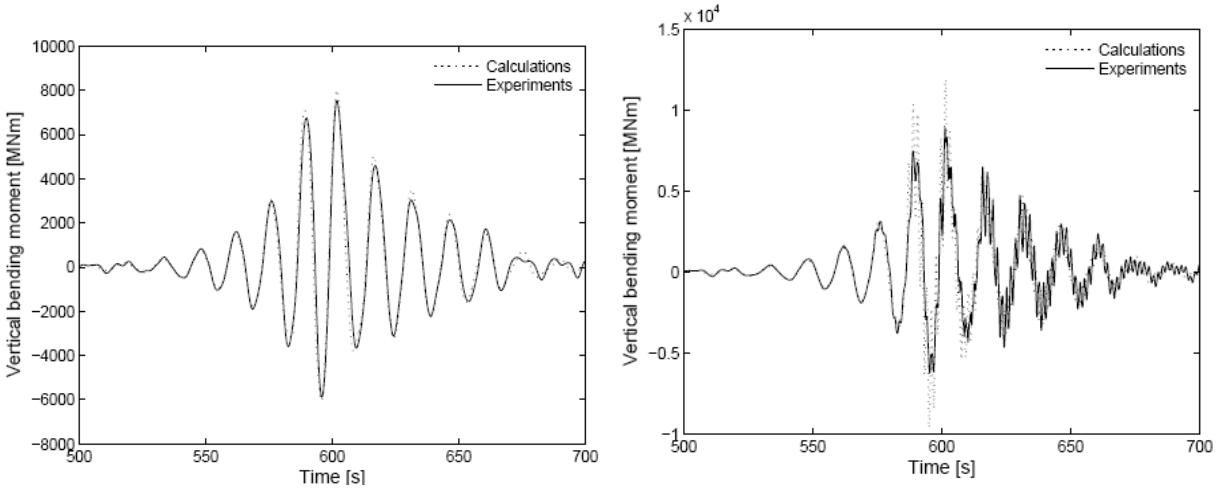

Figure 4.2B *Vertical bending moment midship. Left; Ridged hull. Right Elastic hull. Measured results from model tests. Calculated results also shown for both cases. (From Drummen at. al. (2008))*

In the past few years there has been some focus on whipping vibrations due to slamming loads on the aft part of the ship. This will typically occur for ships where the aftmost part the hull bottom is nearly flat and has a very low draft. Comfort problems on passenger vessels have been reported. The problem is pronounced only at zero or moderate speeds.

The response to slamming loads must be evaluated at two different levels, the local response and the global response. Local response is associated with the response of the plated structure around the position of the impact. Global response is associated with the vibration of the entire ship hull girder (or the entire platform in case of offshore structures). For the local response the local distribution in time and space will be important. For this case the elastic dynamic response of the local plate structure may

interact with and influence on the slamming load. This case is discussed in Chap 7, Hydroelastic slamming.

The global response caused by slamming is governed by how the impact loads can excite the global elastic modes of the hull girder. As the natural periods of the hull girder vibrations is much larger than the duration of the impact, information about the local pressure peaks and durations is not important for this case. For this case the response will be govern by the total force pulse. The local structure can therefore be regarded as rigid for slamming force calculations as input to global response calculations i.e for whipping.

Slamming forces are discussed in the following.

4.2 Water entry and Slamming Loads

4.2.1 Description of slamming

Slamming loads are defined as local impact forces that can introduce local structural deformation and stresses as well as global response in the hull girder. Slamming loads is a large problem for design of ships and offshore structures. For ship design typical slamming problems will be;

- Bottom slamming in head sea waves, ballast condition
- Bow flare and stern slamming
- For Catamaran, wet deck slamming.

For offshore structures additional slamming force situation will be ;

- Impact from breaking waves towards vertical columns
- Salmming underneeth horizontal deck structures
- Impact forces on deck modules and equipment in case of green water above deck level

In Figure 4.3 an example of local damage due to bow flare slamming on a turret moored FPSO is shown.

Slamming loads are associated with a rapid increase of the added mass caused by the presence of the structure and its motion relative to the water. Near the edge of the expanding wet area, there will be high slamming pressures. Slamming loads may therefore be considered as a pressure-pulse that travels across the hull surface with a high velocity. This is illustrated in Fig. 4.4 for the case of water entry of a symmetric wedge.

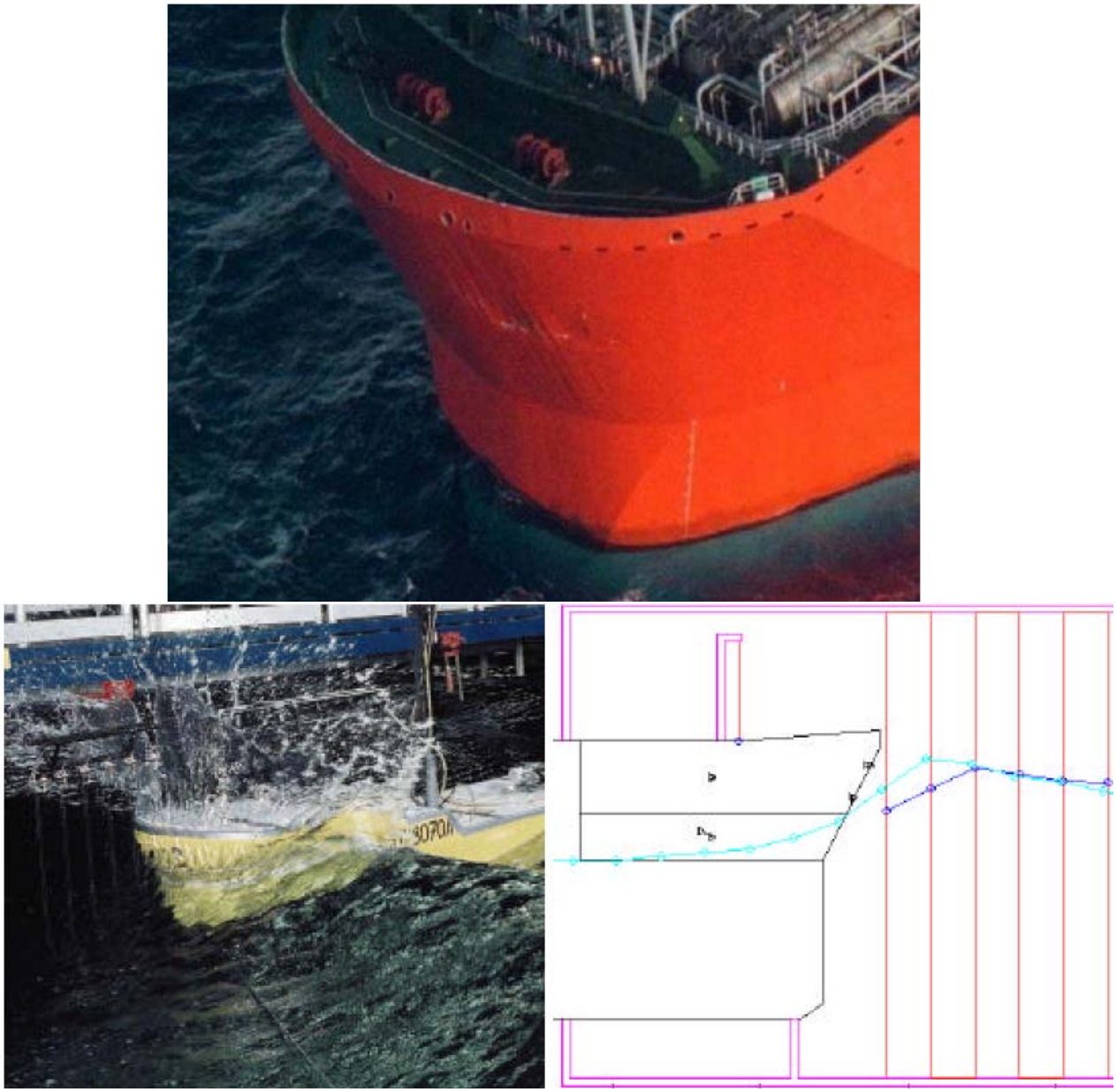

Fig 4.3 *Photo showing wave impact damage to bow of Schiehallion FPSO on UK sector and model testing of bow slamming incident for the same case*

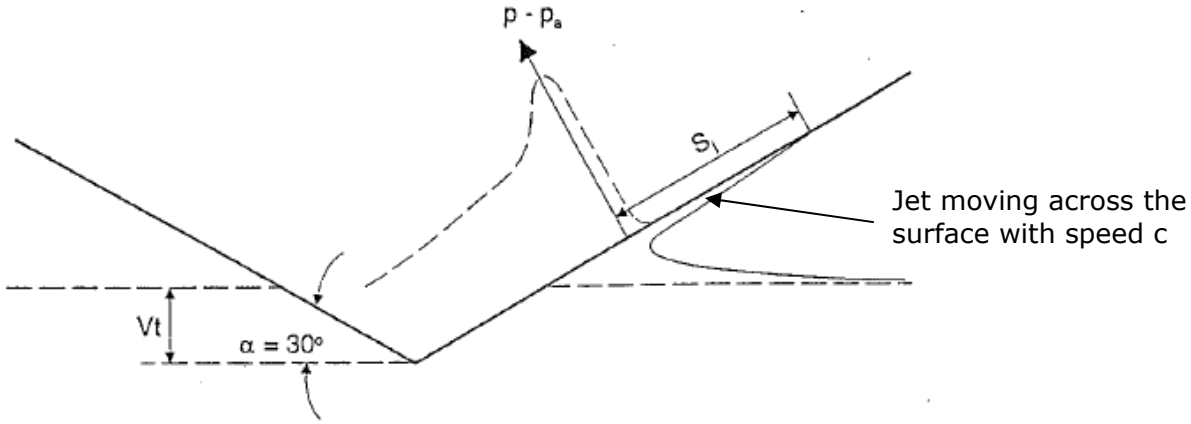

Figure 4.4 *Free surface elevation and pressure distribution on the body surface during water entry.*

An example of measured slamming pressure for a slam event is shown in Fig. 4.5A. The measured pressures are on a vertical wall hit by a very steep wave. The upper pressure cell is hit by the wave front and a very high local pressure is observed. At the position of the lower pressure cell an air pocket is formed and the peak pressure is lower but with a longer and more damped duration. This is due to the compressibility of the air pocket.

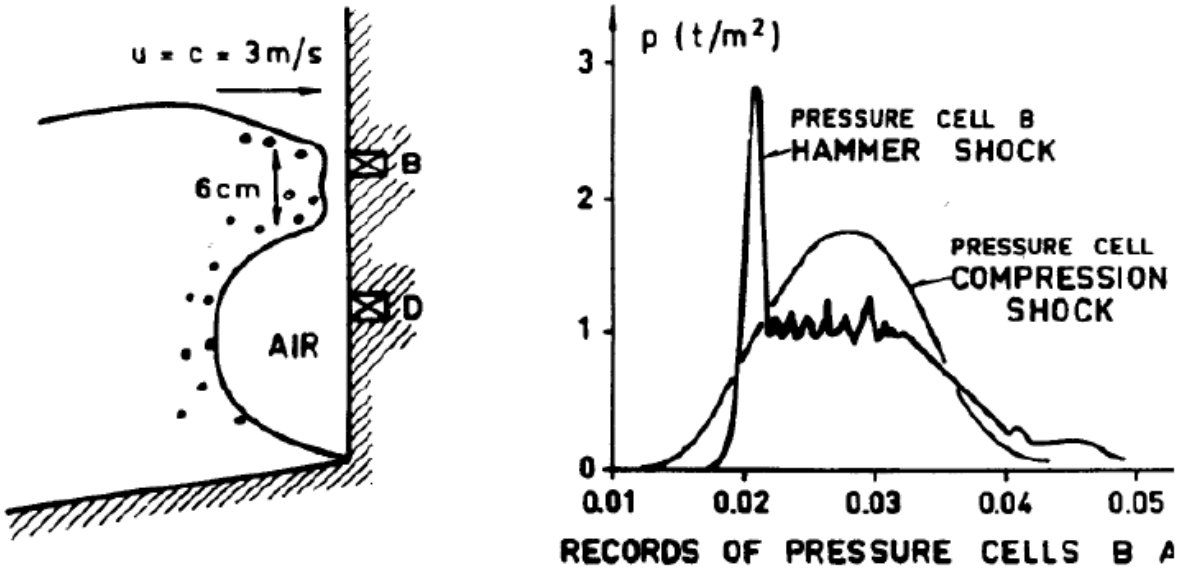

Fig 4.5A *Example of slamming force from a steep wave hitting a vertical wall.*

The average slamming pressure over a certain area will be strongly dependent on the size of the area. This is shown in Figure 4.5B. For local plating design a typical area of interest will be of the order of 5 m^2. For global whipping response the slamming force over a relatively large area is the main interest, typically the bow area.

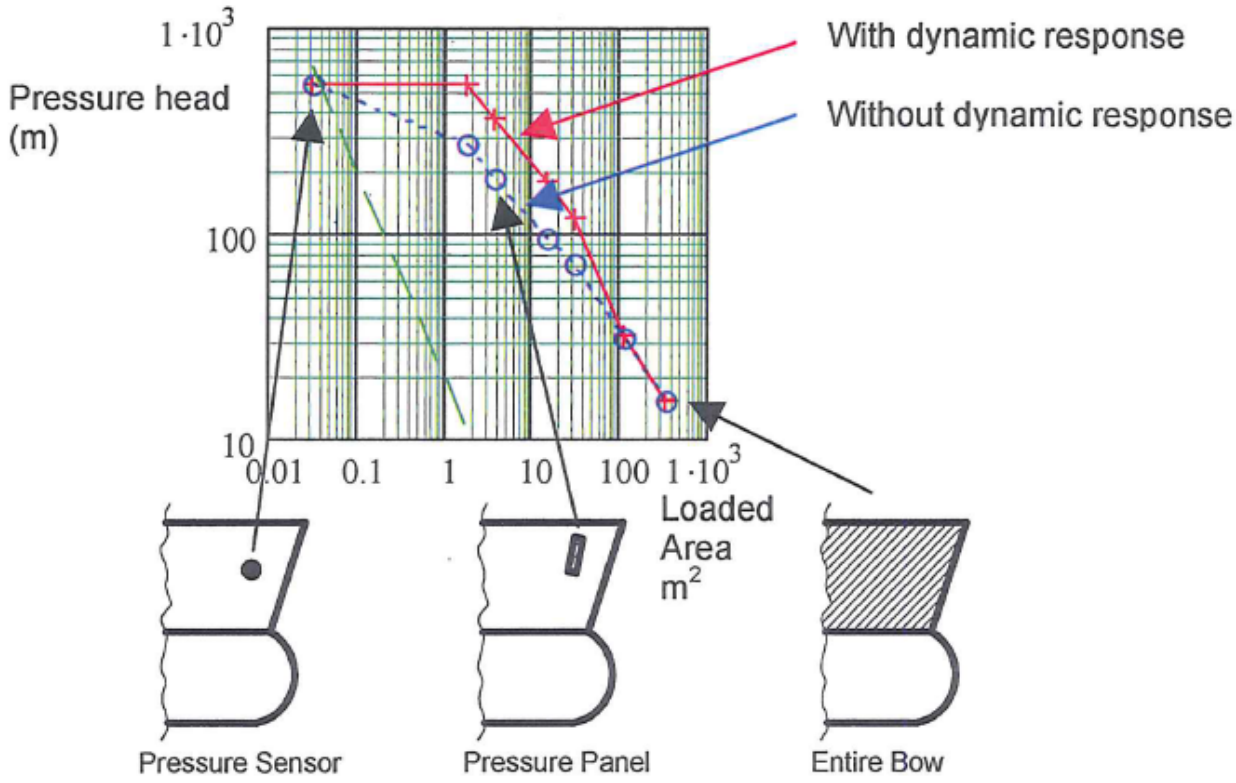

Fig 4.5B *Typical relation between slamming pressure and area.*

4.2.2 Slamming pressure and slamming forces

The slamming loads are governed by the relative velocity at the instant of impact and the angle between the structure and the free surface. Slamming pressures are high when the relative velocity V_R is large and the relative impact angle α_{rel} is small. Impact pressure can than be written as;

$$p = 1/2\rho C_P |V_R|^2 \tag{4.1}$$

Where C_P is the impact pressure coefficient, which can be assumed to be a function of the angle between the structure and the free surface. Examples of calculated C_P values are shown in Fig 4.6 for pressure distribution during water entry of a wedge with different deadrise angles.

The local peak observed for low deadrise angles are very local in space (and time) and therefore not important for the integrated force over a practical plate area. One is more interested in the force acting on the body during an impact.

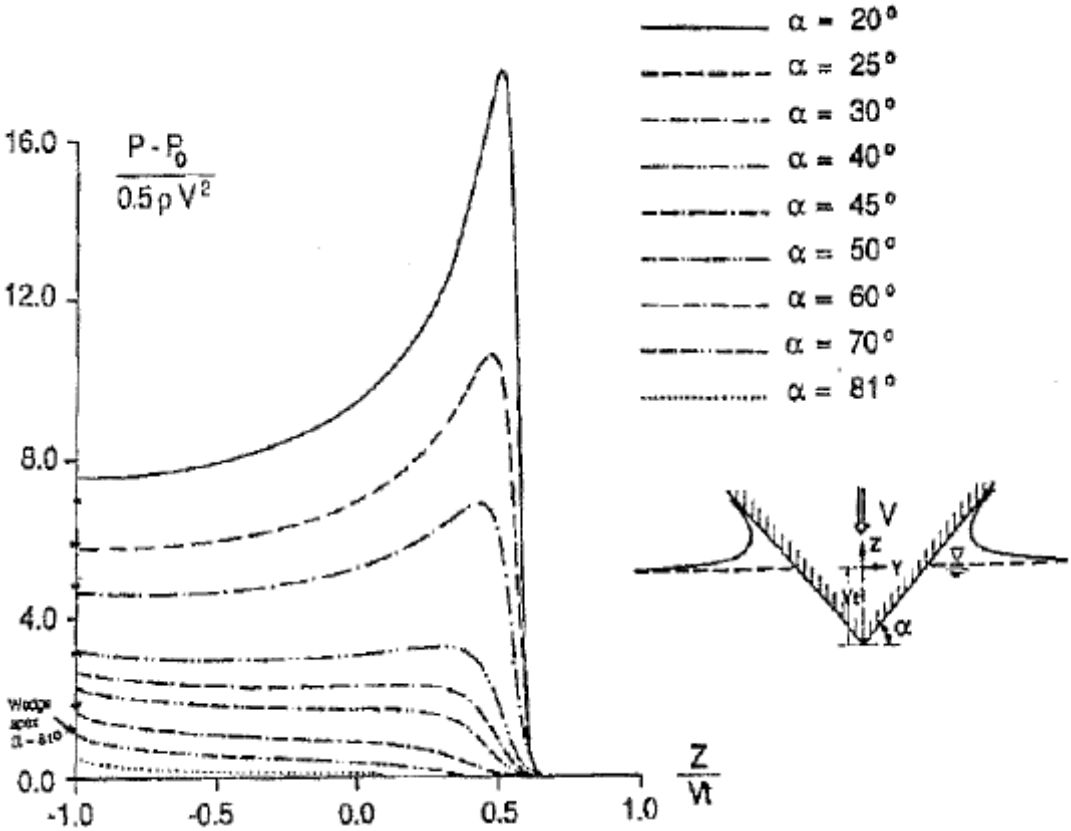

Fig 4.6 *Pressure distribution during water entry of a wedge as function of deadrise angle.*

For slamming calculations two different approaches is frequently used. The two different approaches are commonly referred to as;

- Von Karman Model; neglecting the effect of Pile-up
- Wagner Model; where effect of Pile-up is included

The most simple one is to measure the wetted length of the body from the calm water (or undisturbed) level. This imply neglecting the Pile up of water during the penetration of the body into the fluid. This is illustrated in Fig. 4.7. This solution is commonly referred to as

von Karman solution, see Faltinsen (1990) for details. Neglecting the Pile-Up will underestimate the actual wetted surface during the impact phase.

In the Wagner model the increase in wetted length due to the Pile-Up effect is included in the force calculations. This model require that the solution for the free surface elevation during the water entry phase is known.

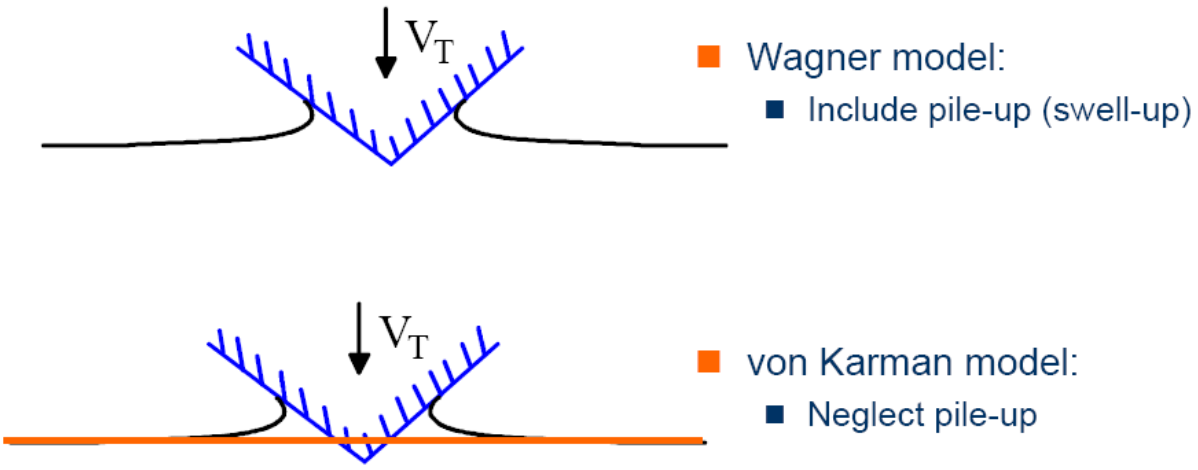

Fig 4.7 *Illustration of Wagner approach and Von Karman approach for slamming pressure calculation.*

As mentioned a slamming event is associated with very high pressure peaks with a very local extent in time and space. For global responses the main interest is not this local pressure peak but rather the integrated force on the body when hitting the water surface and proceeds through the water.

From Momentum considerations a formula for the slamming force acting on a body penetrating the free surface with a vertical velocity equal to *V* can be written as (Faltinsen (1990));

$$F_{SLAM} = \frac{d}{dt}\left(A_{33}V\right) + \rho g V_D \tag{4.2}$$

Where V_D is the submerged volume, and A_{33} is the high frequency added mass in heave, i.e $A_{33}(\omega \to \infty)$ as function of submergence relative to calm water. Neglecting the hydrostatic term $\rho g V_D$ the slamming force can be expressed as:

$$F_{SLAM} = \frac{dA_{33}}{dz}\frac{dz}{dt}V + \frac{dV}{dt}A_{33} = \frac{dA_{33}}{dz}V^2 + a_z A_{33} \tag{4.3}$$

where the first term is the slamming force and the last term is the acceleration times the added mass which is equal to zero for constant impact speed. This shows that the slamming force can be determined from the relative impact velocity and the space derivative of Added mass.

The above slamming force formula based on Momentum considerations applies both for 2-Dimensional and 3-Dimensional flow.

For the 2-Dimensional case the instantaneous value of added mass as function of submergence can be estimated from the flat plate solution for the case $A_{33}(\omega \to \infty)$;

von Karman Solution; $$A_{33}{}^{(2D)}{}_{Karman} = \frac{1}{2}\rho\pi\left(\frac{B}{2}\right)^2 \quad (4.4)$$

Wagner Solution; $$A_{33}{}^{(2D)}{}_{Wagner} = \frac{1}{2}\rho\pi\left(\frac{B_W}{2}\right)^2$$

The interpretation of instantaneous breadth is shown in Fig. 4.8. Using the von Karman approach the breath B is simply the actual breath at the actual free surface. For the Wagner approach the breath B_W also include the effect of Piled-up water, i.e the effecient wetted surface is used in the added mass calculation.

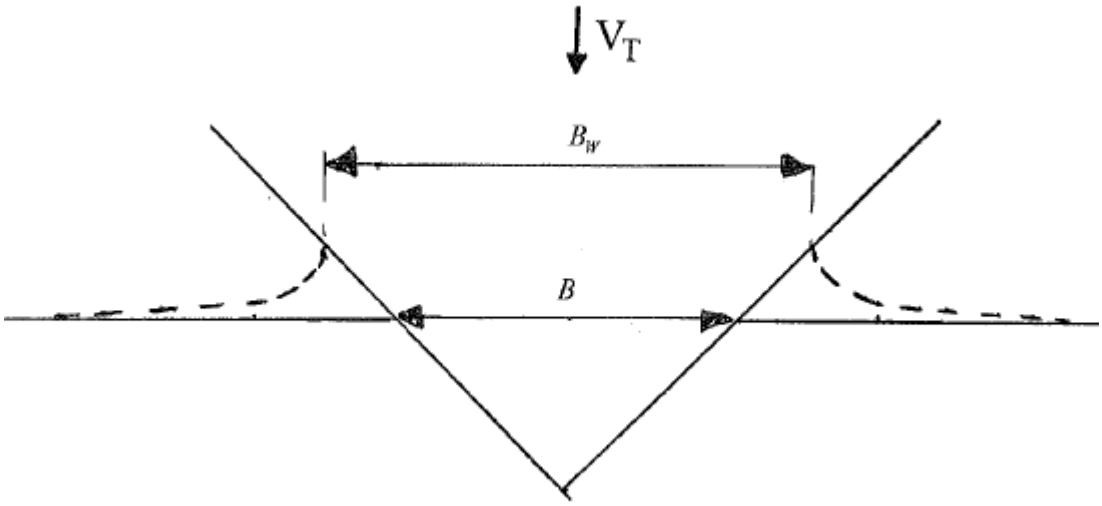

Fig 4.8 *Sketch of equivalent Flat plate breath as used in added mass calculation. von Karman and Wagner Solutions.*

It can be shown that for a wedge case as shown in Fig. 4.8 the difference in B due to pile up can be written as;

$$\frac{B_W}{B} = \frac{\pi}{2} \quad (4.5)$$

which gives;

$$\frac{A_{33}(2D)_{Wagner}}{A_{33}(2D)_{Karman}} = \left(\frac{\pi}{2}\right)^2 \approx 2.47 \quad (4.6)$$

This ratio will also apply for the difference in slamming forces calculated using the two different approaches. This results applies for a wedge solution.

For the case of a 2-Dimensional circular cylinder the following results are obtained for the vertical impact force coefficient for the initial time of impact between a horizontal cylinder and a still water, see Faltinsen (1990).;

von Karman Solution; $$C_S = \frac{F}{1/2\rho {V_R}^2 D} = \pi$$

Wagner Solution; $$C_S = \frac{F}{1/2\rho {V_R}^2 D} = 2\pi$$

Where C_S is the slamming force coefficient derived from the slamming force as shown above. This shows that for the circular cylinder case the slamming force ratio between Wagner and von Karman solution will be 2.0.

The above values represent the *initial* impact. In Fig 4.9 results for measured and calculated slamming force coefficient for the entire water entry phase for a 2-Densional circular cylinder with radius *R.* The calculated C_S is based on the momentum formula, eq. (4.3) using the von Karman approach. The shown A_{33} as function of submergence is based on numerically calculated added mass using a sink-source method. The shown C_S value is than calculated from;

$$F_{SLAM} = \frac{dA_{33}^{2D}}{dz} V^2 = \frac{\rho}{2} C_S \, 2RV^2$$

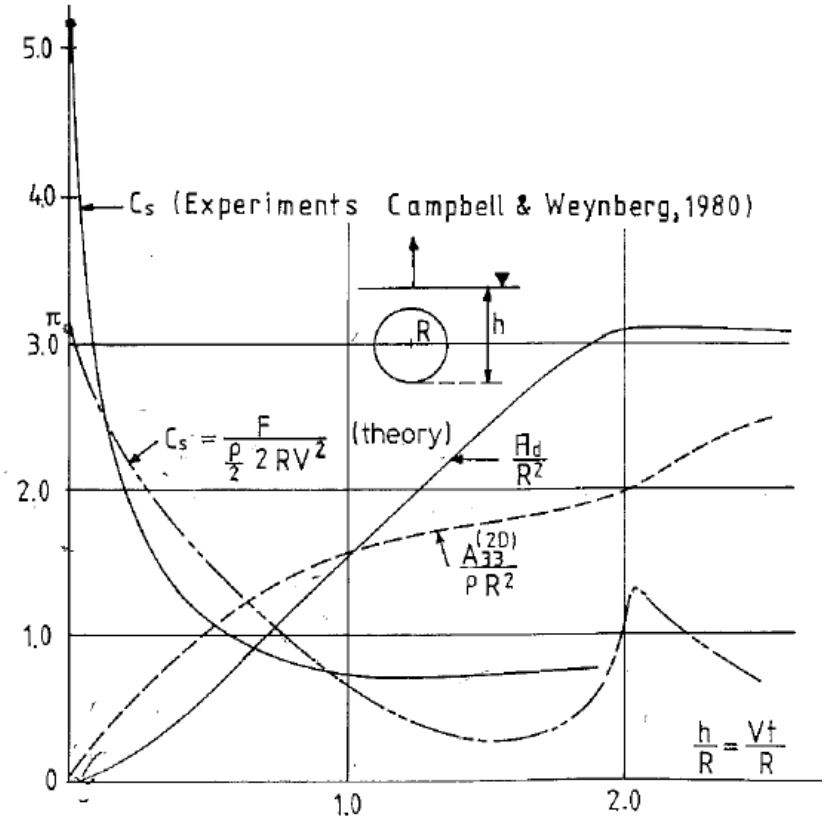

Fig 4.9 *Water entry for Circular cylinder. Constant vertical velocity, V. Slamming Force coefficient C_S.*

The experimental results by Campbell & Weynberg (1980) is also shown in the figure. The agreement between calculated and measured slamming force is reasonable good for *h/R<1.*, although the measured initial slamming force is closer to the Wagner solution value of 2π. For *h/R>1* the jet will leave the cylinder surface and the upper part of the cylinder will remain dry even for h *h/R>2.* This is illustrated in the photos in Fig. 4.10 from water entry of circular cylinder. The theoretical assumptions used for wetted surface and hence as basis for the slamming force formula are therefore no longer valid when *h/R>1.*

Due to the simplicity (no need for calculation of the free surface elevation during the water entry) the von Karman Approach is usually used for slamming load calculations as input to Whipping analysis. From the above results it can be concluded that this approach underestimates the actual slamming forces.

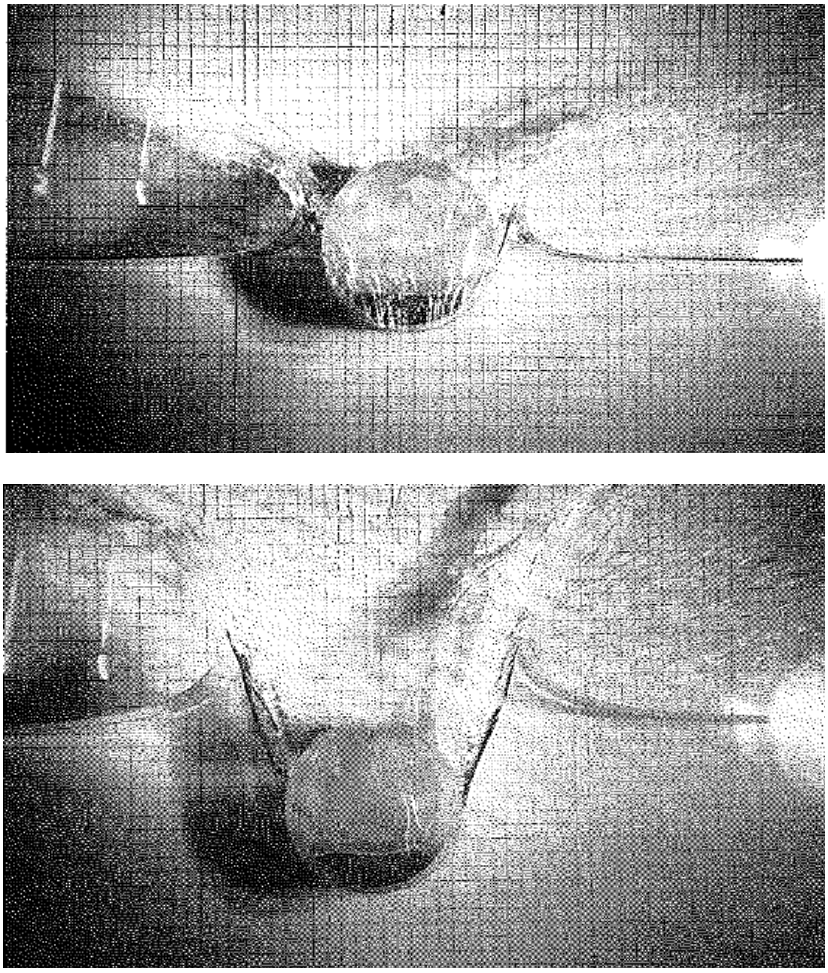

Fig 4.10 *Flow visualization of water entry of a circular cylinder. (from Greenhow & Lin (1983)*

4.2.3 Numerical calculation of Slamming pressure and slamming forces

The momentum method for slamming load calculation as discussed above is a simplification and does not account for the pile-up of water. Moreover it can not be applied directly to a flat ship bottom or to bulbous bow section.

A numerical method for slamming force on a general 2-Dimensional section have been developed by Zhao et al. (1996). The solution is based on using a numerical Boundary Element Method. The method is implemented in the computer program *"Slam2D".* The key feature of the method can be summarized as follows;

- Generalization of Wagner's (1932) method to larger deadrise angles and arbitrary section geometry.
- Includes pile-up of water close to the section
- 2D boundary value problem with kinematic boundary condition applied on the exact body surface.
- Gravity neglected
- Solved by a using a boundary element method (BEM) for each time-step.
- Includes separation from points where geometry changes abruptly (simplified formulation), see Fig 4.10
- Calculates *pressure distribution* – not only total sectional force

One of the problem with slamming force calculation for arbitrary shaped sections how to handle abruptly geometry changes. This is illustrated in Fig. 4.11 for a typical bow section.

In this numerical method this problem is overcome by introducing an artificially body shape following the separated flow as shown with blue line in Fig. 4.10. In this way a very robust code able to handle any 2-Dimensional shape is achieved.

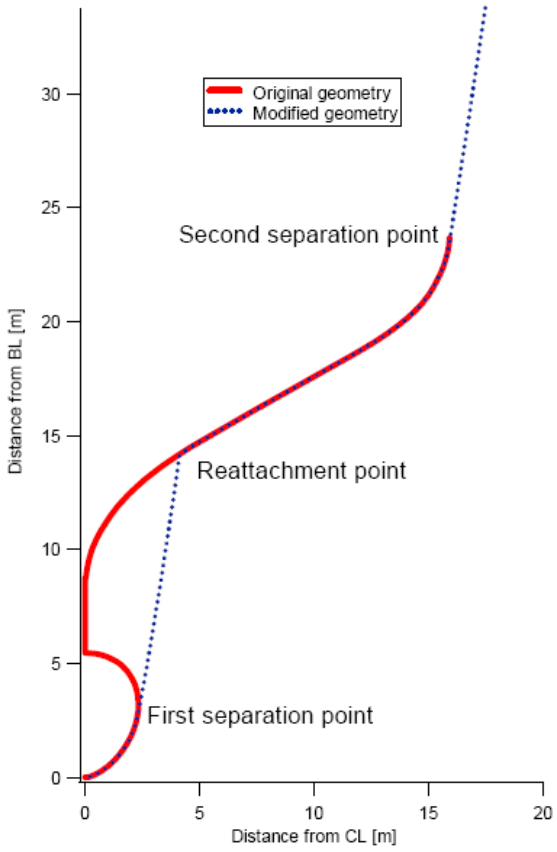

Fig 4.11 *"Slam2D"; Example of automatic modification of Geometry.*

Comparison of different methods for calculations of vertical slamming forces on a symmetric wedge during impact is shown in Fig. 4.12. The slamming force is shown as function of deadrise angle *α*. On the vertical axis the term $\frac{F_{SLAM}}{\rho V^3 t}(\tan\alpha)^2$ is shown. Results from the following solution methods are shown;

- Wagner solution. Gives $\frac{F_{SLAM}}{\rho V^3 t}(\tan\alpha)^2 \approx 7.8$
- "Slam2d"
- Similarity solution
- Von Karman solution. Gives $\frac{F_{SLAM}}{\rho V^3 t}(\tan\alpha)^2 \approx 3.2$
- Von Karman, Momentum approach

It is seen that "Slam2d" gives almost identical results to the similarity solution. As for the earlier comparison the von Karman based method underestimates the slamming forces. The Wagner solution is seen to over predict the slamming forces for increasing deadrise angles.

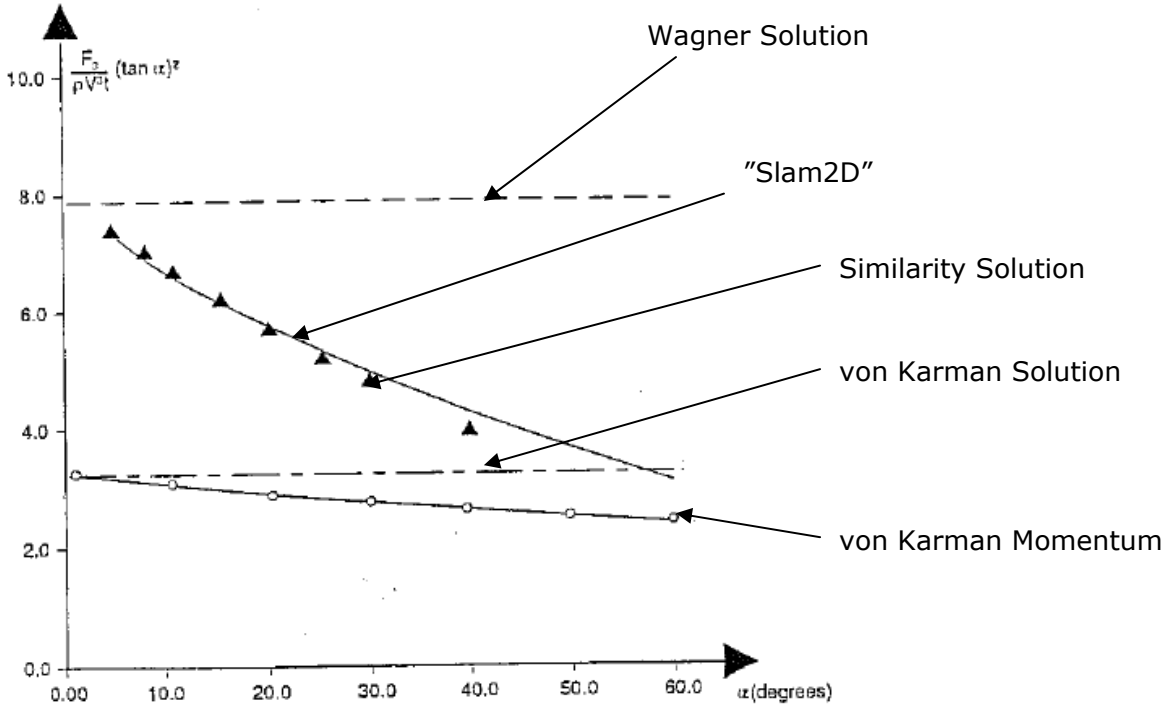

Fig 4.12 *Calculated vertical slamming forces an on symmetric wedges during water entry. Slam2D"; Example of automatic modification of Geometry.*

"Slam2d" is as mentioned a 2-Dimensional method. It can be shown that for bow flare slamming loads the 2-D method will overpredict the slamming forces due to pronounced 3-Deffects in the bow area. Hermundstad and Moan (2005) introduced a correction method for 3-Dimensional effects and showed that this approach compared well with measured data.

"Slam2d" can be regarded as a "state of the art" method for 2-Dimensional slamming force calculations. For 3-Dimensional flow situations slamming load methods have been developed based on different theoretical and numerical approaches;

- 3D BEM methods
- 3D Volume discretization methods (Solving Navier-Stokes equations)

3-D Boundary element methods is used for bow flare slamming and for green water evaluation at the bow of ships and ship-shaped FPSO's. Such methods are also used for fixed gravity based structure and for horizontal impact force calculations towards vertical cylinders.

Navier-Stokes solver is methods becoming increasingly improved, but up to now they are not frequently used for design purposes. These methods require further development and validation before they are ready for commercial use for design purpose.

4.2.4 Experimental Validation of Slamming Force calculation; "Slam2D"

The case considered for validation of numerical calculations using the Slam2D code can be summarized as follow, see also Fig 4.13;

- 290 m Cruse vessel
- Head seas
- Two sea-states: Hs=7m and Hs=9m
- Three speeds: 0, 6 and 9 knots (i.e moderate speeds)
- 4 slamming panels in bow flare

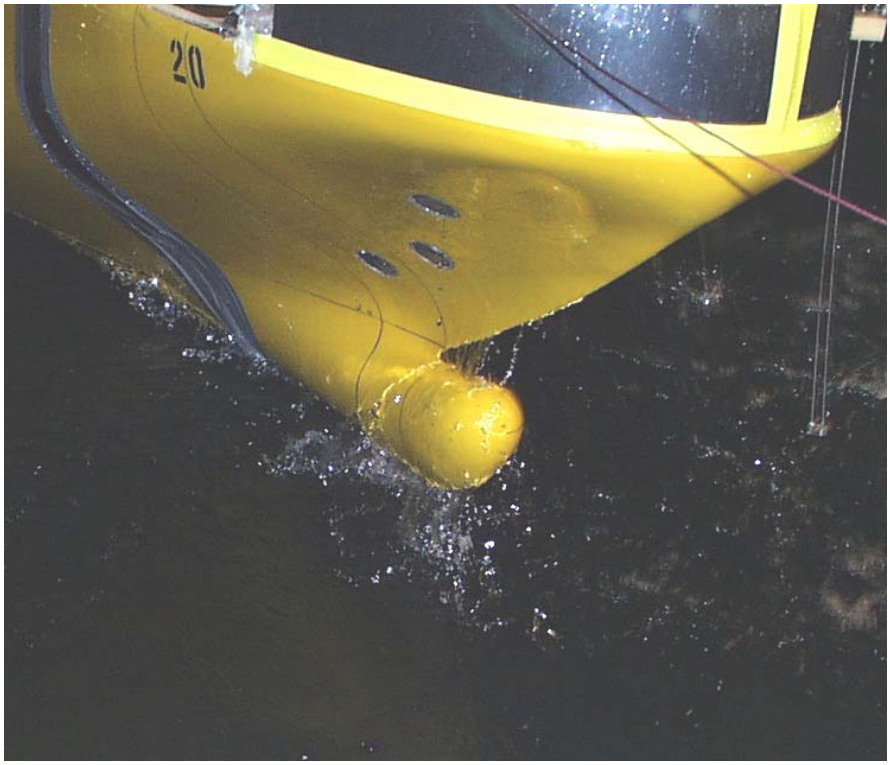

Fig 4.13 *Model test verification of slamming force prediction from Slam2D. Pressure cells at flared part of bow.*

Comparison of calculated and measured time series for heave and Pitch motions are shown in Fig 4.14. The results is for Head sea waves, for forward speed of 9 knots. A quite good agreement for both heave and pitch motion amplitudes is observed. For pitch motions a small phase lag is found.

In Fig. 4.15 time series of measured and calculated slamming forces on 4 different slamming panels in the flared part of bow are shown. The position of the slamming force panels is shown in Fig 4.13. The results illustrate the uncertainties in slamming force measurements. Small differences in relative motions between bow and incoming wave can give large differences in measured slamming loads. This is both due to slamming force being proportional to $U_{REL}^{\ 2}$ and also due the dependency of impact angle between hull panel and the wave surface. The comparison in Fig 4.14 shows that for each of the individual slamming peaks the difference are in general quite large, but the load level are quite similar for measured and calculated slamming loads. The comparison should therefore be evaluated as a good agreement between measurements and calculations of slamming loads.

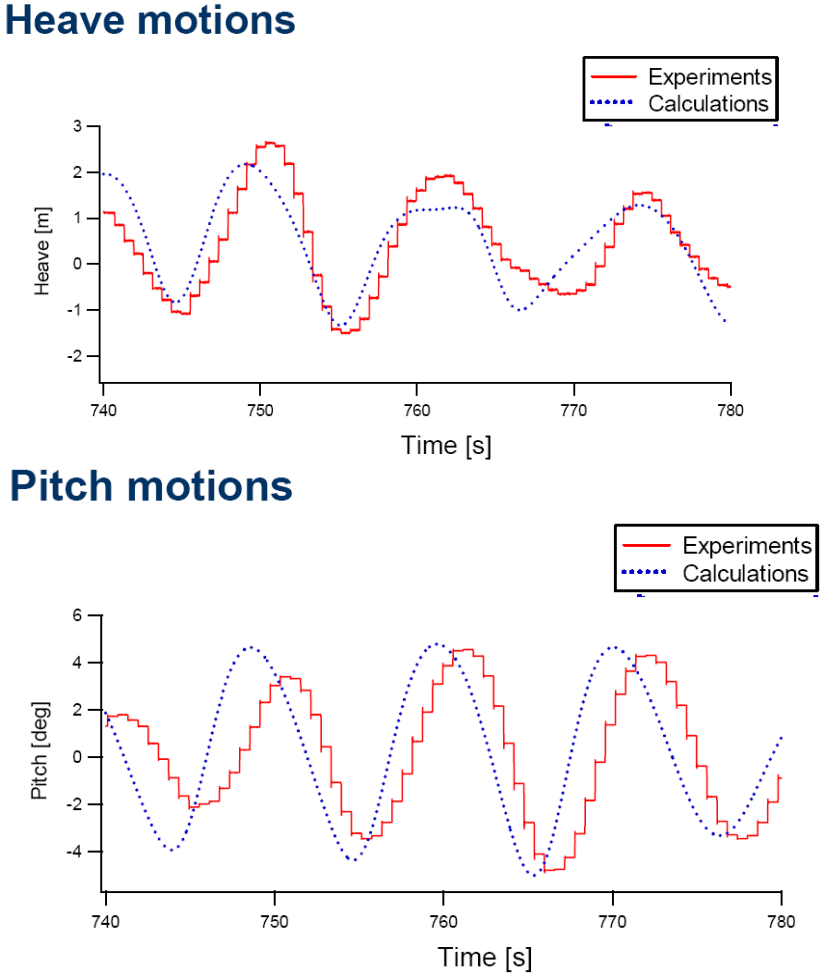

Fig 4.14 *Model test verification of Slam2D. Measured and calculated heave and Pitch motions. U=9 knots, Hs=9.0 m*

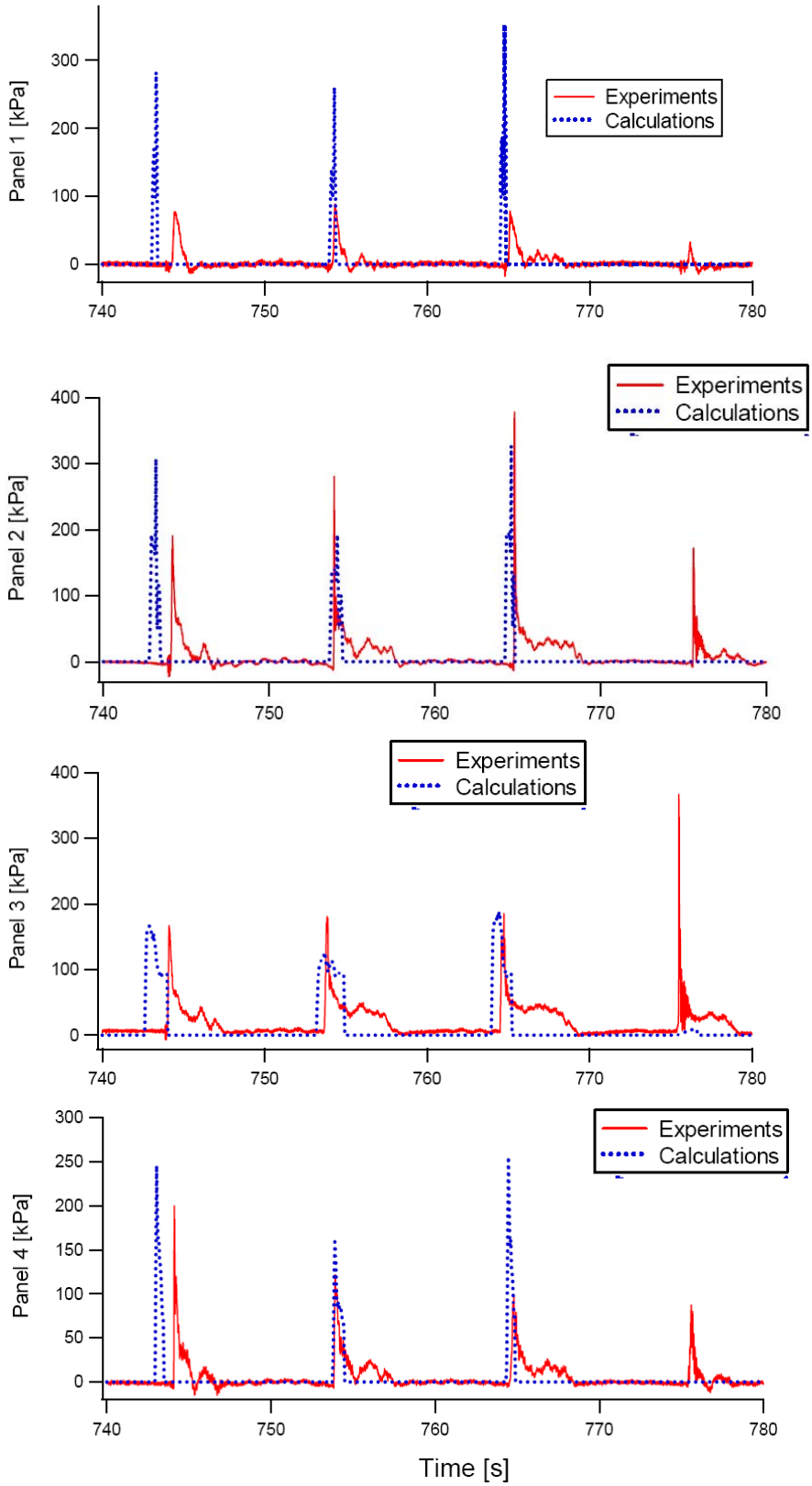

Fig 4.15 *Model test verification of Slam2D. Measured and calculated Slamming force at Slam panels 1-4. U=9 knots, Hs=9.0 m*

4.3 Dynamic effects on slamming loads

4.3.1 Effect of dynamic response – Given Impact load

The slamming force depends on the relative velocity squared between the water and the panel, i.e. $\propto U_{REL}{}^2$. Taking the elasticity of the panel into account the vibrations of the panel will generally affect the relative velocity and hence the magnitude of the slamming force. The dynamic response of the structure is also important for the resulting stresses and hence for design. The magnitude of this amplification depends on the rise time and decay time of the force pulse and the natural period of the affected structure including any added mass of water moving with the plate panel.

Impact loads are transient problems and hence the traditional way of analysis of harmonic response can therefore not be used. To investigate the dynamic amplification of response due to a slamming loads a simple 1 degree of freedom dynamic system is considered;

$$(m+a)\ddot{x} + b\dot{x} + cx = F(t) \tag{4.7}$$

where *m, a, b* and *c* are the mass, added mass, damping and stiffness respectively. *F(t)* is the impact load. The natural frequency of this system is:

$$\omega_N = \sqrt{\frac{c}{m+a}} \tag{4.8}$$

For a harmonic excitation the steady state solution is well established and a function of excitation frequency only. For an general time dependent impact force the equation must be solved with numerical time integration, see Appendix A for a general discussion of response of a 1 dof system. In the following some special cases are considered.

The ratio between the dynamic response and the static response to the maximum force can be expressed as a Dynamic Amplification Factor *(DAF);*

$$DAF = \frac{x_{MAX}}{F_0/c} \tag{4.9}$$

The Dynamic Amplification Factor (DAF) will typically depend on the following parameters;

- Rise time of the impact. Defined as the time from the impact starts to maximum value is reached.
- Decay time
- Natural frequency of the system excited.

A typical impact can be assumed characterized by a linear rise and an exponential decay as shown in Figure 4.16. The parameters Rise Time *(Tr)* and half decay time *(T½d)* is defined in the figure.

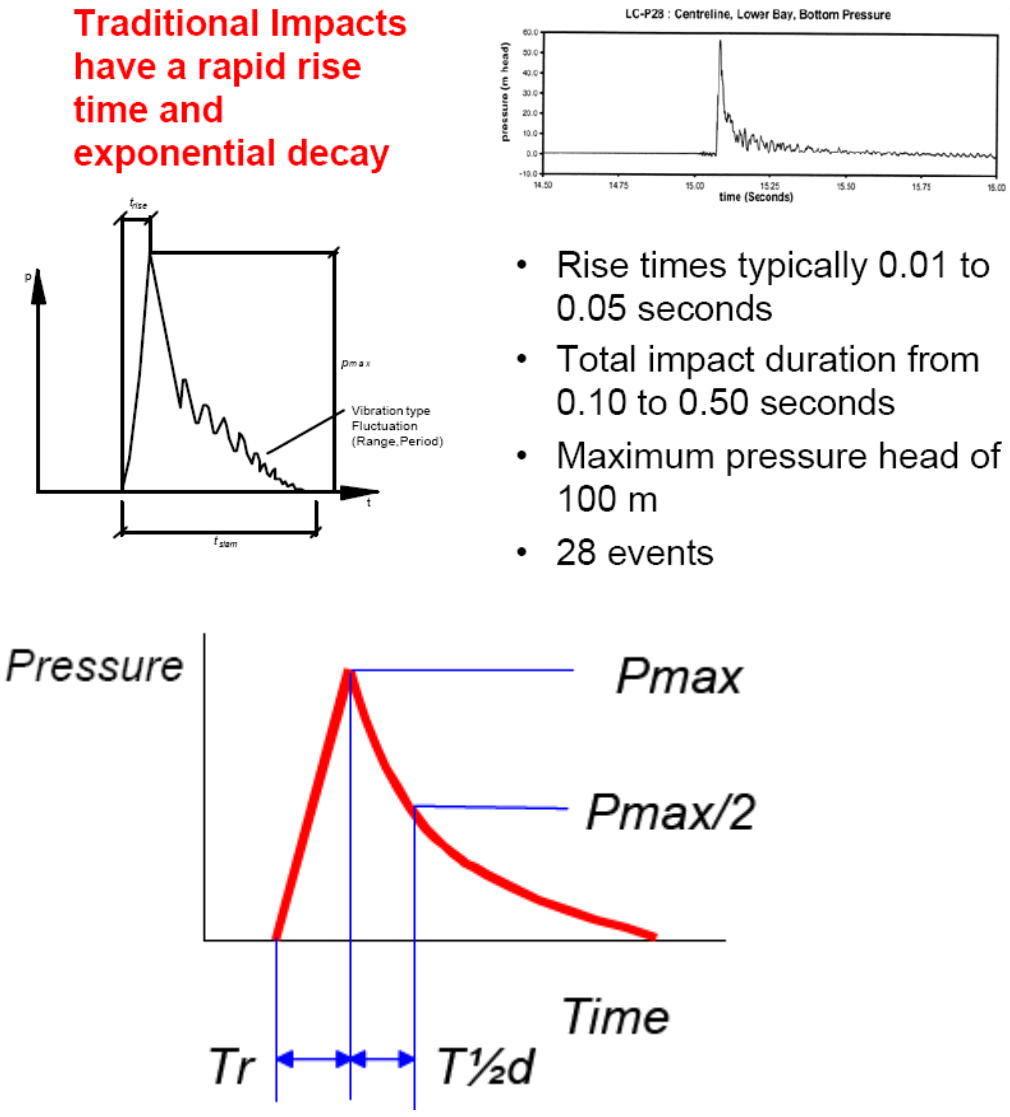

Fig 4.16 *Definition of rise time (Tr) and half decay time (T½d) for a slam.*

Results for the Dynamic Amplification Factor (DAF) for different ratios between Rise Time/Natural period and Decay Half Time/Rise time is shown in Fig. 4.17. Some important results can be drawn from the figure;

- Maximum dynamic amplification is 2.0. This occur for a vary low rise time (i.e much less than the natural period) and with a slow decay after maximum load. Theoretically DAF=2.0 requires a rectangular pulse with duration longer than 0.5 time the natural period.

- For Rise time greater than the natural period, DAF=0.95-1.2 i.e very close to 1. For this case the DAF is not sensitive to the decay time.

- For a triangular impact pulse the maximum DAF will be DAF=1.77

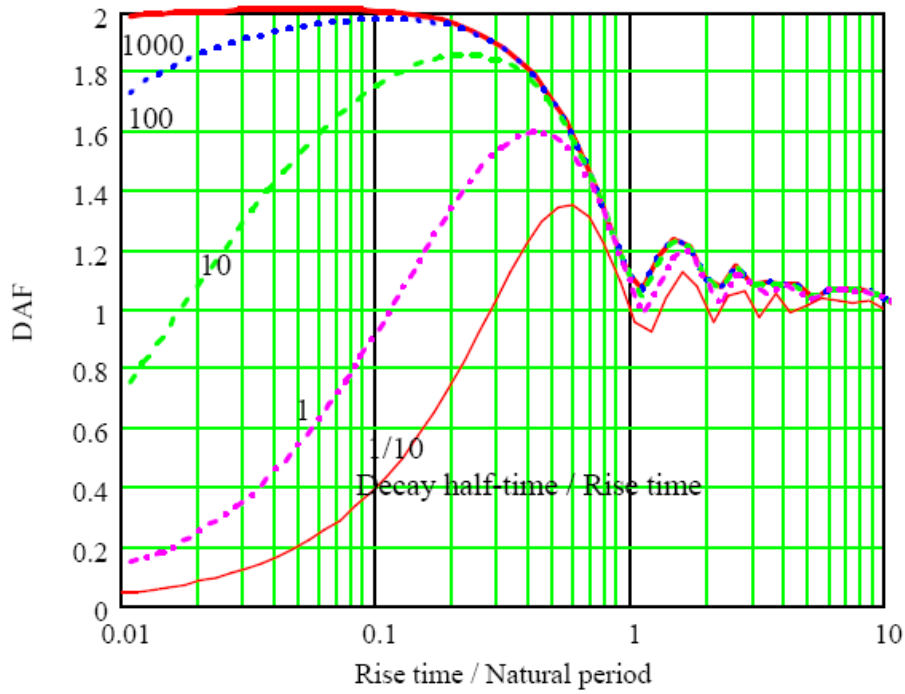

Fig 4.17 *Dynamic Amplification Factor for a linear force rise and exponential decay.*

As an example consider a large local slam with the rise time *Tr=0.01 s* and half decay time *T½d=0.01s.* For a plate panel with natural period T_N*=0.1* the DAF will be approximately DAF=0.96, see Fig. 4.17. The time history of the impact force and response is illustrated in Fig 4.18. This shows that the dynamic amplification of the local panel can be less than 1.

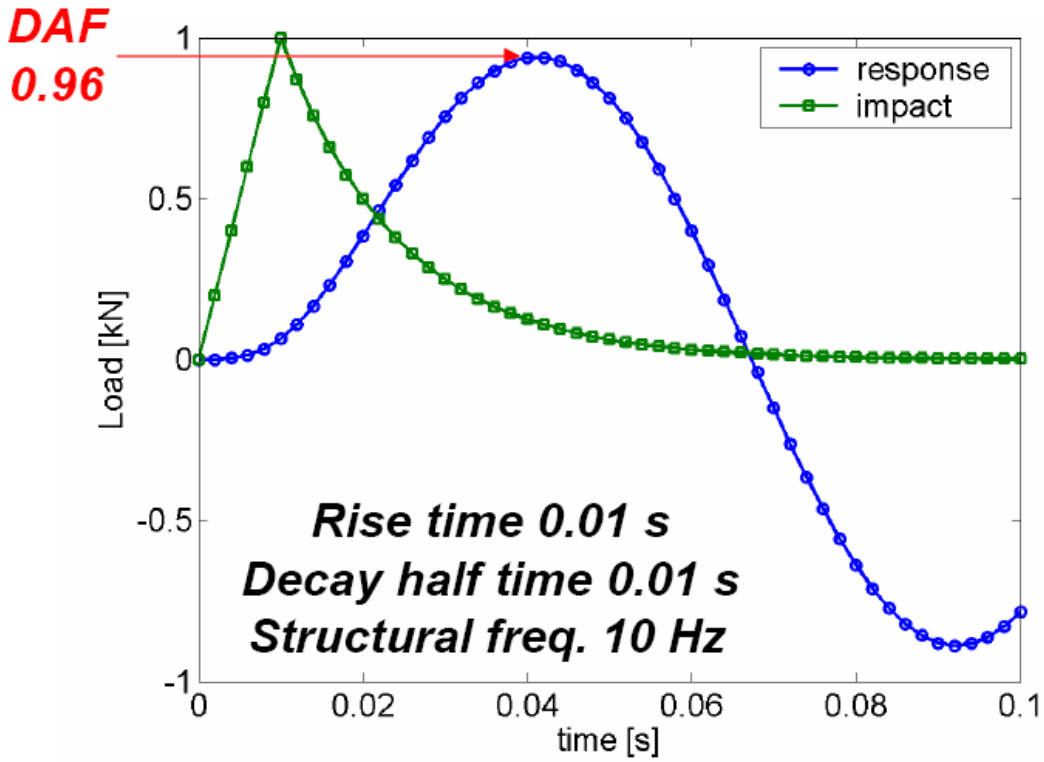

Fig 4.18 *Example of slamming case with DAF<1.0*

Another example is shown in Fig 4.19 for a stiffened panel with an immersed natural frequency of 20 Hz. Assuming a rise time *Tr=0.01 s* and half decay time *T½d=0.03s.* The

Rise time divided by natural period is 0.2 and the ratio decay half time/Rise time is 3. This gives DAF=1.66 as shown in Figure 4.18.

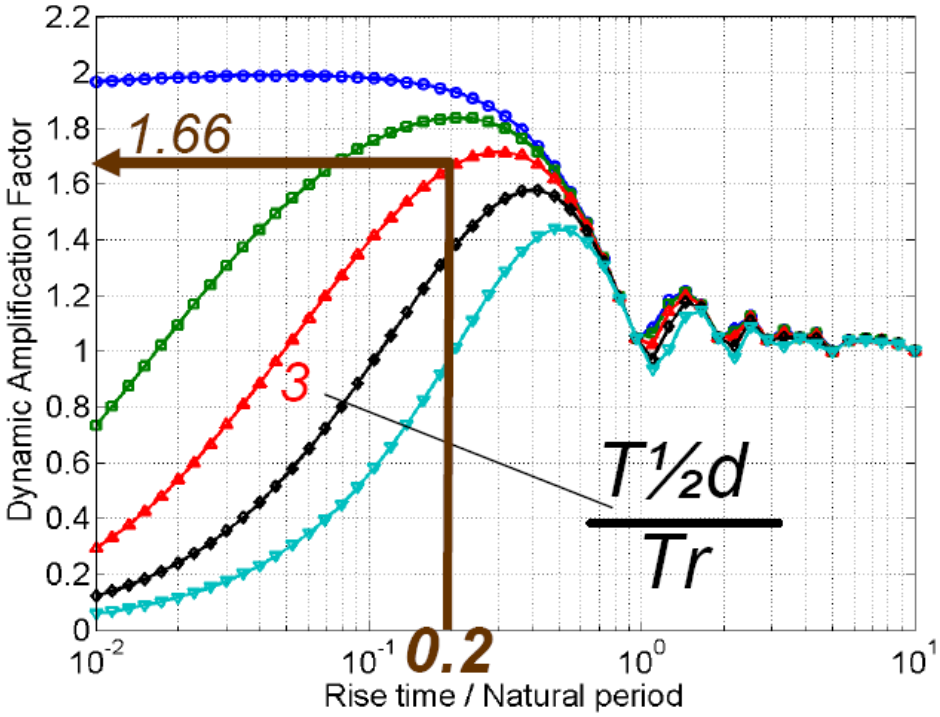

Fig 4.19 *Example of slamming case with DAF>1.0*

The above results can be used for evaluation of dynamic amplifications of stress level for local plated structure.

For the global whipping response this simplified 1 dof model may also be used for a approximately evaluation of dynamic amplification of a slam event. The relevant natural frequency for this case will be the lowest wet mode frequency. The slamming impact parameters for this case have to be based on the total slamming load (integrated over the entire bow flare area in case of bow flare slamming or bottom area in case of bottom slamming).

4.3.2 Measurements of slamming Loads

The transducer system used for measurements of slamming loads will show a similar dynamic behavior as discussed above for stiffened plates. This imply that the measured slamming force is not exactly the slamming pressure integrated over the transducer area but includes the dynamic response of the transducer system governed by the dynamic model as given in eq. (4.7). Two typical examples of measured "slamming force" is shown in Fig. 4.20. The first is for an impact with a long duration compared to the transducer natural frequency where no vibrations were generated. For this case the actual slamming loads can be detected with good accuracy. The second is from a slam where the impact has generated large resonance vibrations in the transducer. For this case it is difficult to estimate the actual slamming force.

The effective oscillating mass of the transducer can be estimated from the oscillating structural mass of the transducer plus the actual added mass of the immersed transducer plate. The stiffness is determined from the natural frequency using the estimated total mass. By using numerical simulations similar to described above the actual slamming force can be determined. The measured response signal is used as input and the parameters as Rise time and duration of slam is tuned to fit the simulated response to the measured signal. An example of this process is shown in Fig. 4.21. As can be seen a very good agreement between measured and simulated response have been achieved. In this way a reliable estimate of the actual slamming force time history have been obtained.

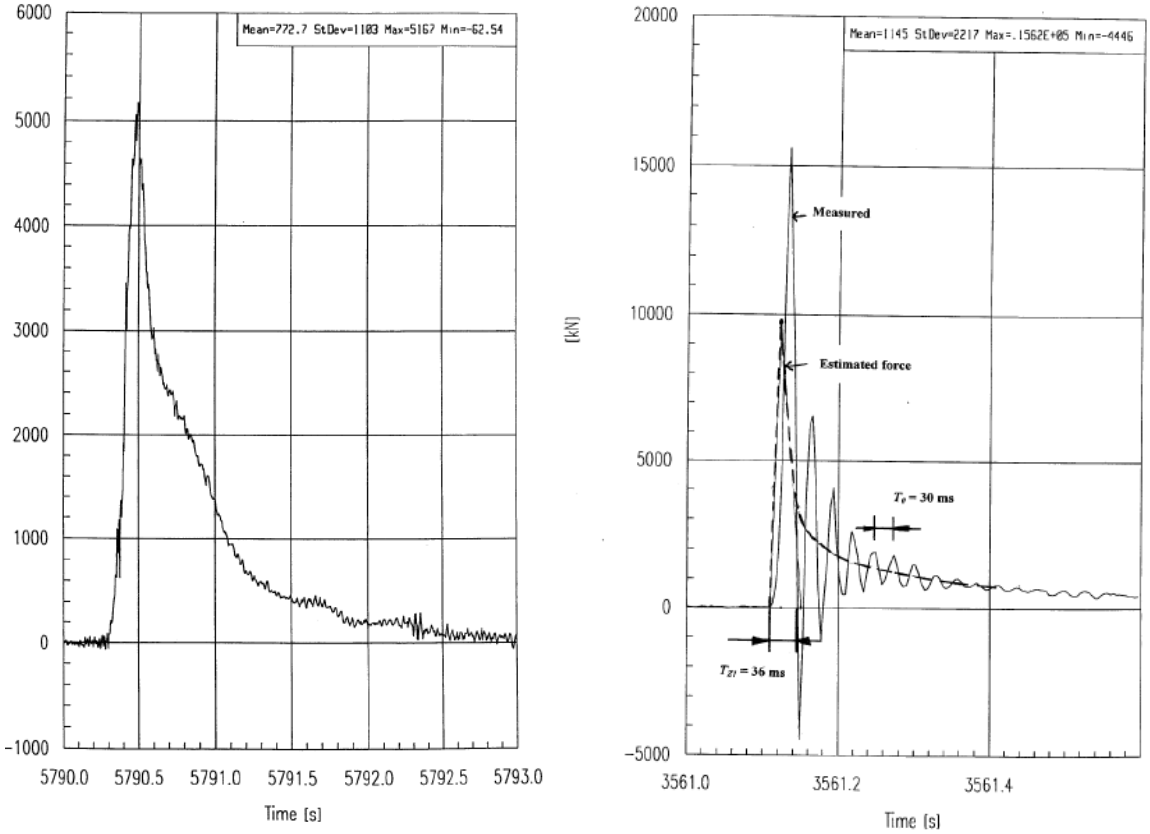

Fig 4.20 *Example of measured slamming forces in Model tests.*
Left; a long slam, i.e with duration well above Natural period.
Right; short impact with dominating transducer resonance vibrations.

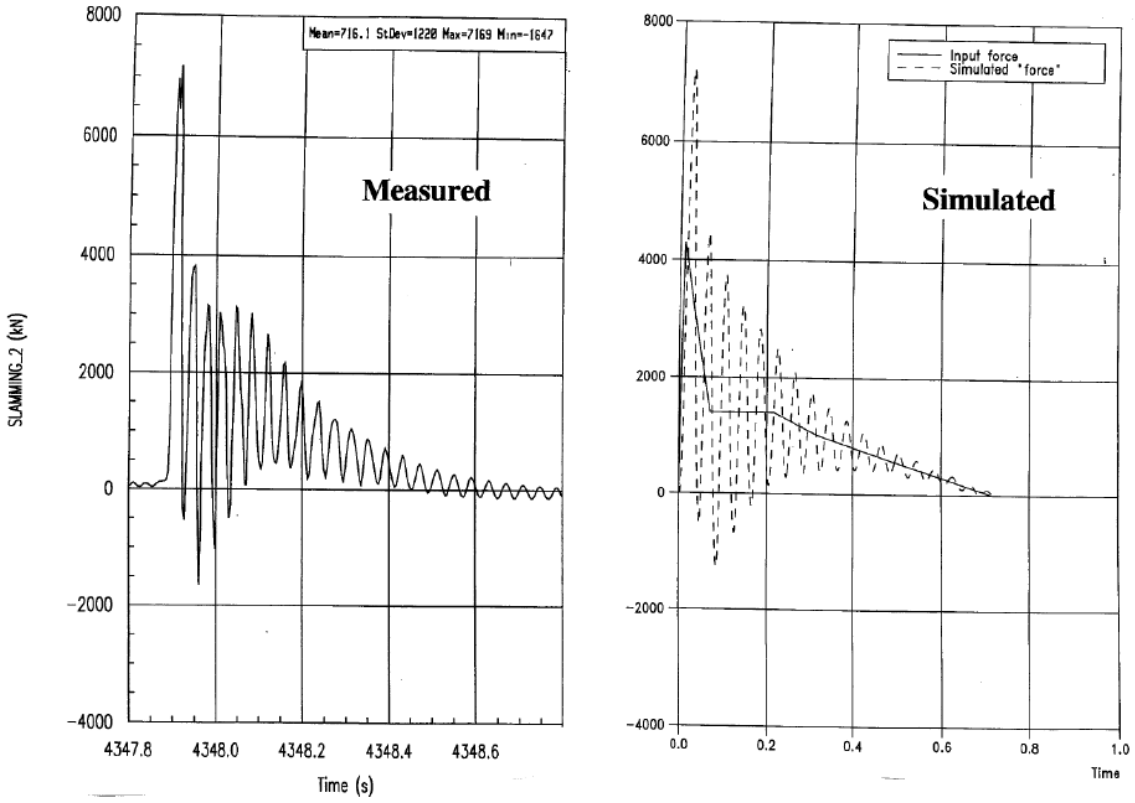

Fig 4.21 *Example of measured slamming force and simulated response. End result is the Input slamming force.*

4.4 Whipping Response Calculation

The prediction of slamming force as input to whipping response calculation can now be summarized as follows;

1. Use linear ship motion program to predict ship motions with forwards speed.
2. Calculate relative vertical motion and velocity for each section
3. Establish the slamming load for each section either by use of Momentum formula, eq. (4.3) or from numerical calculation, i.e. "Slam2d"
4. Correct for 3-Dimensional effect if relevant

For whipping response calculations it is normal to assume that the *local* structure responds statically I.e. structure can be assumed rigid when the slamming loads are calculated.

The *Global* structure (hull girder) responds dynamically to the slamming load. This elastic hull vibrations due to a slamming loads can be described by the beam equation, i.e. using the same equations as for the springing response, see eq. (3.18). The solution was written as a sum of normal modes;

$$y(x,t) = \sum_{i=1}^{N} q_i(t)\,\psi_i(x) \tag{3.14}$$

For the whipping case the hydrodynamic load is not a harmonic function, but a general time dependent function. This is accounted for by rewriting the beam equation on generalized form, eq. (3.18) to the form;

$$\ddot{q}_i + 2\alpha_i \dot{q}_i + \omega_i{}^2 q_i = \frac{\bar{f}_i(t)}{T_i} \tag{4.10}$$

where $2\alpha_i = \dfrac{\bar{b}_i}{\bar{m}_i + \bar{a}_i}$ is the damping ratio, $T_i = \bar{m}_i + \bar{a}_i$ and $\bar{f}_i$ is the generalized time dependent slamming force.

Due to the general time dependency of the slamming force, the solution of this equation will be given as a convolution integral (see Appendix A for details):

$$q_i(t) = \frac{1}{\omega_i T_i} \int_0^t e^{-\alpha_i (t-\tau)} \sin \omega_i (t-\tau)\, \bar{f}_i(\tau) d\tau \tag{4.11}$$

As the typical duration of a slam event is much shorter than the natural period of the first elastic mode of vibration of the hull girder it will not be the slamming force amplitude itself which is of importance, but the force pulse. Assuming a slam event at $t = \tau$ with duration equal to Δt gives:

$$q_i(t) \propto \frac{e^{-\alpha_i(t)}}{\omega_i T_i} \sin \omega_i(t) \int_0^{\Delta t} \bar{f}_i(\tau) d\tau \tag{4.12}$$

Where $\int_0^{\Delta t} \bar{f}_i(\tau) d\tau$ is the impulse of the generalized slamming force.

The slamming force pulse can be calculated as;

$$I(x,t) = \int_0^{\Delta t} F_{SLAM}(\tau)d\tau = \int_0^{\Delta t} \frac{d}{dt}(A_{33}V)d\tau = A_{33}(\Delta t)V \qquad (4.13)$$

Where eq. (4.2) have been used for the slamming force (hydrostatic contributions neglected). Equation (4.13) shows that the slamming force pulse is given from the actual value of vertical added mass times the impact speed.

Numerical methods for whipping response calculations are discussed in more details in Chap 5.

4.5 Discussion of Whipping Response

4.5.1 Parameters governing the whipping response

Since whipping is due to slamming loads, parameters influencing the slamming loads are important. Main parameters for slamming loads can be summarized as follows;

- Bow (and stern) geometry. Wider shapes with pronounced flare give higher slamming loads. Wide and flat hull bottoms may also give large slamming forces
- Draft. Low draft at bow (or stern) gives more frequent and normally more severe slamming.
- Ship speed. Higher speed gives more frequent and normally more severe slamming.
- Ship motions. Large heave and pitch motions will cause more slamming.
- Wave condition. Waves that give large heave and pitch motions will give more slamming. Steep waves generally give more severe bow slamming loads.

Many of the same parameters important for springing, see chap 3.3, will also be important for the whipping response. The dynamic hull girder response due to the slamming loads depends on the dynamic properties of the hull. For a given slam impact the dynamic response will be determined by the hull girder stiffness and mass distribution. Damping is normally of less importance for the extreme whipping responses, since the peak response occurs during the first vibration cycle. For fatigue calculation the damping is of importance as the damping strongly influence the following amplitude levels after the impact.

4.5.2 Contribution from elastic response to fatigue damage

A systematic assessment of the contribution due to wave induced vibration stresses have been carried out by Drummen et. al. (2006). The study was based on extensive model test results and full scale tests for a container vessel. The model test program was carried out using an elastic modeled hull (segmented) and covered a wide range of sea states and forward speed conditions. For each sea state the wave frequency and high frequency responses were identified and analyzed with respect to accumulated fatigue damage. The wave frequency response will be equal to the results obtained by a ridged body approach. The high frequency response is the additional response caused by vibration of the elastic hull girder. This imply that the high frequency response can be interpreted as the contribution from whipping and springing response. From test results, full scale and model tests, it is very difficult to split contribution from whipping and springing as both gives responses at the natural frequencies of the elastic hull beam. Possible contribution from both springing and whipping are therefore included in this evaluation.

In Fig. 4.22 typical result from model tests for wave frequency and high frequency stresses measured at midship are shown. The actual sea condition is with spectral peak period, T_P=19.4 s, and significant wave height, *Hs=5.0m*. Ship speed is 20 kn, head sea. From the plot of the detailed whipping event it is seen that the whipping event gives a

significant contribution not only to the sagging moment but also to the hogging bending moment which is of concern for container vessels.

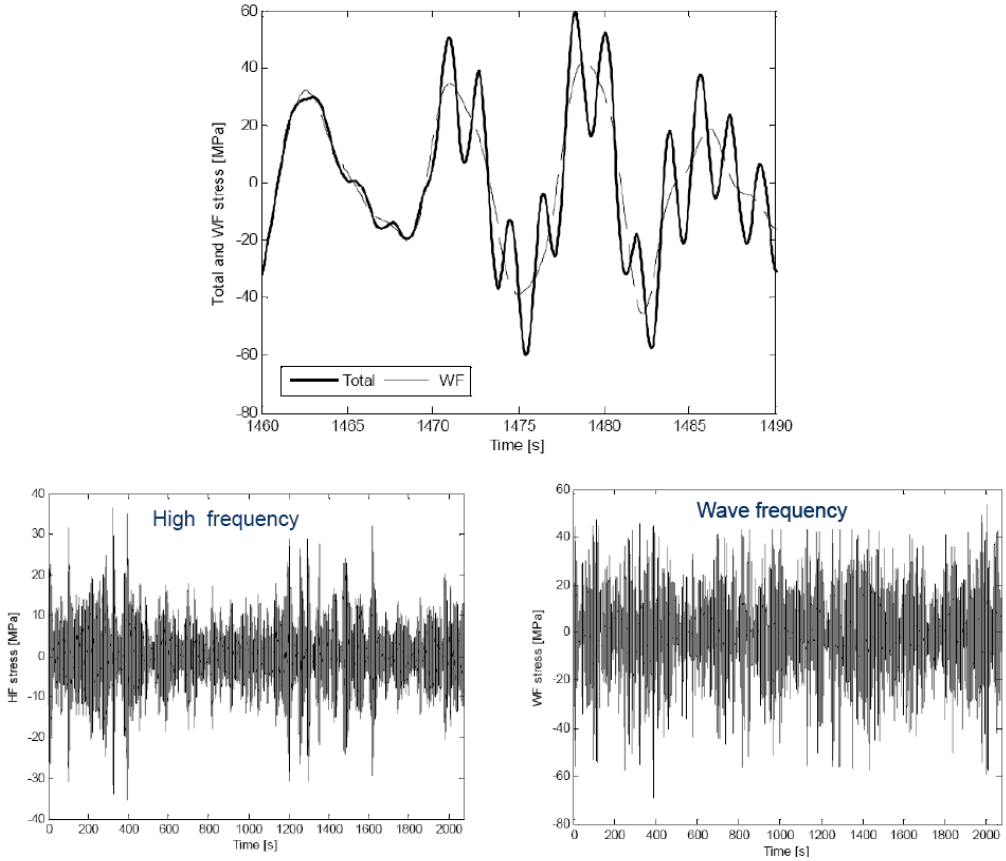

Fig 4.22 *Example of measured midship bending moment stresses. Sea state with Hs=5.0 m, T_P=10.4 s. U=20 kn. Top view; details of a whipping event. Lower left; High frequency contribution. Lower Right; wave frequency contribution. (From Drummen et al (2006))*

In Fig. 4.23 the main results from model tests for contribution to fatigue damage from wave frequency and high frequency bending moment responses are summarized. The results are given as function of the T_P and *Hs.* The results shows that in general the wave frequency contribution to damage is larger than the high frequency damage. Increasing *Hs* is seen to increase the relative importance of the high frequency contribution.

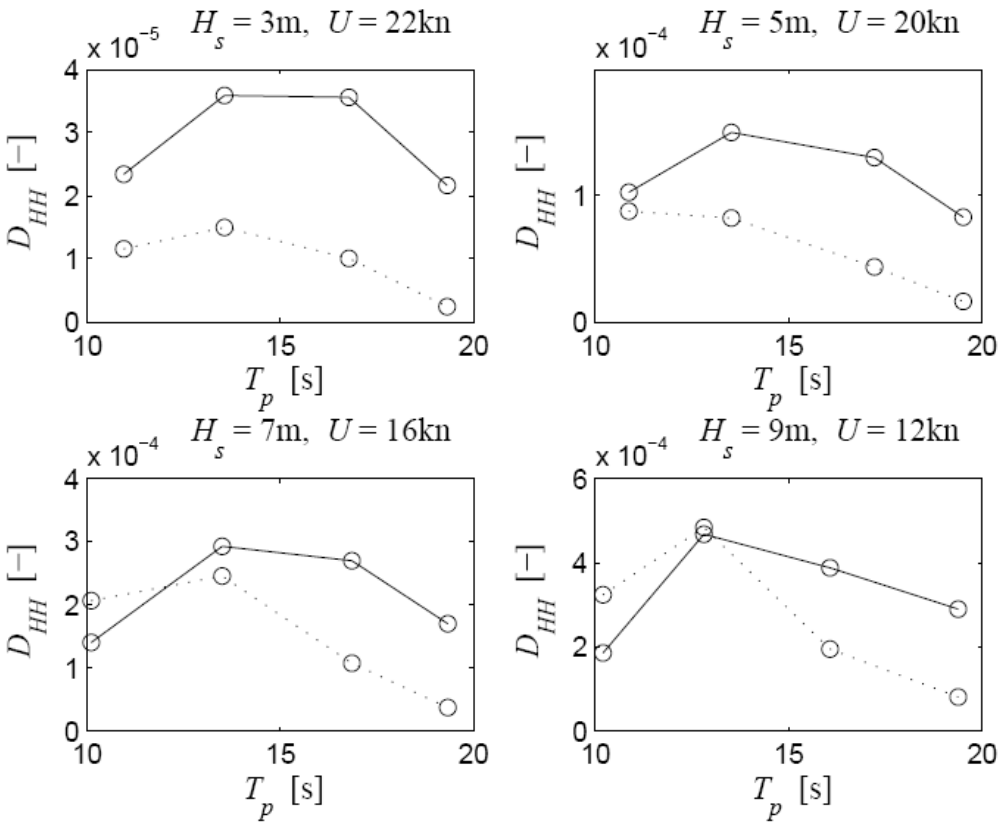

Fig 4.23 *Contribution to fatigue damage from wave frequency (full line) and high frequency responses (dotted line). Results given as function of Spectral peak period, T_P and significant wave height, Hs. (From Drummen et al (2006))*

The above results represent accumulated damage based on ½ hour duration of sea state. To establish the total accumulated damage, these results have to be combined with a wave scatter diagram covering the actual voyage of the ship. Resulting contour plots of lifetime contribution to fatigue damage is shown in Fig. 4.24 based on scatter diagram for North Atlantic. It is observed that the main contributions to fatigue damage occurs for sea states with T_P around 14 s and *Hs* around 5 m for both wave frequency and high frequency contributions.

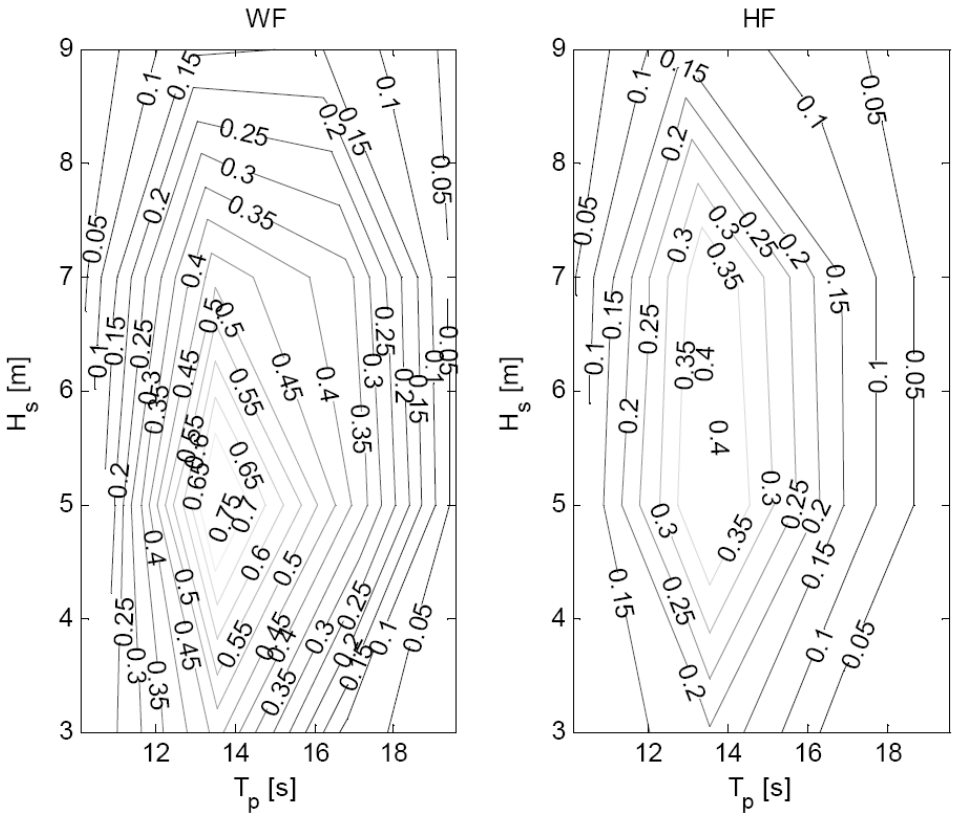

Fig 4.24 *Contour plots of lifetime contribution to fatigue damage based on scatter diagram for North Atlantic. (From Drummen et al (2006))*

By summing up over all sea states the following result were achieved for contribution to total fatigue damage during 20 years of operation in North Atlantic;

- Wave frequency damage; 63 %
- High frequency damage; 37 %

Similar analysis were also carried out based on extensive full scale tests of a container ship operating in the northern part of the Pacific Ocean. The relative magnitude of the high frequency and wave frequency contribution to fatigue damage is shown in Fig. 4.25. The conclusion is in close agreement with the findings from the model test results outlined above.

It should be noted that the common practice for ship design is still only to consider the contribution from wave frequency damage.

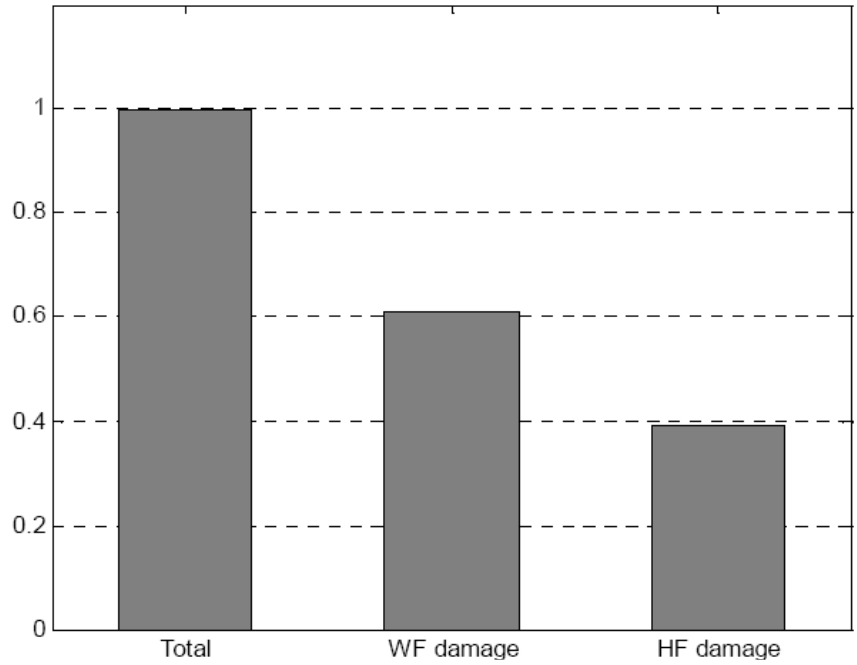

Fig 4.25 *The relative magnitude of the high frequency and wave frequency contribution to fatigue damage based on analysis of full scale results for Container ship. (From Drummen et al (2006))*

4.5.3 Contribution from elastic response to maximum values

The effect of the hull flexibility on the maximum bending moment for a container ship has been considered by Drummen et. al (2008). Both model tests results and numerical analysis results using a nonlinear hydroelastic strip theory were presented. Both in model tests and for numerical calculations the effect of hydroelasticity was evaluated by comparing results for the rigid hull and for the flexible modeled hull.

In Fig. 4.26 the measured and calculated midship vertical bending moment are shown for head sea waves in a sea state with Hs=8.0 m and Tp=12.57 s. Ship speed was U=15 kn. The results are presented in the form of exceedance plots, giving the short term cumulative probability distribution for the different responses. The probability distribution are presented for both assuming Flexible hull and Rigid hull from the different sources;

- From linear calculations
- From Experimentally measured hog amplitudes
- From Experimentally measured sag amplitudes
- From calculated nonlinear hog amplitudes
- From calculated nonlinear sag amplitudes

The experiments shows that the for Hs=8.0 m the sagging bending moment and the hogging bending moment are almost equal. For the rigid hull case the agreement between model test and calculations are very good and it is observed that the nonlinear effects are moderate. The effect of flexibility is seen to significantly increase the maximum bending moment.

In Fig 4.27 similar results is shown for a sea state with Hs=12.0 m, Tp=12.57 s and a ship speed of U=8 kn. For this case the effect of nonlinearity is more pronounced than for Hs=8.0 m. The effect of flexibility is slightly less than for Hs=8.0 m. The reason was explained with the lower forward speed for this case (8 kn v.s. 15 kn) which result in less severe slamming events.

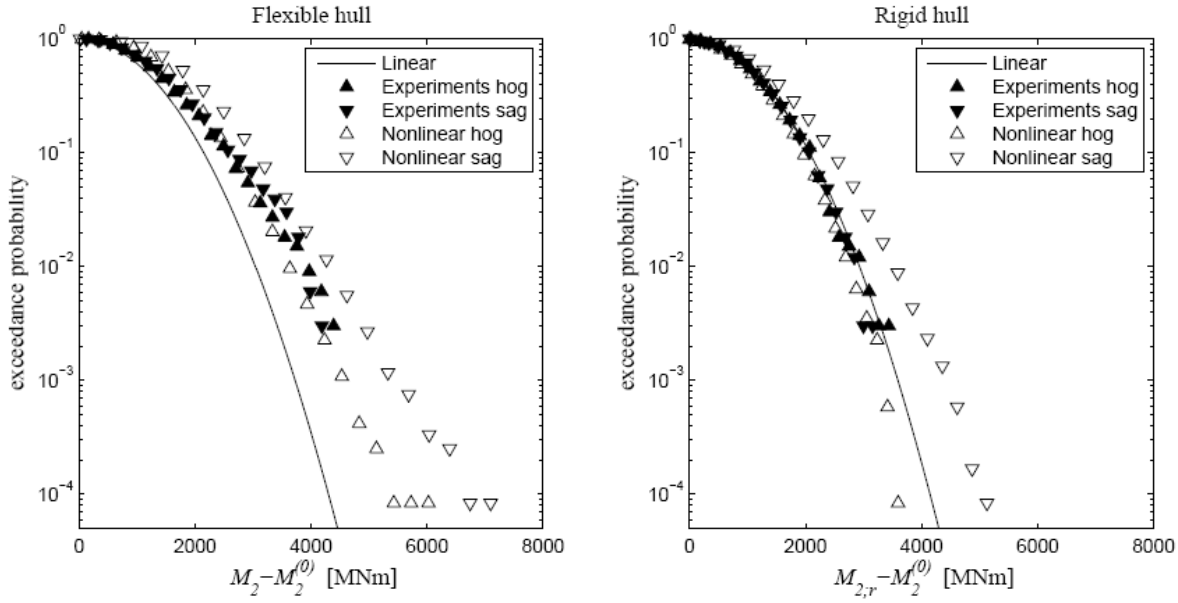

Fig 4.26 *Probability distribution of the vertical midship bending moment. Head sea waves Hs=8.0 m, Tp=12.57 s, U=15 kn. Left; Flexible Hull case. Right; Rigid hull case. (From Drummen et al (2008))*

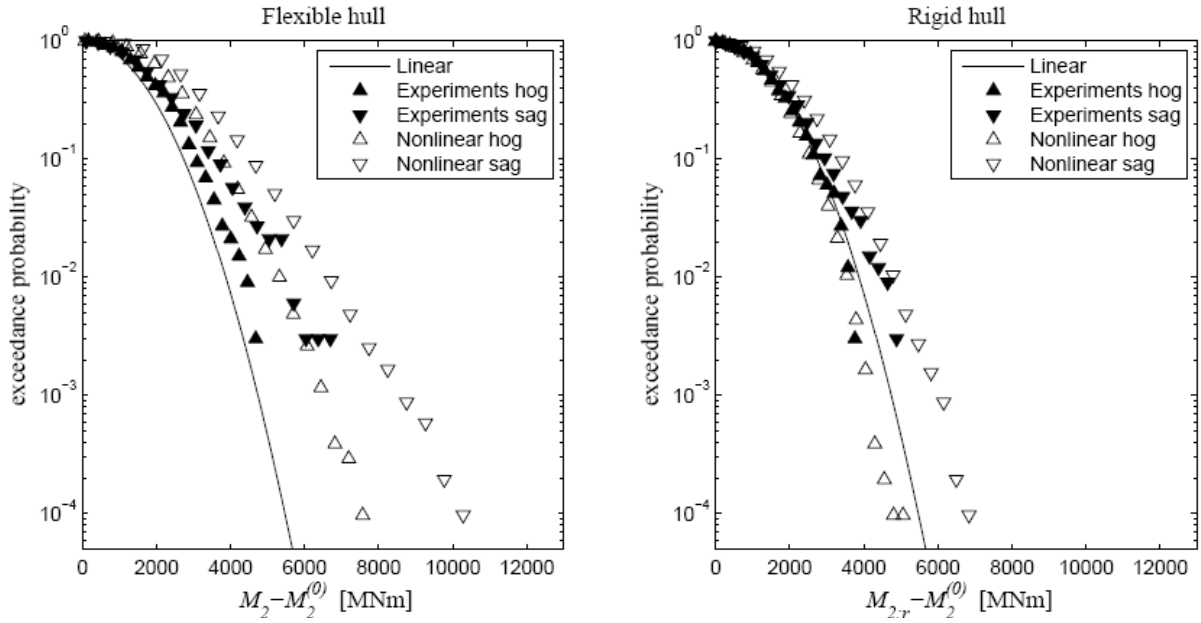

Fig 4.27 *Probability distribution of the vertical midship bending moment. Head sea waves Hs=12.0 m, Tp=12.57 s, U=8 kn. Left; Flexible Hull case. Right; Rigid hull case. (From Drummen et al (2008))*

In summary it has been found that the hull flexibility can increase the maximum vertical bending moment up to 35 % in irregular sea states relevant for ship design loads. The largest effect is for the sagging moment, but also the hogging moment is significantly increased due to the effect of flexibility.

5 RINGING REPONSE OF OFFSHORE PLATTFORMS

5.1 General

High frequency response has been observed in model tests and full scale tests with offshore structures as Gravity Base Structures (GBS) and Tension Leg Platforms (TLP), see Fig. 5.1, These concepts are characterised with some relatively high elastic natural frequencies, which are outside the range of normal (i.e. linear) wave loading. For a TLP, the axial stiffness of the tethers gives natural periods in the range T_N=2-4s for heave and roll/pitch. For GBS designs the first elastic mode of the tower will be the most critical mode and a typical period will be in the same range. A general discussion of the Ringing behaviour is given by Jefferys and Rainey (1994).

It is necessary to distinguish between the terms "springing" and "ringing". As discussed in chap 3, springing is a steady state response at the natural frequency of an elastic mode (for ships; vertical bending mode, for TLP; heave/Pitch response) generated by linear wave loading (linear springing) or by second order wave effects (i.e non-linear springing). These responses are commonly observed both in mild sea states (linear springing) and severe sea states (mainly non-linear springing).

Ringing is the transient high frequency response at the natural frequency of an elastic mode (same mode as for springing) typically occurring in extreme wave conditions with large and steep individual waves. The ringing excitation occurs in sea states with wave periods well above the elastic natural periods. The transient ringing response decay is govern by the actual damping. In Fig. 5.2 the difference between a typical springing response and ringing response is illustrated. Also details of a typical ringing response for a TLP are shown.

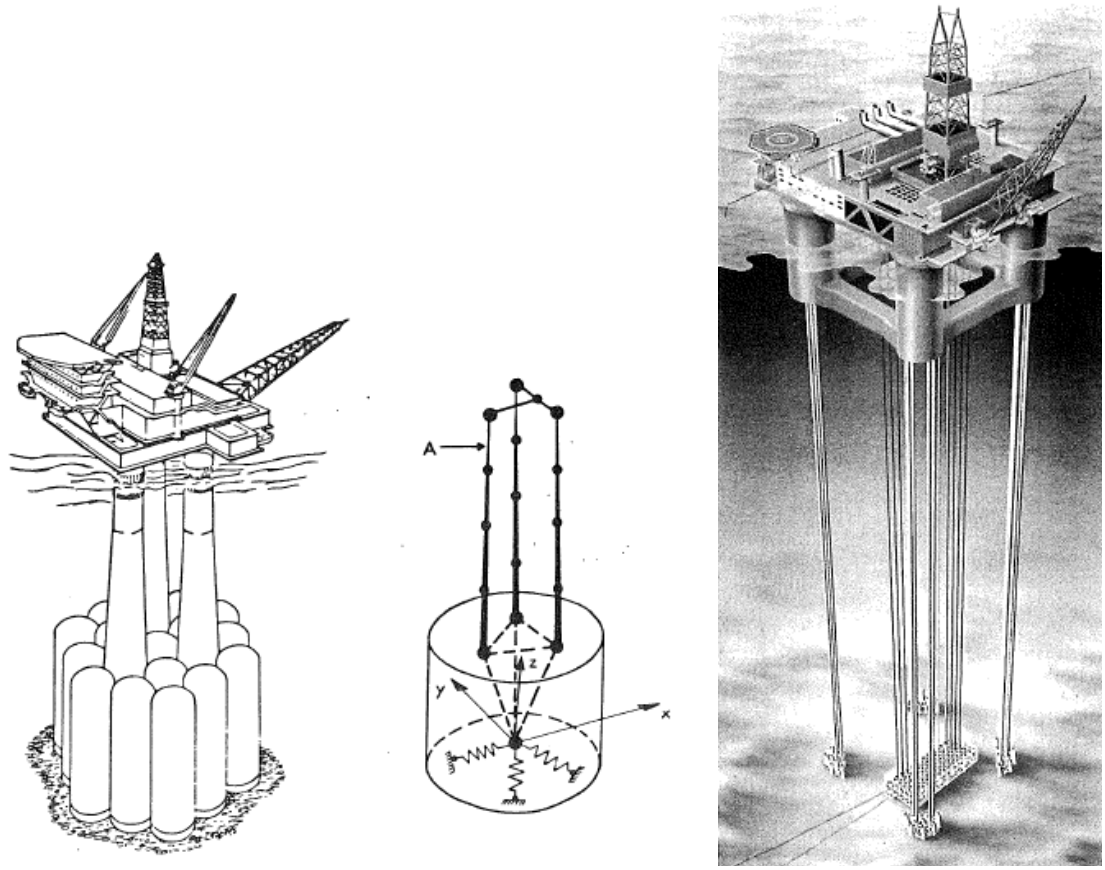

Figure 5.1 *Sketch of structure possibly exposed to Ringing;*

Left; Gravity Base Structure (GBS), Right; Tension Leg Platform (TLP).

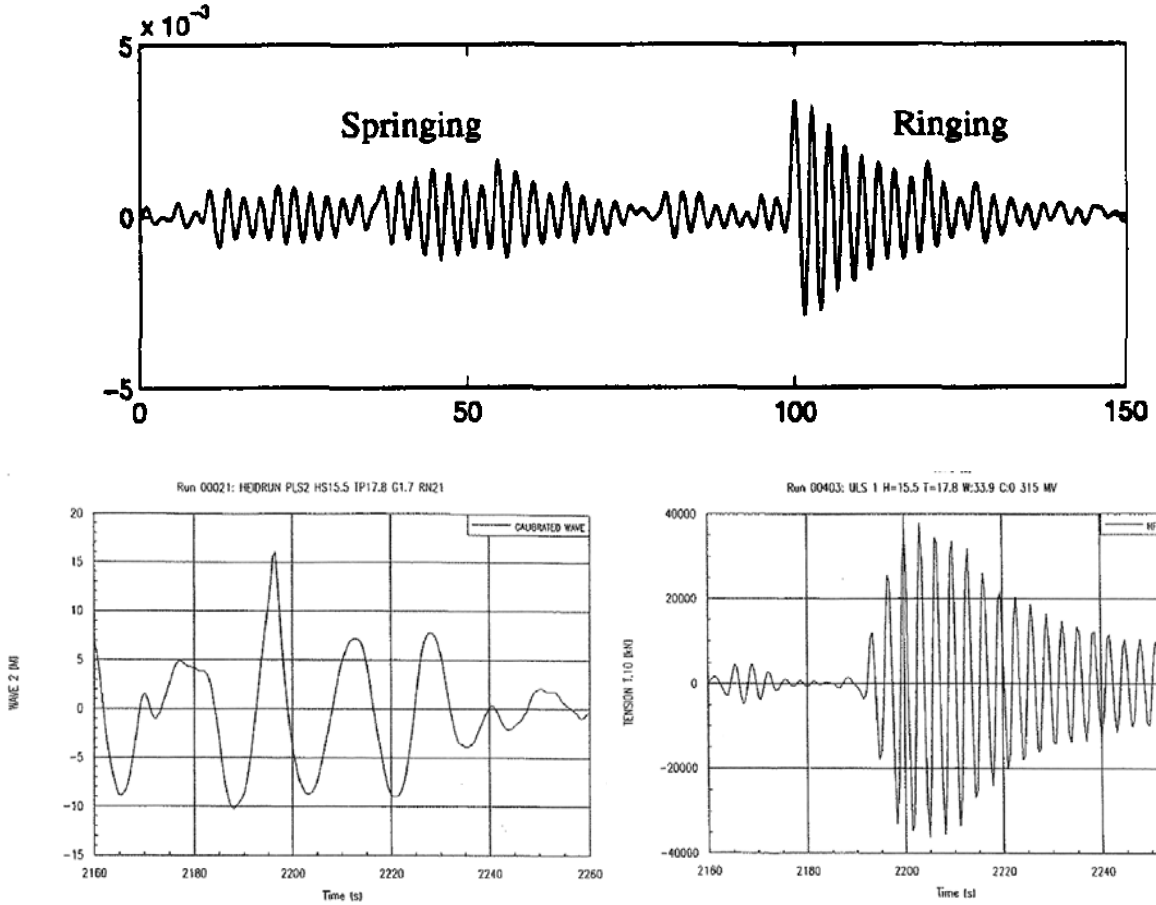

Figure 5.2 *Top view; ;Sketch of a typical springing response (steady state) and ringing response (transient. Bottom view; Measured ringing response in model test with a TLP, wave signal and high-pass filtered tether tension*

5.2 Excitation of Ringing

Ringing behaviour is observed in large, steep individual waves. Possible excitation sources for ringing response can be;

- Higher order diffraction dominated horizontal wave excitation (above second order)
- Horizontal slamming forces on the vertical column (?)
- Viscous forces (?)

For a TLP, horizontal wave forces acting on the vertical columns will trigger a Pitch motions through the Surge-Pitch coupling terms. Direct vertical higher order wave loading on the pontoons or at the column bottom is also a possible excitation source, but most work on ringing response is concentrated on the contribution from horizontal wave forces on the columns. For a GBS structures horizontal wave loading can trigger any of the elastic tower modes directly.

The interesting natural periods for a TLP and GBS are typically in the range one fifth to one third of the peak period of the wave spectrum initiating ringing response. This means that 2nd order diffraction theory may largely underestimate the actual random wave loads as third and fourth order harmonic load terms are needed in the analysis. No consistent theory to 3rd order exist and different simplifications and approximations have therefore been used in attempting to describe the excitation of ringing response. Several studies

have indicated that the non-linear high frequency force contributions are dominated by 3rd order wave effects partly generated by 2nd order free surface wave effects.

In Fig 5.3 an example of measured time series of horizontal forces on a vertical cylinder, intended to represent a typical TLP column is shown, see Stansberg et.al (1995) for details. The actual sea state was Hs=0.28 m and Tp=2.4 s. (in model scale, full scale values Hs=15.4 m, Tp=17 s). In the figure the wave elevation, measured horizontal force, both total and high-pass filtered, are shown. The situation shown represents the passage of an extreme and steep sharp-crested random wave. The high-pass filtered horizontal force signal has a oscillation period of about 1/5 of the peak period. This does not necessarily represent a 5th order force since the wave spectrum also includes significant energy at periods lower than Tp, but it clearly shows that excitation force of 3rd order and higher will be important and can introduce excitation at frequency range of the elastic modes.

From measurements of typical ringing responses it is observed that the ringing response takes 2-3 cycles to build up which indicate that this is not a response initiated by slamming forces.

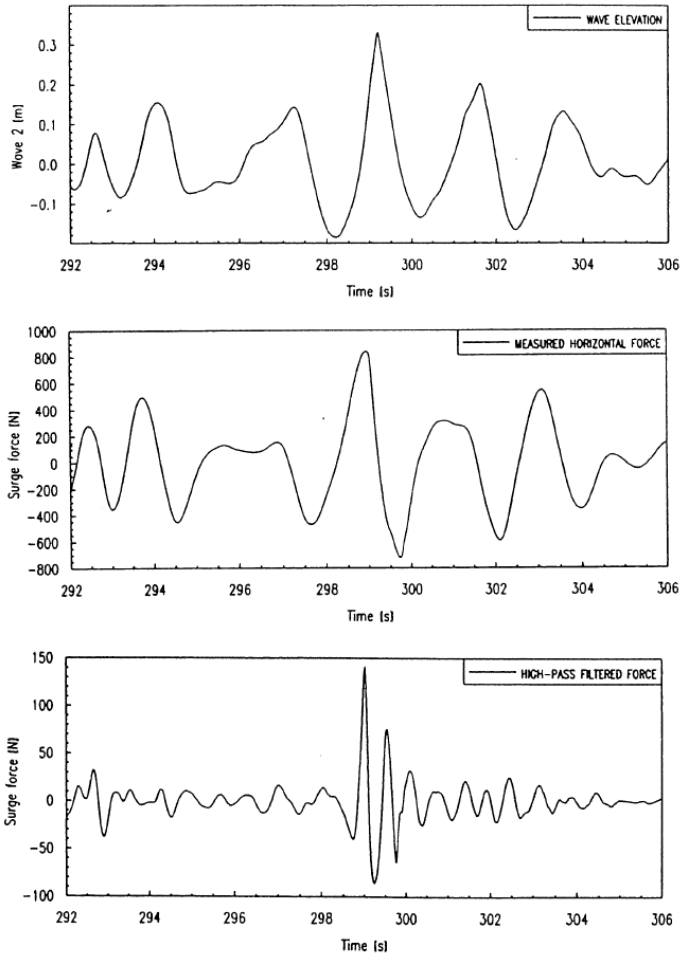

Figure 5.3 *Time series examples from irregular wave test for wave forces on vertical column.. Top view; wave elevation, Midle view; Total horizontal force, Bottom view; High pass filtered horizontal force (From Stansberg et.al (1995))*

Morison drag forces may in principle also generate high frequency excitation and hence ringing like behavior. However the K-C number involved in a situation where ringing may occur is low and will give low drag coefficients. Calculations have shown that the drag effects are small compared to the excitation from higher order diffraction theory / slender

body inertia terms. It is therefore concluded that viscous forces will not give a significant contribution to ringing response for the type of structures considered here.

5.3 Description of results for Ringing response of TLP

Zou et al (1998) presented results for TLP motions and tether tension. The used approach was based on using measured wave forces acting on a TLP model in a sea state with strong asymmetric waves. The used sea state had shown to initiate ringing response in previous model tests. The measure horizontal force was used as input for simulating the nonlinear response of the coupled TLP system. The simulated responses were also analyzed statistically to evaluate extreme values.

Analysis were also carried out using a second order theoretical wave force model. This model produced springing only and was not able to reproduce the ringing response. This shows that a second order force model will not cover the observed springing behaviour.

In Fig 5.4 an example of measured wave elevation and measured vertical force and Pitch moment is shown. At about t=1200s a strong asymmetric wave hit the columns and a peak in the excitation forces is observed.

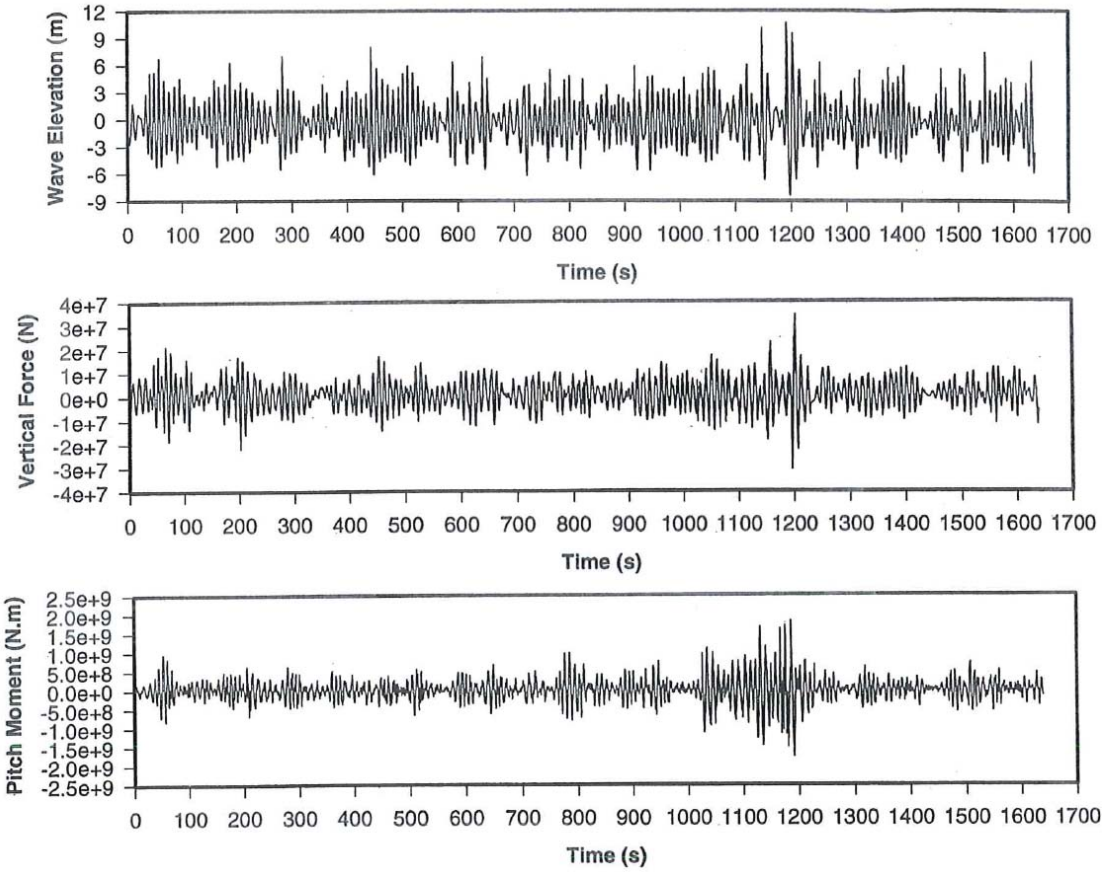

Figure 5.4 *Measured wave elevation, vertical excitation force and pitch excitation moment acting on the TLP model. Wave case 3.*

The response spectrum of the Pitch excitation moment is shown in Fig 5.5 for two different wave condition. Wave 1 is a numerical generated wave with close to zero asymmetry with Hs=10.8 m and Tp=14.1 s. Wave 3 is a slightly lower but steeper wave with Hs=9.9 m and Tp=11.0 s and this sea state contains strong asymmetric waves. The high frequency tail of the pitch excitation spectrum is highly different with a significant high frequency energy for wave 3. This illustrate clearly the effect of the wave asymmetry.

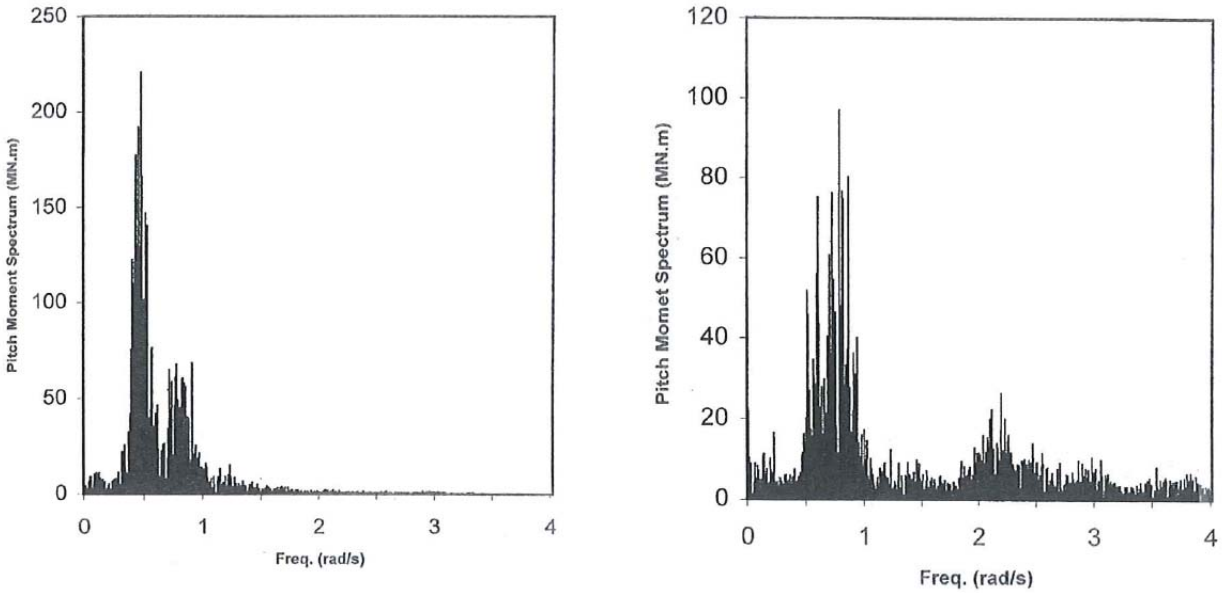

Figure 5.5 *Spectral for measured Pitch excitation moment for different wave condition. Left; Wave 1 with Hs=10.8m and Tp=14.1s, symmetric waves. Right; Wave , Hs=9.9, Tp=11.0s, containing strong asymmetric waves.*

The TLP structure was modeled as a rigid body with the tethers modeled as elastic springs using beam elements. Time domain simulations were used based on excitation forces from measurements as outlined above. Resonance frequency for different modes relevant for ringing were;

- Heave; ω_3=3.53
- Pitch; ω_5=3.37

The simulated results are shown in Fig 5.6 for Wave 3. The results includes surge motion, heave motion, pitch motion and tether tension. The pitch motion and tether tension are seen to give a bursting behaviour when the strong asymmetry wave hit the structure at t=1200s.

The surge motion is seen to be dominated by the low frequency motion. Heave motion also get a significant low frequency contribution due to the coupling with surge through the set down effect (pendulum motion). To further investigate the different contributions to tether tension, the tension amplitude spectrum is shown in Fig. 5.7. The high frequency contribution is seen around the natural frequency for heave/pitch. The contribution to the total signal from this frequency range is significant.

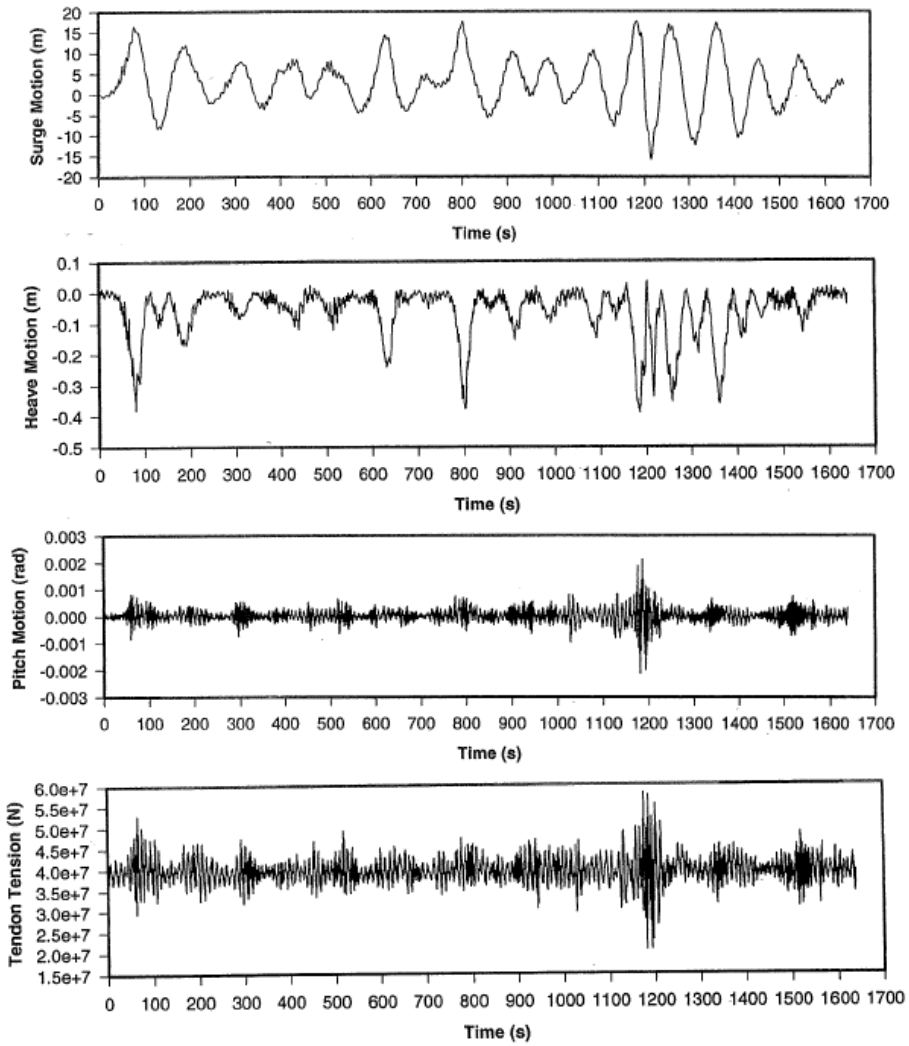

Figure 5.6 *Simulated motion response and tether forces. Wave 3.*

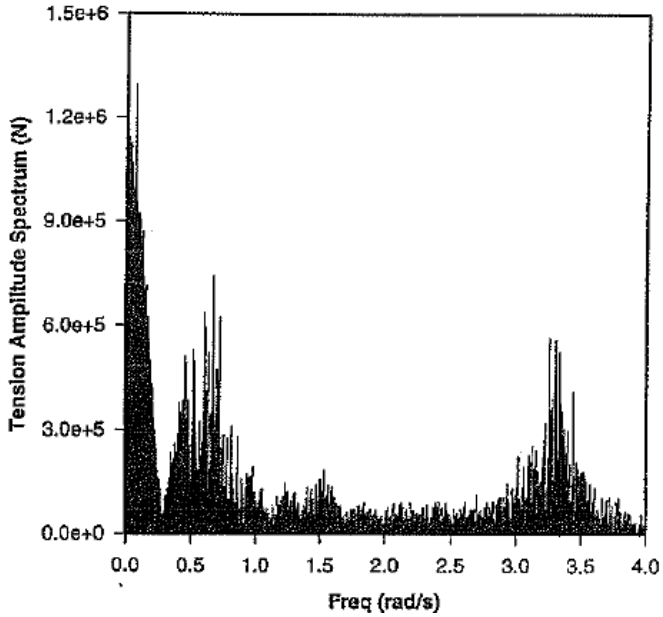

Figure 5.7 *Tension Amplitude spectrum. Wave 3.*

The distribution of extreme tension is established based on the simulated time series for tether tension. The results are shown in Fig. 5.8 for Wave 1 and Wave 3. The amplitude of the tension is normalized by dividing the actual amplitude value by the standard deviation (SD) of the process. Results are shown for the total tension (i.e including both contribution from wave frequency and high frequency response) and for the Maxima and Minima of the high frequency tension. The high frequency response were obtained by high-pass filtering of the total response. In the figures also the amplitude distribution using the Rayleigh distribution, commonly used for linear, wave-induced responses, is included. For a probability of exceedence level of 10^{-3} (meaning one of 1000 amplitudes exceed this level) the Rayleigh distribution gives a response amplitude equal to approx 3.7*SD. For Wave 1 the total tension follows quite close to the Rayleigh distribution. For Wave 3 it is seen that the high frequency response largely deviate from the Rayleigh distribution and gives maximum amplitude values up to 7*SD. Normalised peak values for the high frequency tension at the level of 7*SD is a typical properties characterizing ringing response. This large normalized peak value indicate also a strongly non-linear response behaviour.

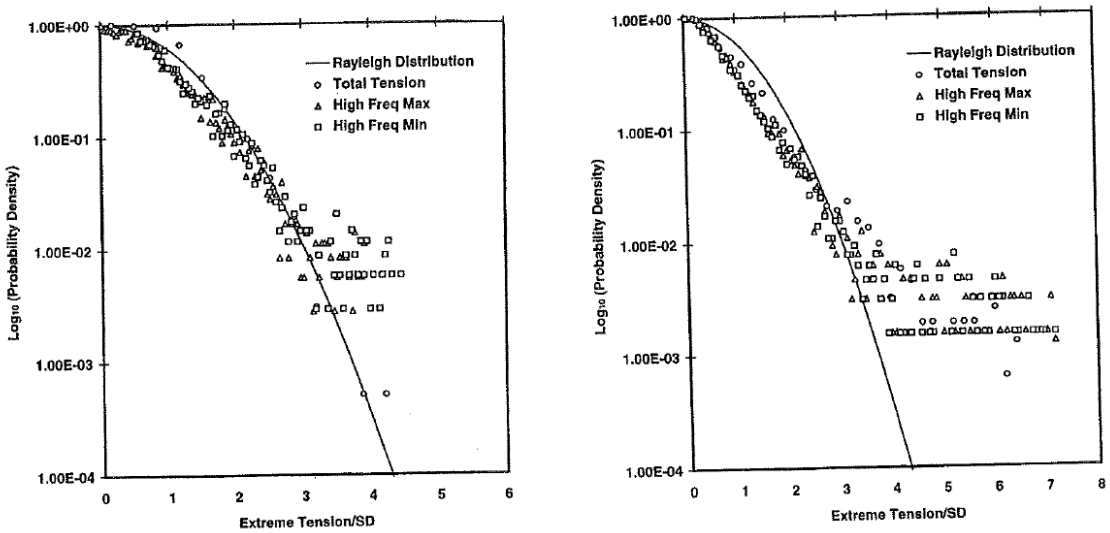

Figure 5.8 *Distribution of extreme tension.*
Left; Wave 1 with Hs=10.8m and Tp=14.1s, symmetric waves.
Right; Wave , Hs=9.9, Tp=11.0s, containing strong asymmetric waves.

6 NUMERICAL ANALYSIS - SPRINGING AND WHIPPING RESPONSE

6.1 General

The solution of the equation of motion can be presented on two, in principle, different ways;

- Time domain solution
- Frequency domain solution

Time domain solution is used for non-linear systems and for systems excited by a general time dependent load history or a load which is nonlinearly dependent on the structural responses. The solution can be obtained either as a numerical integration of the equation of motion in time or by the use of the impulse-response function.

For the *frequency domain solution* the equation of motion is solved for harmonic excitation for a number of different frequencies. The system must be linear (or linearized). The solution gives directly the load frequency sensitivity of the structure. For a general excitation the loading can be described as a infinite sum of harmonic components. The frequency domain solution is specially well suited for problems with frequency dependent mass, damping or stiffness.

If the method of solution of the equation of motion is based on the coupled equation of motion the method is called *Direct method*. Alternatively the equation of motion can be transformed to a set of uncoupled equations which can be solved independently. The transformation to uncoupled equations are performed by using modal superposition (or "normal modes")

Both for whipping and springing response analysis the flexible hull response can be assumed to be linear to a given hydrodynamic loading. Linear structural models will therefore be used. For this linear case the principle of superposition is valid and time series of responses due to different load contributions can be added to give the total response.

For Harmonic loading the frequency response function method can be directly applied for solution of the equation of motions.

For a general time dependent excitation the equation of motion may be solved either by analytical or numerical solutions as follow;

1. Frequency Response method in combination with Fourier theory by representing the general time dependent excitation as a sum of harmonic components. This is a frequency domain solution.
2. Impulse-Response method (or Convolution integral method). This is a time domain solution
3. Direct numerical time integration of the equation of motion. This is a time domain solution.

Solution for a one degree of freedom system for method 1 and 2 is discussed in Appendix A. All three methods can in principal be used both for the coupled (i.e as a Direct method) or the uncoupled equation of motions based on Modal superposition Method. However the second method is most frequently applied for the equation of motions as they are transformed to uncoupled equations.

For springing response which is excited by harmonic loads, frequency domain analysis is most frequently used. As whipping is a transient response with highly non-linear excitation time domain solution will normally be used for numerical analysis.

6.2 Equation of motion- Structural Formulation

Two main approaches are commonly used for modelling of the ship structure for elastic structural response calculation;

- Representation of Hull girder as a Timoshenko or Euler Beam , i.e a 2-D approach. Difficult/impossible to model local structural effects as openings etc. Analytical and simple to use. Often used for initial design stage. Torsion difficult to model.
- 3-D Fem modelling. Details as openings can be modelled. Required for catamarans and multihull vessels. Time consuming and complex modelling and analysis.

The Beam model was applied in the springing and whipping analysis discussed in Chap. 3.2 and 4.3 respectively. However for numerical analysis of springing and whipping response the 3-D fem modelling approach is the commonly used method. This approach is therefore discussed in the following.

The ship structure is assumed discredited by e.g. the finite element method. The equations of motions (or dynamic equilibrium equation) can be written as;

$$\mathbf{m}\ddot{\mathbf{r}}(x,y,z,t)+\mathbf{c}\dot{\mathbf{r}}(x,y,z,t)+\mathbf{k}\mathbf{r}(x,y,z,t)b\dot{x}=\mathbf{f}(x,y,z,t) \tag{6.1}$$

Where ***m*** is structural mass matrix, ***c*** is the structural damping matrix, ***k*** is the structural stiffness matrix, ***f*** is the vector of external forces including fluid pressure forces and ***r*** is the vector of unknown motions (includes both displacements and rotations). ***m, c*** and ***k*** is matrixes with dimension *mxm*, where *m* is the number of degrees of freedom. Using a direct solution method eq. (6.1) is used directly for the solution procedure.

For Direct numerical integration methods eq. (6.1) is used directly. Using the Modal superposition method, the global displacement may be approximated by an aggregate of the *N* lowest eigenmodes or eigenvectors $\boldsymbol{\psi}_i(x,y,z)$;

$$\mathbf{r}(x,y,z,t)\approx\sum_{i=1}^{N}\boldsymbol{\psi}_i(x,y,z)\,p_i(t) \tag{6.2}$$

Where $p_i(t)$ are the unknown displacement amplitudes called generalized coordinates. The eigenmodes or normal modes $\boldsymbol{\psi}_i(x,y,z)$, is determined from the free vibration analysis, i.e. for eq. (6.1) with ***c=0*** and ***f=0.*** Assuming harmonic oscillations, i.e. $\mathbf{r}=\boldsymbol{\psi}e^{i\omega t}$ gives

$$(\mathbf{k}-\omega^2\mathbf{m})\mathbf{r}=0$$

$$(\mathbf{k}-\omega^2\mathbf{m})\boldsymbol{\psi}=0$$

The first 6 modes in eq. (6.2) are the rigid body motions; surge, sway, heave, roll, pitch and yaw. The remaining are eigenmodes of the flexible "dry" structure. In theory infinitely many flexible modes are needed to describe responses of the vessel. For practical purposes however, the N first natural modes of the structure will describe the global response with sufficient accuracy.

An Example of calculated eigenmodes of the segmented catamaran model is shown in Fig. 6.1. Example of calculated and measured eigenmodes for an elastic model of container vessel is shown in Fig. 6.2

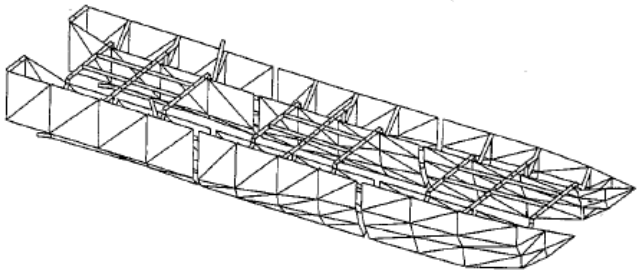

Fig. 3 The finite element model used in the numerical analysis.

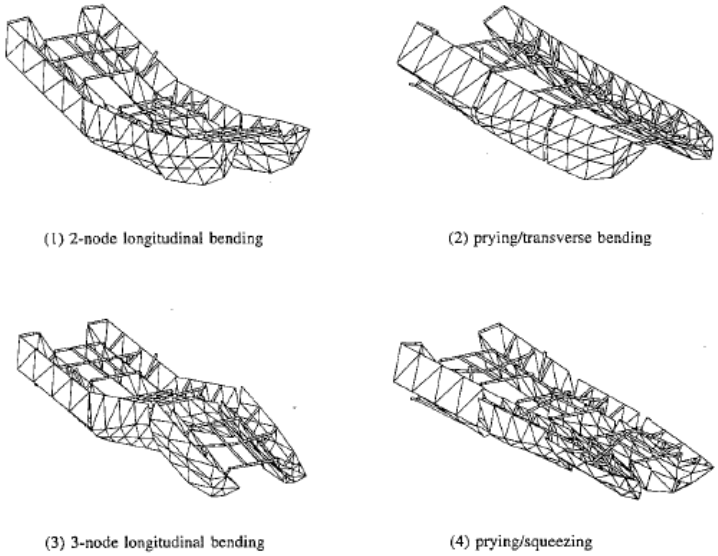

Figure 6.1 *Calculated eigenmodes of the first four symmetrical flexible modes for the segmented model of a catamaran.*

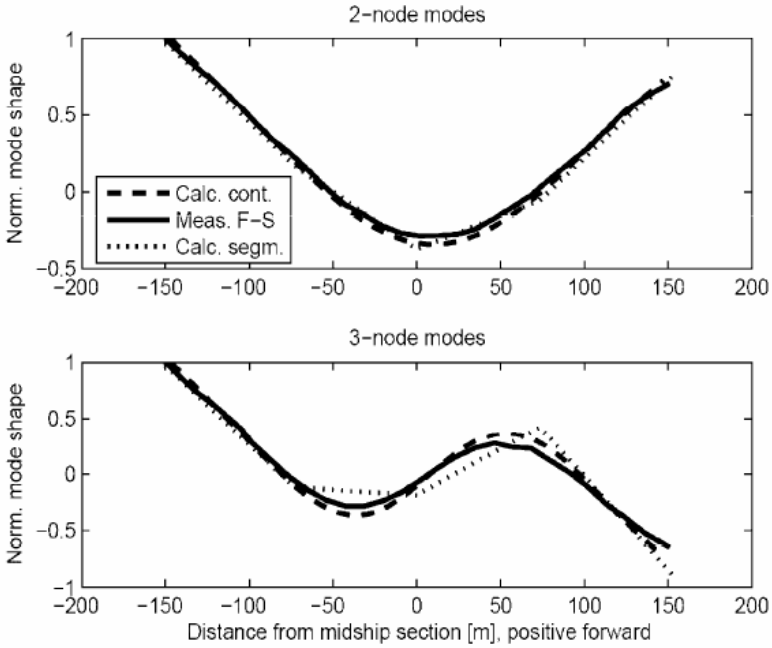

Figure 6.2 *Calculated and measured 2 and 3-node modes for Monohull. Meassured on model*

By inserting eq. (6.2) into (6.1) and pre-multiply with the k'th eigenvector transposed we obtain the equation of motion on generalized form;

$$\sum_{i=1}^{N}\left(M_{ki}\ddot{p}_i + C_{ki}\dot{p}_i + K_{ki}p_i\right) = F_k(t) \tag{6.3}$$

For *k=1,....N,* where $M_{ki} = \boldsymbol{\psi}_k{}^T \mathbf{m}\boldsymbol{\psi}_i$, $C_{ki} = \boldsymbol{\psi}_k{}^T \mathbf{c}\boldsymbol{\psi}_i$ $K_{ki} = \boldsymbol{\psi}_k{}^T \mathbf{k}\boldsymbol{\psi}_i$ are elements in the generalized mass-, damping- and stiffness matrices respectively. $F_k = \boldsymbol{\psi}_k{}^T \mathbf{f}$ is a element of the generalized external force vector.

The generalized hull damping matrix is usually represented by the Rayleigh damping model;

$$C_{ii} = \alpha_1 M_{ii} + \alpha_2 K_{ii}$$

Using this formulation the orthogonally properties of the mass and stiffness matrix will also apply to the damping matrix. If the property of orthogonally of the eigenmodes is used, see eq. (3.15) the equation of motion may be further simplified to an uncoupled system as follows;

$$M_{ii}\ddot{p}_i + (\alpha_1 M_{ii} + \alpha_2 K_{ii})\dot{p}_i + K_{ii}p_i = F_i(t) \tag{6.4}$$

Comparing eq (6.1) with eq. (6.4) the introduction of *N* lowest eigenmodes to represent the global displacement, one has reduced the coupled system with infinite number of degree of freedom to a uncoupled system with *N* degrees of freedom. The solution of each of the *N* equations can then be solved independently and similar to the equations for a system with one degree of freedom (ref. also Appendix A).

The generalized external force vector consist of the forces due to hydrodynamic pressure on the wetted hull surface, *S.* The hydrodynamic pressure forces are discussed below.

6.3 Hydrodynamic Forces

6.3.1 General formulation

The fluid pressure forces in a particular mode *k* can be written on generalized form as;

$$F_k = -\iint_S \mathbf{u}_k \cdot \mathbf{n} \cdot p \cdot dS \tag{6.5}$$

The vector $\mathbf{u}_k{}^T = \left[u_k, v_k, w_k\right]$ represent the three local displacement components of the *k*th eigenvector. ***n*** is the unit normal vector of *S*, positive into the fluid domain.

The fluid pressure *p* is obtained from Bernoulli's equation;

$$p = -\rho\left(\frac{\partial\Phi}{\partial t} + \frac{1}{2}\nabla\Phi\cdot\nabla\Phi + gz - \frac{1}{2}U^2\right) \tag{6.6}$$

where ρ is the mass density of water and $\Phi(x,y,z,t)$ is the total velocity potential, written on principal form as;

$$\Phi(x,y,z,t) = Ux + \phi_s(x,y,z,t) + \phi_u(x,y,z,t) \tag{6.7}$$

Where $\phi_s(x,y,z,t)$ is the potential due to the steady disturbed flow and $\phi_u(x,y,z,t)$ is the unsteady potential due to the incoming waves, diffracted wave and perturbation potentials caused by ship motions in the different eigenmodes.

Assuming linear wave theory the unsteady potential can be written as;

$$\phi_u = \phi_I + \phi_D + \sum_{i=1}^{N} p_i \phi_i \tag{6.8}$$

Where;

ϕ_I is the incident wave potential

ϕ_D is the potential due to the diffracted waves

ϕ_i is the radiation velocity potentials due to unit excitation in mode *i*

The total hydrodynamic force will for most practical applications be split up into the two main parts, radiation forces and excitation forces on the form;

$$F_k(t) = F_k{}^R(t) + F_k{}^E(t) \tag{6.9}$$

The unknown potentials given above are found by solving a hydrodynamic boundary value problem, including the effect of forward speed. A number of different approximations for this problem have been presented depending on the actual case. This includes approximations for special cases as the strip theories, see Salvesen et.al (1970), high speed formulation see Faltinsen and Zhao (1991). See also Hermundstad et.al (1999) for further details.

For our case of dynamic response calculations, the contribution from the unsteady potential will be the main interest. Only this contribution will therefore be considered in the following.

6.3.2 Hydrodynamic Radiation forces

Radiation forces are associated with forced harmonic motions of the structure in the different modes, *i*. For a harmonic response of the vessel generalized coordinates takes the form;

$$p_i(t) = \overline{p}_i e^{i\omega_e t}$$

The radiation potential can then be expressed as;

$$\phi_R = \sum_{i=1}^{N} \phi_i \overline{p}_i e^{i\omega_e t} \tag{6.10}$$

For the radiation pressure the quadratic terms in eq. (6.6) can be neglected and the generalized force in mode *k* can be expressed on the form;

$$F_k{}^R = -\rho \iint_S \mathbf{u}_k \cdot \mathbf{n} \frac{(\partial \phi_R)}{\partial t} dS = -\rho \iint_S \mathbf{u}_k \cdot \mathbf{n} (i\omega_e \phi_R) dS \equiv \sum_{i=1}^{N} \left(\omega_e{}^2 A_{ki} - i\omega_e B_{ki} - R_{ki} \right) \overline{p}_i e^{i\omega_e t} \tag{6.11}$$

The generalized added mass, damping and hydrostatic restoring coefficients are derived by using eq. (6.5) and the definition of added mass and damping as given in eq. (6.11) to be on the form;

$$A_{ki} = \frac{\rho}{\omega_e^{\,2}} \mathrm{Re}\left[\iint_S \mathbf{u}_k \cdot \mathbf{n}(i\omega_e \phi_i) dS \right]$$

$$B_{ki} = -\frac{\rho}{i\omega_e} \mathrm{Im}\left[\iint_S \mathbf{u}_k \cdot \mathbf{n}(i\omega_e \phi_i) dS \right]$$

$$R_{ki} = -\rho g \iint_S \mathbf{u}_k \cdot \mathbf{n} w_i dS$$

Where w_k is the vertical displacement due to unit excitation of mode *i.*

The hydrodynamic added mass and damping coefficients are generally dependent on the frequency of oscillation. For high frequency i.e. for $\omega \to \infty$, asymptotic value is reached. For frequency domain solutions the frequency dependency is covered directly in the analysis as the equation of motion is solved for each frequency. For time domain solution for whipping response calculations the high frequency limit is often used. This is discussed in more details in chap. 6.5.

6.3.3 Excitation forces

The total excitation force can be split up into one linear contribution and one non-linear contribution, i.e. on the form.;

$$F_k^{\,E}(t) = F_{lin,k}(t) + F_{nm,k}(t) \tag{6.12}$$

The linear contribution contains the linear part of Froude-Krylov and diffraction forces. The non-linear contributions includes the non-linear forces as slamming forces, and non-linear modifications to Froude-Krylov and diffraction forces.

The potentials ϕ_I and ϕ_D in eq. (6.8) gives the Froude-Krylov forces and Diffraction forces respectively. Neglecting the quadratic terms in eq. (6.6) the linear generalized form in mode *k* can be written as;

$$F_k^{\,FK} = \rho \iint_S \mathbf{u}_k \cdot \mathbf{n}(i\omega_0 \phi_I) dS \cdot e^{i\omega_e t} \tag{6.13}$$

$$F_k^{\,D} = \rho \iint_S \mathbf{u}_k \cdot \mathbf{n}\left(i\omega_0 \phi_D + U \frac{\partial \phi_D}{\partial x} \right) dS \cdot e^{i\omega_e t} \tag{6.14}$$

The linearized Froude-Krylov forces and Diffraction force gives a harmonic excitation contribution. The linear excitation force is now obtained as;

$$F_{lin,k}(t) = F_k^{\,FK}(t) + F_k^{\,D}(t) = \rho \iint_S \mathbf{u}_k \cdot \mathbf{n}\left(i\omega_0 (\phi_I + \phi_D) + U \frac{\partial \phi_D}{\partial x} \right) dS \cdot e^{i\omega_e t} \tag{6.15}$$

Nonlinear contributions to Froude-Krylov and diffraction forces will be partly due to the velocity squared terms in Bernoulli's equation, see eq. (6.6) and partly from integration of the linear pressure up to the actual water line. Hydrostatic restoring forces will also give a nonlinear contribution when integrated up to the actual water line. The calculation of the nonlinear excitation force $F_{nm,k}(t)$ is not straight forward and a number of simplifications and assumptions are used for practical applications depending on the actual case

considered. Slamming force calculations are discussed in Chap 4.2. A detailed discussion of representation of slamming forces for whipping response calculations is also given by Økland (2002).

One often used approach for monohuls for the nonlinear excitation force $F_{nm,k}(t)$ is as follows, see Wu et al (1997);

$$F_{nm,k}(t) = \rho g \int_L \delta_{z,k}(x)\{[Q(x,t) - Q_0(x)] + b_0(x) w_{REL}(x,t)\}dx + \int_L \delta_{z,k}(x) \frac{\partial (a_{33}(x,t))}{\partial t} \cdot \frac{Dw_{REL}(x,t)}{Dt} dx \quad (6.16)$$

The first term represent the nonlinear modification of the Froude Kryloff force and the nonlinear modification of the hydrostatic restoring force. $\delta_{z,k}$ is the vertical displacement of a cross section in mode *k*, $Q(x,t)$ and $Q_0(x,t)$ represent the areas of the instantaneous and mean submergence of the cross section respectively. $b_0(x)$ is the sectional beam at mean draft. $w_{REL}(x,t)$ is the vertical displacement of the ship hull relative to the wave surface. These two contributions are frequently assumed to represent the main nonlinear effects for the ordinary hydrodynamic force.

The second term is the slamming force based on the momentum method $a_{33}(x,t)$ is the high frequency 2-D added mass for the instantaneous submerged cross section.

This equation shows that the slamming force depends on the following parameters;

- Relative velocity, V_{rel}, between the water surface and the ship section.
- The velocity of the ship section may get an important contribution from the *vibration* velocity (e.g. vibrations caused by the previous slam).
- The velocity/motion of the water surface gets contributions from the steady wave elevation, the diffraction and radiation waves.

All other nonlinear contributions are neglected in the approach as given by eq. (6.16) above.

6.4 Response calculation.

6.4.1 Response due to General loading – Direct Method.

We may in principle solve the nonlinear hydrodynamic boundary value problem for every time-step. The schematic calculation sequence can than be summarized with the following main steps;

- Evaluate the pressure (6.6) on the instantaneous wetted part of the hull.
- Position of hull including elastic deflection to be updated each time step.
- Integrate the pressure to obtain the generalized hydrodynamic force from equation (6.5)
- Solve the equations of motion (6.3) using a relevant time integration procedure.
- Continue with next time-step

This approach is extremely computationally demanding as it requires solution of the boundary value problem for each time step at the actual position of the body. The instantaneous position includes contributions from wave elevation, rigid body motions as well as the elastic deformations. For a practical application of this approach a number of assumptions have to be introduced.

Different simplifications for the solution of the hydrodynamic force have therefore been proposed. For the case with linear harmonic excitation (i.e the linear springing problem) the frequency response method can be used. For nonlinear loading (applies to both non-linear springing and whipping response analysis) the most commonly used approach for a general time dependent excitation force is to use the impulse response method (or convolution method).

The frequency response method solution for linear, harmonic excitation and the impulse response method for general time dependent hydrodynamic loading are discussed in the following.

6.4.2 Response due to Linear Harmonic excitation – The Frequency Response Method.

By introducing eq. (6.9) into the generalized equation of motion, eq. (6.3) and using equation (6.11) for the Radiation forces and only including the linear contribution to the excitation forces as given by equation (6.15) we obtain the following equation for a harmonic excitation force;

$$\sum_{i=1}^{N}\left[-\omega_e{}^2\left(M_{ki}+A_{ki}\right)+i\omega_e\left(C_{ki}+B_{ki}\right)+\left(K_{ki}+R_{ki}\right)\right]\cdot\overline{p}_i e^{i\omega_e t}=F_k{}^{FK}+F_k{}^{D}=(\overline{F}_{lin,k})e^{i\omega_e t} \qquad (6.17)$$

The above equation can be solved for any frequency and for each mode by conventional methods for linear frequency response solutions. (*N* equations and *N* unknowns). The solution can be written on the form;

$$\mathbf{p}(\omega_e)=\mathbf{H}(\omega_e)\cdot\mathbf{F}(\omega_e) \qquad (6.18)$$

Where;

$$\mathbf{H}(\omega_e)=\frac{1}{\left[-\omega_e{}^2\left(\mathbf{M}+\mathbf{A}\right)+i\omega_e\left(\mathbf{C}+\mathbf{B}\right)+\mathbf{K}+\mathbf{R}\right]} \qquad (6.19)$$

is the generalized linear frequency-response transfer function matrix on complex form. Phase information is implicitly included in the complex numbers. Note that using this approach the frequency dependency of hydrodynamic coefficients as added mass and damping is included in the solution.

The above solution represents the particular solution (i.e. the steady-state solution).

The global displacements are obtained from eq. (6.2) as;

$$\mathbf{r}(x,y,z,t)\approx\sum_{i=1}^{N}\boldsymbol{\psi}_i(x,y,z)p_i(t)=\sum_{i=1}^{N}\boldsymbol{\psi}_i(x,y,z)\overline{p}_i e^{iw_e t} \qquad (6.20)$$

For linear springing analysis the loading will be harmonic wave excitation. The above frequency domain solution can therefore be directly used for linear springing analysis. For details, see Hermundstad et.al. (1999).

6.4.3 General nonlinear loading - Convolution integral method

Using the above deviations for hydrodynamic forces the generalized equation of motion (6.3) is written on the form;

$$\sum_{i=1}^{N}\left[\left(M_{ki}+A_{ki}\right)\ddot{p}_i+\left(C_{ki}+B_{ki}\right)\dot{p}_i+\left(K_{ki}+R_{ki}\right)p_i\right]=F_k{}^{E}(t)=F_{lin,k}(t)+F_{nm,k}(t) \qquad (6.21)$$

The total generalized response $\mathbf{p}(t)$ is decomposed into its linear and nonlinear parts (similar to as for the excitation force);

$$\mathbf{p}(t) = \mathbf{p}_{lin}(t) + \mathbf{p}_{nm}(t) \tag{6.22}$$

The linear response can now be obtained directly from the frequency domain solution, see eq. (6.19) and eq. (A.18) on the form;

$$\mathbf{p}_{lin}(t) = \frac{1}{2\pi}\int_{-\infty}^{\infty} \mathbf{H}(\omega_e)\cdot\mathbf{F}_{\mathbf{lin}}(\omega_e)\cdot e^{\omega_e t} d\omega_e \tag{6.23}$$

Using this formulation for the time history of the linear response the solution can be found from one single integration of the generalized linear frequency-response transfer function.

The nonlinear responses are found by applying convolution integration for each time step (see Appendix A for details of convolution integral);

$$\mathbf{p}_{nm}(t) = \int_{-\infty}^{t} \mathbf{h}(t-\tau)\cdot\mathbf{F}_{\mathbf{nm}}(\tau) d\tau \tag{6.24}$$

Where $\mathbf{h}(t)$ is the impulse response function matrix. The impulse response function matrix is given from eq. (6.19) as;

$$\mathbf{h}(t) = \frac{1}{2\pi}\int_{-\infty}^{\infty} \mathbf{H}(\omega_e) e^{i\omega_e t} d\omega_e \tag{6.25}$$

Based on the linear and nonlinear response solutions given by eq. (6.24) and (6.25) any response quantity *x(t)* can now be calculated provided the modal value, x_i, is known for each of the *N* nodes. The modal values for actual responses are found during calculations of the eigenmodes. The total response is now obtained from eq. (6.2) on the form;

$$x(t) = \sum_{i=1}^{N} x_i \left(p_{i,lin}(t) + p_{i,nm}(t) \right) \tag{6.26}$$

Fundamental assumptions in the convolution method approach are:

- We assume that the structural dynamic system is linear. This imply that there is a linear relationship between force and response
- A nonlinear force model is allowed. The relationship between incident wave and force may be nonlinear

As an alternative to using convolution integral method, equation 6.21 can also be solved directly by a numerical integration scheme.

6.4.4 Frequency dependency of added mass and hydrodynamic damping

The hydrodynamic added mass and damping matrices is generally dependent on the frequency of oscillation. This imply that the actual value will depend on the mode of oscillation. For the general time dependent load case, frequency dependency of added

mass and damping will introduce a memory effect which should be included in the response calculations. This will be a problem if direct numerical integration is used for solving the Equation of Motion, see eq. (6.21). One approach to account for this effect is outline below.

For high frequencies an asymptotic value of added mass and damping is reached. The following split of added mass and hydrodynamic damping is therefore introduced;

$$A(\omega_e) = A^{\infty} + A^{0}(\omega_e) \qquad (6.27)$$
$$B(\omega_e) = B^{\infty} + B^{0}(\omega_e)$$

Where ∞ indicate the high frequency asymptote and 0 means the deviation from the asymptotic value. Introducing the above approach into eq. (6.21) gives;

$$\sum_{i=1}^{N}\left[\left(M_{ki} + A_{ki}{}^{\infty}\right)\ddot{p}_i + \left(C_{ki} + B_{ki}{}^{\infty}\right)\dot{p}_i + \left(K_{ki} + R_{ki}\right)p_i\right] = F_k{}^{E}(t) - \sum_{i=1}^{N}\left[\int_0^t g_{k,i}(\tau)\dot{p}_i(t-\tau)d\tau\right] \qquad (6.28)$$

Here $g_{k,i}(t)$ is the retardation function for the different mode of motions. The retardation function is determined from frequency dependent added mass and damping as follow;

$$g_{k,i}(t) = -\frac{1}{2\pi}\int_{-\infty}^{\infty} G_{k,i}(\omega_e)e^{i\omega et}d\omega$$

Where

$$G_{k,i} = i\omega_e A_{k,i}{}^{0}(\omega_e) + B_{k,i}{}^{0}(\omega_e)$$

Eq. (6.28) can now be used for an arbitrary time dependent loading and is solved in time domain by numerical integration. However the numerical implementation of the integral term for the retardation function to include the frequency dependency of added mass and damping is not straight forward. This memory effect is therefore often neglected in whipping response calculations and the added mass and damping is taken as the actual values corresponding to the natural frequency.

7 MODEL TEST – SPRINGING AND WHIPPING

7.1 General

Detailed comparison has shown that available numerical methods for springing response calculations significantly under predict the springing response. Also the whipping response is difficult to handle numerically. Model testing for investigation of these phenomena will therefore be of large importance. The use of model test results will be both for establishing design values and design verification for actual practical and for verification and validation of numerical methods.

For model testing of concepts where hydroelastic response is important the elastic properties of the model need to be reasonably correctly scaled. Examples where this will be the case are:

- Marine risers (bending stiffness) and loading hoses (bending stiffness and axial elasticity)
- Tethers for Tension leg platforms (both axial and bending stiffness)
- Mooring lines (axial stiffness)
- Springing and whipping of ships, both monohuls and catamarans (bending stiffness and tensional stiffness)
- Floating bridges
- Fish farming plants
- Seismic cables

This imply that for ship testing including springing and whipping response and for most offshore and coastal structure testing, one or more elements will require modeling of elastic properties. For cases where the elasticity is not important the model is made "sufficient" stiff or "as stiff as possible" to avoid any artificially hydroelastic effects in the model.

7.2 Scaling Laws

In hydroelastic problems the hydrodynamic forces will depend on the structural response which again is governed by the inertial and elastic forces on the structure. The modeling of the elastic properties of structures will therefore give several additional problems compared to the modeling of wave induced dynamic response of rigid structures. Important examples where correctly scaled elastic behavior of the model is springing and whipping of ships, dynamic behavior of marine risers and mooring lines. Additional requirements to the elastic model can be summarized as follows:

- Correctly scaled global structural stiffness
- Structural damping must be similar to full scale values
- The mass distribution must be similar.

Geometrical similarity between model and full scale for an elastic structure will require that elastic deformations are similar. To illustrate this we will consider the deflection of a cantilever beam as an example. The deflection, δ, is given from:

$$\delta \propto \frac{FL^3}{EI} \tag{7.1}$$

where EI is the flexural rigidity and F is the hydrodynamic force which can be expressed as;

$$F \propto C\rho U^2 L^2 \tag{7.2}$$

where C is a force coefficient dependent on F_n, R_e etc. The requirement of similarity in deformation in model and full scale gives:

$$\frac{\delta_F}{L_F} = \frac{\delta_M}{L_M} \Rightarrow \delta_F = \lambda \delta_M \tag{7.3}$$

Using eq. (7.1) and (7.2) this requirement is satisfied if the ratio:

$$\frac{C\rho U^2 L^4}{EI} \tag{7.4}$$

is equal in model and full scale. Assuming equal force coefficient and density we obtain the following requirement to the structural rigidity:

$$\left(\frac{U^2 L^4}{EI}\right)_F = \left(\frac{U^2 L^4}{EI}\right)_M \Rightarrow (EI)_F = (EI)_M \lambda^5 \tag{7.5}$$

If all dimensions of the cross sectional shape of the beam are scaled geometrical similar, the moment of inertia, *I,* will satisfy the relation:

$$I_F = I_M \lambda^4 \tag{7.6}$$

We are than left the following requirement to the Young's modulus, *E,:*

$$E_F = E_M \lambda \tag{7.7}$$

This imply that the Young's modulus for the model must be *1/*λ times the value of the full scale structure.

It should be noted that eq. (7.6) and (7.7) is not to be regarded as requirements to the model. The bending stiffness requirement is given by eq. (7.5). In practical model testing the requirement given by (7.5) is often satisfied by manipulating the different parameters by applying other materials, other wall thickness or modifying the structural build up of the beam. The outer geometry, which is exposed to the hydrodynamic forces, has however to be geometrical correct modeled. Also the requirements to correct modeling of mass distribution and structural damping have to be satisfied. This will be further discussed as part of the physical modeling.

A similar results will be found for the axial stiffness and torsion stiffness. The requirement for the axial stiffness case is:

$$(EA)_S = (EA)_M \lambda^3 \tag{7.8}$$

where *EA* is the axial stiffness. This relation gives equal strain in model and full scale. The cross sectional area, *A,* will satisfy the relation $A_F = A_M \lambda^2$, which gives the same requirement to the Young's modulus as shown above.

For the dynamic response of an elastic structure the mass *m* and structural damping *b* should also be correctly modeled. This requirement gives;

$$m_F = m_M \lambda^3$$

$$b_S = b_M \lambda^{2.5}$$

It is a requirement that the modeling do not introduce additional damping. Materials which shows hysteresis behavior should therefore not be used for modeling. Other source

for unwanted damping can be frictional forces between different components in the build up of the model.

In general requirements of correctly scaled elasticity of ship model will significantly increase the complexity (and hence cost) for model production and also test execution. In addition detailed information about the full scale elastic properties will be required to arry out the required modeling

7.3 Ship modeling

For elastic modeling of ships three different solutions have so far been used, see Maeda (1991):

- Backbone model
- Fully elastic model
- Hinged model

7.3.1 Backbone model

In Figure 7.1 the two first alternatives are shown schematically for a monohull. For the backbone modeling, the elasticity of the model is represented by an elastic beam to which rigid segments are connected, see also Fig. 7.2. Using this modeling technique it is relatively easy to model the stiffness and materials as steel or aluminum with stable and well documented properties can be used. Further it is easy to modify the structural properties and the structural damping is low. One problem with this modeling is the gap between the different sections. They may be closed using an elastic membrane, as shown in Fig 7.2, but it is difficult to avoid transfer of tension through the membrane. If the gaps are open, each section have to be built water tight. Further the dynamic pressure at gaps may to some extent influence the results. For ship models with forward speed the gaps will give additional resistance due to the influence on the flow field around the ship.

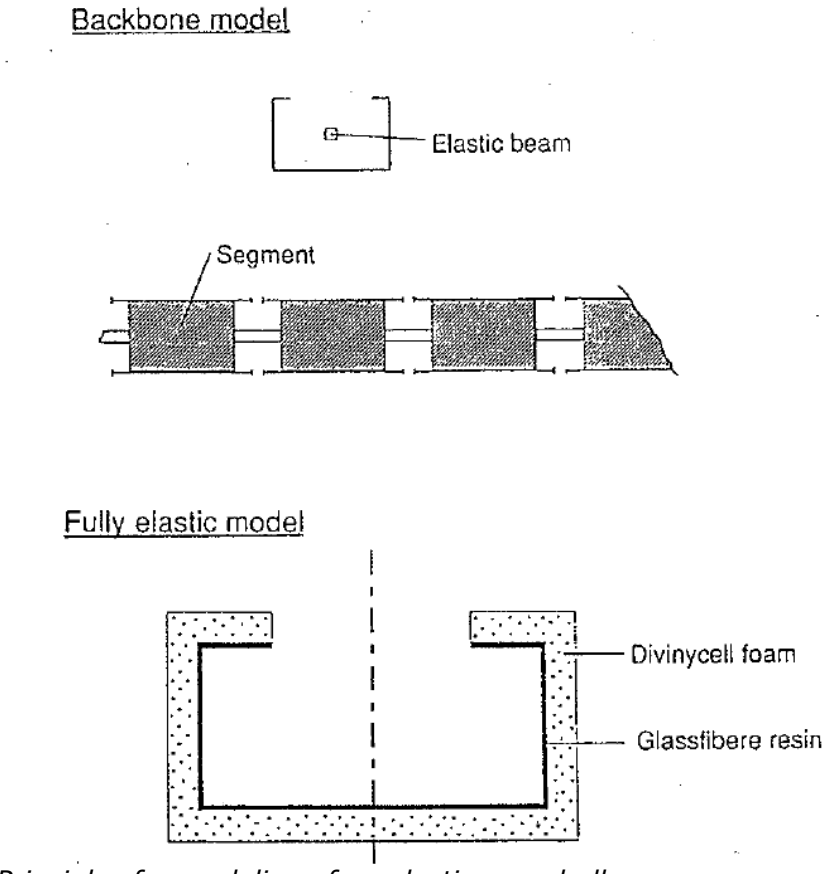

Figure 7.1 *Principles for modeling of an elastic monohull.*

One drawback with the backbone modeling is that it is difficult to adjust the stiffness and hence to obtain the correctly scaled mode shapes and natural frequencies.

The responses as shear forces and bending moments are measured directly at the backbone, usually by means of strain gauges.

7.3.2 Fully elastic model

The fully elastic model is built up using cross sections with one or two different layers with different elasticity as shown in Figure 7.1. Glassfibere resin in combination with a foam material can be used. The thickness of the inner resin layer can be varied to achieve the correct elasticity. This method of modeling avoids the gap problems, but it is difficult to achieve the correct bending stiffness distribution. Further the use of foam material introduce some hysteresis effects and the structural damping may be too high for the model. For testing of springing response this is critical for the results. For whipping response the structural damping level is less critical.

For the fully elastic model, measurements of shear forces and bending moments require extensive strain gauge instrumentation and the calibration is more difficult to carry out compared to the alternative modeling principles. The accuracy of the measurements may therefore be less good compared to the alternative methods.

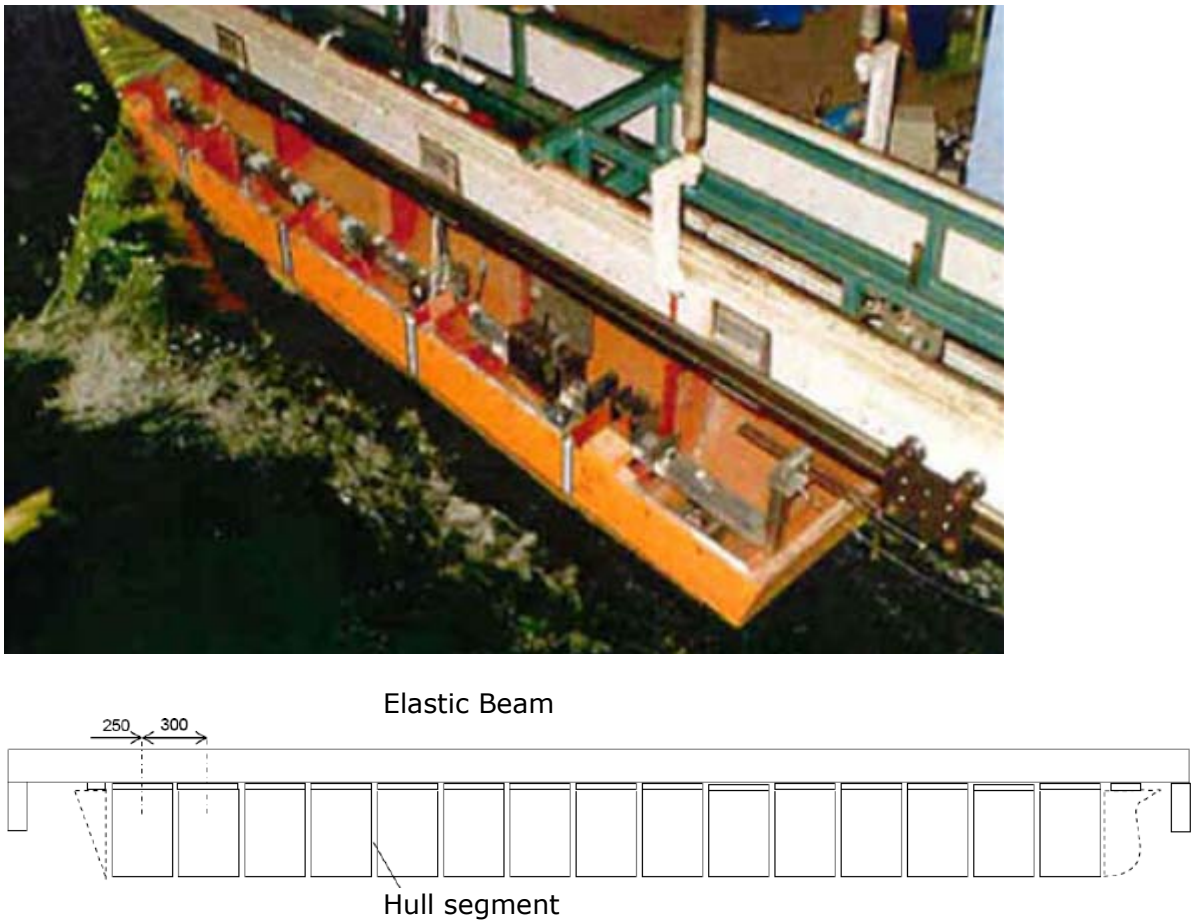

Figure 7.2 *Elastic Backbone model of an elastic monohull.*

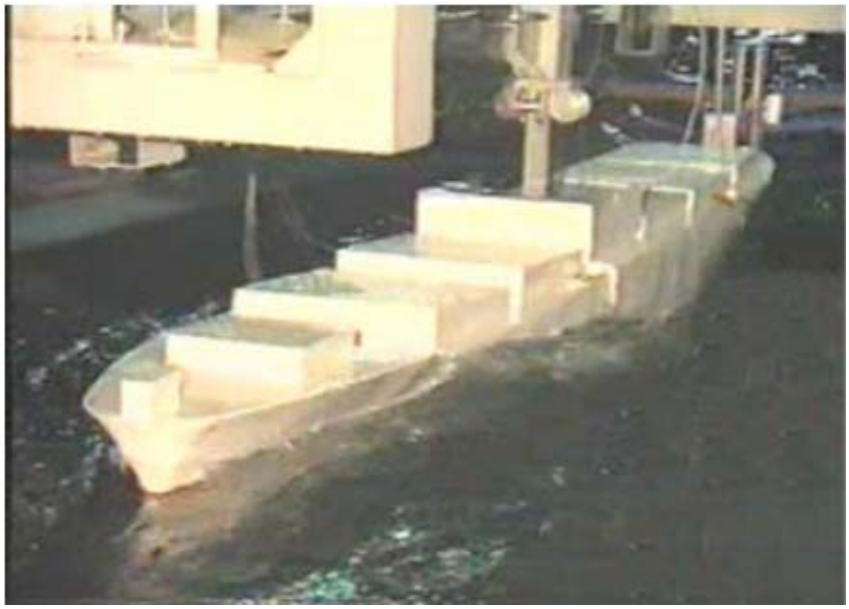

Figure 7.3 *Example of a fully elastic model.*

7.3.3 Hinged Models

The hinged modeling is based on dividing the hull girder into a number of stiff segments connected by elastic spring as shown in Fig. 7.4. The springs can be made with adjustable stiffness. In this way it becomes easy to obtain the correct scaling of the first flexible mod(s). The spring stiffness may also be varied for systematical investigation of effect of natural frequencies. Within the rigid segments a framework is often used to ensure stiffness and give support for the springs and force transducers. The gap between the different segments may be closed using an elastic membrane.

For springing response only the 1st elastic mode will be important and a 2 segmented model have been found to give a reasonable good modeling of the elastic performance, see Økland (2002). For whipping response 3 or 4 segment models is recommended. With a 4 segmented model the first 3 global flexible vertical modes of the full scale ship may in principle be represented. The position of the cuts is important to give the best possible representation of the elastic modes. Usually the cut is located at $x = \pm L/4,$ and at $x = 0,$, i.e. at quarter lengths and at midship. The mode shapes for the hinged model can be quite similar to the actual mode shapes for the full scale ship. An example is shown in Fig 7.5, from Drummen (2008), where both measured and calculated 1st and 2nd elastic modes for model as well as calculated for full scale vessel are shown.

In the connections between the stiff segments well defined force transducers can be used. Very good accuracy of the measurements can therefore be obtained for this modeling. The drawback is that forces and moments can only be measured at the cut positions.

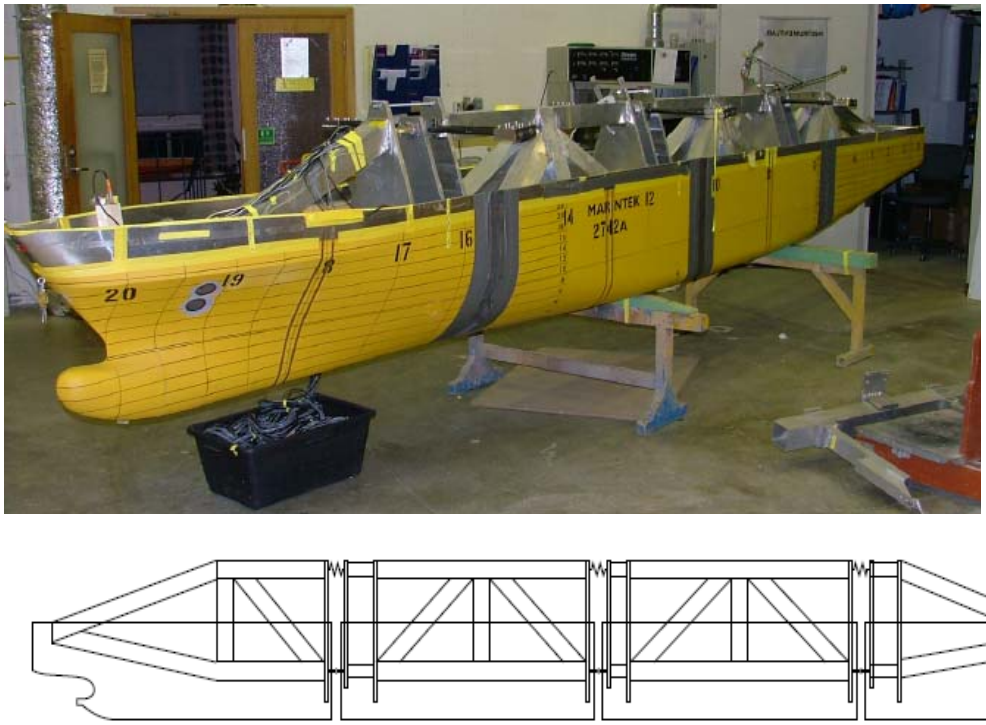

Figure 7.4 *Sketch of a four segmented hinged model of a Monohull*

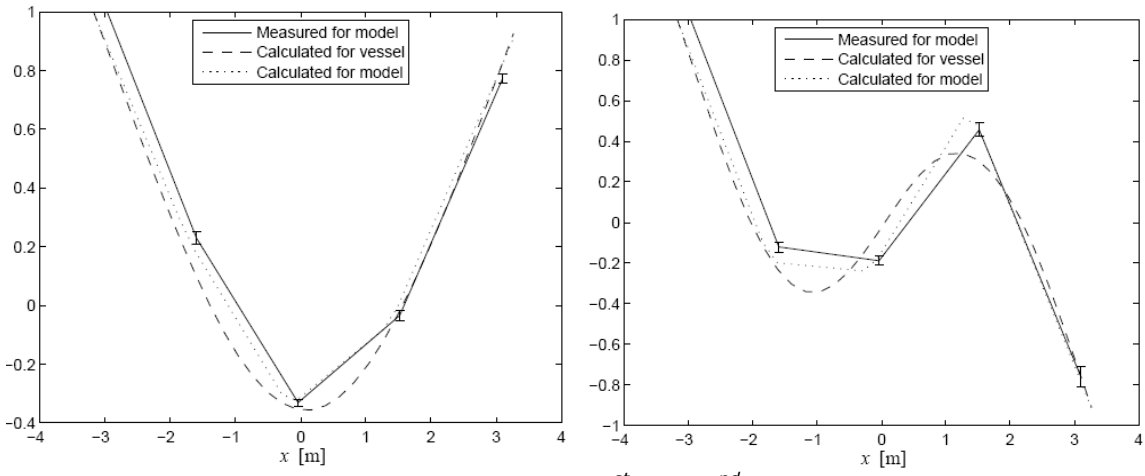

Figure 7.5 *Example of mode shapes for 1st and 2nd modes for the segmented model as shown in Fig 7.3. Both measured and calculated for model as well as calculated for full scale vessel. (From Drummen, (2008))*

While the Backbone and fully elastic model is best suited for monohuls the hinged model solution has also been used for catamarans, see Hermunstad et.al. (1995). An example elastic modeling of catamaran using hinges model is shown in Figure 7.6. Each hull is divided in three rigid segments which are connected by springs. The springs are slender steel beams with dimensions determined to give correct bending and tensional stiffness. The two hulls are connected trough three transverse springs as shown in the figure. The hull segments are made of Foam/GRP similar to what is used for standard rigid model production. To make the segments stiff, an aluminum frame is mounted within each section. Rubber straps is attached between each segment to make the model water-tight.

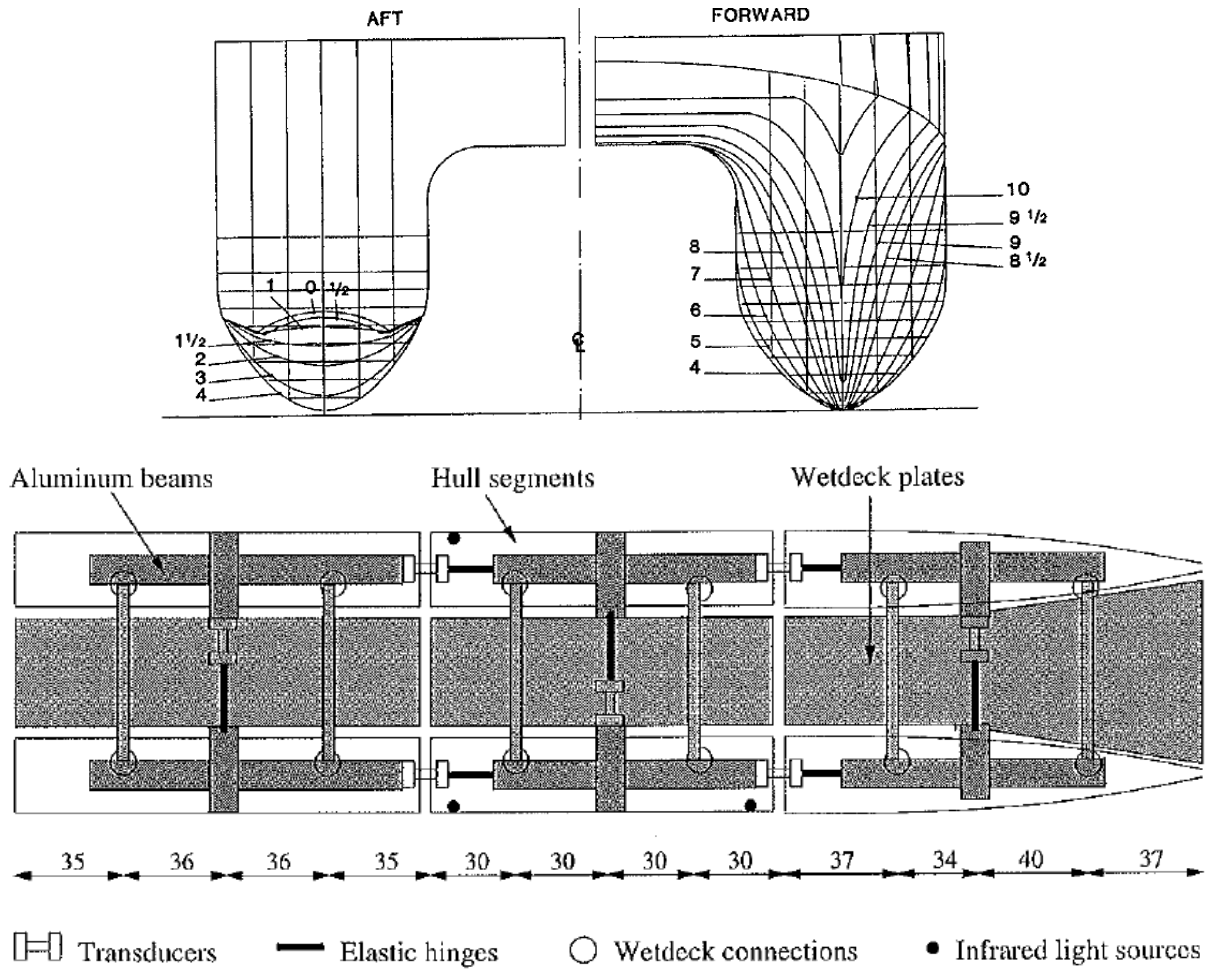

Figure 7.6 *Hinged model of an elastic catamaran*

7.4 Measurements / Instrumentation

A typical set for measurements and instrumentation for model testing of flexible hull models can be summarized as follows;

- 6 DOF motion measurements (e.g. optical system)
- Accelerometers (FP, amidships, AP) (x,y,z-directions)
- Wave probes (ahead of ship + fixed to ship bow for relative vertical motions)
- Slamming panels (at hull bottom or in flare)
- Pressure gauges at bottom and at flared part of bow section /wet deck
- Hinged models: Force/moment transducers at hinges
- Backbone and fully flexible models: Strain gauges at several sections

The rigid body motions is measured by optical system based on sensors on one of the stiff segments close to midship.

In fig 7.7 is shown an example of position and type of transducers for force and bending moment measurements at a cut for a hinged model. 3 transducers are used at each cut. At each force transducers forces in 3 d.o.f's are measured. Combined with the distance between the transducers, axial force, shear forces, bending moments and torsional moment is obtained in the cut.

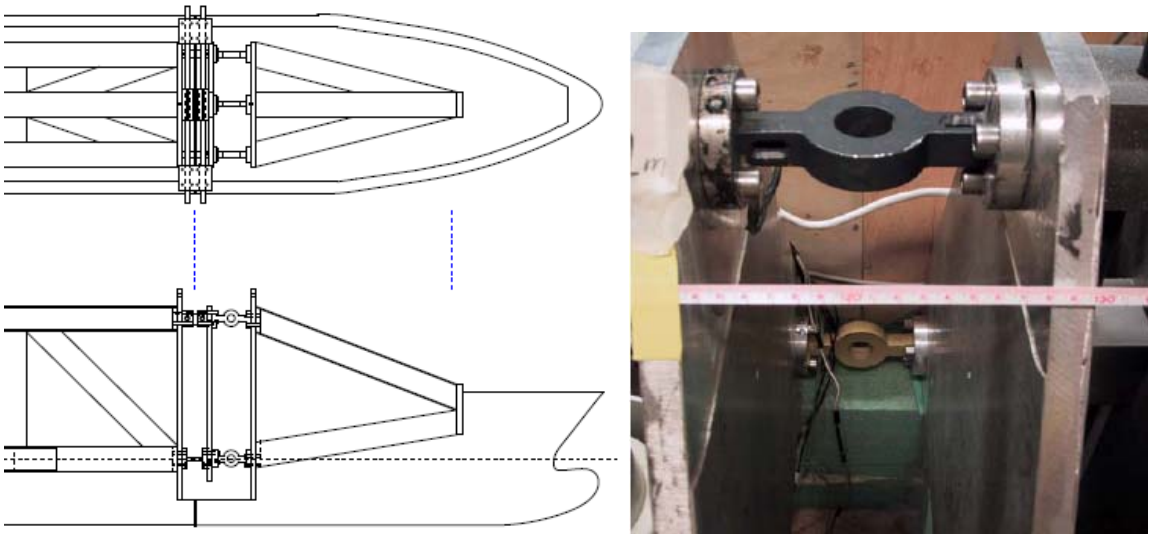

Figure 7.7 *Example of force / bending moment measurements for hinged model.*

In Fig. 7.8 typical instrumentation and position of transducers are shown for a test set up with a hinged Monohull.

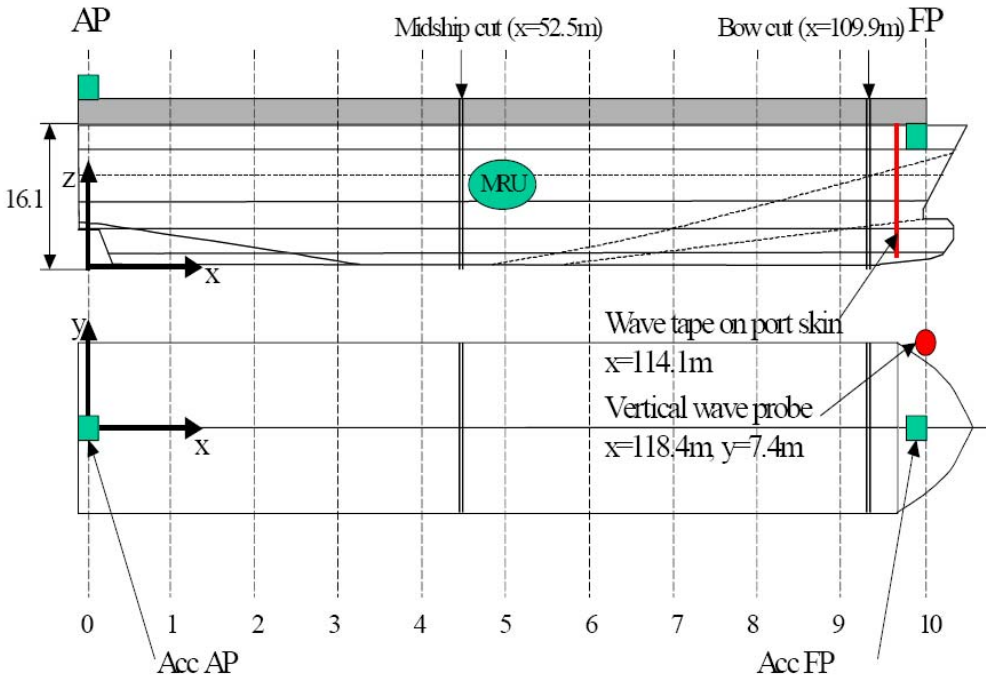

Figure 7.8 *Typical Instrumentation for testing with flexible hull models.*

7.5 Test Execution.

For model testing of elastic models it is of fundamental importance to verify the structural properties of the model. This includes mass distribution, tuning of natural frequency and mode shapes for the different elastic modes as well as documentation of the structural damping ratios. These verification activities are typically carried out prior to wave tank test and includes the following;

- Dry tests:
  - Calibration of all sensors
  - Hammer impact tests to measure natural frequencies and damping ratios
  - Static tests with known forces to verify force/moment measurements

- Calm water tests:
  - Hammer impact tests at zero speed to measure wet natural frequencies and damping (frequencies decrease due to added mass) in the relevant modes
  - Hammer impact tests at forward speed (hydrodynamic damping may increases with speed – lift effects)
  - Tests at various forward speeds to measure trim and sinkage
  - Roll decay tests at zero speed and forward speeds to measure roll natural frequency and damping

Tests in waves can be carried out in a towing tank or in a Ocean Basin. For both cases both towed model (or for zero speed, position keeping by springs) and self propelled model are used. Depending on the purpose of the test the following wave tests will normally be included;

- Regular wave tests:
  - 1 - 3 headings (head seas and bow quartering seas) + other headings less relevant for springing/whipping. Following seas if stern slamming at zero speed.
  - 8 – 12 wave periods for each heading
  - Repetitions for the most critical periods

- Repetitions with steeper waves (for the most critical periods) to study nonlinear effects

- Irregular wave tests:
  - A number of different sea-states (moderate, high , very high (survival condition), depending on purpose of tests)
  - 1 -3 headings (as above)
  - Duration of time-series corresponding to 1 - 3 hrs full-scale (for whipping)
  - Long time-series are obtained by running the model many times across the tank/basin and then merging the different runs.

- Speeds: Service speed, survival speed + possibly intermediate speed

7.6 Decay test

Decay tests will give important information about natural frequencies and mode shapes, added mass and damping (linear and quadratic) of a dynamic system. Decay tests are frequently carried out both for dry (i.e. in air) and wet (i.e floating in water) conditions.

An example of measured response from decay test with an elastic modeled monohull is shown in Fig. 7.9. The model is excited by a force pulse and the resulting response is measured.

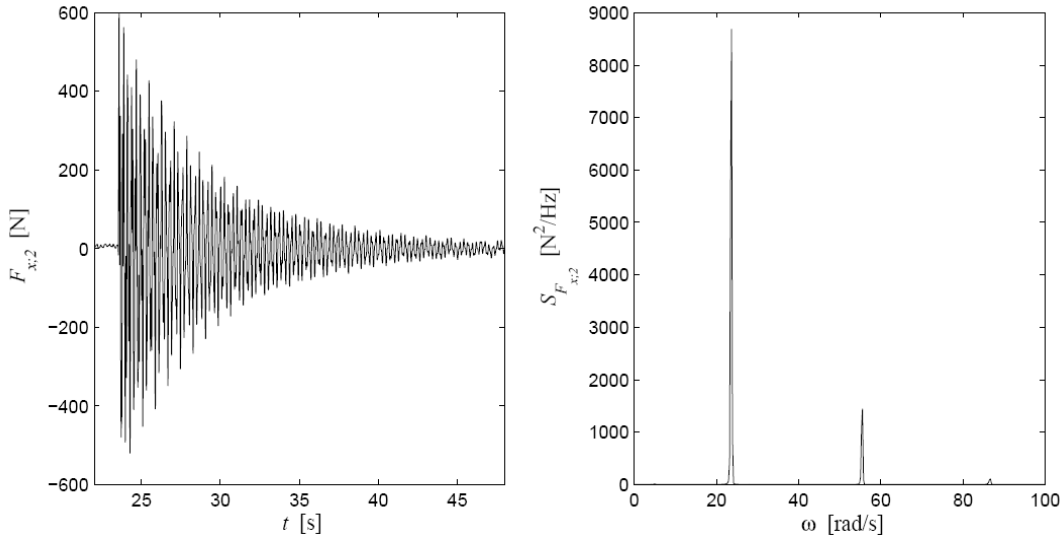

Figure 7.9 *Time series of midship horizontal force after application of an impulse force. Right; Time series. Left; spectral density function.*

The natural frequencies (representing the 2-node and 3-node modes) are clearly identified from the spectral density function of the response.

In order to determine the damping ratio for the different modes the signal needs to be band pass filtered around the actual natural frequency to identify the response at the different modes. Result for time series after filtering around the 2-node mode is presented in Fig. 7.10.

The damping ratio is now obtained from the ratio of two peaks, separated *m* cycles as;

$$\xi = \frac{1}{2\pi m} \ln \frac{F_{X,A}^{n}}{F_{X,A}^{n+m}}$$

Where $F_{X,A}^{n}$ is the n^{th} peak of the time series $F_X(t)$. The result for the damping ratio is also included in Fig 7.10. The actual modal damping of the mode, *c,* is now obtained from the definition of the ratio between the modal damping and the critical damping:

$$\xi = \frac{c}{2k/\omega_0}$$

Where k represent the modal stiffness and ω_0 is the natural frequency of the mode.

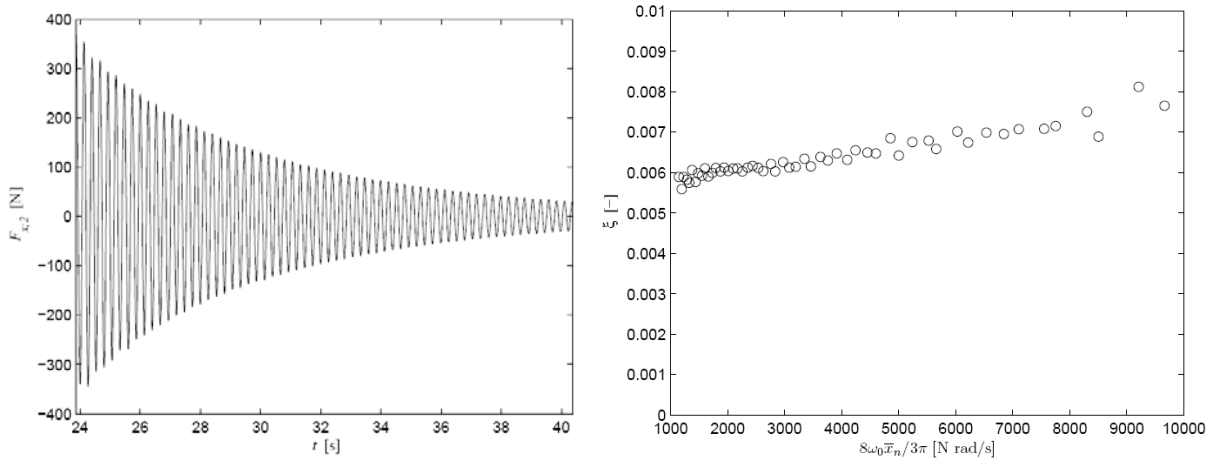

Figure 7.10 *Left; Time series from fig 7.9 after band pass filtering around the natural frequency of the 2-node mode. Right; Damping ratio obtained from filtered time series*

7.7 Analysis of Results from Wave tests – Whipping and Springing.

7.7.1 General about test result analysis

Standard analysis method of results from wave tests will be;

- Measured time series from *regular* waves:
  - Fourier analysis to obtain RAO's (linear and higher order responses) and phase between the different responses.

- Measured time series from *irregular* waves:
  - Filtering to split wave frequency contributions and high frequency response for responses influenced by elastic modes
  - Spectral analysis to investigate frequency content
  - Statistical analysis to estimate statistical distributions and extreme values
  - Rain flow counting to evaluate fatigue damage

Some examples will be discussed in the following

7.7.2 Results for Springing Response.

For regular waves with encounter frequency close to $\omega_e \approx 1/2\omega_N$ or $\omega_e \approx 1/3\omega_N$ significant springing response will be generated. This will be most pronounced in relative steep waves where nonlinear wave excitation effects (not slamming forces) are important. A typical example is shown in Fig. 7.11 where the measured time history of the vertical shear forces and vertical bending moment at midship and relative vertical motions at bow are shown. The corresponding energy spectra for the responses are also included. The encounter frequency is close to 1.1 Hz. For the vertical shear forces and bending moment the dominating response frequency is 3 times larger, i.e at 3.3 Hz which corresponds to the lowest natural frequency (wet mode) of the model. These results clearly shows that

higher order wave excitation forces can generate springing type response. This is denoted as Nonlinear Springing (see also chap 3.5)

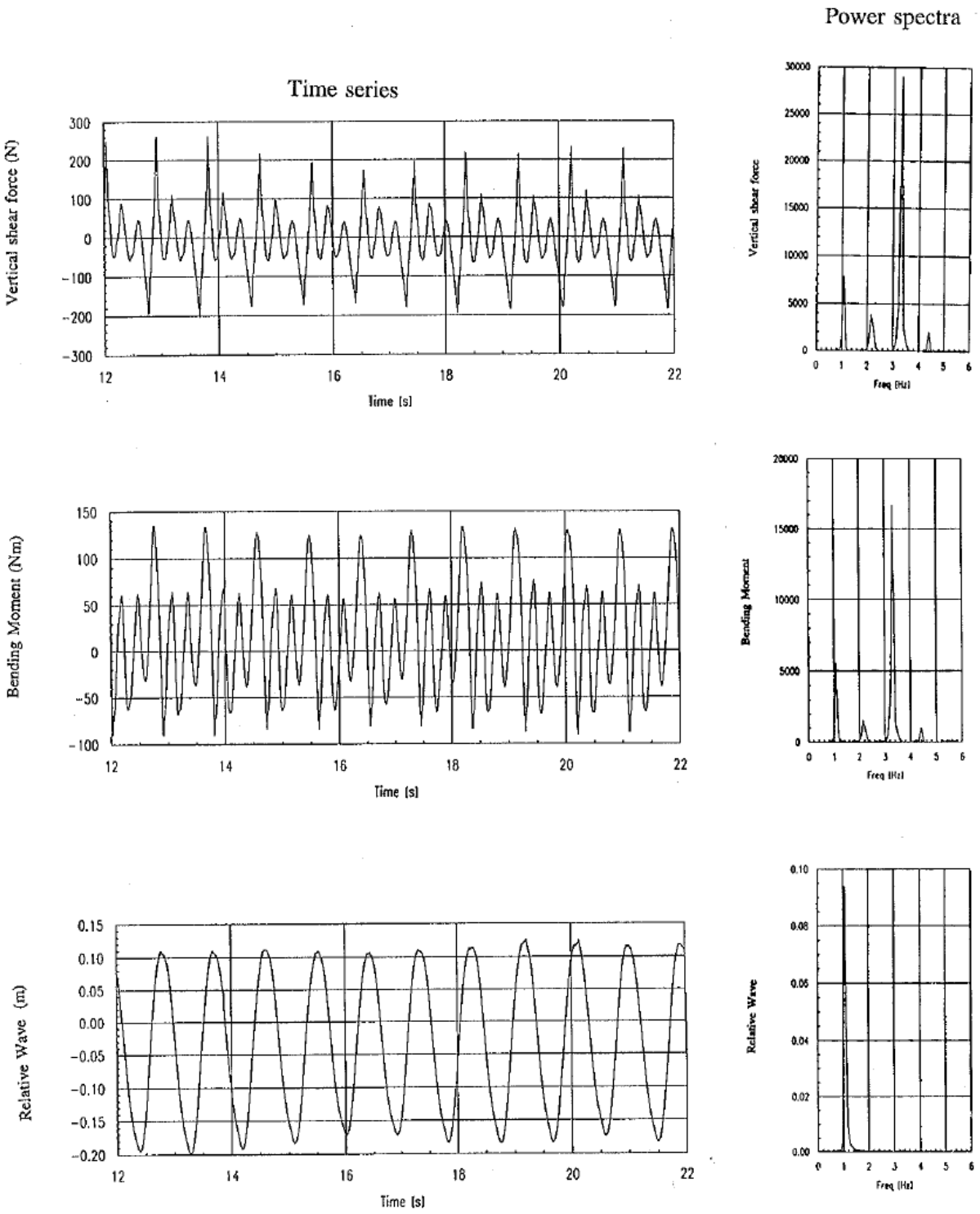

Figure 7.11 *Measured time history and corresponding energy spectra of the vertical shear forces , vertical bending moment and relative vertical motions at bow (FP). Regular waves, H=0.1 m, T=1.8 s, Froude number Fn=0.5.*

7.7.3 Results for Whipping Response.

En example of measured whipping response for a catamaran in head sea waves is shown in Fig. 7.12. The actual sea state is Hs=0.17 m and Tp=1.65 s. Froude number, Fn=0.5. The upper time series plot shows the measured total vertical bending moment in a cut. The total signal was low pass and high pass filtered to split into the wave frequency contribution and response at higher frequency. The power spectra for relative vertical motion at bow and the vertical bending moment are also shown in the figure. For this wave condition significant wet deck slamming was measured. The relative motion response contain only energy at the encounter frequency of the incident waves, seen to give a peak frequency at $f_e \approx 1.2Hz$. For the bending moment and shear forces two different peaks occur. The low frequency region corresponds to the encounter frequency of the incident wave. The energy at higher frequencies is a result of the resonant vibration close to the first elastic mode and natural frequency of the model. This high frequency response is partly generated by springing (nonlinear in this case) and partly due to wet deck slamming, i.e whipping. It is not possible to split these two contributions from the test results.

In Fig. 7.13 the cumulative probability distribution for the amplitudes of the vertical shear force and bending moment and for the heave and pitch motions are shown. The heave and Pitch motions are seen to follow quite closely to the Rayleigh distribution and hence indicating that the motions are not significantly effected by slamming forces or other nonlinear effects. Both the shear forces and bending moments deviate significantly from the Rayleigh distribution. The maximum amplitude value at probability level 0.999 (i.e 1 of 1000 amplitudes exceed this level) is seen to be 1-5-2 times the amplitude value predicted from the Rayleigh distribution indicating a strong influence of non-linear effects. Hence assuming Rayleigh distribution for this case will largely underpredict the maximum values.

The distribution shown in Fig 7.13 was for the total measured signal. In Fig 7.14 the cumulative distribution of the high pass and low pass filtered responses are shown for the vertical shear forces. The low pass filtered response, i.e the wave frequency part, is seen to follow very closely to the Rayleigh distribution. The high frequency response, i.e. response at resonant vibration part, is seen to be close to the exponential distribution. The maximum value of the two different contributions is seen to be of the same order of magnitude for this case. Using a rigid model for this case the response contribution at the resonant elastic vibration would have been lost and the total response for bending moment and shear forces would therefore have been largely underestimated.

This clearly show the importance of accurate modeling of the elastic properties of the ship and carful analysis of the measured results to give a realistic result for the global structural responses.

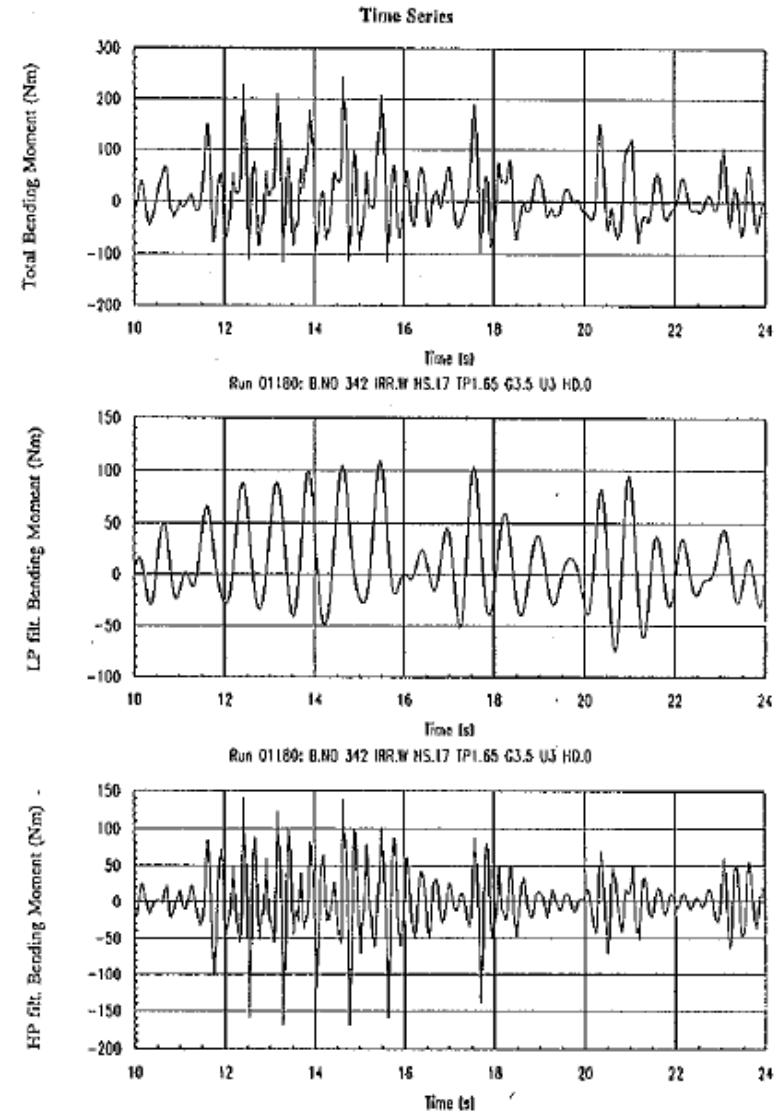

b:

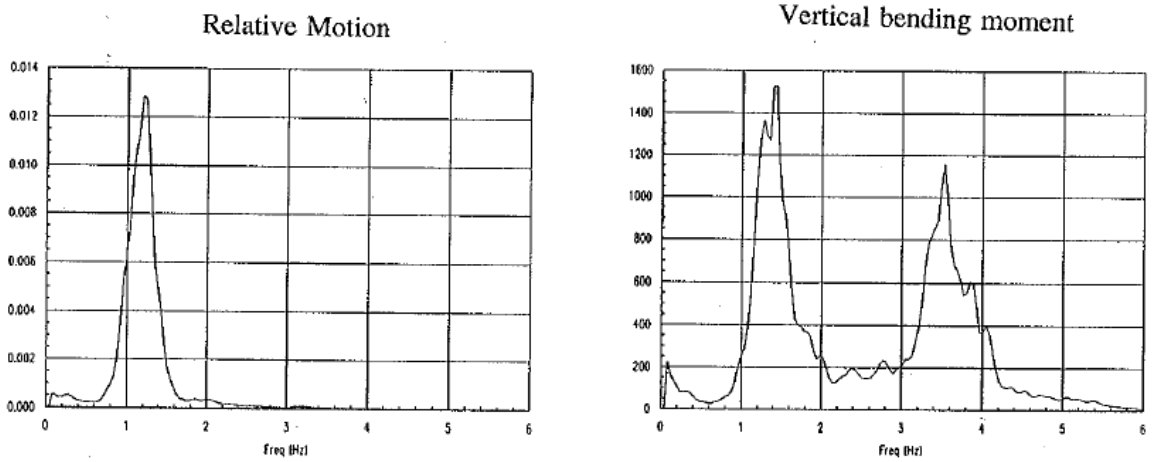

Figure 7.12 *Whipping response measurements. Results for catamaran in head sea. Irregular waves with Hs=0.17 m, Tp=1.65 s. Fn=0.5.*
a: Time history plot of measured vertical bending moment. Total signal, low pass filtered (i.e wave frequency part), and high pass filtered (i.e due to whipping response.
b: Power spectra for relative vertical wave motions at Bow and power spectra of vertical bending moment.

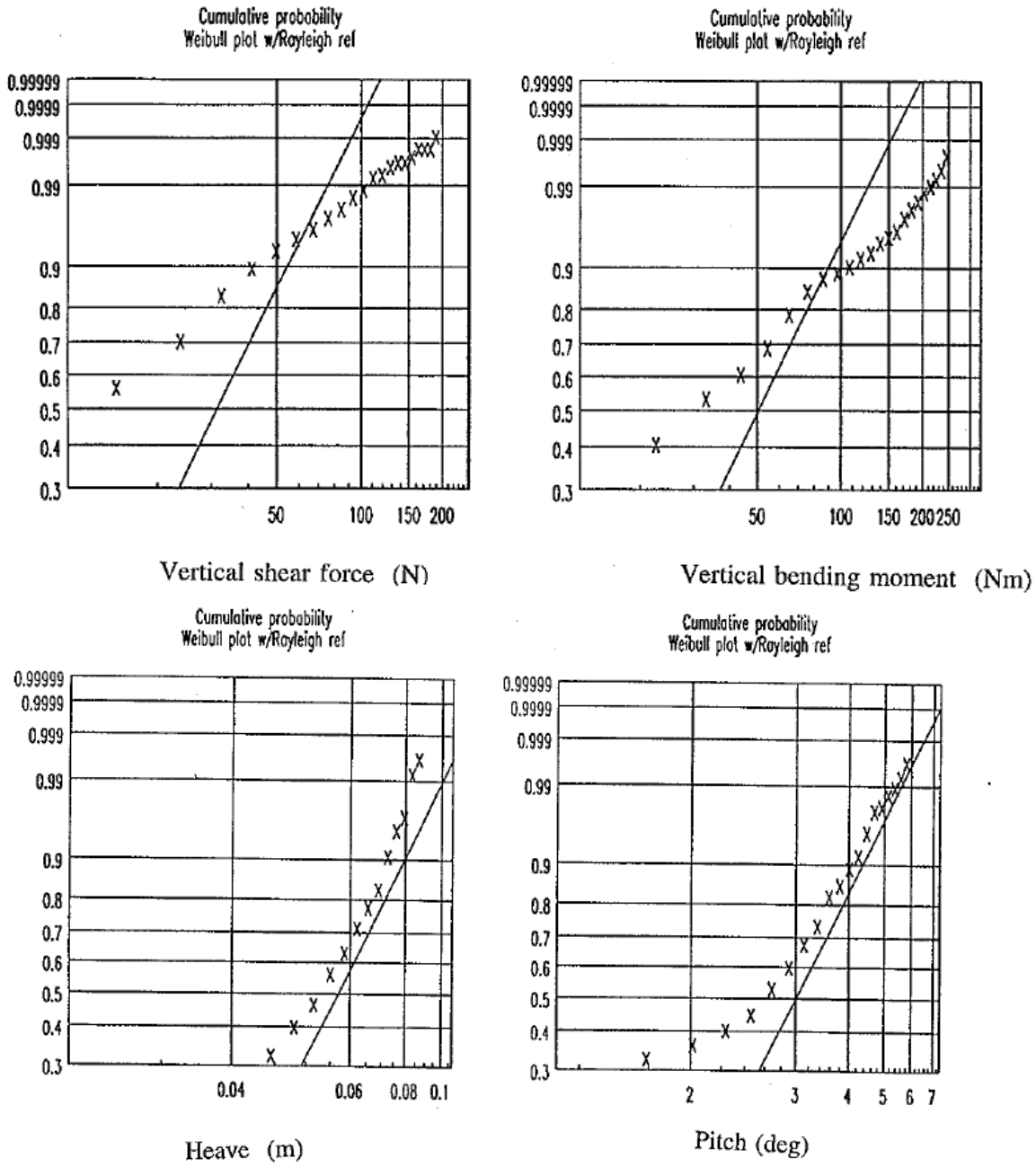

Figure 7.13 *Cumulative probability distribution for the vertical shear force, vertical bending moment and heave and pitch motions. Results for catamaran in head sea. Irregular waves with Hs=0.17 m, Tp=1.65 s. Fn=0.5.*

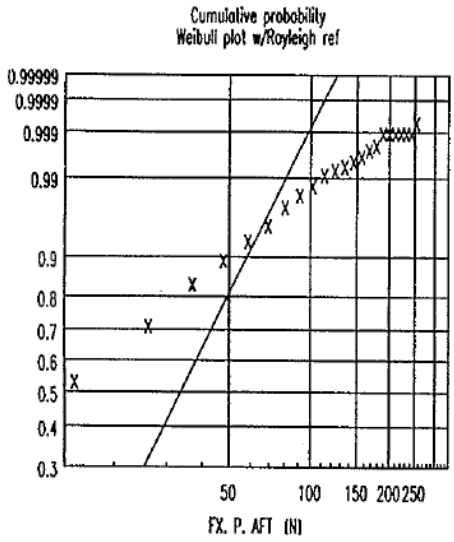

Total shear force

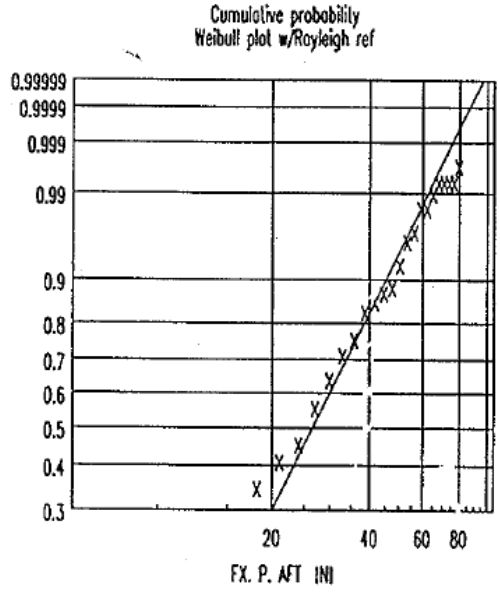

Wave frequency component

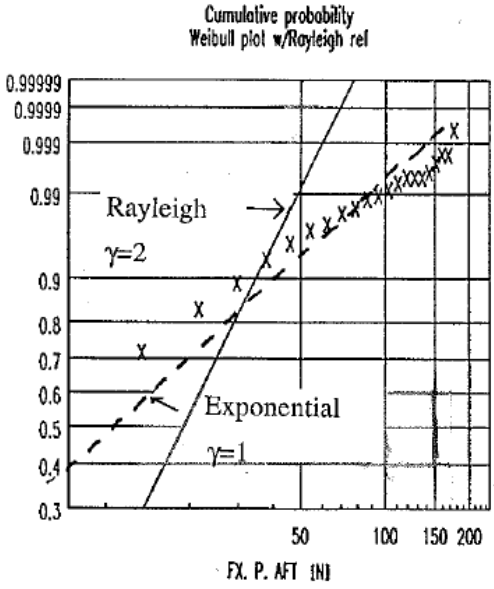

High frequency component

Figure 7.14 *Cumulative probability distribution for the total measured vertical shear force and for the wave frequency and high frequency part of the vertical shear force. .Irregular waves with Hs=0.17 m, Tp=1.65 s. Fn=0.5.*

7.8 Scaling from model to Full scale.

Requirements to physical modeling of the elastic properties of a full scale ship in model scale are discussed in chap 7.2 above. Scaling of model test results to full scale values (assuming properly scaled elastic properties of the model!) is based on Froude Scaling.

The following scaling relations from model to full scale are obtained;

- Time: $t_S = t_M \cdot \sqrt{\lambda}$
- Wave frequency: $\omega_S = \frac{\omega_M}{\sqrt{\lambda}}$
- Surge, sway, heave motions: $\eta_S = \eta_M \cdot \lambda$
- Roll, pitch, yaw motions: $\eta_S = \eta_M$
- Accelerations: $a_S = a_M$
- Pressures: $p_S = p_M \cdot \lambda$
- Forces: $F_S = F_M \cdot \lambda^3$
- Moments: $M_S = M_M \cdot \lambda^4$

8 HYDROELASTIC SLAMMING

8.1 General

A dynamic structural response will arise if the duration of the impact load is comparable to, or shorter than, the relevant natural period of the structure. For bow flare slamming on ships, the duration of the slamming load will often be long compared to the short natural period of the hull plating. Hence a quasi static approach is applicable. On the other hand slamming on the wetdeck of a catamaran may give rise to a dynamic structural response in the local plating since the rise time of the pressure is shorter than the plating natural period. Such cases where the duration of the slamming load is much shorter than the natural period of the structure is denoted *Hydroelastic slamming*

For multihull vessels heavy wetdeck slamming may occur in waves. The wetdeck is the structural part connecting the side hulls of a catamaran. The high slamming loads on the wetdeck structure will introduce local and global hydroelastic effects of the vessel. Other applications where local hydroelasticity can be important is for stern slamming towards structural part of the hull which is close to horizontally. Also for horizontal deck structure on fixed and floating platforms with insufficient freeboard, the effect of hydroelasticity may be important for slamming load and response due to wave run up and direct slamming loads.

In summary, for an impact to be hydroelastic, it is essential that a large force pulse occurs during a small time period relative to the wet natural period of the analyzed structural part. For a general discussion of hydroelastic slamming, see the review article by Faltinsen (2000).

8.2 Theoretical description – One Elastic Beam

8.2.1 Structural modelling

The local hydroelastic effects will be considered by investigating a typical wetdeck structure exposed to slamming loads from a incoming wave hitting the wetdeck. A typical wetdeck structure between the hulls of a multihull vessel is shown in Fig. 8.1.

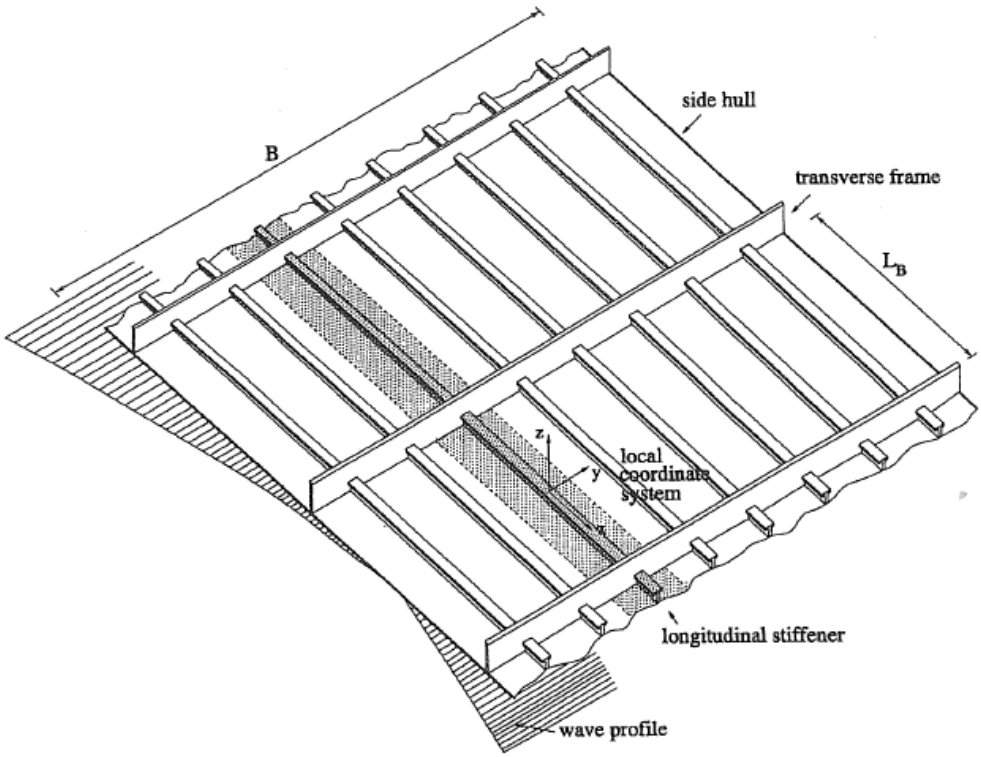

Figure 8.1 *A detail of the wetdeck structure of a Multihull vessel..*

The wetdeck between two transverse stiffeners (see Fig. 8.1) is modeled as an elastic beam. The beam properties includes both the plate and the longitudinal stiffeners. The beam equation of motion is written as (see also eq. (3.1));

$$M_B \frac{\partial^2 w}{\partial t^2} + EI \frac{\partial^4 w}{\partial x^4} = p(x, w, t) \tag{8.1}$$

Where M_B is the structural mass pr length unit, $w(x,t)$ is the elastic beam deflection, t is time and x is a longitudinal coordinate along the length L_B of the beam. E is the Young's module, EI is the bending stiffness. Note that the above figures include both the effect of the plate and the longitudinal stiffeners. L_B is the length between the transverse stiffeners. M_B and EI are assumed to be constant. See also Fig. 8.2

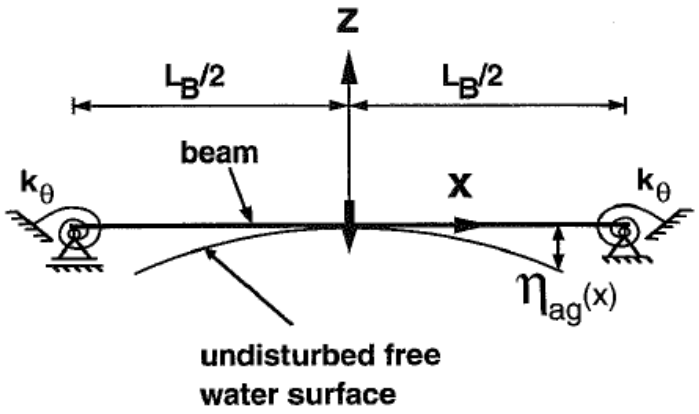

Figure 8.2 *Definition of single beam model.*

The term $p(x,w,t)$ is the hydrodynamic pressure. Note that for this case the pressure is assumed to be a function of the elastic beam deflection w.

Effect of rigid body accelerations are neglected since it will be small compared to the beam deflection acceleration term in eq. (8.1)

In the above structural formulation (Euler Beam) the effects of shear and axial deformation have been neglected. Studies by Kvålsvold (1994) have shown that these simplifications had insignificant effects on the maximum response values.

One basic assumption is that the elastic beam deflections $w(x,t)$ can be written as a linear sum of "dry" normal modes;

$$w(x,t) = \sum_{i=1}^{N} a_i(t) \cdot \psi_i(x) \tag{8.2}$$

where $a_i(t)$ are the time dependent principal coordinates. "dry" indicating that the effect of surrounding water on the normal modes $\psi_i(x)$ is not included. The normal modes have to satisfy the boundary conditions given by;

$$w(x,t) = 0 \qquad \text{for} \qquad x = \pm \frac{L_B}{2}$$

and

$$\frac{k_\theta}{EI} \frac{\partial \psi_i}{\partial x} \pm \frac{\partial^2 \psi_i}{\partial x^2} = 0 \qquad \text{for} \qquad x = \pm \frac{L_B}{2} \tag{8.3}$$

The last boundary condition is based on continuity of the bending moment at the ends. The assumed spring stiffness at the ends of the beam is equal to k_θ, see Fig. 8.2, which gives a restoring end moment equal to $-k_\theta \theta_{be}$. θ_{be} is the rotation angle at a beam end.

The natural frequencies and normal mode shapes are determined from the free vibration case, see the discussion in chap 3.2.2.

The general solution of eq. (8.1) with eq. (8.2) implemented are discussed under springing in chap 3.2.2, see eq. (3.7). The solution can be written as;

$$\psi_i(x) = A_i \sin(p_i x) + B_i \cos(p_i x) + C_i \sinh(p_i x) + D_i \cosh(p_i x) \tag{8.4}$$

Where the coefficients A_i B_i C_i and D_i are determined from the boundary conditions, eq. (8.3).

The modal solution of $w(x,t)$ expressed by eq. (8.2) is substituted into eq. (8.1), multiplied with $\psi_j(x)$ and integrated over the length of the beam (see also the discussion in chap 3.2.3). By using the orthogonally property of the normal modes, the governing modal beam equation of motions in vibration mode *i* becomes;

$$M_{ii}\ddot{a}_i(t) + C_{ii}a_i(t) = \int_{-c(t)}^{c(t)} p(x,w,t)\psi_i(x)dx = F_i^H(w,t) \tag{8.5}$$

Where M_{ii} and C_{ii} are the modal mass and restoring coefficient respectively written as;

$$M_{ii} = \int_{\frac{-L_B}{2}}^{\frac{L_B}{2}} M_B \psi_i{}^2(x)dx \tag{8.6}$$

$$C_{ii} = \int_{\frac{-L_B}{2}}^{\frac{L_B}{2}} EI \frac{\partial^4 \psi_i(x)}{\partial x^4} \psi_i(x)dx \tag{8.7}$$

The natural circular frequency is given from;

$$\omega_i{}^2 = \frac{C_{ii}}{M_{ii}} \tag{8.8}$$

The term *c(t)* in eq. (8.5) represent the position of the edge of the jet flow following the impact. This value determines the integration limits for the hydrodynamic pressure.

In the above discussion the effect of rigid body acceleration have been neglected.

8.2.2 Impact Loads - Hydrodynamic Boundary Value Problem

The hydrodynamic pressure is found by solving a two-dimensional boundary value problem in an incompressible fluid and irrotational flow. The fluid accelerations are assumed to be much larger than gravity. The formulation of the boundary value problem is shown in Fig 8.3. ϕ is the velocity potential in the fluid due to the impact. The velocity potential satisfies a 2-D Laplace equation in the fluid.

The boundary conditions on the wetted part of the beam;

$$\frac{\partial \phi}{dz} = V(t) + \frac{\partial w(x,t)}{\partial t} \qquad \text{on } z = 0, \quad -c(t) \le x \le c(t) \tag{8.9}$$

Where $V(t)$ is the vertical velocity of the beam (from global ship motions including heave and pitch motions). Here $V(t)$ should be interpreted as the total relative vertical velocity between the water surface and the rigid body.

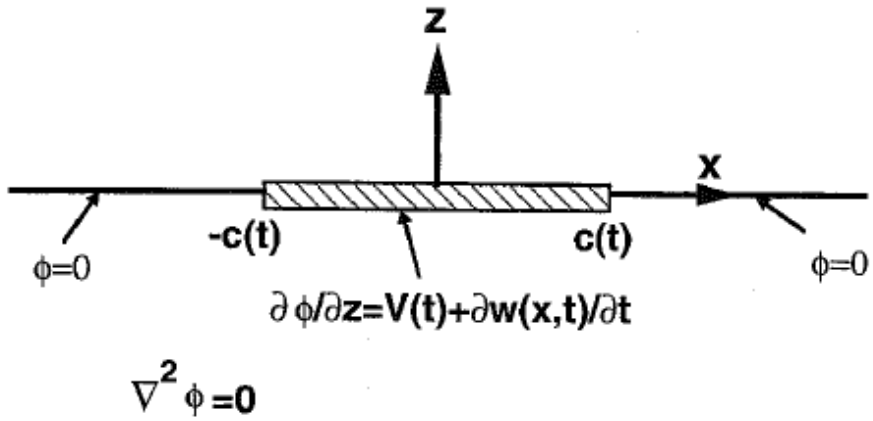

Figure 8.3 *Boundary value problem for analysis of impact between plate and wave crest*

The instantaneous wetted area of the plate is given from the outer position of the yet flow measured from *x=0*, denoted as *c(t)*.

The free surface boundary condition is;

$$\phi = 0 \left| x \right| \ge c(t) \qquad \text{on } z = 0, \qquad \left| x \right| \ge c(t) \tag{8.10}$$

The most simple solution of the above defined boundary value problem is obtained by assuming that the vertical velocity in the water impact region is independent of space and only time dependent. The vertical velocity on the wetted length of the beam is approximated by its mean value in space. This gives a pure time dependent velocity;

$$w(x,t) = \overline{w}(t)$$

The solution of the velocity potential for this case becomes the classical solution of heaving plate in infinite fluid, see e.g Newman (1977).

$$\phi(x,t) = \left[V(t) + \frac{\partial \overline{w}(t)}{\partial t} \right] \sqrt{c^2(t) - x^2}$$

Where $\partial\overline{w}(t)/\partial t$ is the mean vertical beam vibration velocity over the wetted length of the beam. The hydrodynamic pressure force is now obtained from;

$$p = -\rho \frac{\partial \phi}{\partial t}$$

The flow situation at an initial phase of the impact is shown schematically in Fig. 8.4. High local pressure occurs at the vicinity of *x=c(t)*.

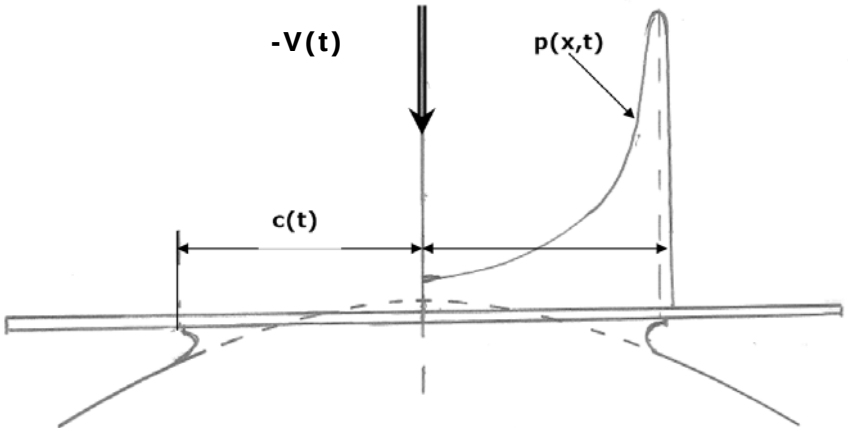

Figure 8.4 *Sketch of pressure distribution p(x,t) and wetted length including pile-up, c(t).*

The wetted length c(t) can be obtained either from a von Karman approach or a Wagner (1932) approach. A generalization of both methods is required due to the effect of the elastic deflection of the beam. Further details about solution of the boundary value problem for this hydroelastic case can be found in Kvålsvold (1994) and Kvålsvold and Faltinsen (1995).

The above discussion is based on a simplified approach for the deflection of the beam. Different more complete solution methods can be used for solution of the above boundary value problem:

1. Exact solution in case of a wedge (similarity solution)
2. Nonlinear numerical solution
3. Generalized Wagner solution

Further details about the different solution methods are given by Kvålsvold (1994).

In the above discussion zero forward speed, i.e. U=0, is assumed. Effect of forward speed on the above defined boundary value problem is discussed by Faltinsen (1997).

8.2.3 Simplified Solution

In the original study of hydroelastic slamming for beam model by Kvålsvold and Faltinsen (1995), many modes were included in the structural response calculations. However the experimental studies, Aarsnes (1994), showed clearly that the lowest mode had the dominant effect on the maximum strain values. Based on this result a simplified method were derived by Faltinsen (1997). The method is outlined below.

The structure is represented by a beam model, see eq. (8.1)-(8.4) above.

The problem is divided into two phases:

1. Structural inertia phase
2. Free vibration phase

The first phase is associated with large acceleration of the plate caused by the large hydrodynamic impact force and the small structural mass. The second phase is the free vibration phase with initial conditions obtained from the first phase. The time scale of the first phase is relatively short relative to the second phase. The duration of the second phase is of the order of the 1st wet natural period of the beam. The two phases are illustrated in Fig 8.5.

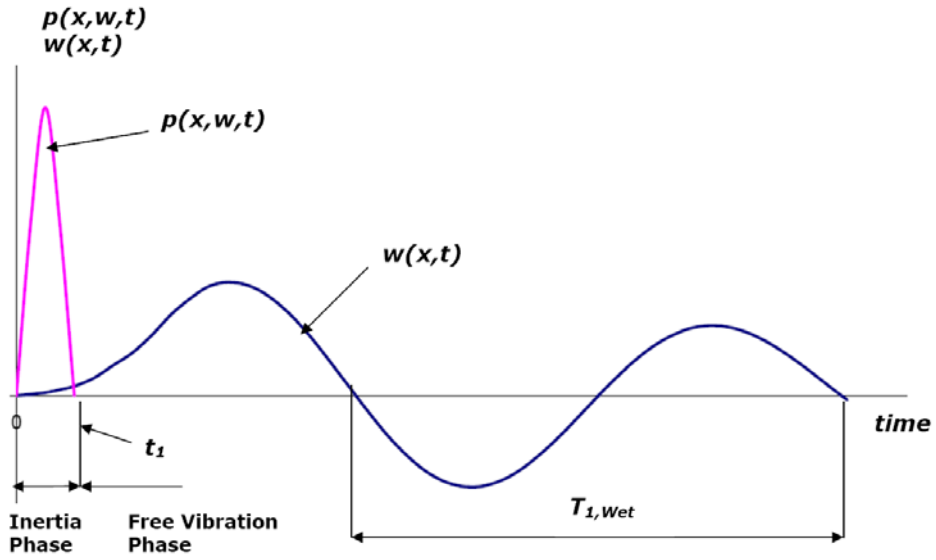

Figure 8.5 *Sketch of the two phases of a hydroelastic impact used in the simplified solution*

Inertia phase:

In the beam equation the effect of structural elasticity (i.e the bending stiffness) is neglected for this phase as the inertia term will dominate due to the high hydrodynamic load. The impact force is balanced by structural inertia forces in this phase. The Beam equation (8.1) can than be written as;

$$M_B \frac{\partial^2 w}{\partial t^2} = p(x,w,t) = -\rho \frac{\partial \phi}{\partial t} \qquad \text{for} \quad |x| \le c(t)$$

$$M_B \frac{\partial^2 w}{\partial t^2} = 0 \qquad \text{for} \quad -L_B/2 < x < -c(t) \quad \text{and} \quad c(t) < x < L_B/2$$

Boundary conditions on wetted part of beam and on free surface are given by eq. (8.9) and (8.10).

The contribution from velocity terms in Bernoulli's equation is neglected in the above equation. By integrating the above equation in time we get;

$$\frac{\partial w}{\partial t} = -\frac{\rho}{M_B}\int_0^{t_1}\frac{\partial \phi}{\partial t}dt = -\frac{\rho}{M_B}\phi(x,t_1)$$

where t_1 is the duration of the inertia phase.

Based on a detailed analysis of the above defined boundary value problem, Faltinsen (1997) showed that at the end of the inertia phase the following approximations could be used;

$$\frac{\partial w(x,t_1)}{\partial t} = \sum_{i=1}\dot{a}_i(t_1)\psi_i(x) = V$$

and for deflection;

$$w(x,t_1) \approx 0$$

These approximations are used as initial conditions for the free vibration phase discussed below.

Free vibration phase:

Only the lowest mode shape corresponding to the highest natural period is important in the solution. From complete analysis and model test results it is found that higher modes have initial small amplitudes and these modes will disappear due to relative high damping for these modes. The elastic beam deflections eq. (8.2) can then be written as;

$$w(x,t) = \sum_{i=1}^{N} a_i(t)\psi_i(x) = a_1(t)\psi_1(x)$$

After the structural inertia phase the beam starts to vibrate as a free vibration with an initial vibration velocity V and zero deflection. This phase has a time scale of the highest natural wet period of the beam, T_1. The problem can hence be regarded as an initial value problem where at t=0;

$$w(x,0) = a_1(t)\psi_1(x) = 0$$
$$\dot{w}(x,0) = \dot{a}_1(0)\psi_1(x) = V$$

This follows from the matching with the Inertia phase.

The structural vibration is obtained from eq. (8.1), but now the hydrodynamic pressure causes an added mass and damping effect only. As the beam is totally submerged in this phase, the wetted length is fixed and $c(t)$ is not a part of the solution.

The generalized added mass and damping are found by forcing the beam to oscillate harmonically with a vertical deflection;

$$w(x,t) = a_1(t)\psi_1(x) = \bar{a}_1\psi_1(x)e^{i\omega t} \qquad (8.11)$$

where it is understood that the real part has physical meaning. Steady state oscillations are assumed. The radiation potential can for fixed beam length be written by separation of time and space as;

$$\phi = \dot{a}_1(t)\phi_1(x)$$

The boundary value problem for the velocity potential ϕ_1 is determined from its boundary conditions on the wetted part of the beam;

$$\frac{\partial \phi}{dz} = \frac{\partial w}{\partial t} = \dot{a}_1 \psi_1(x) \qquad \text{on } z = 0, \quad |x| \le \frac{L_B}{2}$$

The free surface boundary condition is;

$$\phi_1 = 0 \qquad \text{on } z = 0, \quad |x| > \frac{L_B}{2}$$

The pressure is;

$$p(x,w,t) = -\rho \frac{\partial \phi}{\partial t} = \ddot{a}_1(t)\phi_1(x)$$

Inserted eq. (8.11) into the beam equation on generalized form we obtain:

$$\ddot{a}_1(t)\left[M_B \int_{-L_B/2}^{L_B/2} {\psi_1}^2(x)dx + \rho \int_{-L_B/2}^{L_B/2} \phi_1(x)\psi_1 x)dx \right] + EI \cdot a_1(t) \int_{-L_B/2}^{L_B/2} \frac{\partial {\psi_1}^4(x)}{\partial x^4}\phi_1(x)\psi_1(x)dx = 0 \tag{8.12}$$

Generalized Mass, added mass and stiffness are defined as:

$$M_{11} = M_B \int_{-L_B/2}^{L_B/2} {\psi_1}^2(x)dx$$

$$A_{11} = \rho \int_{-L_B/2}^{L_B/2} \phi_1(x)\psi_1(x)dx$$

$$C_{11} = EI \int_{-L_B/2}^{L_B/2} \frac{\partial^4 \psi_1(x)}{\partial x^4}\psi_1(x)dx$$

Inserting above expressions in eq. (8.12) and using eq. (8.11) for the elastic deflection we obtain;

$$\left[-\omega_1^2 (M_{11} + A_{11}) + C_{11} \right] \cdot \overline{a}_1 = 0$$

The wet natural circular frequency for the first elastic mode is now given from;

$$\omega_{1,WET} = \sqrt{\frac{C_{11}}{M_{11} + A_{11}}} \tag{8.13}$$

Analytical formula for the generalized added mass is given by Kvålsvold and Faltinsen (1995). Equations for mode shapes and the resulting bending stresses for this case are presented by Faltinsen et. al (1997).

8.3 Model test results - Single Beam

To support the development of the theoretical methods for hydroelastic slamming and for validation of theoretical results, model tests have been carried out with horizontal elastic plates by using drop tests. Drop tests give very well defined conditions for slamming response testing giving reliable results and are therefore well suited for verification purpose.

Results are described by Aarsnes (1994) and Kvålsvold et.al. (1995). The shape of the plates used in the tests is shown in Fig. 8.6

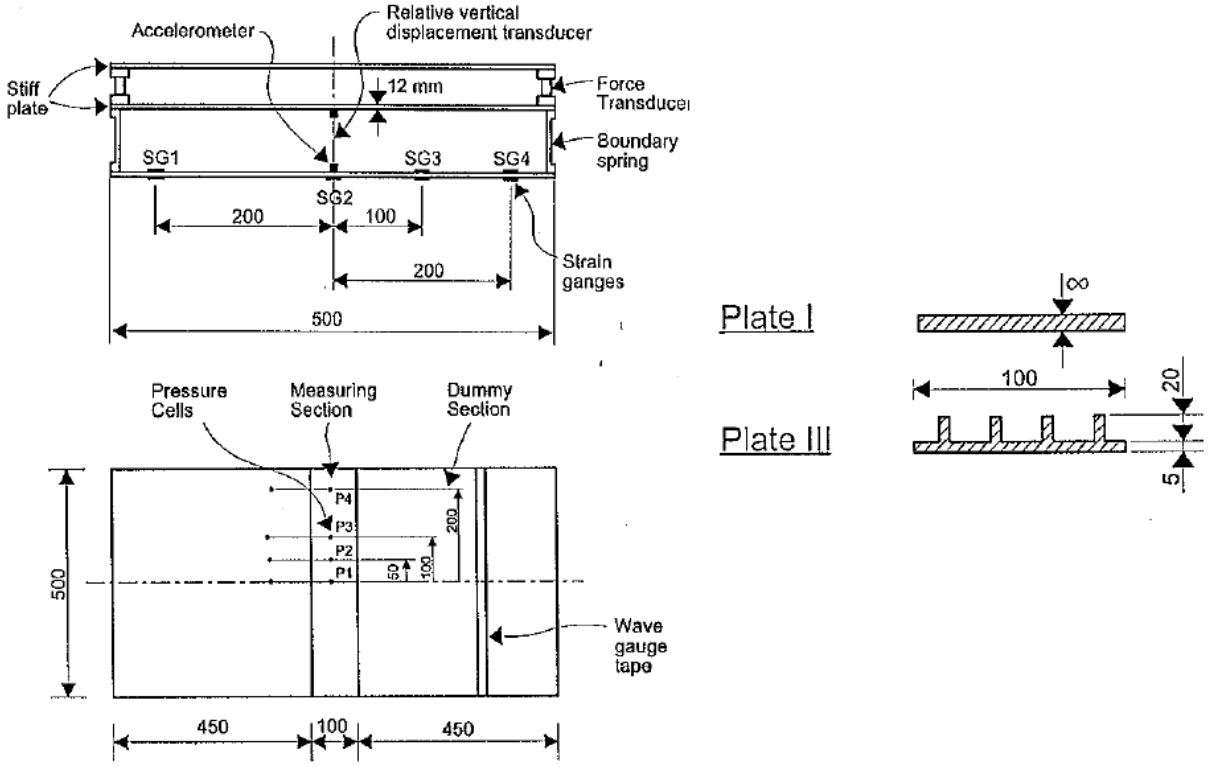

Figure 8.6 *Details of the elastic test plates used in drop tests.*

The total drop section was divided into three parts, one measuring section with a dummy section on each side as shown in the figure. The measuring section was connected to the drop rig using two force transducers.

The instrumentation includes pressure cells, vertical force transducers connected to the measuring section, wetted surface measurements, accelerometers for acceleration and velocity measurements for the rig and for the elastic plate and strain measurements on the plate using strain gauges, see Figure 8.6. Vertical deflection in center of measuring plate was also included.

Systematical drop tests were carried out for drop speed range 2.2 m/s to 6.2 m/s. The plate were dropped towards wave crest for regular waves with different radius of curvature, R. $R = \infty$ represent drop towards calm water. The results for measured strain in center of the plate (i.e at SG2 in Fig. 8.6) are shown in Fig. 8.7 as function of nondimensional drop speed. The strain is made non-dimensional using;

$$\varepsilon' = \frac{\varepsilon_m}{z_a V}\sqrt{\frac{EI}{\rho L_B}} \tag{8.14}$$

where ε_m is the measured strain and z_a is the distance from neutral axis of the beam to the strain measurement position.

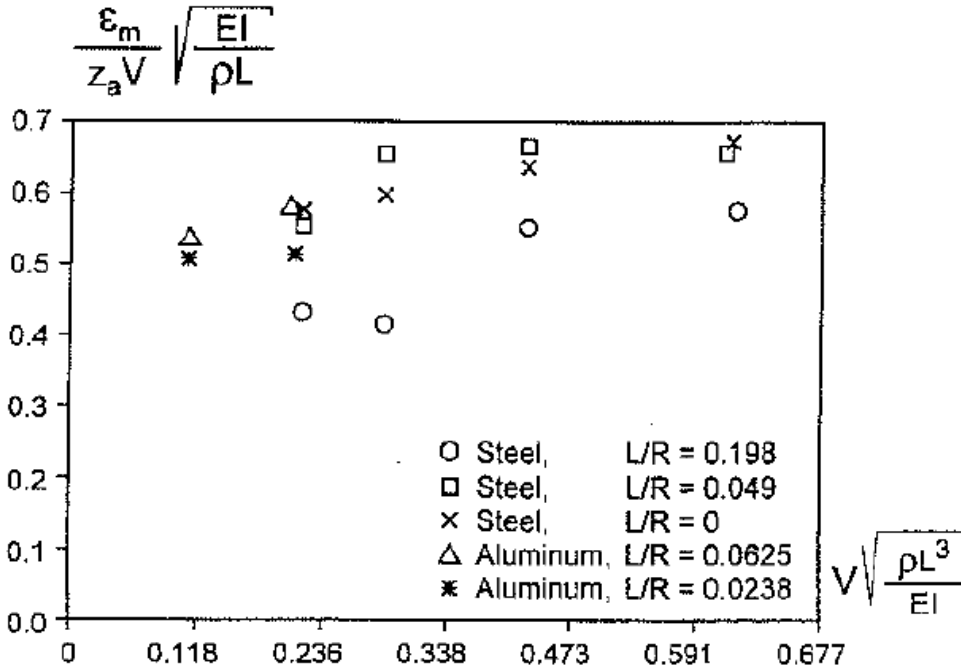

Figure 8.7 *Measured maximum nondimensional strain amplitude in center of the horizontal steel and aluminum plates as function of nondimensional impact velocity.*

The results shows that the maximum strain is proportional to the velocity. It is also observed that the effect of the ratio L_B/R is small except for the largest ratio, i.e. for $L_B/R = 0.198$. The structural mass of the steel plate is approx. 3 times larger than the mass of the aluminum plate, but the difference in measured strain is insignificant.

For forward speed U and an angle of attack of the plate equal to α the effective drop velocity can be defined as;

$$V_T = -(V - U \cdot \alpha - u_Z) \tag{8.15}$$

Where u_Z is the vertical velocity of the incident waves at the impact position. The velocity term V used in the nondimensional strain values in Fig 8.7 can be replaced by the effective drop velocity, V_T .

In Fig 8.8 measured maximum pressure from different drop tests of horizontal plates are plotted as function of drop speed. Some very high pressures are measured. It is observed that the maximum pressure is very dependent on the physical conditions as the exact wave profile and where the wave initially hit the wetdeck plate relative to the position of the pressure cells. In fig 8.9 an example of measured pressure time history in P1 and P3 (see Fig 8.6) are shown. It is observed that the time duration of very high pressures is very small, and typically less than 10^{-4} s. Also the pressure peaks will be very concentrated in space.

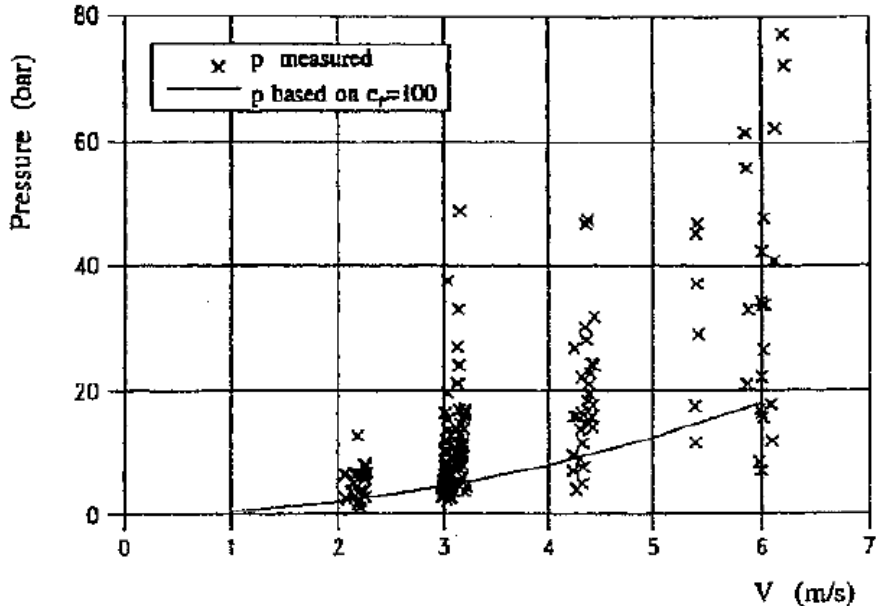

Figure 8.8 *Measured maximum pressure from different drop tests with horizontal plates as function of drop speed.*

En example of measured strain time histories in two positions of the elastic plate, SG1 and SG3 (see Fig 8.6 for details) are shown in Fig 8.10. Comparing the time scale in Fig 8.9 for pressure and 8.10 for strain it is seen that maximum strain occurs after approx 0.005 s which is much later than the occurrence of maximum pressure. The peak pressure shows large scatter even for similar test conditions, while the observed maximum strain shows little scatter as can be seen from Fig. 8.8. The large scatter for the pressure and the difference in time scale for maximum pressure and maximum strain shows that the measured pressure peaks do not give any valuable information about the actual structural loading for the hydroelastic slamming case.

The pressure time history shown in Fig. 8.9 includes also a comparison between the measured and calculated pressure using the simplified approach of Faltinsen (1997). This approach describe only the free vibration phase, i.e. not the initial phase of the impact. Neglecting the initial high pressure peaks it is seen that the theory gives a reasonable agreement with measured pressure for the first half of the plate oscillation period. For the second half oscillation period it is observed that the under pressure relative to atmospheric pressure occur. The minimum pressure is seen to be approx -1 bar i.e. close to the vapor pressure. This means that cavitations occur in this phase. It is also noted that the two pressure cells gives almost identical pressure for this phase. Due to the large underpressure in combination with small distance to the free surface in this phase air may be drawn in under the palate and ventilation may occur. This imply that the plate will not be fully wetted in this phase and the response calculation based on "wet" modes overpredict the added mass effect of the fluid pressure.

In Fig 8.10 a comparison between measured and calculated strain in the elastic plate using the simplified approach of Faltinsen (1997) is shown. As for the pressure the agreement is quite good for the first half of the oscillation period. The maximum strain is seen to occur at approximately ¼ of the lowest wet natural period. For the second half of the oscillation period the theory is seen to overpredict the response. For this phase the test results also gives a significant lower response period compared to the first half of oscillation and also compared to the calculations which is based on the 1st "wet" mode. This can be explained by the effect of cavitation/ventilation discussed above which will make the plate partly dry for this phase and the response is more closely related to the "dry" free vibration solution. This can explain both the lover oscillation period and the lower response amplitude.

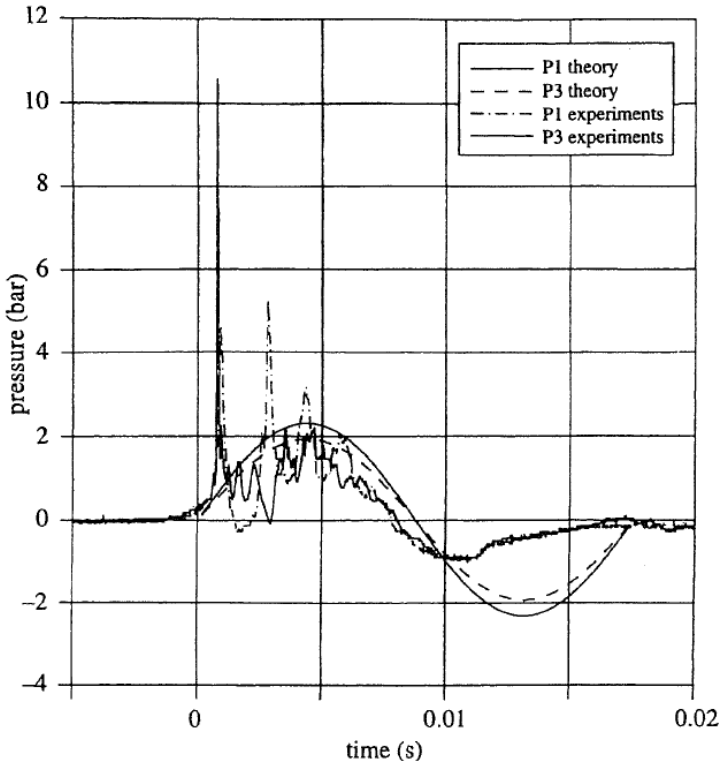

Figure 8.9 *Example of measured pressure during impact towards an elastic plate. Measured in drop test and from simplified approach (Faltinsen (1997)).*

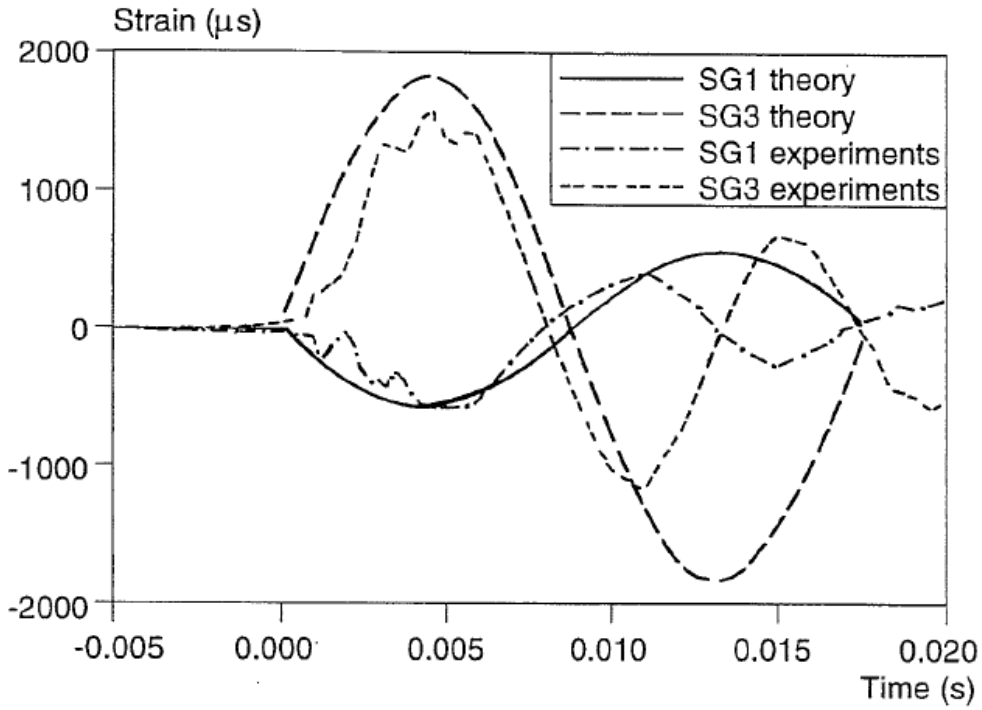

Figure 8.10 *Strain as two position on plate as function of time. Measured in drop test and from simplified approach (Faltinsen (1997)). Drop height 0.5 m.*

8.4 Effect of Air Pocket.

In the above discussion of hydroelastic slamming possible effect of air pocket has not be included. From the drop test with horizontal plate it was observed from pressure distribution and wet surface measurements that an air pocket was present. The formation process for an air pocket is shown in Fig 8.11.

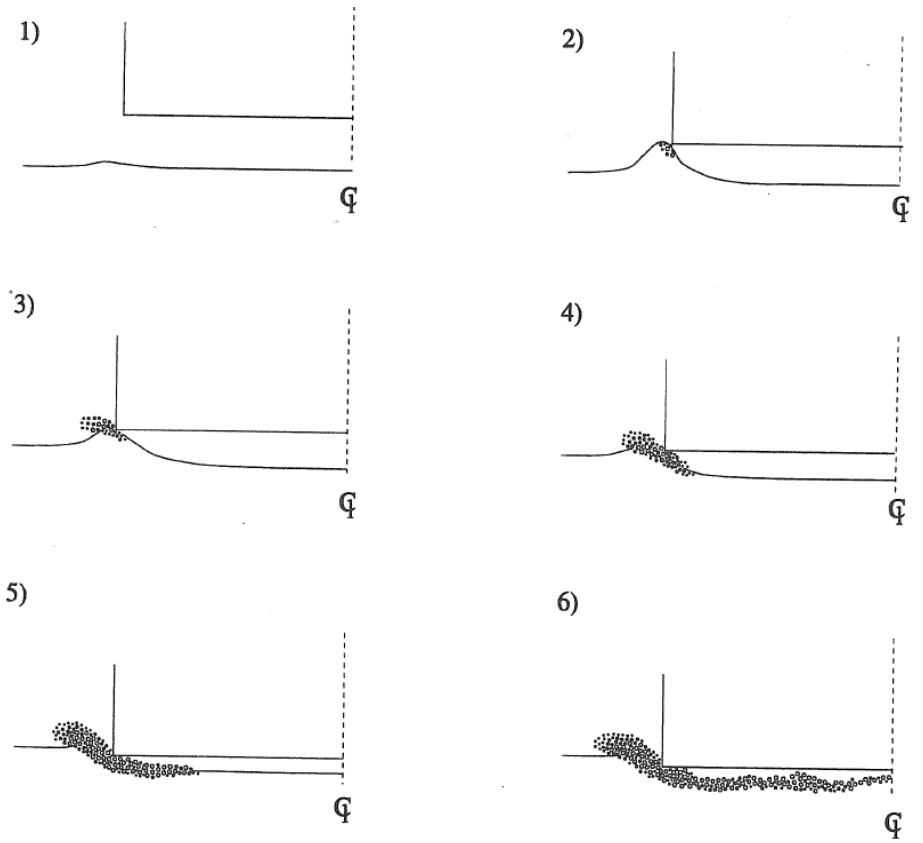

Figure 8.11 *Course of events as the air pocket is created and collapsed From Miyamoto and Tanizawa (1985)*

As the plate approach the still water surface an underpressure is created at the corners due to high velocity of air forced out towards the corners. This lift up the water surface at the corners and an air pocket is created underneath the plate. The air cushion pressure will increase caused by the vertical velocity of the plate. During this process the pressure the pressure will be almost space independent. It was shown by Faltinsen (1997) that the time duration of the air cushion process is small compared to the time scale of the free vibration phase. The consequence on the maximum strain amplitude of the possible formation of an air pocket underneath the plate was therefore found to be insignificant. However the local pressure distribution (in time and space) for the Inertia phase will be very different for the case with and without air pocket generated.

8.5 Three Beam Model

8.5.1 Theoretical formulation

The one beam model discussed in previous section has also been extended to a 3 beam model, see Fig. 3.11. As for the one beam case the beam equation, eq. (8.1) with eq. (8.2) is also used for the structural representation for this 3 beam case. A restoring spring is introduced at each node as shown in Fig. 8.12.

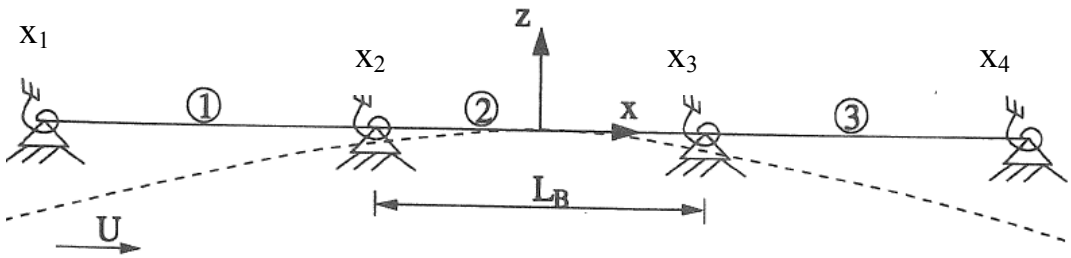

Figure 8.12 *Definition of wetdeck modeled as 3 beams..*

For the 3 beam case the required number of boundary conditions for solving the normal mode shapes and natural frequencies will be 12, i.e. 4 for each beam. The boundary conditions become;

$$w^j(x,t) = 0 \qquad \text{for} \quad x = x_j, x_{j+1} \qquad \text{(j=1,2,3)} \qquad \text{(Gives 6 b.c.)}$$

$$\frac{\partial w^j(x,t)}{\partial x} = \frac{\partial w^{j+1}(x,t)}{\partial x} \qquad \text{for} \quad x = x_{j+1} \qquad \text{(j=1,2)} \qquad \text{(Gives 2 b.c.)}$$

$$\frac{\partial^2 w^j(x,t)}{\partial x^2} = \frac{\partial^2 w^{j+1}(x,t)}{\partial x^2} - \frac{k_\theta}{EI}\frac{\partial w^{j+1}(x,t)}{\partial x} \qquad \text{for} \quad x = x_{j+1} \qquad \text{(j=1,2)} \qquad \text{(Gives 2 b.c.)}$$

$$\frac{\partial^2 w^1(x,t)}{\partial x^2} = \frac{k_\theta}{EI}\frac{\partial w^1(x,t)}{\partial x} \qquad \text{for} \quad x = x_1 \qquad \text{(Gives 1 b.c.)}$$

$$\frac{\partial^2 w^3(x,t)}{\partial x^2} = -\frac{k_\theta}{EI}\frac{\partial w^3(x,t)}{\partial x} \qquad \text{for} \quad x = x_4 \qquad \text{(Gives 1 b.c.)}$$

The superscript *j* means that $w^j(x,t) = 0$ is referred to beam *j, (j=1,2,3),* see Fig 8.12. In total 12 boundary conditions.

The normal mode shapes for this 3 beam model is shown in Fig. 8.13.

The solution of the hydrodynamic boundary value problem for the 3 beam case is in principal similar to the single beam model. Details are given by Haugen (1997).

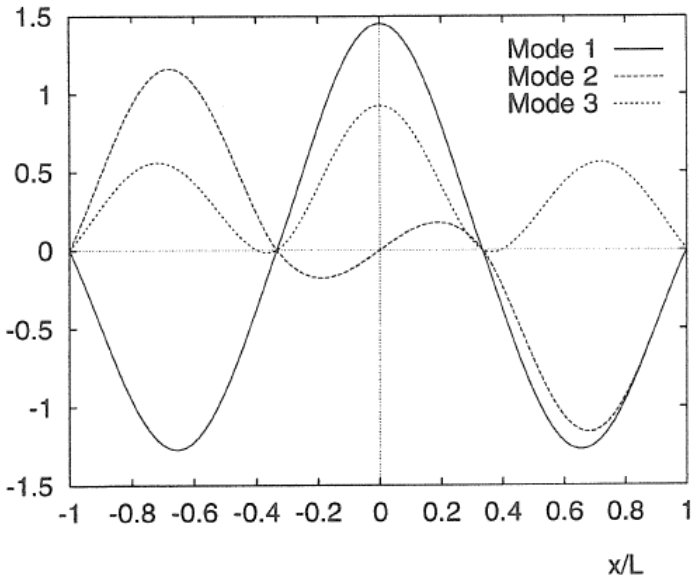

Figure 8.13 *Calculated mode shapes for the elastic plate consisting of 3 beams*

8.5.2 Model test results

Drop test have also be carried out for the 3 beam model case. The 3 plate model is shown in Fig. 8.14. Tests were carried out for two different cases;

- Horizontal Plates and zero forward speed.
- Plates mounted with a constant pitch angle $\eta_5 = 5.8^\circ$ and forward speed U=3.5 m/s

The drop rig was connected to the towing carriage in the towing tank and for the forward speed case towed towards the wave direction. The relative angle between the plate and the wave surface at the time of initial impact is given by;

$$\alpha_{REL} = \eta_5 - k\zeta_A \sin(kX_T) \tag{8.16}$$

Here ζ_A is the regular wave amplitude, *k* is the wave number and X_T is the distance from the wave crest to the centre of the plate at time instant of initial impact. $\alpha_{REL} = 0$ means that the plate hits the wave parallel to the wave surface.

The effective drop velocity is obtained from eq. (8.15), but now with α replaced by α_{REL}

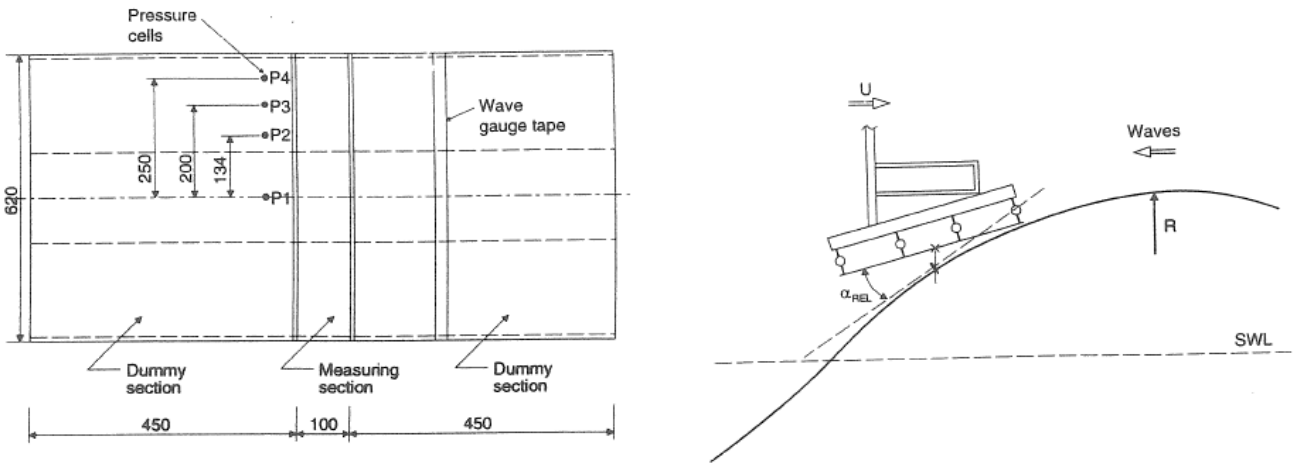

Figure 8.14 *Sketch of model used for in drop tests with 3 beam model.*

The measured maximum nondimensionalized strain amplitudes (see eq. (8.14)) in the center of the plates is shown in Fig. 8.15 as function of the relative angle between the plate and the wave surface α_{REL}. The results are for the drop tests with zero speed. The results are shown for different values of the wave crest radius, *R.* For $|\alpha_{REL}| \leq 2^{\circ}$ the measured strain is approximately independent of the position where the wave crest hits the plate. The strain decrease significantly for large values of α_{REL}

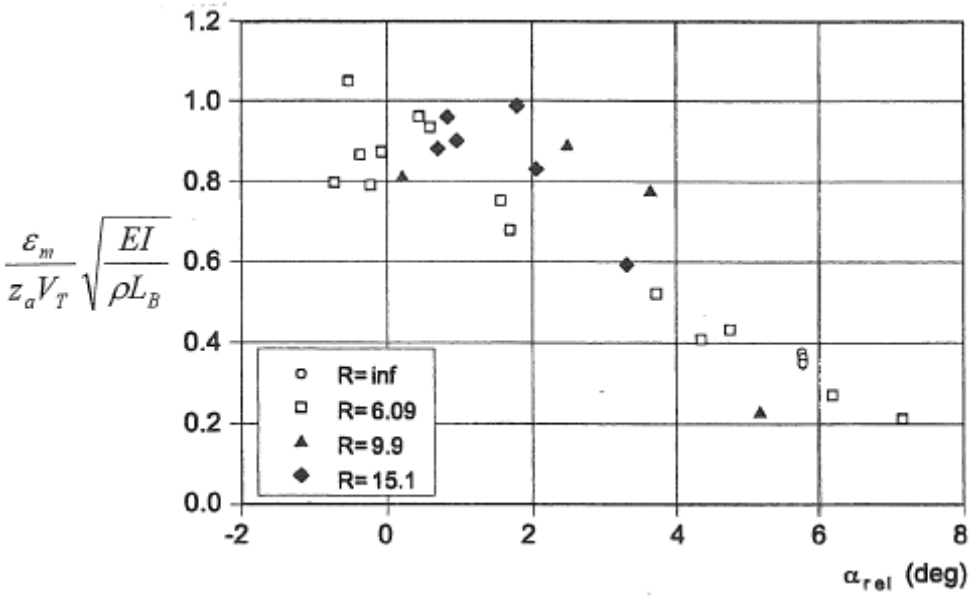

Figure 8.15 *Measured maximum nondimensional strain amplitude in the center of the plates as function of α_{REL} model. Zero forward speed.*

The effect of forward velocity and effective drop velocity on the resulting strain in center of the plate is shown in Fig 8.16. Results are shown only for tests where the plate hit parallel to the wave surface. The results show that there are small differences in measured nondimensional strain. The effect of effective drop velocity and radius of the wave, V_T and *R*, is seen to be insignificant. These results imply that the combined effect of forward speed and a pitched plate is properly accounted for by correcting the total drop velocity as given by eq (8.14).

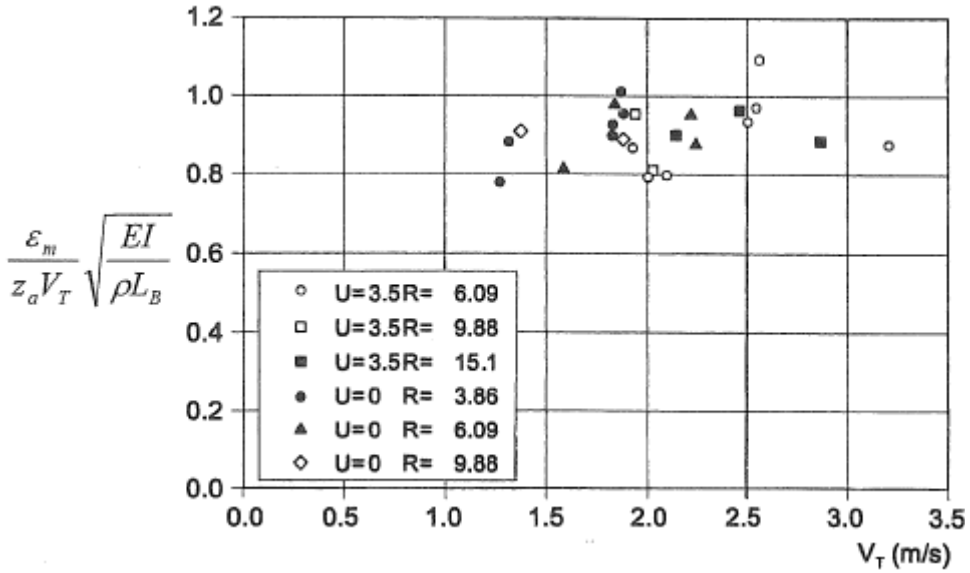

Figure 8.16 *Measured maximum nondimensional strain amplitude in the center of the plates as function of the total relative normal velocity.*

Comparing with the results for measured strain for the one beam case shown in Fig. 8.7 the results for the 3 plate case shows slightly higher values.

Based on the results presented above the following conclusions apply for hydroelastic slamming for elastic plates hit by waves;

- The maximum stress amplitude will be proportional to effective drop velocity V_T
- For realistic ratios of the L_B/R the maximum stress amplitude will not be influenced by the radius of the wave crest, *R*
- The combined effect of forward U and the pitch of the plate η_5 is included by adding the term $U\eta_5$ to the drop velocity
- For $|\alpha_{REL}| \leq 2^\circ$ the measured strain is approximately independent of the position where the wave crest hits the plate. The strain decrease significantly for large values of α_{REL}
- Measured maximum peak pressure is very local in time and space and do not give any indication of maximum strain for an impact situation

8.6 3-D Approach

The above discussion of hydroelastic slimming is based on 2-D theory. The theory have been extended to the 3-D case by Faltinsen (1999) considering an elastic hull with V-shaped cross sections. The geometry of the cross section and stiffened plating are shown in Fig 8.17. β is the dead-rise angle of the section.

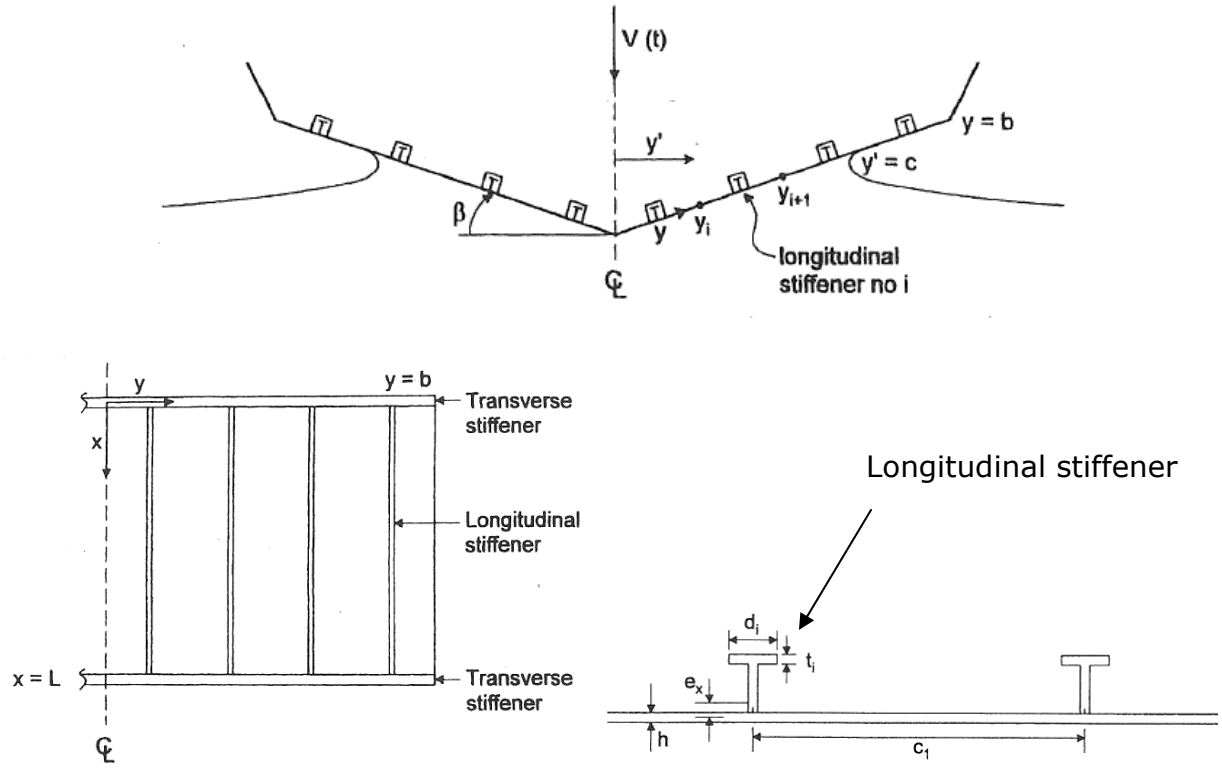

Figure 8.17 *Wedge shaped cross section. Stiffener arrangement on plating and Cross sections of longitudinal stiffeners.*

The differential equation for the lateral deflection of the 3-D plate is written as;

$$\overline{m}\frac{\partial^2 w}{\partial t^2}+D_x\frac{\partial^4 w}{\partial x^4}+2B\frac{\partial^4 w}{\partial x^2\partial y^2}+D_y\frac{\partial^4 w}{\partial y^4}=p(x,y,t;w) \tag{8.17}$$

Where $\overline{m}$ is the average structural mass pr unit area. D_x and D_y are the flexural rigidity parameters and B is the torsional rigidity parameter which can be expressed as;

$$D_x=\frac{Eh^3}{12(1-\nu^2)}+\frac{Ehe_x{}^2}{1-\nu^2}+\frac{EI_{0x}}{c_1}$$

$$D_y=\frac{Eh^3}{12(1-\nu^2)}$$

$$B=\frac{Eh^3}{12(1-\nu^2)}+\frac{E}{12(1+\nu^2)}\frac{\sum d_i t_i{}^3}{c_1}$$

See Fig. 8.17 for definition of structural parameters used in the above equations.

As for the 2-D case it is assumption is that the elastic deflections of the plate, $w(x,y,t)$ can be written as a linear sum of "dry" normal modes;

$$w(x,y,t)=\sum_{j=1}^{M}\sum_{i=1}^{N}W_{ij}(t)\cdot X_i(x)\psi_j(y)$$

where $W_{ij}(t)$ is the time dependent principal coordinates and $X_i(x)$ and $\psi_j(y)$ is the "dry" normal modes of vibrating beams.

The hydrodynamic boundary value problem was solved using a generalization of Wagner's method to include the effects of elastic vibrations. This is similar to the method used for the 2-D case, but now with a 3-D correction. Local 2-D flow is assumed for each cross section but allowing for different pile-up of water for each cross section. A 3-D coupling is achieved through the 3-D plate deflection.

The results from the 3-Dimensional analysis of the wedge shaped case as defined in Fig 8.17 are presented in Fig 8.18 in terms of maximum nondimensional strain. The result is shown as function of the dead-rise angle, β and the dimensionless impact velocity, V_{ND}, defined from;

$$V_{ND}=V_T\sqrt{\frac{\rho L_B{}^3}{EI}} \tag{8.18}$$

Note that the measured strains are for this case made non-dimensional as;

$$\varepsilon'=\frac{\varepsilon_m EI\tan\beta}{z_a V^2\rho L^2} \tag{8.19}$$

This is based on the assumption that the maximum strain is proportional to impact velocity $V_T{}^2$ as in quasi static pressure loading (and not proportional to V_T as used in Fig. 8.7, 8.15 and 8.16). *tan(β)* is introduced to account for the way the slamming load depend on the dead-rise angle, see also Fig. 4.12.

From the results shown in Fig 8.18 deviation from straight horizontal line indicate that hydroelastic effects will be important, see the line denoted "Plate Theory" in the figure. It is observed from the figure that the dead-rise angle limit for when hydroelastic effects will be important depends on the nondimensional drop velocity, V_{ND}. Increasing velocity tends to increase the dead-rise angle range for where hydroelasticity is important.

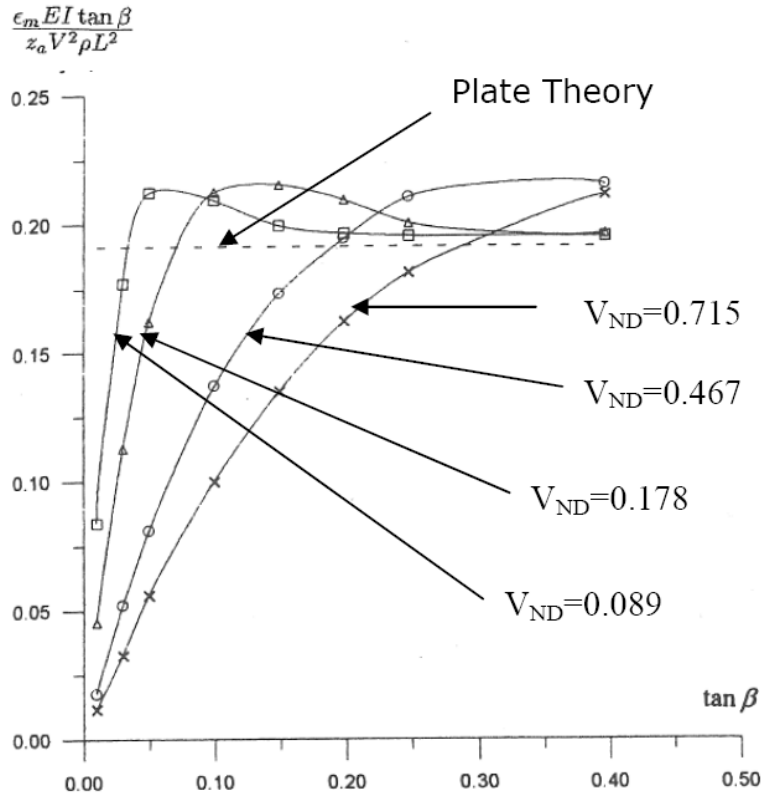

Figure 8.18 *Maximum nondimensional strain amplitude in middle of longitudinal stiffener. Presented as function of tan(β)*

Introducing the parameter;

$$\frac{\tan\beta}{V_{ND}} = \frac{\tan\beta}{V_T \sqrt{\rho L_B{}^3 / EI}} \tag{8.20}$$

and re-plotting the results for maximum nondimensional strain in Fig 8.18 s function of this parameter, gives result as shown in Fig 8.19. It is found that the results merge into one line and hydroelastic effects become important when;

$$\frac{\tan\beta}{V_{ND}} = \frac{\tan\beta}{V_T \sqrt{\rho L_B{}^3 / EI}} \le 0.25$$

or

$$\tan\beta \le 0.25 \cdot V_T \sqrt{\frac{\rho L_B{}^3}{EI}} \tag{8.21}$$

In the hydroelastic range the solution fits very well with the hydroelastic beam theory as discussed above. For this case the maximum strain is proportional to velocity i.e. $\varepsilon_m \propto V_T$ as discussed in detail for the 1 beam and 3 beams cases above.

From Fig. 8.19 it is observed that for $\tan\beta \geq 0.25 \cdot V_T \sqrt{\frac{\rho L_B{}^3}{EI}}$ the quasi steady theory may underpredict the maximum strain. This represent cases where the dynamic amplification of the plate give a DAF larger than 1, see the discussion in Chap 4.3 and Fig. 4.17 based on dynamics of response of 1 degree of freedom systems due to impulse loads.

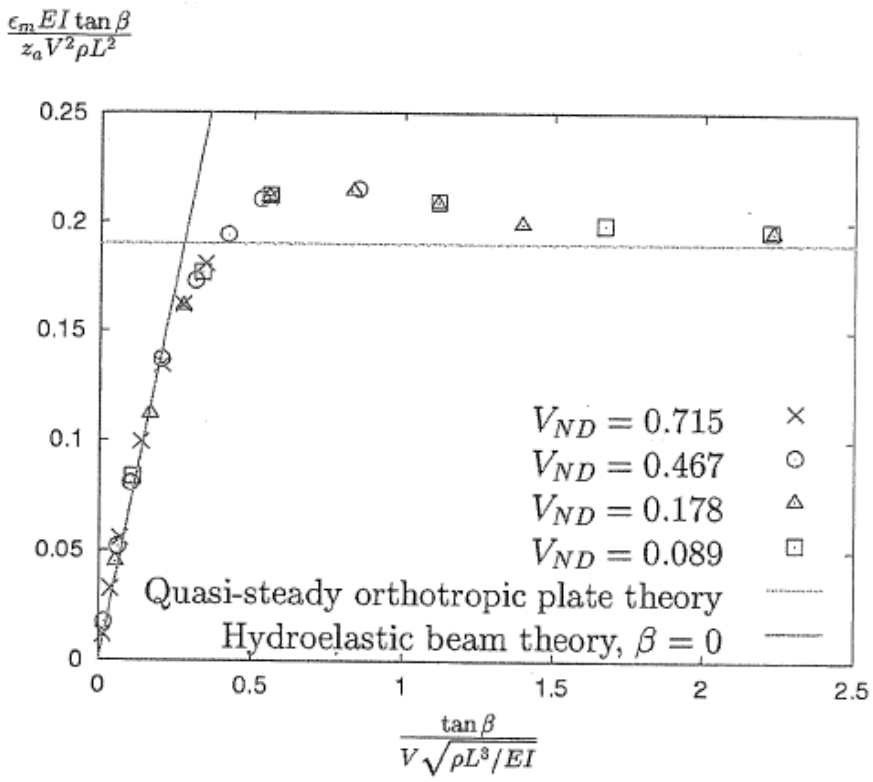

Fig 8.19 *Maximum nondimensional strain amplitude in middle of longitudinal stiffener.*

9 VERY LARGE LOATING STRUCTURES

9.1 General Description

Very Large Floating structures (VLFS) have been used for a variety of purposes;

- As floating airports or floating runways
- Bridges
- Breakwaters
- Piers and docks
- Storage facilities
- Wind and solar power plants

Examples of built or planned VLFS are shown in Fig. 9.1 and 9.2. The shown application are characterized by it's huge dimensions. Typical dimensions can be Length x Breadth, LxB=5 km x 1 km. Design and construction of these structures are therefore associated with massive cost and labour. As this is novel technology, also significant risk will be involved with the execution of these projects. Another special feature of these structures is very long design lives, typically 50-100 years, compared to 20-25 years most frequently used as basis for design of ships and other offshore structures.

Fig 9.1 *VLFS used as Floating Air Port, Japan.*

Fig 9.2 *VLFS used as Floating Oil Storage, Shirashima and Kamigoto, Japan.*

A key feature of VLFS's is their large horizontal extension relative to the vertical one. This leads to a significant elastic behaviour which is dominant relative to the rigid-body motions. Hence the flexibility and the coupling effect between structural deformation and hydrodynamic loads strongly affect the response. This property is illustrated in Fig. 9.3 which shows a typical response to a static point load for a ship structure and for a typical VLFS. In this way the VLFS must be regarded as a hydroelastic structure.

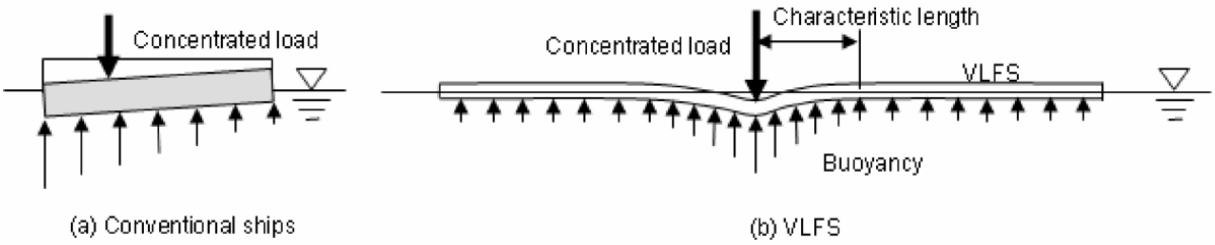

Fig 9.3 *Typical response from Point Load. Right; Conventional ship design. Right; Typical response of o VLFS.*

The VLFS can be classified into two main types of structures;

- Pontoon-type VLFS; Box type of structure, usually designed for relatively sheltered areas. Examples of such designs are shown in Fig. 9.1. Characterised with very large size and low draft / freboard.

- Semisubmersible type; Designed for open water application. Hulls composed of many flexible modules interconnected by joints with certain flexibility. Example of this type of VLFS designs are shown in Fig. 9.4

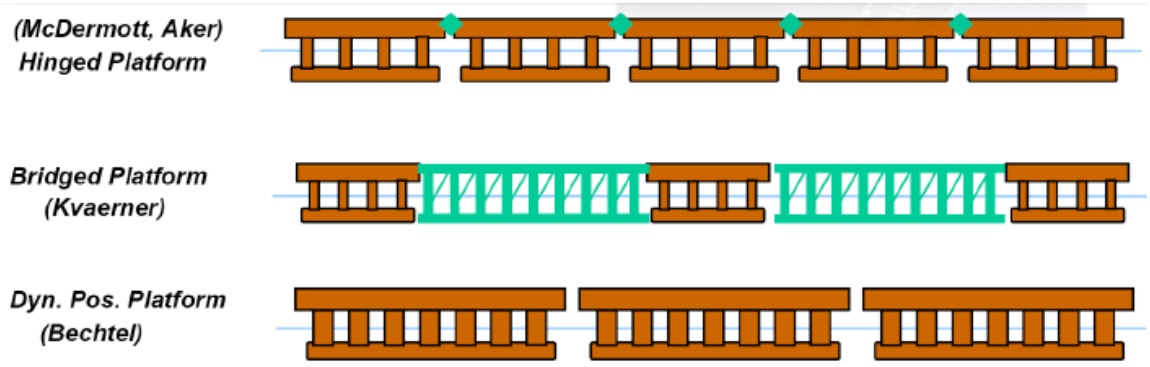

Fig 9.4 *Examples of semisubmersible type of VLFS*

9.2 Hydroelastic Analysis

9.2.1 General description

A number of theories and methods have been developed for predicting the hydroelastic wave induced response of VLFS. For simple structures as beams and plated structures, one, two and three dimensional hydroelastic theories have been developed by using analytical formulations and numerical methods. Based on modal representation of the structural behaviour combined with linear potential theory for the hydrodynamic loads, the hydroelastic formulation have been developed to predict the response of beam like and arbitrary shaped structures.

In the following a method for hydroelastic analysis developed Taghipour et.al. (2006) is described in some detail. The method is based on using a Boundary Element Code (BEM) for the hydrodynamic part of the analysis and a Finite Element Method Code (FEM) for the structural formulation, WAMIT and ABAQUS respectively. The approach is based on linear, frequency domain analysis, but may be extended to time domain to include nonlinear viscous effects and structural nonlinearities in connections between structural elements.

9.2.2 Linear, Wave Frequency analysis

The VLFS structure is assumed modeled by the Finite Element Method. The generalized displacements $\mathbf{r}(x,y,z,t)$ can be expressed by the Mode expansion method as a weighted sum of the eigenmodes or eigenvectors $\boldsymbol{\psi}_i(x,y,z)$ as follow;

$$\mathbf{r}(x,y,z,t) = \sum_{i=1}^{N+6} \boldsymbol{\psi}_i(x,y,z) q_i(t) = \boldsymbol{\Psi}\mathbf{q} \qquad (9.1)$$

Where $q_i(t)$ are the unknown displacement amplitudes or generalized coordinates. The eigenmodes or normal modes $\boldsymbol{\psi}_i(x,y,z)$, is determined from the free vibration analysis as described in chap. 6.2. The first 6 modes in eq. (9.1) are the rigid body motions; surge, sway, heave, roll, pitch and yaw. The remaining modes are eigenmodes of the flexible "dry" structure. The solution for the different elastic generalized eigenmodes can be obtained by using finite element packages like ABAQUS or ANSYS.

In theory infinitely many eigenmodes (or modes shapes) are required to represent the displacement vector, but for practical purpose the modal superposition is used which implies that only a limited number of the lowest eigenmodes are applied.

The hydrodynamic formulation used here is described by Newman (1994). Linear potential theory is applied. Irrotational flow of an inviscid incompressible fluid is assumed. Infinite water depth is also assumed. The total velocity potential is then defined as the sum of the incoming wave potential, diffraction potential and the sum of the radiation potentials as follows;

$$\Phi = \phi_I + \phi_D + \sum_{j=1}^{6+N} q_j \phi_j \qquad (9.2)$$

Where;

- ϕ_I is the incident wave potential
- ϕ_D is the potential due to the diffracted waves
- ϕ_j is the radiation velocity potentials due to unit excitation in mode *j*

j=1,6 represent the rigid body motions. *j=7-(6+N)* represent the elastic modes. The two first contributions to the total velocity potential in eq. (9.3), ϕ_I and ϕ_D, represent the wave excitation part i.e the velocity potential for the case with a fixed body. The last potentials, $\phi_j \quad j = 1...6+N$ represent the velocity potential due to forced motion of the body in the different modes.

The unknown potentials ϕ_D and ϕ_j, shall satisfy the following conditions;

1. Continuity equation (Laplace's); $\nabla^2\Phi = 0$
2. Linearized free Surface Condition; $\partial\Phi/\partial z - k\Phi = 0 \quad \text{on} \quad z = 0$
3. Body boundary condition; $\partial\phi_D/\partial n = \partial\phi_I/\partial n$ for diffraction pot.
   $\partial\phi_j/\partial n = i\omega\,\mathbf{u}_j \cdot \mathbf{n}$ for radiation potentials
4. Radiation condition; The waves radiate away from the body, i.e. outgoing waves.
5. Bottom Condition; $\partial\Phi/\partial z = 0 \quad \text{on} \quad z = -h$

$\mathbf{n} = [n_1, n_2, n_3]$ is the unit normal vector of the wetted surface *S* with the Cartesian components n_1, n_2 and n_3, positive into the fluid domain. The vector $\mathbf{u}_j{}^T = [u_j, v_j, w_j]$ represent the three Cartesian components of the *j*th eigenvector $\boldsymbol{\psi}_j(x, y, z)$. This gives;

$$n_j = \mathbf{u}_j \cdot \mathbf{n} = u_j n_1 + v_j n_2 + w_j n_3 \tag{9.3}$$

The above formulated boundary value problem for the unknown velocity potentials ϕ_D and ϕ_j, *j=1,N+6*, are obtained from software as WAMIT, see Lee and Newman (2000) for details.

When the velocity potentials are known the fluid pressure *p,* is obtained from Bernoulli's equation;

$$p = -\rho\left(\frac{\partial\Phi}{\partial t} + \frac{1}{2}\nabla\Phi \cdot \nabla\Phi + gz\right)$$

where ρ is the mass density of water. For linear analysis the second order term is neglected and we are left with;

$$p = -\rho\frac{\partial\Phi}{\partial t} - \rho g z \tag{9.4}$$

The fluid pressure forces in a particular mode *i* is obtained by integrating the pressure over the mean wetted surface of the body, *S*. On generalized form this gives;

$$F_i = -\iint_S \mathbf{u}_i \cdot \mathbf{n} \cdot p \cdot dS \tag{9.5}$$

From the different contributions to the total hydrodynamic potential given in Eq. (9.2) and using eq. (9.4) and (9.5) for pressure and forces, the total hydrodynamic force on generalized form F_i^{HYD}, can be split into the following contributions;

$$F_i^{HYD} = F_i^{EX} + F_i^{RAD} + F_i^{HS} \tag{9.6}$$

Where

$$F_i^{EX} = \rho \iint_S \mathbf{u}_i \cdot \mathbf{n} \frac{\partial(\phi_I + \phi_D)}{\partial t} dS = \rho i\omega \iint_S \mathbf{u}_i \cdot \mathbf{n}(\phi_I + \phi_D) dS \tag{9.7}$$

$$F_i^{RAD} = -\rho \iint_S \mathbf{u}_i \cdot \mathbf{n} \sum_{j=1}^{N+6} \frac{\partial(q_j \phi_j)}{\partial t} dS = -\rho i\omega \iint_S \mathbf{u}_i \cdot \mathbf{n} \sum_{j=1}^{N+6} q_j \phi_j dS \equiv \sum_{j=1}^{N+6} \left(\omega^2 A_{ij} - i\omega B_{ij}\right) q_j e^{i\omega t} \tag{9.8}$$

$$F_i^{HS} = \rho g \iint_S \mathbf{u}_i \cdot \mathbf{n} \sum_{j=1}^{N+6} \left(w_j q_j\right) dS = \sum_{j=1}^{N+6} D_{ij} q_j e^{i\omega t} \tag{9.9}$$

Where F_i^{EX} is the generalized wave excitation forces, F_i^{RAD} is the generalized radiation force expressed in terms of a added mass coefficient A_{ij}, and damping coefficients B_{ij}. The term F_i^{HS} is the generalized hydrostatic force expressed through the hydrostatic restoring coefficient D_{ij}. ω is the incident wave frequency. w_i is the vertical displacement due to unit excitation of mode *i.*

For a harmonic loading the dynamic equilibrium equation on generalized form for the structure can be written as (see also eq. (6.3);

$$\sum_{j=1}^{N+6} \left(-\omega^2 M_{ij} + i\omega C_{ij} + K_{ij}\right) q_j = F_i^{HYD}(t) \tag{6.3}$$

For *i=1,....N,* where $M_{ij} = \boldsymbol{\psi}_i^T \mathbf{m} \boldsymbol{\psi}_j$, $C_{ij} = \boldsymbol{\psi}_i^T \mathbf{c} \boldsymbol{\psi}_j$ $K_{ij} = \boldsymbol{\psi}_i^T \mathbf{k} \boldsymbol{\psi}_j$ are elements in the generalized structural mass-, damping- and stiffness matrices, $\mathbf{M}$, $\mathbf{C}$ and $\mathbf{K}$,respectively. $F_i^{HYD} = \boldsymbol{\psi}_i^T \mathbf{f}$ is a element of the generalized external force vector which for this case is equal to the hydrodynamic force.

Inserting from eq. (9.6)-(9.9) into eq. (6.3) gives the generalized equation of motion for a flexible structure floating in waves;

$$\sum_{j=1}^{N+6} \left[-\omega^2 \left(M_{ij} + A_{ij}\right) + i\omega \left(C_{ij} + B_{ij}\right) + \left(K_{ij} + D_{ij}\right)\right] q_j = F_i^{EX} \tag{9.10}$$

The generalized mass and stiffness matrix $\mathbf{M}$ and $\mathbf{K}$ can be obtained by using finite element packages like ABAQUS and ANSYS. The structural damping in the above equation can be modeled by Rayleigh damping, i.e.;

$$C_{ii} = \alpha_1 M_{ii} + \alpha_2 K_{ii}$$

Theoretically, an infinite number of flexible modes are needed to represent the structural behavior in elastic vibration. For practical purposes a finite number of them to effectively express the behavior in practical cases. Convergence tests is often used to establish the required number for each case.

9.2.3 Non-Linear effects

Most studies of VLFS dynamic behaviour assume that the linear analysis is valid. However some local phenomena will require a nonlinear investigation. Due to the limited draft of many VLFS, parts of the structure can experience water-exit and water-entry phenomena's leading to bottom slamming and green water on deck. These phenomena require a nonlinear analysis. A method to include local nonlinear effects for VLFS has been described by Greco et. al. (2006). The nonlinear loading is established based on linear analysis motion response and then added to the other linear loads for a "corrected" linear global motion analysis. When including this "corrected" loads, time domain analysis have to be carried out. In this way the effect of local nonlinear loads on the global response can be accurately accounted for.

9.3 Case Study

A case study have been carried out for a very large offshore mat structure. Experimental results have been reported Yago and Endo (1996). Numerical results for the same case have been presented by Fu et. al. (2006) and Taghipour et. al. (2006).

The main particulars of the offshore mat structure are summarised in Table 9.1 and in Fig 9.5.

Property	Symbol	Quantity
Length (m)	L	300
Beam (m)	B	60
Height (m)	T	2
Draft (m)	D	0.5
Mass (tons)	M	9.225×10^3
Bending Stiffness (kg.m^2)	EI	4.87×10^{10}

Table 9.1 *General parameters of the offshore mat structure.*

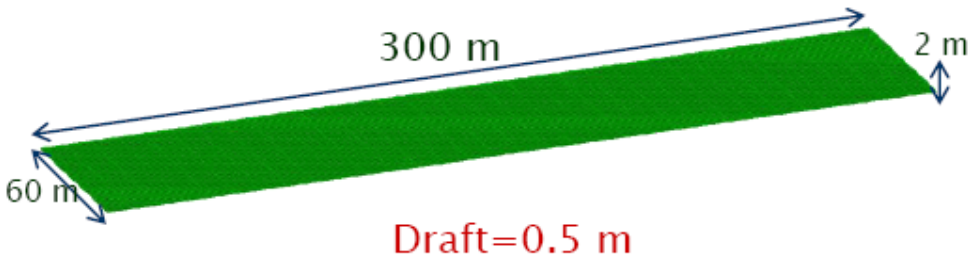

Fig 9.5 *Main dimensions of the flexible mat structure used in Case Study.*

The structural analysis was carried out based on 3 dimensional FEM analysis using shell elements in ABACUS. Typical FEM Shell element size was 1 x 1 m on bottom and on free surface and 1 x 0.25 m on sides and ends. Results for some of the normalized mode shapes are shown in Fig. 9.6. The natural frequencies of the 10 first elastic modes are summarized in Table 9.2. Mode shape No 7, 8 and 10 represent the 2-node, 3-node and 4-node modes (or first, second and third Bending Modes) respectively. Mode 9 is the first Torsion mode.

Mode No.	Frequency (Hz)	Mode number	Frequency (Hz)
7	0.15394	12	1.3771
8	0.42462	13	1.5441
9	0.48867	14	2.0571
10	0.83287	15	2.1476
11	0.99707	16	2.8243

Table 9.2 *Natural frequency of the 10 first elastic modes of the offshore mat (from Taghipour et. al (2006)).*

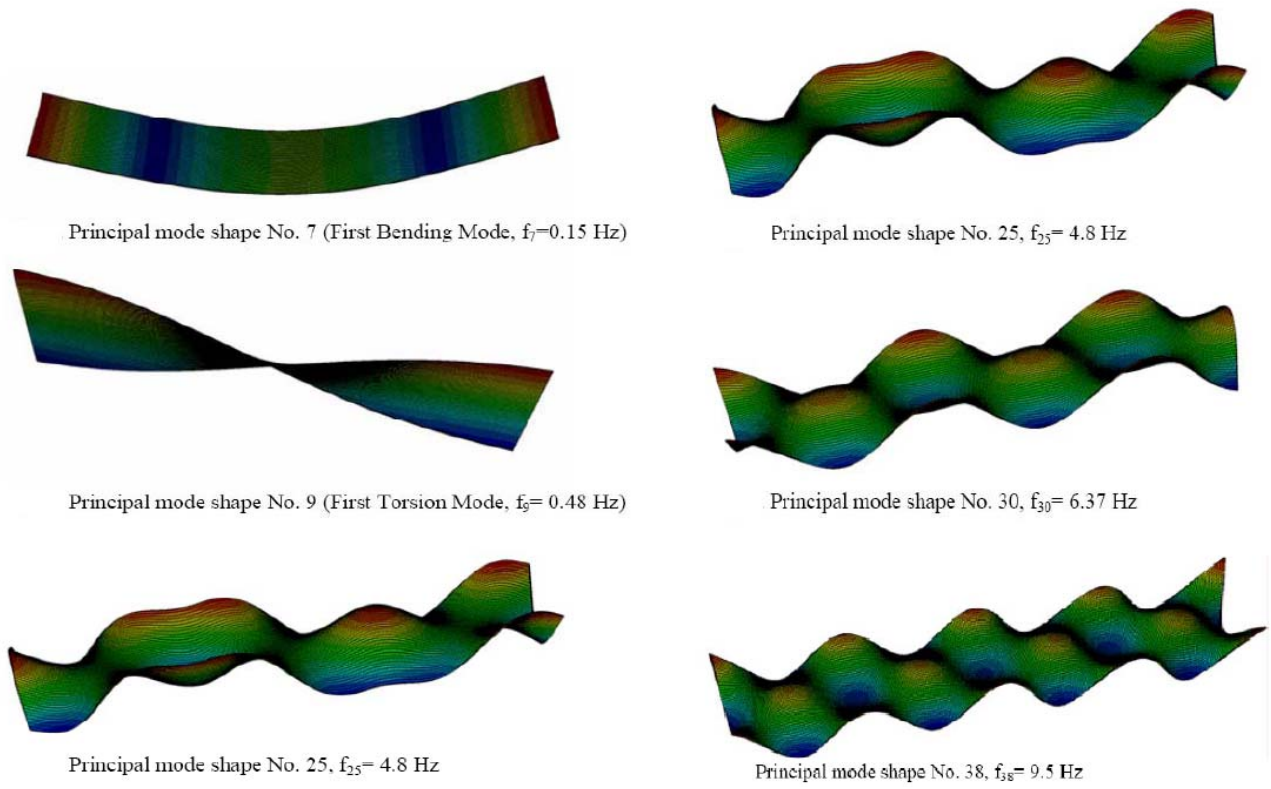

Fig 9.6 *Results for some of the normalized mode shapes of the offshore mat (from Taghipour et. al (2006)).*

The results for principal coordinate responses ($\mathbf{q}$) are shown in Fig. 9.7 as function of wave frequency. The results are shown for mode 7, 8 and 10 for head sea, wave heading 0 degrees. The torsional mode, mode 9 is as expected not excited for head sea waves. The agreement between the different approaches is seen to be very good for Mode no 7, but for the higher modes an increasing discrepancy is observed for high wave frequency (i.e short waves).

In fig 9.8 similar results are shown for wave heading 150 degrees for mode 7, 8, 9 and 10. When using the 2-D method only bending modes is excited. The result from this method is therefore not included for mode no 9. The torsional mode, mode 9 is as expected not excited for head sea waves. Also for this case some discrepancy is observed between the results from Fu and the calculations of Taghipour et al. for the higher modes.

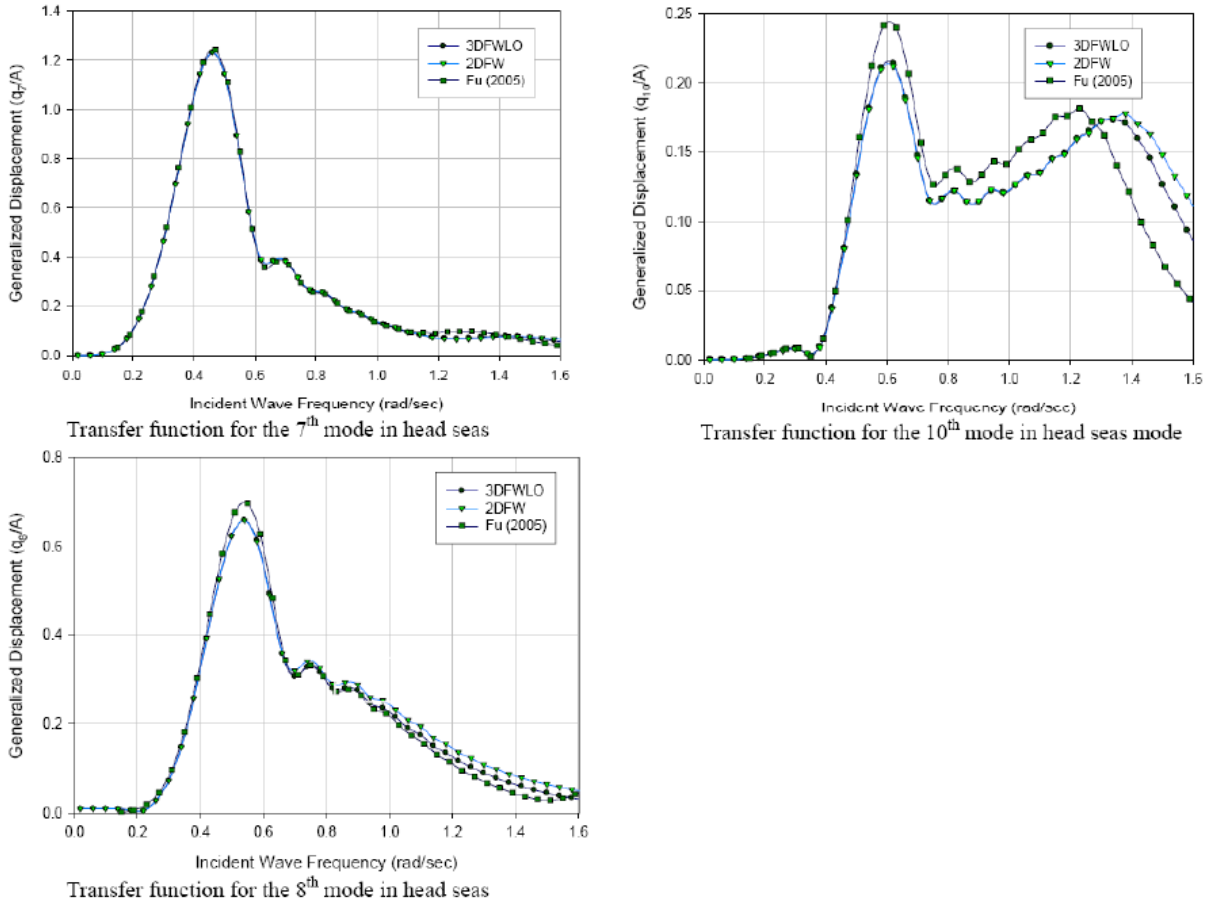

Fig 9.7 *Results for principal coordinate response transfer functions for mode 7, 8 and 10 for head sea waves. (from Taghipour et. al (2006)).*

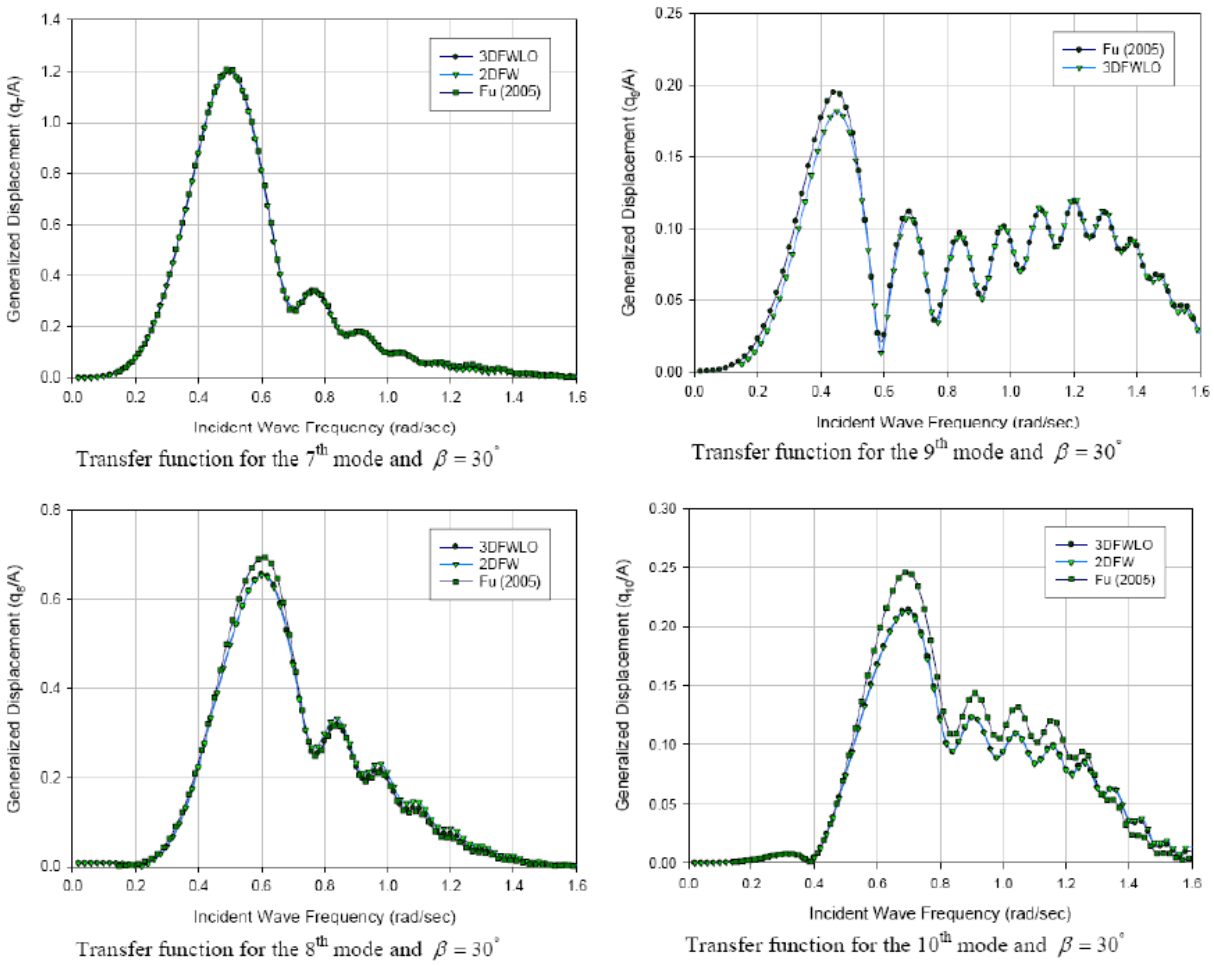

Fig 9.8 *Results for principal coordinate response transfer functions for mode 7, 8, 9 and 10 for wave heading 30 degrees. (from Taghipour et. al (2006)).*

Another key result from the calculations is the hydroelastic vertical displacement along the length of the structure. Experimental data for this parameter is available from the test carried out by Yago and Endo (1996). The comparison between the calculated vertical displacement measured along the center line of the structure and measurements is shown in Fig 9.9 for head sea waves. The results are shown for wave lengths ranging from 60 m to 300 m. In the numerical calculations 37 mode shapes were included in this study. For all cases the two numerical models gives almost equal results. The agreement between numerical calculations and model tests is seen to be very good for wave length λ=60 m and λ=120 m. The difference in response at fore and aft end is seen to be equal in both calculations and experiments. This difference in response will be due to the diffraction potential which are quite different at the fore and aft end of the structure.

For λ=240 m discrepancies with experimental results are observed. Possible error sources will be due to nonlinearities in the hydrodynamic loading e.g. slamming or viscous effects which cannot be taken into account in this linear hydroelastic theory.

Results for Rigid body motions are also included in the figure. It is observed that the difference between rigid body motion and elastic motion increase with increasing wave length. This imply that the effect of elasticity on the dynamic response increase with increasing wave length.

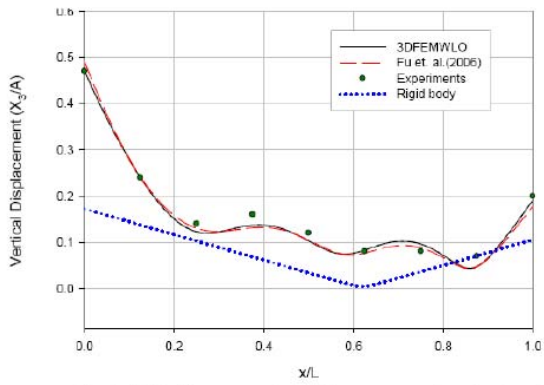

Vertical displacement along the structure for $\beta = 0$ and wave length=60 m

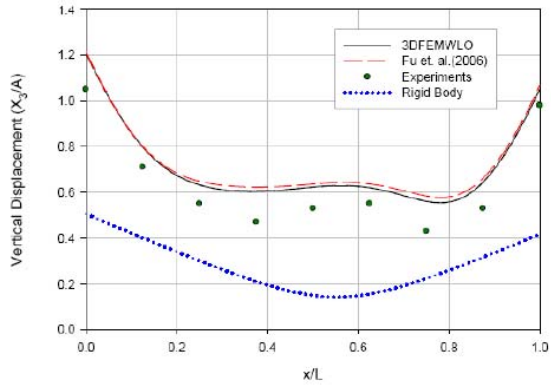

Vertical displacement along the structure for $\beta = 0$ and wave length=240 s

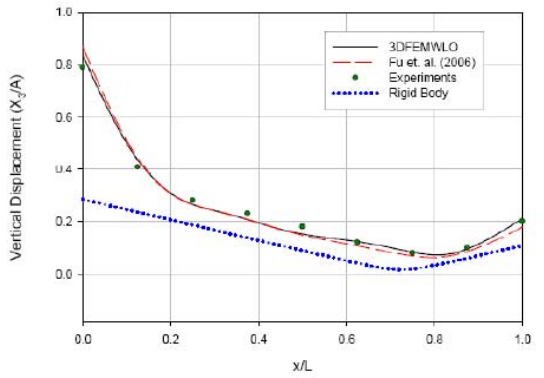

Vertical displacement along the structure for $\beta = 0$ and wave length=120 m

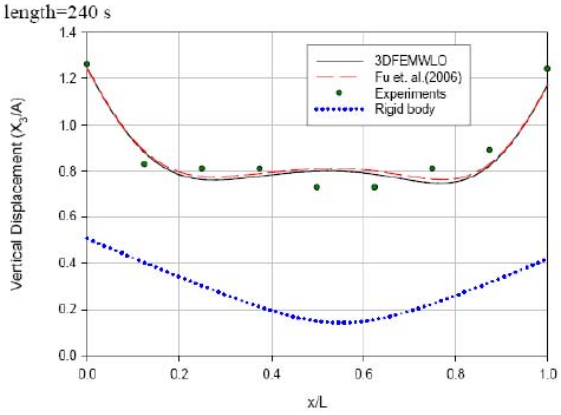

Vertical displacement along the structure for $\beta = 0$ and wave length=300 m

Fig 9.9 *Comparison between calculated and measured vertical displacement along the structure for head sea, wave heading 0 degrees. Wave length of 60 m, 120 m, 240 m and 300 m is included. (from Taghipour et. al (2006)).*

10 MEMBRANE STRUCTURES

10.1 General

Applications of liquid filled membrane structures is restricted to liquids with density lighter than sea water. Examples of existing applications are storage container, transportation of fresh water and collection of oil spill from a damaged tanker or from a blow out. Fabric structures have also been used as pens for fish farming, but then connected to a frame structure or to a floating flexible collar.

The development of the "Dracone" barge which is a long and flexible tube designed to carry and transport oil and liquids lighter than sea water was the first reported application of membrane structure for transportation purpose. This is described by Hawthorne (1961). More recently bags for water transport with volume up to 30.000 m^3 have been built, see fig. 10.1 which shows a 10.000 m^3 bag during full scale testing. The size of the 10.000 m^3 bag was length equal to 108 m, Breadth equal to 23 m and draft equal to 6.5 m. These bags ware used to transport of fresh water from Greek Mainland to islands and from Turkey to northern Cyprus.

Figure 10.1 *Nordic water Bag with volume of 10.000 m^3 for transport of Fresh water. Picture taken during full scale test in Sognefjorden*

Another example of application of membrane structure is the Unitor Oil bag designed for collection of Oil spill. The size of the bags were from 50 m^3 to 500 m^3. In Fig. 10.2 a picture from towing test with the 500 m^3 version is shown.

The main motivation for application of fabric structure is that the fabrication costs for flexible containers are much lower than for conventional structures used for sea-transportation as barges and ships.

From a hydrostatic and hydrodynamic point of view there are 3 major problems which are important for design of such floating membrane structures;

1. Static tension and shape of a flexible floating bag.
2. Stresses, motions and shapes of the flexible bag in waves
3. Towing resistance and directional stability of a flexible bag under tow.

Figure 10.2 *Towing tests with Unitor Oil Bag.*

The membrane structure is very thin, typically 2-4 mm thick. It is flexible with almost zero bending stiffness. Depending on the used material and texture the breaking strength of the fabric can be up to 500 N/mm. The elasticity module will also depend on materials, but a typical elongation at break will be 10-15 %.

10.2 Static Shape of membrane structure

10.2.1 2-Dimesional membrane structure.

In Fig 10.3 a typical static shape of a membrane structure in calm water is shown. The fluid density inside and outside the membrane structure are ρ_i and ρ_o respectively. It is assumed that $\rho_o > \rho_i$. Further it is assumed that the thickness of the membrane is infinitely thin. The mass of the membrane can therefore be neglected.

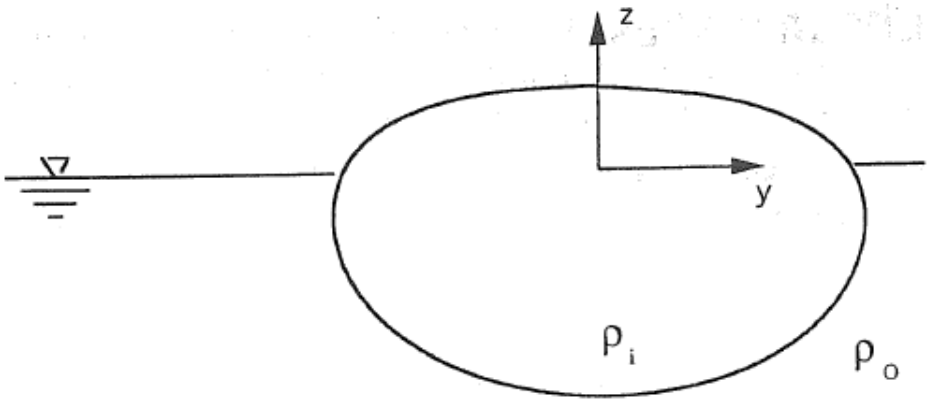

Figure 10.3 *Typical shape of a 2-Dimensional membrane structure in calm water*

The static shape and static tension is dependent of the fractional filling ratio and the difference in inside and outside density. The fractional filling ratio is defined from;

$$\gamma = \frac{A_0}{A_{MAX}} = \frac{A_0}{\pi R^2} \tag{10.0}$$

where A_0 is the actual area inside the 2-dimensional membrane and A_{MAX} is the cross sectional area for maximum filling. *R* is the radius of a cylinder with the same circumference length.

The static shape for a membrane structure is given from the equation of equilibrium of a small membrane element, see fig. 10.4;

$$2 \cdot T \cdot \sin(\frac{d\theta}{2}) = \Delta p \cdot ds \tag{10.1}$$

where θ and s are defined in Fig 10.4. Δp is the difference in static pressure between the inside and outside of the membrane and *T* is the static hoop tension. By assuming that frictional forces are small compared to pressure forces (equal to zero for static case) the tension will be constant in the circumferential direction, i.e. *dT=0*.

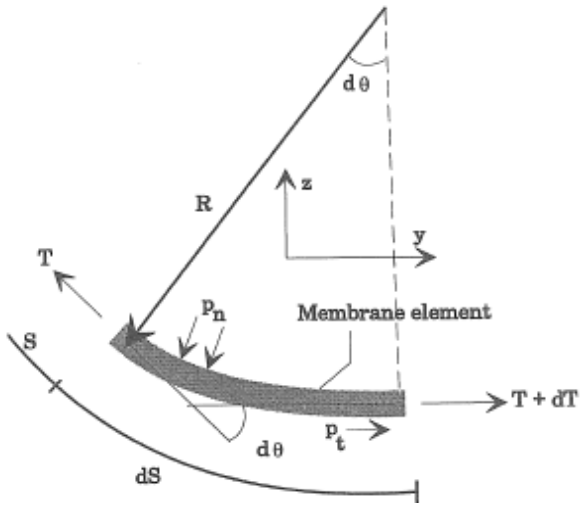

Figure 10.4 *Definition of forces acting on a infinitesimal membrane element.*

For small angles $d\theta$, Eq. (10.1) can be rewritten as;

$$\frac{d\theta}{ds} = \frac{\Delta p}{T} \tag{10.2}$$

This differential equation is used for determining the shape of the 2-Dimensional membrane structure. The equation can be solved by;

1. Analytical method available for a few special cases, see Leonard (1988)
2. Using a numerical iteration scheme.

The numerical iteration scheme has to be used for the general case. It is used that the static 2-D shape will be symmetric about the vertical axis. This imply that the fabric element at y=0 will be horizontal, i.e. $\theta = \pi$. The steps in the method of solution can be summarized as follows, see also Fig. 10.5;

- Start the solution from a point on the vertical axis a_s with coordinates $(0, z_w)$, see Fig 10.5.
- Assume the pressure inside the membrane is p_{in}^0
- For the given point a_s and pressure p_{in}^0 there exist only one static shape. The hoop tension for the static shape is *assumed* to be T_s
- If we assume the lowest point on the membrane is b_e, so the angle θ is 0 and π at the points a_s and b_s respectively, see Fig. 10.5.
- Using eq. (10.2) to evaluate the development in y-z coordinates from $\theta = 0$ to $\theta = \pi$ numerically for an assumed hoop tension value, *T,* gives;

$$\Delta\theta_s^{\,i} = \theta_s^{\,i+1} - \theta_s^{\,i} = \frac{\Delta p_s}{T} \cdot \Delta s$$

which gives

$$\theta_s^{\,i+1} = \theta_s^{\,i} + \frac{\Delta p_s}{T} \Delta s$$

where Δs is the length of the membrane element

- The final hoop tension T_s is not known at the start of iteration. For $T \neq T_s$ the y-coordinate for $\theta = \pi$ will differ from 0 as shown in Fig. 10.5. The next step in the iteration is to use a new tension value either higher or lower dependent on the solution from the previous time step.
- This procedure is repeated until a solution is obtained which gives $\theta = \pi$ for y=0.

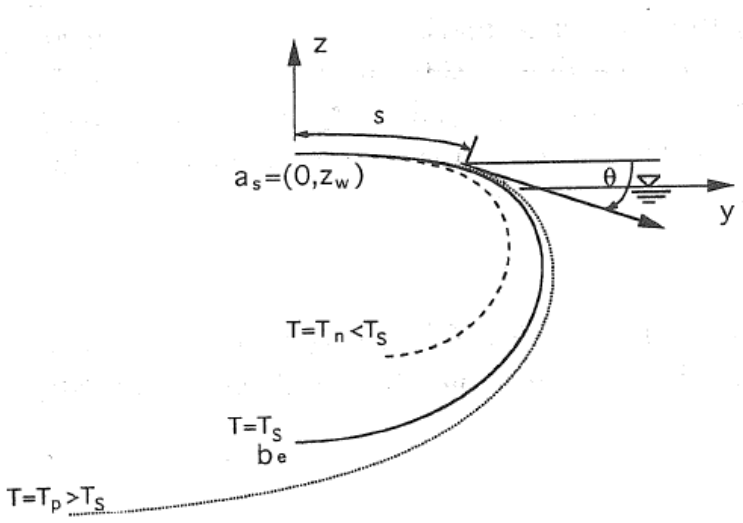

Figure 10.5 *Iteration process for solution of static shape. Illustration of the dependency of y-z coordinates of the hoop tension T.*

The iteration procedure are described in more detail in Zhao and Triantafyllou (1994) and Løland and Aarsnes (1994). For small filling ratios the overpressure at the top, p_{in}^0, is very small compared to the maximum pressure in the outside fluid. It may therefore be difficult to get convergence of the shooting method for such cases.

Based on the x-y coordinates of the membrane structure, the filling ratio of the static shape can be calculated using eq. (10.1).

For a given point a_s, the filling ratio is dependent on the chosen pressure $p^0{}_{in}$. To predict the static shape for a given filling ratio, iteration by assuming different values of $p^0{}_{in}$ will be required.

Results for static shape for different filling ratios are shown in Fig. 10.6. Results for static shape for different density differences ρ_i/ρ_o are shown in Fig. 10.7. For both case the circumference length have been kept fixed for all cases. It is observed that the static shape is strongly dependent on the filling ratio. Increasing filling ratio gives reduced beam and increased draft. Filling ratio equal to 1.0 gives a circular shape.

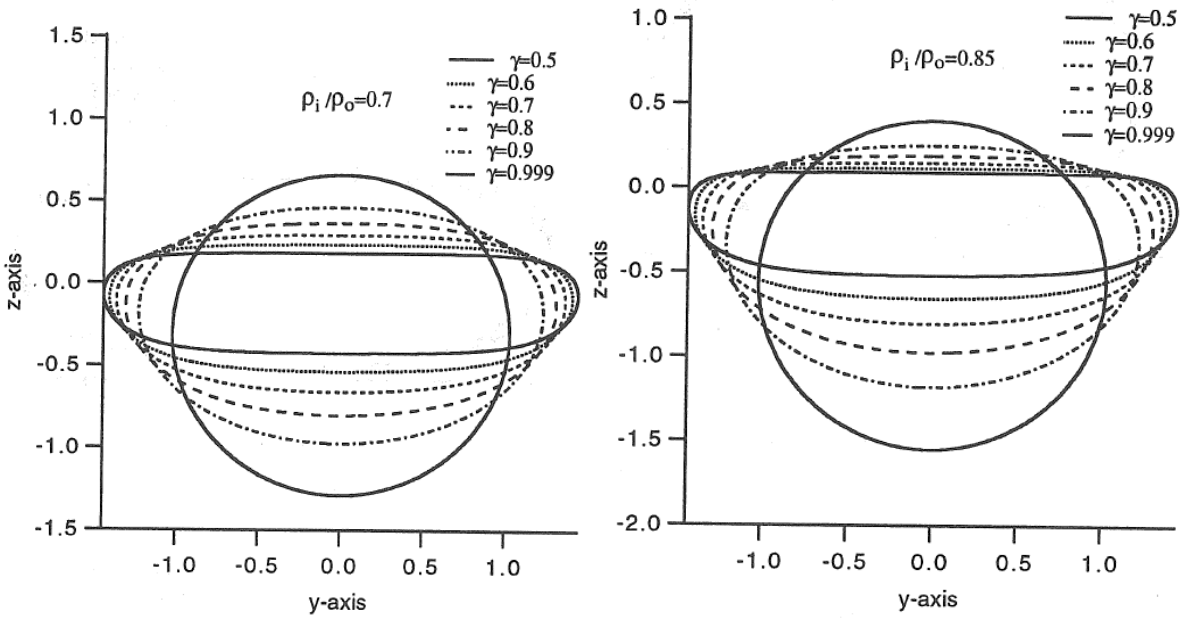

Figure 10.6 *Static 2-Dimensinal cross sectional shape of membrane structure as function of fractional filling*

From Fig 10.7 it is seen that the density difference give a small effect on the static shape. It is observed that the lowest point for each curve is almost the same for the different relative fluid densities ρ_i/ρ_o

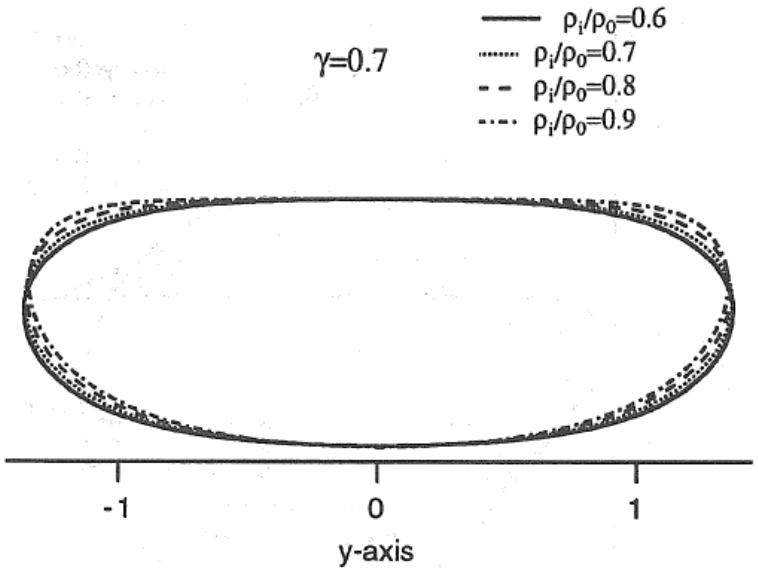

Figure 10.7 *Static 2-Dimensinal cross sectional shape of membrane structure as function of relative density difference* ρ_i/ρ_o *.*

In Fig. 10.8 the hoop tension is shown as function of filling ration and density difference. It is observed that for fractional filling above 0.8 the hoop tension increase very fast with increasing filling ratio.

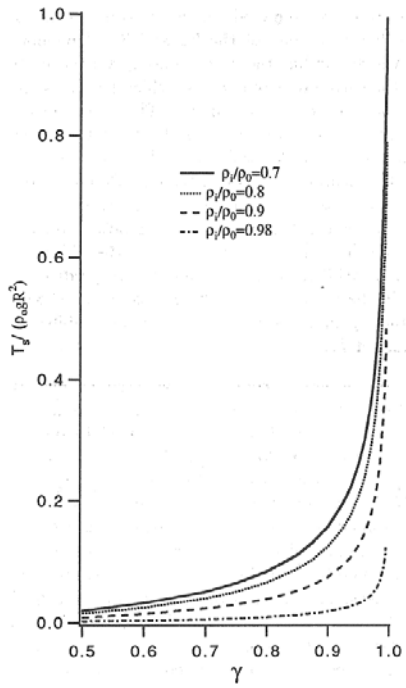

Figure 10.8 *Hoop tension for a static 2-Dimensinal cross sectional shape of membrane structure as function of filling ratio and relative density difference* ρ_i/ρ_o *.*

In Fig. 10.9 the relative tension for the different fluid densities ρ_i/ρ_o is shown. The results show that the relative tension is almost linearly dependent on the filling ratio.

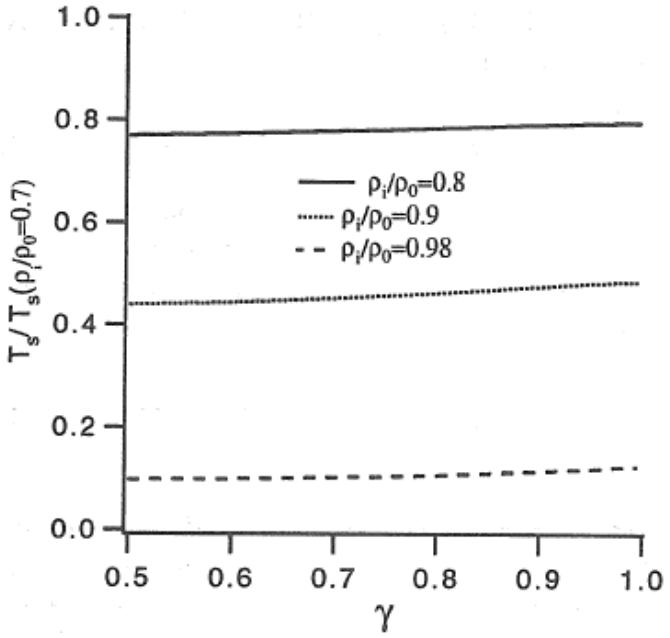

Figure 10.9 *The relative tension for different relative densities* ρ_i/ρ_o *as function of filling ratio.*

10.3 Dynamic tension in waves – 2-Dimensional Case.

10.3.1 Theoretical formulation

A linear 2-Dimensional theory for wave induced dynamic tension in waves of a floating membrane structure have been developed for the beam sea case (Zhao (1995). The approach is based on the assumption that the amplitude of the incident waves are small compared to the characteristic dimensions of the membrane. The problem is solved in the frequency domain. Viscous effects are neglected and the problem is solved using potential theory.

Two velocity potentials are introduced; $\Phi_I = \mathrm{Re}\left\{\phi_I e^{i\omega t}\right\}$ and $\Phi_O = \mathrm{Re}\left\{\phi_O e^{i\omega t}\right\}$ which is the velocity potential inside and outside the membrane structure respectively. Formal requirements to the potentials; Laplace equation;

$$\nabla^2\Phi_I = 0 \qquad \nabla^2\Phi_0 = 0 \tag{10.3}$$

The velocity potential outside the membrane structure can be divided into the following contributions;

$$\Phi_O = \Phi_1 + \Phi_2 + \Phi_3 \tag{10.4}$$

Where Φ_1 is the velocity potential of the linear incident wave which can be written as;

$$\Phi_1(x,z,t) = \mathrm{Re}\left\{\frac{g}{\omega}\varsigma_A e^{i\omega t - iky + kz}\right\} \tag{10.5}$$

Here ς_A, ω and k are the incident wave amplitude, the circular frequency of oscillations and the wave number. The relation between ω and k are given by the dispersion relation;

$$k = \frac{\omega^2}{g} \tag{10.6}$$

Φ_2 is the diffraction potential when the motion of the membrane is ignored (i.e "fixed") and Φ_3 is the velocity potential due to the motions of the membrane. This last term covers the hydroelastic behavior of the membrane structure.

The linear boundary condition on the free surface for the different potentials in Φ_O is;

$$-\omega^2\Phi_O + g\frac{\partial\Phi_O}{\partial z} = 0 \qquad \textit{on} \quad \textit{z=0} \tag{10.7}$$

The body boundary condition for Φ_2 and Φ_3 are;

$$\frac{\partial\Phi_2}{\partial n} = -\frac{\partial\Phi_1}{\partial n} \qquad \textit{on} \quad S_{B1} \tag{10.8}$$

$$\frac{\partial\Phi_3}{\partial n} = \mathbf{V}\cdot\mathbf{n} = \frac{\partial\Phi_I}{\partial n} \qquad \textit{on} \quad S_{B1} \tag{10.9}$$

Where $\mathbf{V}$, $\mathbf{n}$ and S_{B1} are the velocity for each point on the membrane structure, the normal vector with positive direction into the fluid and the mean wetted body surface, see Fig. 10.10.

A similar boundary condition is satisfied for Φ_I namely;

$$\frac{\partial \Phi_I}{\partial n} = \mathbf{V} \cdot \mathbf{n}_1 \qquad on \quad S_B \tag{10.10}$$

Where $S_B = S_{B1} + S_{B2}$ is the mean surface of the membrane as shown in Fig. 10.10 and $\mathbf{n}_1$ is the normal vector with positive direction into the inner fluid.

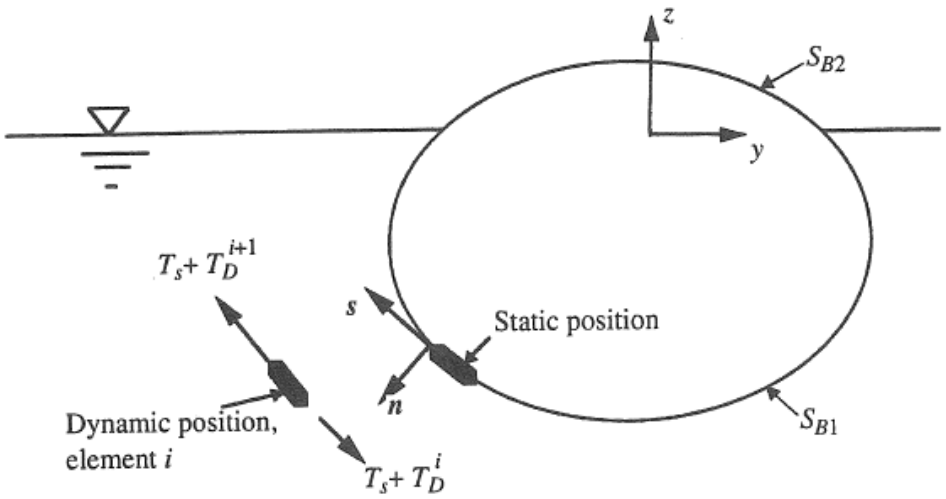

Figure10.10 *Definition of boundary value problem for2-Dimensional membrane structure in beam sea.*

In addition to the above defined boundary conditions Φ_2 and Φ_3 must satisfy the radiation condition, which imply that the body can only generate waves which propagate away from the body.

Due to the hydroelastic deformation of the membrane structure, we need linear dynamic equations for the motion of each element of the membrane in the $\mathbf{n}$ and $\mathbf{s}$ directions, see Fig. 10.10. The mass of the membrane is neglected and zero thickness is assumed. The following force equilibrium equations are then obtained for a small membrane element in $\mathbf{n}$ direction (see Triantafyllou (1990));

$$F_n = m\ddot{\eta}_n = -(T_D + T_S)\frac{d\theta_S + d\theta_D}{ds} + P_S + P_D = -T_D\frac{d\theta_S}{ds} - T_S\frac{d\theta_D}{ds} + P_D = 0 \tag{10.11}$$

where eq. (10.2) has been used for the static pressure and the term $T_D \dfrac{d\theta_D}{ds}$ is neglected.

In $\mathbf{s}$ direction;

$$F_S = m\ddot{\eta}_S = \frac{\partial T_D}{\partial s} = 0 \tag{10.12}$$

Where T_D and T_S are the dynamic and static tension respectively and θ_D and θ_S are the dynamic and static part of $\theta = \theta_D + \theta_S$. P_D is the dynamic pressure difference obtained as;

$$P_D = P_{ID} - P_{OD} \tag{10.13}$$

where

$$P_{ID} = -\rho_I \frac{\partial \Phi_I}{\partial t} - \rho_I g \Delta z \qquad on \quad S_B = S_{B1} + S_{B2} \tag{10.14}$$

are the dynamic pressure inside the membrane due to the motion of the membrane. The dynamic pressure outside the membrane can be written as;

$$P_{OD} = -\rho_O \frac{\partial \Phi_O}{\partial t} - \rho_O g \Delta z \qquad on \quad S_{B1} \tag{10.15}$$

Δz is the vertical component of the displacement of the membrane.

The unknowns in the above formulated boundary value problem, see eq. (10.3)–(10.15) are Φ_2 , Φ_3 and Φ_I. These potentials must be solved with a numerical method. The diffraction potential Φ_2, can be solved in the same way as used for rigid body motions, see e.g. Zhao and Faltinsen (1988).

By applying Green's second identity the potential Φ_3 and Φ_I can be written as (see e.g. Faltinsen (1990) p 128);

$$2\pi\Phi(y,z,t) = \int_S \left[\log r \frac{\partial \Phi(\eta,\xi,t)}{\partial n} - \Phi(\eta,\xi,t) \frac{\partial \log r}{\partial n} \right] dS(\eta,\xi,t) \tag{10.16}$$

Where;

$$r = \sqrt{(y-\eta)^2 + (z-\xi)^2}$$

For the outer problem, $S = S_{B1} + S_{F1} + S_{F2} + S_C$, see figure 10.11. S_{F1} and S_{F2} is the mean free surface and S_C is the control surface which is far from the body.

For the inner problem $S = S_{B1} + S_{B2}$

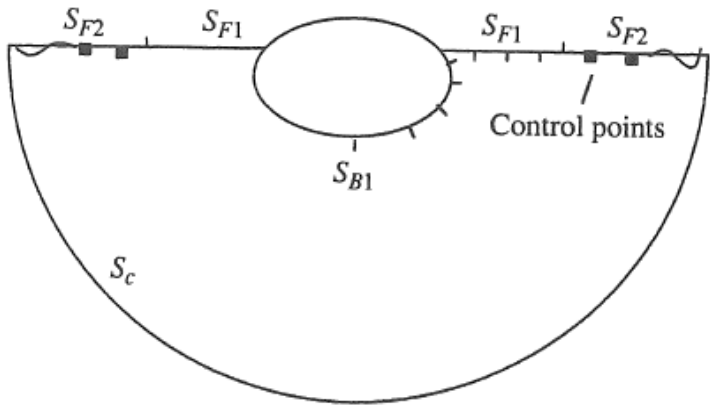

Figure 10.11 *Definition of the surfaces used in the boundary element method.*

For the numerical solution of the above formulated problem, the surfaces is divided into straight line segments as indicated in Fig. 10.11. For each element we assume Φ_3 is unknown and $\partial\Phi_3/\partial n$ is known (from boundary conditions (10.7) and (10.9)). Then the

total number of unknown is $N_{B1} + N_{F1}$ where N_{B1} and N_{F1} is the number of elements on S_{B1} and S_{F1} respectively.

The integral equation eq. (10.16), is satisfied at the midpoint of each element on S_{B1} and S_{F1}, thus we obtain $N_{B1} + N_{F1}$ equations.

It should be noted that Φ_3 and the potential for the inside fluid Φ_I have to be solved for simultaneously. Further details of the numerical solution method are presented by Zhao (1995).

10.3.2 Numerical results.

An example of numerical calculated results for dynamic deformation of the membrane structure is shown in Fig. 10.12. The instantaneous displacements of the membrane surface are shown for three different frequencies. The case considered is filling ratio γ=0.9 and relative density $\rho_i / \rho_o = 0.7$. The incident wave amplitude $\varsigma_A = 0.2 \cdot R$. Case b; shown in the figure corresponds to the frequency which gave the highest membrane tension. From the figure it is seen that the membrane structure closely follow the waves for long waves, i.e case a;. For short waves, case c; the membrane motions is seen to be small.

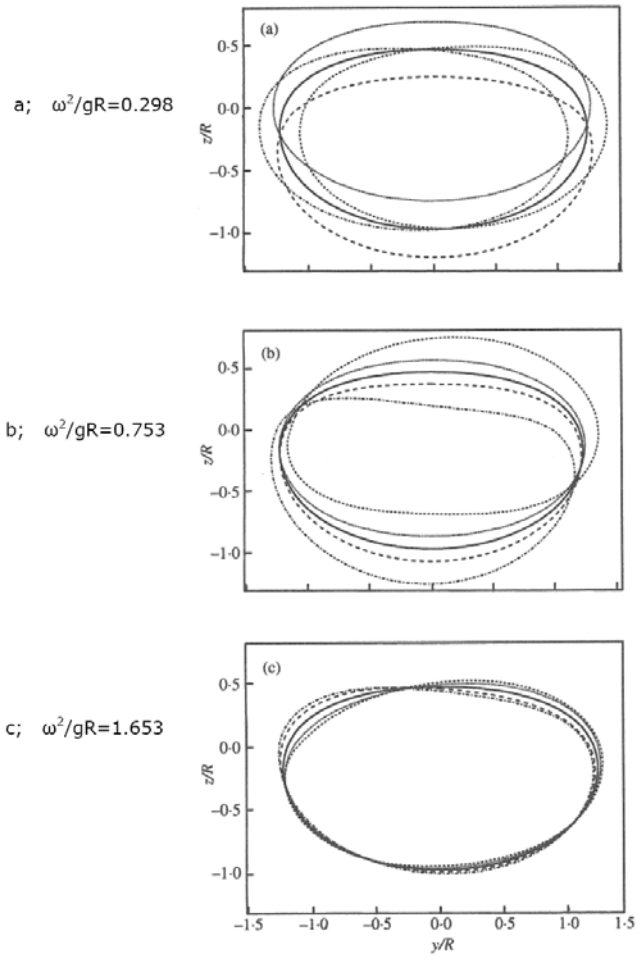

Figure10.12 *Static and dynamic position of the membrane structure at 3 different frequencies. The filling ratio is γ=0.9 and relative density $\rho_i / \rho_o = 0.7$. The incident wave amplitude $\varsigma_A = 0.2 \cdot R$. Static position (full line) and position at ωt=0, π/2 , π and 3π/2 shown.*

The dynamic tension in beam sea waves is shown in Fig. 10.13 as function of incident wave frequency for different filling ratios. In Fig 10.14 the dynamic tension is shown for different relative density differences ρ_i/ρ_o . It is seen that the maximum dynamic tension is increasing with increasing filling ration and with decreasing relative density.

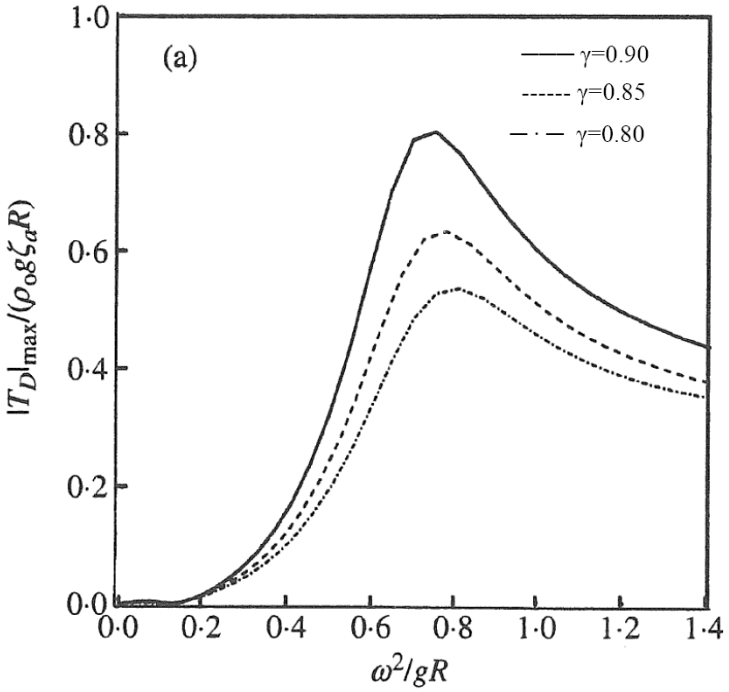

Figure10.13 *Dynamic tension for different filling ratios. Results shown for relative density* $\rho_i/\rho_o = 0.7$ *. The incident wave amplitude* $\zeta_A = 0.2 \cdot R$ *.*

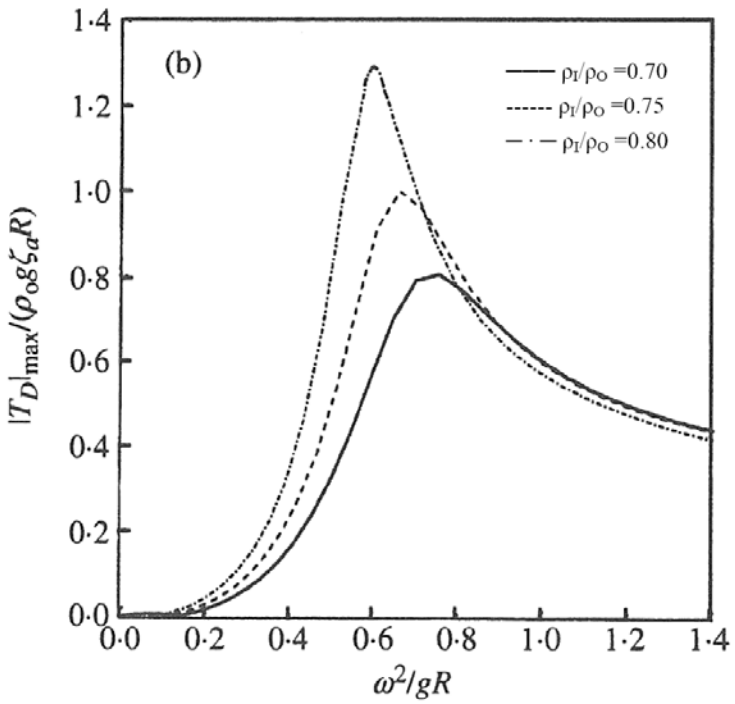

Figure10.14 *Dynamic tension for different relative density differences* ρ_i/ρ_o *. Results shown for filling ratio is γ=0.9. The incident wave amplitude* $\zeta_A = 0.2 \cdot R$ *.*

10.4 3-Dimensional Solution for Head sea.

10.4.1 Theoretical formulation

For head sea (or following sea) a strip theory approach is used for the calculation of response of the membrane structure in waves.

The coordinate system used in the analysis is shown in Fig. 10.15. The y-axis is on the mean water surface. It is assumed that the length of the container, *L*, is large compared with the cross sectional dimension, *D,* (i.e. *D/L* small). Due to the slenderness assumption the flow inside the membrane is treated as a one-dimensional problem for the cases when the wave length, λ, is much larger than the cross sectional dimension. Outside the membrane the boundary element method based on the 2-Dimensional strip theory approach is used. This approach is valid for wave lengths smaller than the length of the container.

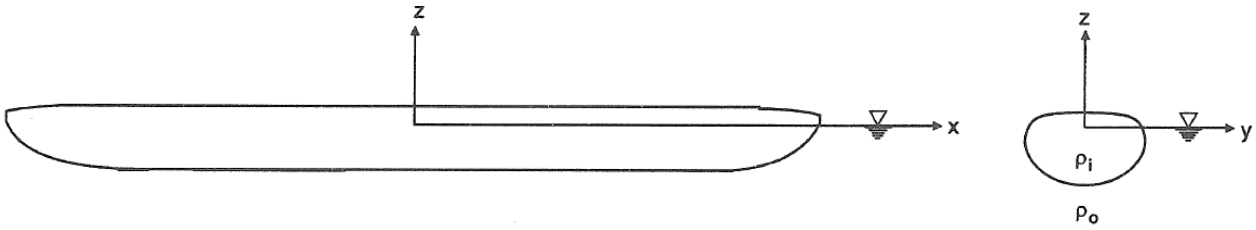

Figure10.15 *The used coordinate system for 3-Dimensional analysis of Membrane structure.*

Formally the above assumptions results in the requirement; $D << \lambda << L$. For a practical application one may apply the theory for a larger range of λ.

The problem is solved in the frequency domain. For each strip (cross section) we have the following 4 unknowns;

- $P_1(x,t)$; is the average dynamic pressure inside the membrane structure for each section
- $\eta_3(x,t)$; is the vertical motion of the rigid body (based on 2-D static shape)
- $A_1(x,t)$; is the change of the filling of fluid for each section
- $V_1(x,t)$; is the longitudinal velocity (one-dimensional) inside the structure.

The four equations for solving the problem are;

$$\frac{\partial P_1}{\partial x} = -\rho_I \frac{\partial V_1}{\partial t} - \rho_I g \frac{\partial z(\eta_3, A_1)}{\partial x} \tag{10.17}$$

$$\frac{\partial A_1}{\partial t} + \frac{\partial V_1}{\partial x} A_0 = 0 \tag{10.18}$$

$$\Delta F_3 - \Delta m g = m \ddot{\eta}_3 \tag{10.19}$$

$$P_1 = \frac{\partial P_1}{\partial P_{A1}} A_1 + \frac{\partial P_1}{\partial P_{\dot{A}1}} \dot{A}_1 + \frac{\partial P_1}{\partial P_{\ddot{A}1}} \ddot{A}_1 + \frac{\partial P_1}{\partial P_{\eta 3}} \eta_3 + \frac{\partial P_1}{\partial P_{\dot{\eta} 3}} \dot{\eta}_3 + \frac{\partial P_1}{\partial P_{\ddot{\eta} 3}} \ddot{\eta}_3$$
$$+ \frac{\partial P_1}{\partial P_{\mathrm{Re}(Fex)}} e^{i\omega t} + i \frac{\partial P_1}{\partial P_{\mathrm{Im}(Fex)}} e^{i\omega t} + \frac{\partial P_1}{\partial P_{\frac{\partial^4 z}{\partial x^4}}} EI + \frac{\partial P_1}{\partial P_{\frac{\partial^2 z}{\partial x^2}}} T \qquad (10.20)$$

where;

$$\Delta F_3 = F_{ex} e^{i\omega t} - A_{33} \ddot{\eta}_3 - B_{33} \dot{\eta}_3 - C_{33} \eta_3 - A_{A1} \ddot{A}_1 - B_{A1} \dot{A}_1 - C_{A1} A_1 - EI \frac{\partial^4 z}{\partial x^4} + T(x) \frac{\partial^2 z}{\partial x^2} \qquad (10.21)$$

$$\Delta m = A_1 \rho_I \qquad (10.22)$$

$$z = \eta_3 + \frac{\partial z}{\partial A_1} A_1 \qquad (10.23)$$

Eq. (10.17) is the one-dimensional equation for the motion of the fluid inside the membrane structure, eq. (10.18) is the one-dimensional equation for continuity and eq. (10.19) is applied Newton's second low for each section. The last equation assumes that the pressure $P_1(x,t)$ for each section can be expressed as function of $\eta_3(x,t)$, $A_1(x,t)$ and it's derivatives, as well as F_{ex}(x), $EI(x)$ and $T(x)$. Here;

- $F_{ex}(x)$ is the 2-dimensional vertical excitation force of the incident wave
- A_{33}, B_{33} and C_{33} is the 2-dimensional added mass, damping and stiffness force in the vertical direction due to heave motions of the rigid body.
- A_{A1}, B_{A1} and C_{A1} is the 2-dimensional added mass, damping and stiffness force in the vertical direction due to the mode motion A_1 (i.e. change of the filling for each section).
- $EI(x)$ is the bending stiffness of the membrane structure.
- $T(x)$ is the part of longitudinal tension which has contribution to the vertical force.
- $z(x,t)$ is the average vertical motion of the fluid inside the two-dimensional membrane as function of time
- $A_0(x)$ is the static filling of the membrane, total filling is $A = A_0 + A_1$.
- $m(x)$ is the mass of each section at the static equilibrium position.
- P_{A1}, $P_{\dot{A}1}$, $P_{\ddot{A}1}$, $P_{\eta 3}$, …… are the dynamic pressure components outside the tube which are proportional to A_1, $\dot{A}_1$, $\ddot{A}_1$, η_3 .....

Details for calculation of the hydrodynamic coefficients used in Eq. (10.21) are given in chap 10.4.2 below.

The coefficients used in Eq. 10.20; $\frac{\partial P_1}{\partial P_{A1}}$, $\frac{\partial P_1}{\partial P_{\dot{A}1}}$, $\frac{\partial P_1}{\partial P_{\ddot{A}1}}$, $\frac{\partial P_1}{\partial P_{\eta 3}}$,…., can be evaluated using a similar approach as for the static problem. One assumes the total dynamic pressure for each section ***outside*** of the tube, $P_{D,O}(y,z,t)e^{i\omega t}$, can be written as;

$$P_{D,O} = P_{A1} A_1 + P_{\dot{A}1} \dot{A}_1 + P_{\ddot{A}1} \ddot{A}_1 + P_{\eta 3} \eta_3 + P_{\dot{\eta} 31} \dot{\eta}_{31} + P_{\ddot{\eta} 3} \ddot{\eta}_3 + P_{Fex} e^{i\omega t} + P_{\frac{\partial^4 z}{\partial x^4}} EI + P_{\frac{\partial^2 z}{\partial x^2}} T$$

For each component of dynamic pressure outside the tube one may evaluate the corresponding dynamic pressure inside the tube and the dynamic tension. The dynamic pressure and tension we obtain are the coefficients in eq. (10.20) and eq. (10.24), se below. The term $\frac{\partial P_1}{\partial P_{A1}}$ can therefore be interpreted as the change of internal pressure, P_1, due to change of the part of the outer pressure which is proportional to A_1. Similar interpretation can be established for the other coefficients. Further details about the calculation of these coefficients are given by Zhao and Triantafyllou (1994).

After one have obtained all the coefficients in Equations (10.17) – (10.20), we can solve these four equations numerically.

As shown in Fig. 10.16 the membrane container is divided into *N* segments and *N+1* sections. For each section we have 4 unknowns; $P_1(x,t)$, $\eta_3(x,t)$, $A_1(x,t)$ and $V_1(x,t)$. The problem is solved using a finite difference method. The boundary conditions are;

- $V_1(x,t)=0$ at the ends (i.e. for section *1* and *N+1*)
- Bending Moment, $M(x,t)=0$ at the ends (i.e. for section *1* and *N+1*)
- Shear Forces, $Q(x,t)=0$ the ends (i.e. for section *1* and *N+1*)

Which gives a total of 6 boundary conditions.

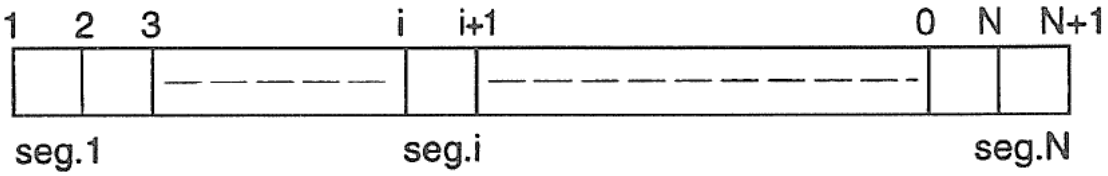

Figure10.16 *Illustration of segments and sections used in the numerical computation.*

After one has solved the problem for the 4 unknowns as function of longitudinal position, the dynamic tension in the transverse direction can be evaluated by the following equation;

$$T_1 = \frac{\partial T_1}{\partial P_{A1}} A_1 + \frac{\partial T_1}{\partial P_{\dot{A}1}} \dot{A}_1 + \frac{\partial T_1}{\partial P_{\ddot{A}1}} \ddot{A}_1 + \frac{\partial T_1}{\partial P_{\eta 3}} \eta_3 + \frac{\partial T_1}{\partial P_{\dot{\eta} 3}} \dot{\eta}_3 + \frac{\partial T_1}{\partial P_{\ddot{\eta} 3}} \ddot{\eta}_3$$
$$+ \frac{\partial T_1}{\partial P_{\mathrm{Re}(Fex)}} e^{i\omega t} + i \frac{\partial T_1}{\partial P_{\mathrm{Im}(Fex)}} e^{i\omega t} + \frac{\partial T_1}{\partial P_{\frac{\partial^4 z}{\partial x^4}}} EI + \frac{\partial T_1}{\partial P_{\frac{\partial^2 z}{\partial x^2}}} T \qquad (10.24)$$

The coefficients in Eq. 10.24, $\frac{\partial T_1}{\partial P_{A1}}$, $\frac{\partial T_1}{\partial P_{\dot{A}1}}$, $\frac{\partial T_1}{\partial P_{\ddot{A}1}}$, $\frac{\partial T_1}{\partial P_{\eta 3}}$,…., can be evaluated in the same way as described above for $\frac{\partial P_1}{\partial P_{A1}}$, $\frac{\partial P_1}{\partial P_{\dot{A}1}}$, $\frac{\partial P_1}{\partial P_{\ddot{A}1}}$, $\frac{\partial P_1}{\partial P_{\eta 3}}$,… above.

10.4.2 Hydrodynamic coefficients

The added mass and damping coefficients and the wave excitation force as used in eq. (10.21) can be obtained by solving a 2-D boundary value problem. The fluid outside the membrane structure is represented by the velocity potential;

$$\Phi_T = \phi_0 e^{i\omega t} + \phi_3 e^{i\omega t} + \phi_1 \eta_3 + \phi_2 A_1 \qquad (10.25)$$

where $\phi_0 e^{i\omega t}$ is the velocity potential of the incident wave, $\phi_3 e^{i\omega t}$ is the diffraction potential of the incident wave, $\phi_1 \eta_3$ is the potential due to the heave motion of the rigid body (based on static shape) and $\phi_2 A_1$ is the potential due to the mode motion A_1 (change of the filling for the cross section).

The above potentials ϕ_i, i=1,2,3, shall satisfy the linear free surface condition;

$$-\omega^2 \phi_i + g \frac{\partial \phi_i}{\partial z} = 0 \qquad on \quad z=0 \qquad (10.26)$$

and the body boundary condition;

$$\frac{\partial \phi_i}{\partial n} = \mathbf{V} \cdot \mathbf{n} \qquad on \quad S_B \qquad (10.27)$$

The velocity potential can be solved by applying Green's second identity in a similar way as discussed above. Further details about the numerical method are given by Zhao and Faltinsen (1988).

After obtaining the solution for the potential ϕ_i the hydrodynamic coefficients can be calculated from;

$$F_{ex} = \rho \int_{S_B} i\omega n_3 (\phi_0 + \phi_3) ds$$

$$A_{33} = \mathrm{Re}\left(\rho \int_{S_B} i\omega n_3 \phi_1 ds \right) \Big/ \omega^2$$

$$B_{33} = -\mathrm{Im}\left(\rho \int_{S_B} i\omega n_3 \phi_1 ds \right) \Big/ \omega$$

$$A_{A1} = \mathrm{Re}\left(\rho \int_{S_B} i\omega n_3 \phi_2 ds \right) \Big/ \omega^2$$

$$B_{A1} = -\mathrm{Im}\left(\rho \int_{S_B} i\omega n_3 \phi_2 ds \right) \Big/ \omega$$

Numerical calculated results for the above coefficients and excitation forces are presented in Fig. 10.17-10.21. The results show that the coefficients are strongly dependent on the filling ratio γ, and the relative density ρ_i / ρ_o.

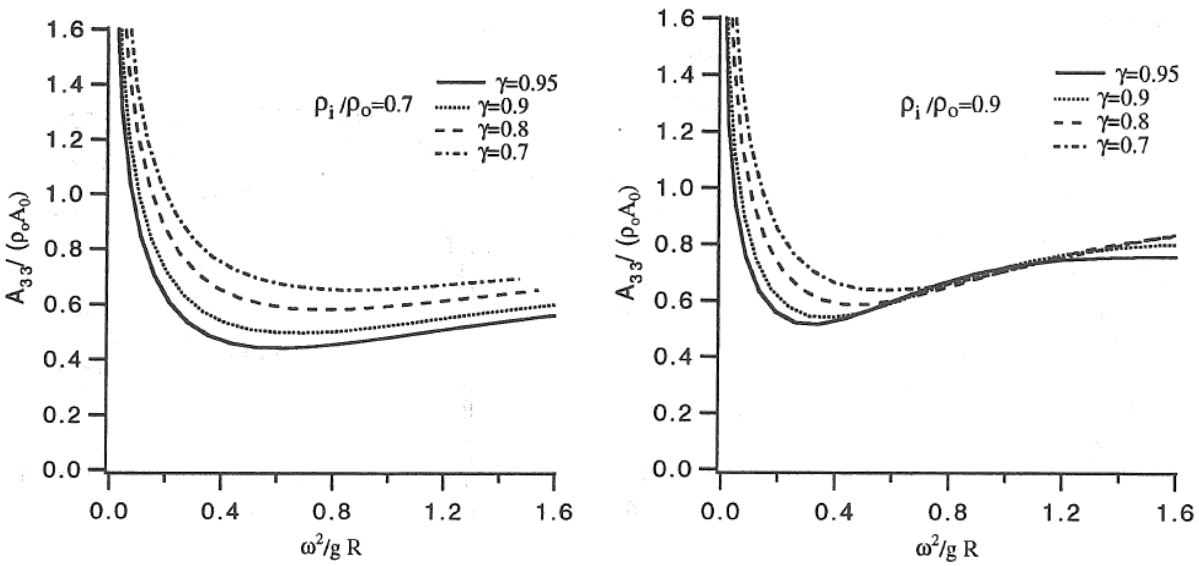

Figure 10.17 *Added mass coefficient A_{33} as function of filling ratio γ and the Relative density ρ_i/ρ_o*

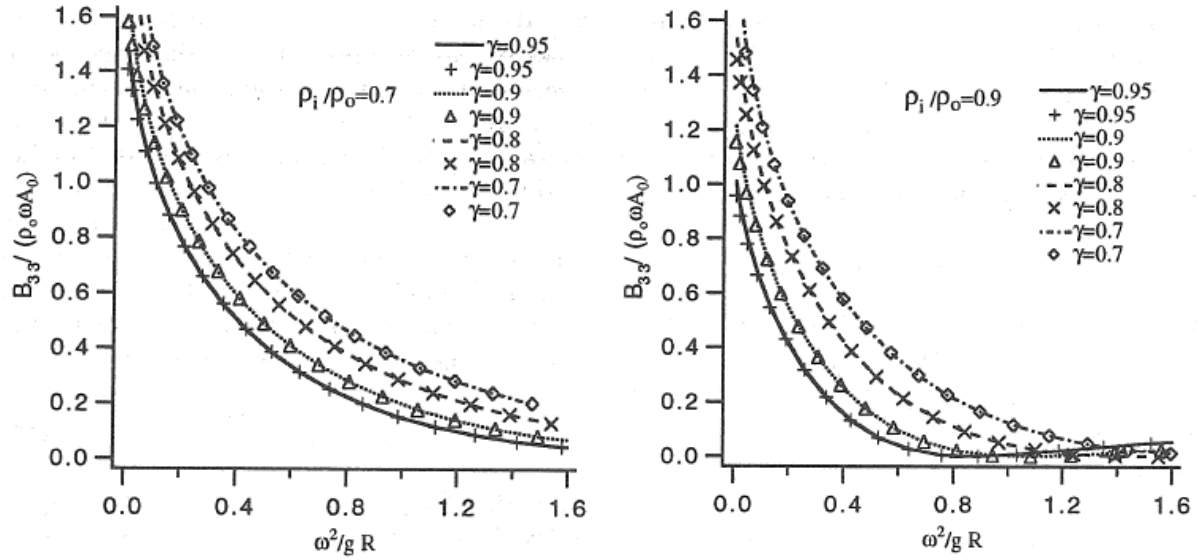

Figure 10.18 *Damping coefficient B_{33} as function of filling ratio γ and the relative density ρ_i/ρ_o*

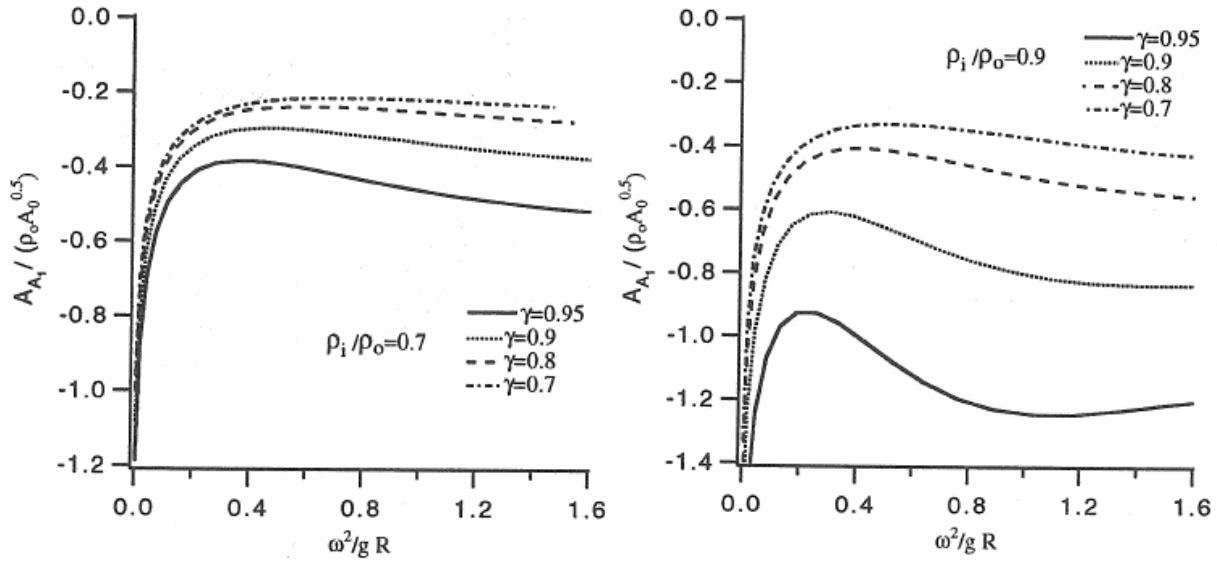

Figure 10.19 *Added mass coefficient A_{Al} as function of filling ratio γ and relative density ρ_i/ρ_o*

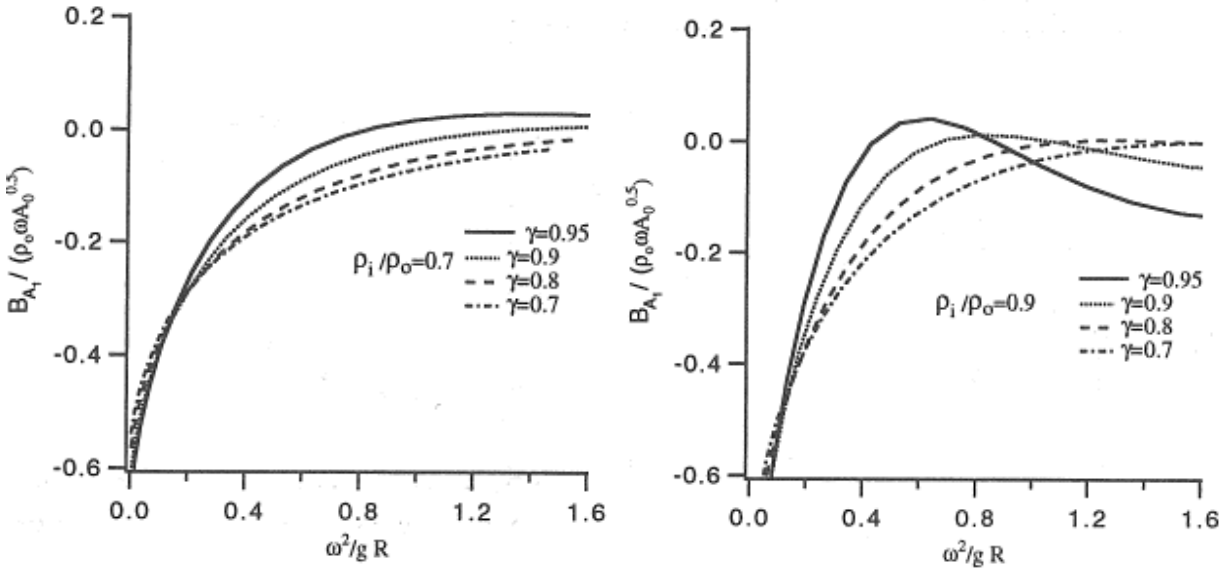

Figure 10.20 *Damping coefficient B_{Al} as function of filling ratio γ and relative density ρ_i/ρ_o*

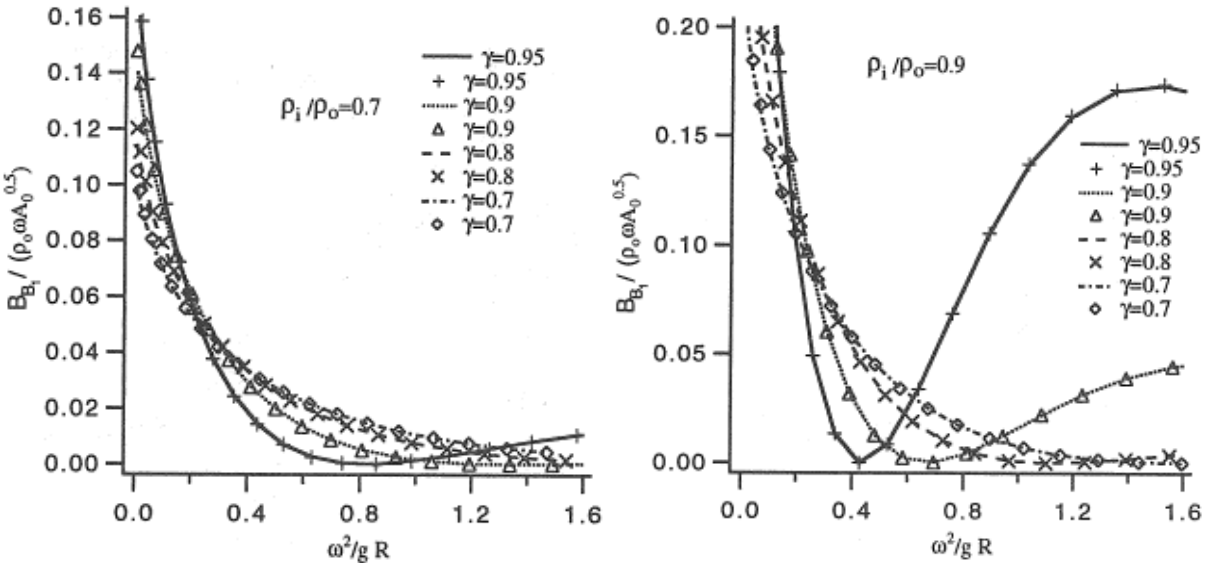

Figure 10.21 *Damping coefficient B_{B1} as function of filling ratio γ and relative density ρ_i/ρ_o*

10.4.3 Numerical results for Membrane responses.

Equation (10.17) – (10.20) is solved by a finite difference method. In general the hydroelastic deformations and tension of the membrane structure depends on many parameters so only some key results are presented in the following.

The case considered was a structure with L=20D, where D is the diameter of the tube when filling ratio $\gamma = 1.0$. The cross sectional shape has been assumed to be constant along the length. In Fig 10.22 the maximum values of heave motion (i.e the result for the cross section giving the maximum response) as function of wave frequency are shown.

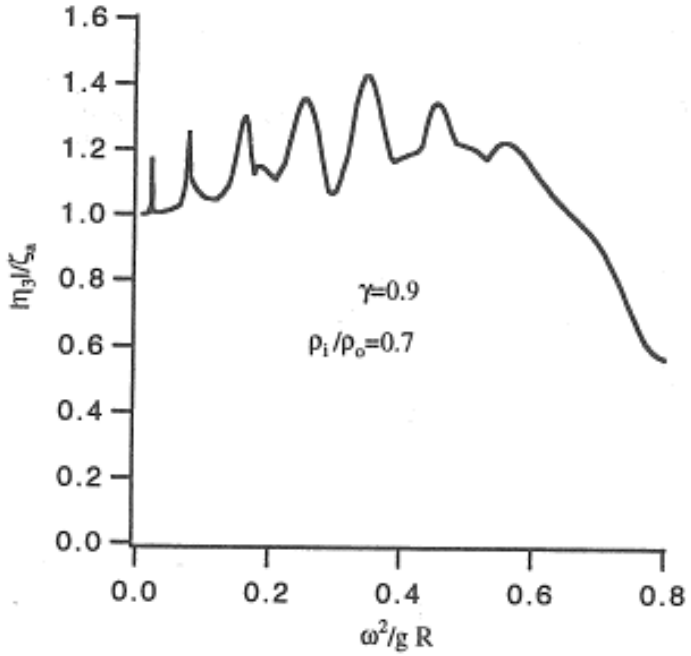

Figure 10.22 *Heave motion for the section which gave maximum response*

In Fig 10.23 and 10.24 the results for maximum dynamic pressure inside the membrane structure, P_1, and the maximum dynamic membrane tension, T_1, are shown as function of wave frequency. For most cases the maximum tension and pressure occurs at the region close to the end points of the tube. The peaks in the results for tension and pressure are due to resonance of the internal surge motion. The two first peaks (i.e low frequencies) can be significantly reduced if viscous damping is introduced for the internal surge motion.

The effect of elasticity (i.e elongation of the fabric) is not included in the present analysis. For practical applications this effect will be important and tend to reduce the peak pressure and membrane tension.

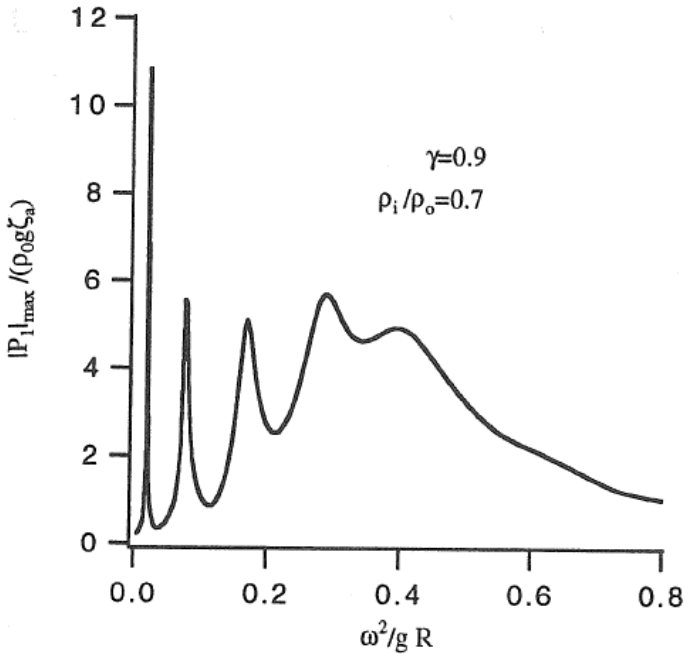

Figure 10.23 *Maximum dynamic pressure inside the membrane structure,* P_1

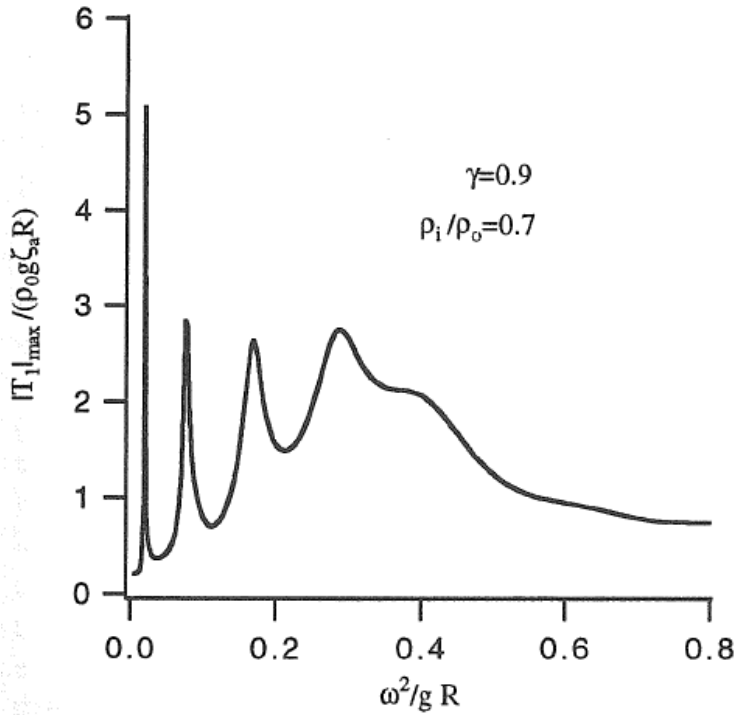

Figure 10.24 *Maximum dynamic Tension in the membrane structure,* T_1

From model test it has been observed that the nonlinear effects are very important for the dynamic membrane tension in waves. This is especially important when the density ρ_i is close to ρ_O which is the case for many practical applications. Fig. 10.6 shows that the intersection between the water line and the membrane structure is not wall-sided and the distance between water line and top of the membrane structure is small. Under normal sea states the vertical motion may be large and the tube can be totally submerged. Position dependency of added mass, hydrostatic forces and excitation force (which is not covered in the present analysis) will therefore be important.

The theory presented above is based on the assumption that dynamic pressure and tension are small compared to the static values. This is not the case for low filling ratios or the relative density ρ_i/ρ_o is close to 1, see Fig. 10.8. In the case that the dynamic tension is larger than the static tension the used approach will break down because the total tension cannot be less than zero. Model test have shown that flexible bag can have large hydroelastic deformations when the incident waves are larger than some limit. Such cases cannot be predicted by the theory.

10.5 Comparison with experiment.

Model tests have been performed with a 3-D membrane structure in the Marintek Towing Tank. The shape of the model is shown in Fig 10.25. Tests were carried out both for beam sea (for verification of 2-D model) and in head sea (for verification of 3-D model). The test results have been compared to numerical calculations, see Zhao and Aarsnes (1998) for details.

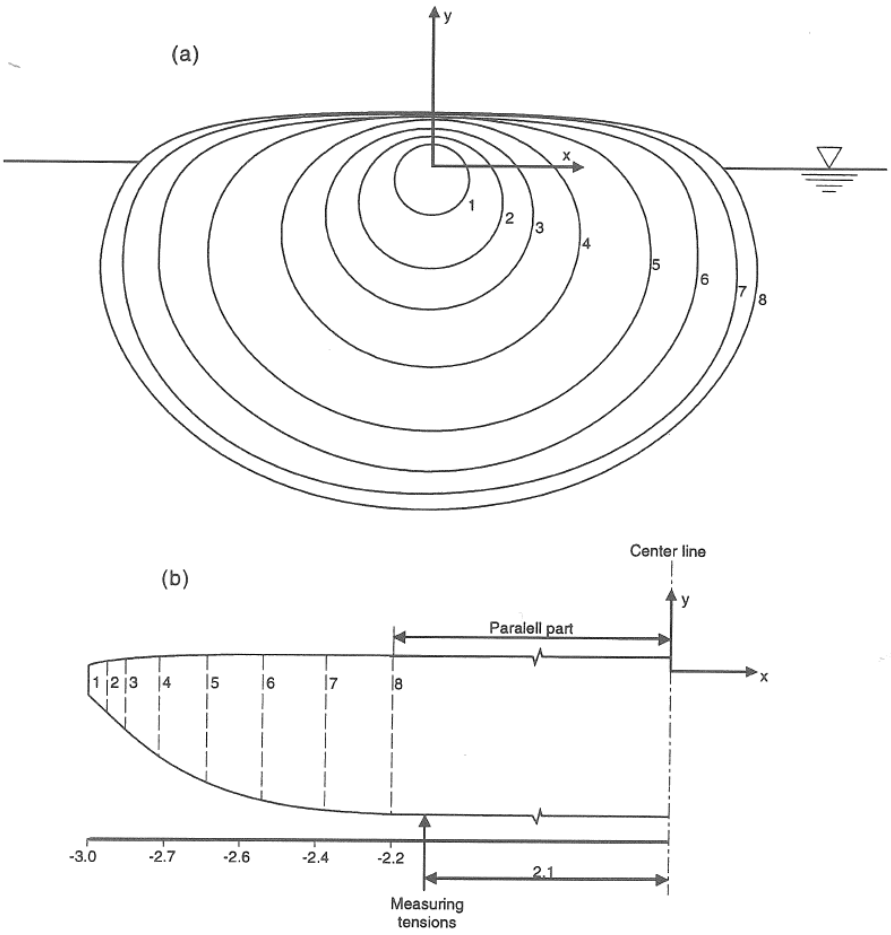

Figure 10.25 *Shape of model and position of measuring the transverse elongation.*

In fig. 10.26 comparison between theoretical and experimental results in beam sea waves are shown. The filling ratio was $\gamma = 0.9$ and relative density $\rho_i / \rho_o = 0.914$. The wave amplitudes were in the range 1-3 % of the diameter. For all tests the wave amplitude was sufficient low to avoid negative tension. Nonlinear effects are therefore believed to be relatively unimportant in these tests, see the discussion above. A reasonable agreement between test results and calculations is achieved.

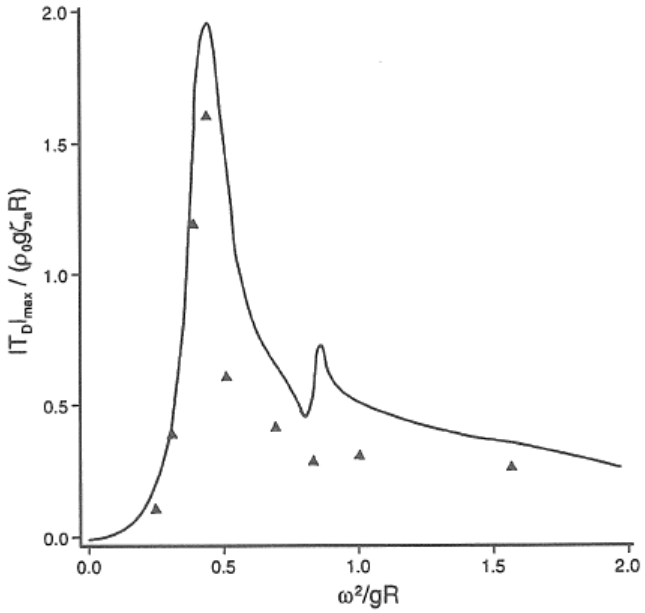

Figure 10.26 *Comparison between theoretical and experimental results for hoop tension in Regular beam sea waves. Full line is from calculations*

In fig. 10.27 the comparison between theoretical and experimental results in head sea waves are shown. The filling ratio was 0.9 and relative density $\rho_i / \rho_o = 0.914$. Also for this case a reasonable agreement between test results and calculations is achieved, but the numerical approach overpredict tension for lower frequencies.

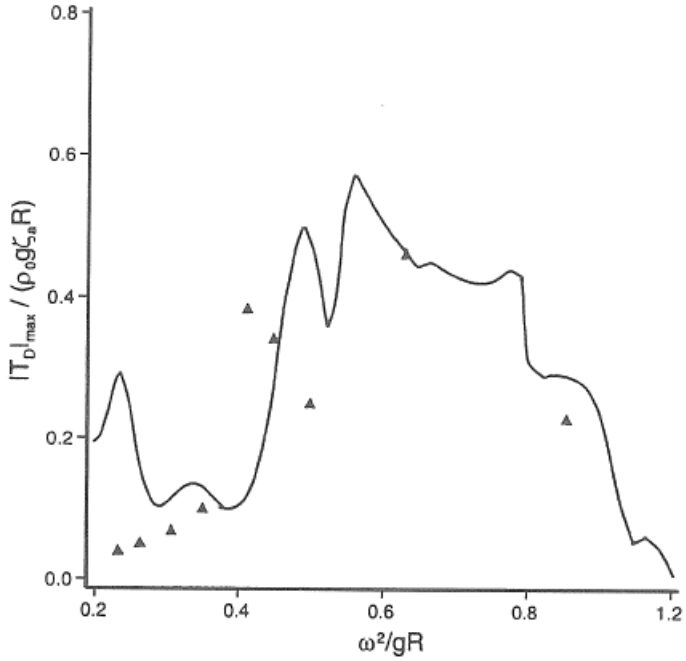

Figure 10.27 *Comparison between theoretical and experimental results for hoop tension in Regular head sea waves. Full line is from calculations*

11 AQUACULTURE STRUCTURES

11.1 Description of Aquaculture structures

The marine fish farms used for aquaculture purpose consist of highly flexible structural components such as fish nets, anchor lines and elastic or hinged floating collar structures in the free surface zone. The mooring lines and the nets are connected to the collar floaters. The installations are exposed to loads from wind, waves and current and due to the dominating elastic behavior of the different components, a hydroelastic approach will be required for analysis.

Categorization of type of cages used for fish farming;

- Gravity nets;
- Net structures enclosed by stiff framework

Gravity nets retain their shape based on gravity connected at the cage bottom. This is the dominant net cage type in use today. The nets are connected to a collar frame floating at the surface. The floating collar may be either built up of a flexible polyethylene rings or built as a hinged steel structure. The mooring lines are connected to the floater.

An example of a hinged steel floater supporting the nets is shown in Fig. 9.1. A typical size of each cage is 25m x 25m. Draft of the nets will be typically 20-30 m with weights connected at the bottom of the nets. Number of cages will be typically 4-10 for each fish farm / location.

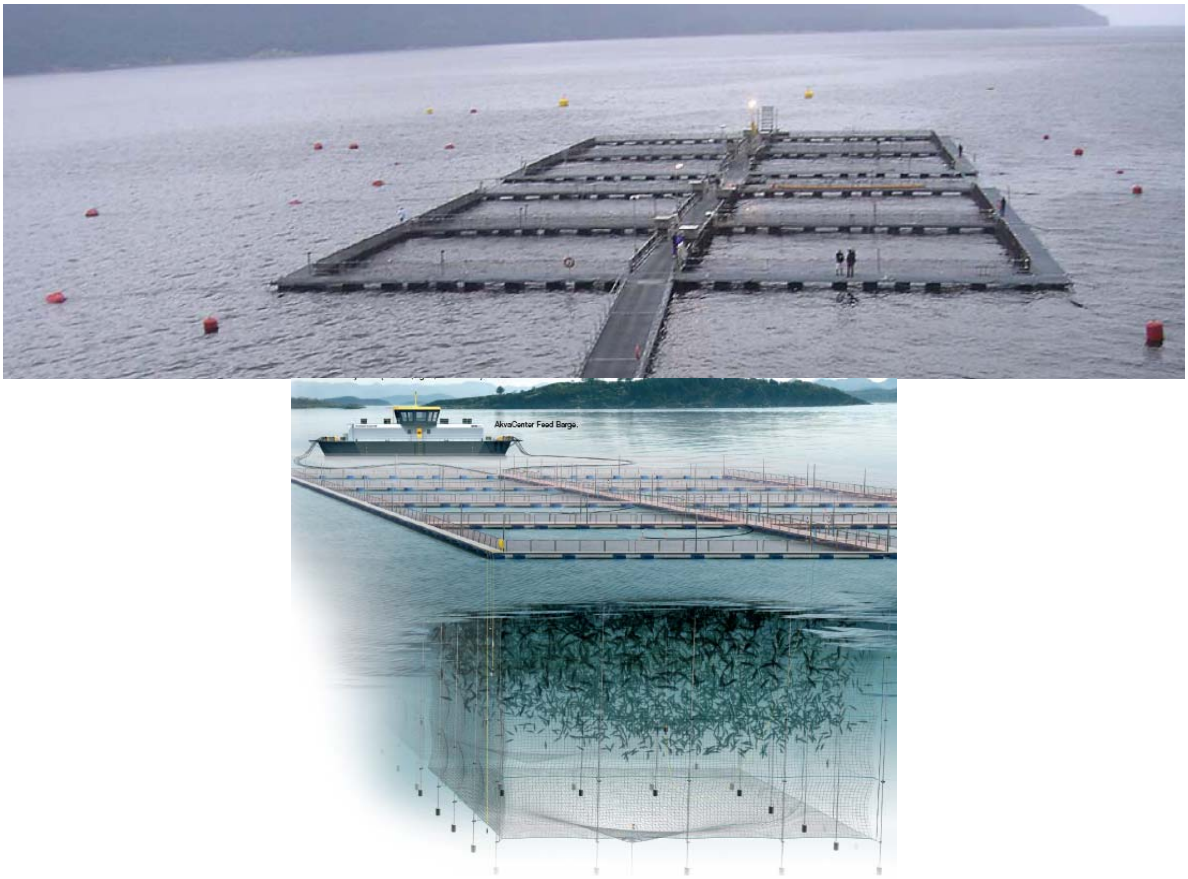

Figure 9.1 *Example of Net pens of gravity type. Hinged steel cages.*

An example of using flexible Polyethylene Rings as floater supporting the nets and mooring system is shown in Fig. 9.2. A typical size of each cage is Diameter D=20-30 m. The weights are connected at the bottom of the nets either as clump weights or an elastic ring with integrated weight for stretching out the net as shown in Fig 9.2.

Figure 9.2 *Example of Net pens of gravity type. Polarcirkel cage with flexible PEH ring as strength element.*

In Fig 9.3 the Form Ocean Cage system intended for exposed locations is shown. The net is kept in position by the stiff sinker tube which again is connected to the stiff top frame.

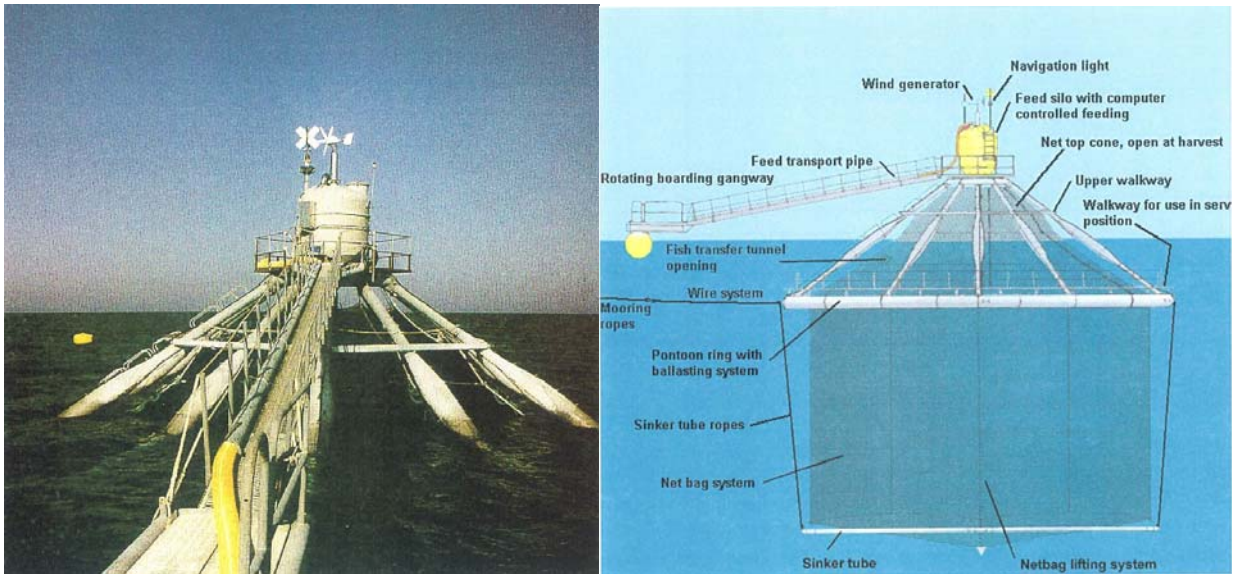

Figure 9.3 *Example of Net pens enclosed by stiff framework. Farmocean Offshore Cage system*

From a hydrodynamic and structural analysis point of view, aquaculture structures as described above are a rather new type of marine structures with special challengers for analysis different from those usually found for offshore structures and ships. The floating part may be a compliant or hinged with very low buoyancy. The cross sectional

dimensions are normally small compared to the wave height, which implies that the structural members can be exposed to large displacements and hence also large changes of submergence during a wave cycle. The mooring system is an integrated part of the structure, and due to the small buoyancy, the effect of vertical mooring forces have to be considered. Also the contributions from horizontal mooring forces may be of the same order of magnitude as the stiffness forces of the floating collar. The total system including effect from the fish net and mooring system, therefore represent a highly complicated structural / hydrodynamic problem. The large structural deformations in waves and current, see Fig. 9.4, implies that a hydroelastic analysis will be required.

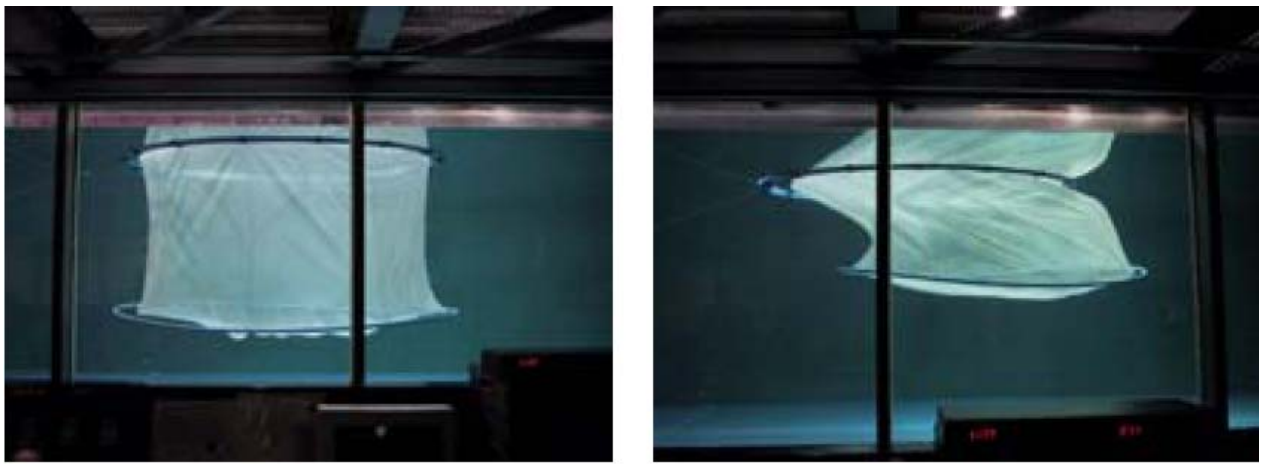

Figure 9.4 *Example of deformation of a Net pen in current.*

11.2 Numerical simulation of response in Wave and Current

As described in the previous section a typical aquaculture plants can be divided into a floater part (stiff or elastic), a net part connected to the floater collar and a mooring system. In the numerical analysis the following force contributions are included;

- Hydrodynamic forces on the nets
- Tension forces in the nets (or net structural forces)
- Hydrodynamic forces on the floater collar
- Mooring forces
- Structural modeling of floater collar

Doe to the highly elastic behavior of the structure and nets it is of fundamental importance that the hydrodynamic forces are established at the actual position of the different structural elements in each time step. This imply that the numerical analysis has to be carried out in the time domain.

11.2.1 Hydrodynamic forces on Nets

The nets are assumed modeled by single elements and nodes as shown in Fig. 9.5. The elements are four sided with a node in each corner. A mass and a weight (gravity) are associated with each node. The nodes can be either free, fixed or have their motion prescribed (from the structural interface towards the top frame).

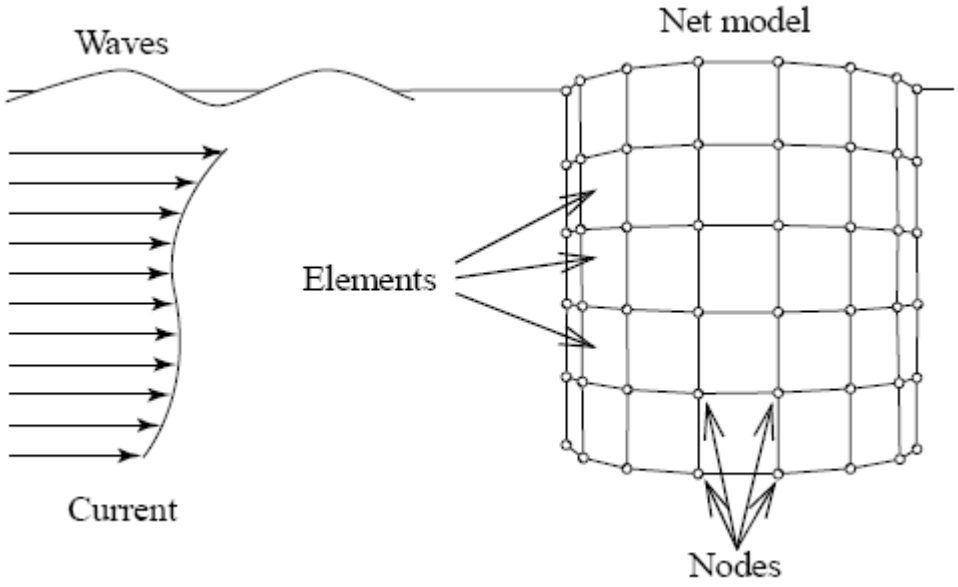

Figure 9.5 *Overview of the net model*

The hydrodynamic forces for each net element is divided into drag and lift forces, $\mathbf{F}_D^N$ and $\mathbf{F}_L^N$ respectively. The forces on each net element is given from;

$$\mathbf{F}_D^N = \frac{1}{2}\rho C_D A|\mathbf{U}|^2 \mathbf{n}_\mathbf{D} \tag{9.1}$$

$$\mathbf{F}_L^N = \frac{1}{2}\rho C_L A|\mathbf{U}|^2 \mathbf{n}_L \tag{9.2}$$

where C_D and C_L are the drag and lift coefficients respectively, A is the element area, $\mathbf{U}$ is the relative velocity vector between the fluid and the net element while $\mathbf{n}_D$ and $\mathbf{n}_L$ are the unit vectors of the net element in direction of the drag and lift forces respectively. The Drag forces is parallel to the flow while the lift force is perpendicular to the flow direction. It is assumed that $\mathbf{U}$ is constant over the whole area of the element and that the velocity is evaluated in the element centre;

$$\mathbf{U} = \mathbf{U}_W + \mathbf{U}_C - \mathbf{U}_S \tag{9.3}$$

where $\mathbf{U}_W$ is the wave particle velocity, $\mathbf{U}_C$ is current velocity and $\mathbf{U}_S$ is the structural velocity of the element. The wave particle velocity is calculated from the incident wave kinematics (linear theory or a higher order wave theory may be applied). The wave and current velocity is assumed to be undisturbed by the net structure, which imply that shielding is not taken into account.

The unit vector for drag and lift are given from the following relations;

$$\mathbf{n}_D = \frac{\mathbf{U}}{|\mathbf{U}|} \tag{9.4}$$

$$\mathbf{n}_L = \frac{(\mathbf{U}\times\mathbf{n}_e)\times\mathbf{U}}{|(\mathbf{U}\times\mathbf{n}_e)\times\mathbf{U}|} \tag{9.5}$$

where $\mathbf{n}_e$ is the unit normal vector of the net element, positive in the flow direction. This vector is found by taking the cross products of two unit vectors parallel to the diagonals of the element, see Fig 9.6:

$$\mathbf{n}_e = \frac{\mathbf{n}_{13} \times \mathbf{n}_{24}}{\left|\mathbf{n}_{13} \times \mathbf{n}_{24}\right|} \tag{9.6}$$

where

$$\mathbf{n}_{13} = \frac{\mathbf{x}_1 - \mathbf{x}_3}{\left|\mathbf{x}_1 - \mathbf{x}_3\right|}$$

$$\mathbf{n}_{24} = \frac{\mathbf{x}_2 - \mathbf{x}_4}{\left|\mathbf{x}_2 - \mathbf{x}_4\right|}$$

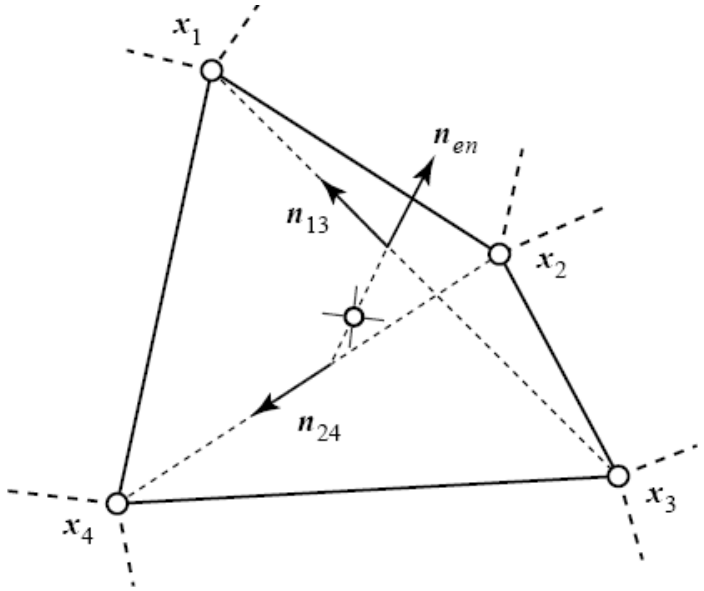

Figure 9.6 *Definition of element normal vector* $\mathbf{n}_e$

The drag and lift coefficients can for a net structure be calculated from the following empirical formulas, see Aarsnes et. al (1990);

$$C_D = 0.04 + (-0.04 + S_n - 1.24{S_n}^2 + 13.7{S_n}^3)\cos\alpha \tag{9.7}$$

$$C_L = (0.57S_n + 3.54{S_n}^2 + 10.1{S_n}^3)\sin 2\alpha \tag{9.8}$$

where S_n is the solidity of the net defined as the ratio between the area covered by the twins of the net A_n (i.e the solid area), and the total area enclosed by the net, A;

$$S_n = \frac{A_n}{A} = \frac{2t}{d}. \tag{9.9}$$

where *t* is the diameter of the thread and *d* is the mesh size.

α is the angle of attack and is defined as the angle between the direction of $\mathbf{U}$ and the normal vector of the net element as shown in Fig 9.7.

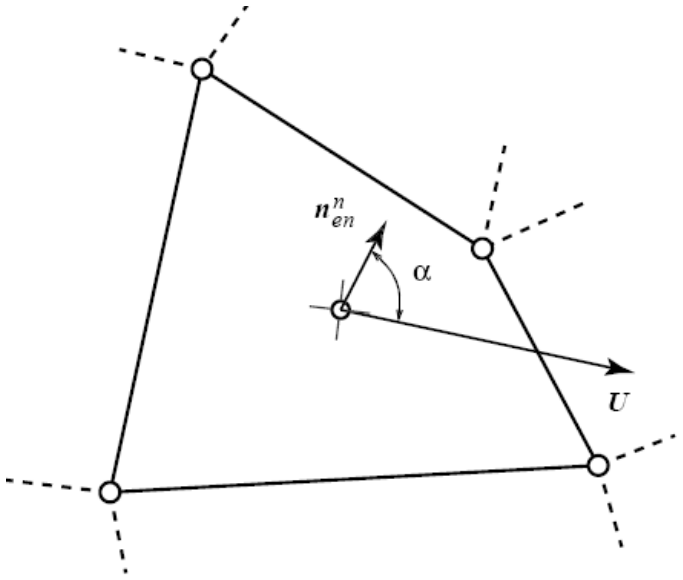

Figure 9.7 *Definition of angle of attack* α

The element area is not constant, but varies with the deformation of the element. Consequently the solidity ratio, S_n, will also varies accordingly since the solid area A_n is constant. The effective solidity must therefore be corrected to account for the change of element area as follows;

$$S_n = S_{n,0} \frac{A_0}{A} \tag{9.10}$$

where $S_{n,0}$ and A_0 are the solidity ratio and element area corresponding to un-deformed net element.

The hydrodynamic force acting on each element is distributed equally to each element node, where the equation of motion is solved.

11.2.2 Hydrodynamic forces on the floater collar

The floater collar is for simplicity represented by a tube in the numerical model. The tube is divided into a number of elements. In waves, part of the collar may be in the surface, totally submerged or totally out of water. It is therefore required that the hydrodynamic forces are calculated in the instantaneous position of the element, taking into account both the position of the element and the wave elevation at the actual position. It is important that the collar elements are sufficient small to have reasonable equal submergence over the element length. A more detailed description of this topic is given by Ormberg (1991) and Huang et.al. (2006)

The hydrodynamic load model is based on two-dimensional strip theory, which requires the structural elements to be long and slender. The load normal to the element consist of;

- wave excitation forces
- Wave impact forces
- added mass and damping forces
- Viscous drag forces

Each of these contributions is discussed in the following.

The drag forces acting on a tube elements is illustrated in Fig. 9.8.

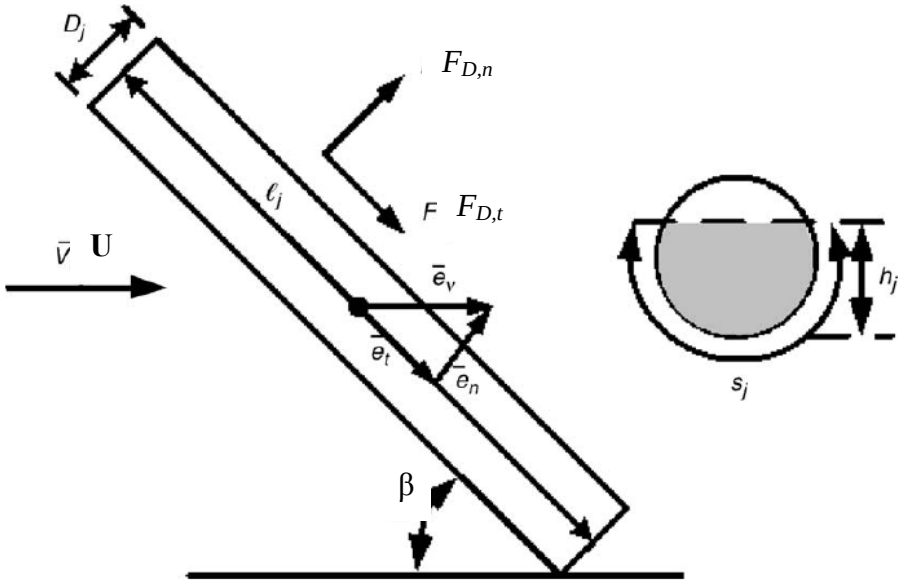

Figure 9.8 *Illustration of hydrodynamic forces acting on a floater collar element, top view (left) and side view (right).*

The drag forces are calculated assuming the cross flow principle from the following equation;

$$\mathbf{F}_{D,n}^{C} = \frac{1}{2}\rho C_{DC} h_j l_j \left|\mathbf{U}\sin\beta\right|^2 \cdot \mathbf{e}_n \tag{9.11}$$

where now C_{DC} is the drag coefficient of the collar element, h_j and l_j are the submerged draft and the length of the collar element, $\mathbf{U}$ is now the relative velocity vector between the fluid and the collar element while $\mathbf{e}_n$ and $\mathbf{e}_t$ are the unit vectors normal to and along the collar element axis as shown in Fig 9.8. β is the angle of attack and is defined as the angle between the direction of $\mathbf{U}$ and the collar element axis as shown in Fig 9.10. The force is assumed to attack in the center of the submerged part of the collar element.

The tangential skin friction forces shown as $\mathbf{F}_{D,t}$ will by much smaller than the cross flow drag and is neglected.

The wave induced excitation force includes the Froude Kriloff and the diffraction forces as well as the buoyancy forces. This force contribution can be calculated from;

$$\mathbf{F}_{E}^{C} = \rho A_j l_j \left[(1 + C_M) \frac{\partial \mathbf{U}_W}{\partial t} + g\mathbf{e}_g \right] \tag{9.12}$$

where C_M is the added mass coefficient for the collar element (for simplicity assumed to be independent of submergence of the element), A_j is the submerged cross sectional

area of the collar element which means that $A_j l_j$ is the instantaneous submerged volume of the element *j*. $\partial \mathbf{U}_W / \partial t$ is the wave particle acceleration. $\mathbf{e}_g$ is unit vector for gravity. The first term represent the wave excitation force. The second term is the buoyancy force.

The vertical wave impact forces are calculated using the momentum approach;

$$\mathbf{F}_{\mathrm{Im}\,p}^{C} = \rho A_j l_j \frac{\partial C_M}{\partial z} U_Z^2 \mathbf{e}_\mathbf{g}$$

where U_Z is the relative vertical velocity. For small volume structure this contribution is relatively unimportant for most cases.

The added mass force contribution can be calculated from;

$$\mathbf{F}_A^C = -\rho A_j l_j C_M \frac{\partial^2 \mathbf{x}}{\partial t^2} \tag{9.13}$$

where $\partial^2 \mathbf{x} / \partial t^2$ is the acceleration vector of the element. Note that the potential damping term has been neglected in this deviation (will be small for this type of small volume structure).

11.2.3 Structural modelling of floating collar.

The structural modelling of the floating collar is done by f.e.m. The model needs to be able to handle hinged structures as well as highly elastic components. Large deflection of the structure may occur and a non-linear model should therefore be applied. Application of non-linear f.e.m. models is given by Ormberg (1991) based on using Riflex and by Berstad et. al. (2004).

11.2.4 Mooring Forces

The mooring forces are usually assumed to be represented by linear springs connected to the floater collar. The forces can then be calculated as

$$\mathbf{F}_M^C = \mathbf{k}_M \mathbf{x} \tag{9.14}$$

where $\mathbf{k}_M$ is the quasi static stiffness matrix for the mooring system.

Alternatively the mooring lines can be modeled as submerged collar elements in the f.e.m model with given geometry, weight, buoyancy and axial elasticity properties.

11.2.5 Equation of motion – Time integration

The strongly nonlinear behavior both for hydrodynamic loads and in structural responses needs to be covered by the analysis. Using a nonlinear f.e.m. code for solution of the coupled floating collar / net panels / mooring line system, a large number of elements will be required to give a realistic representation of the this complex structural behavior. Due to the strong coupling effects, the entire Fish farming plant needs to be described by one model. The analysis will hence be quite time consuming (both in terms of modeling time and computer time).

The basic idea of the f.e.m. analysis solution is to establish equilibrium between the total external loads, $\mathbf{R}_{ext}$, acting on the structure at a given time instant (forces established in actual position) and the total internal reaction forces, $\mathbf{R}_{\text{int}}$, i.e;

$$\sum \mathbf{F} = \mathbf{R}_{ext} + \mathbf{R}_{\text{int}} = 0 \tag{9.15}$$

In order to establish equilibrium, the tangential stiffness method is be used. External loads are incremented to find the state of equilibrium. Having established equilibrium in time step *i-1*, the conditions for step *i*, is predicted as;

$$\Delta\mathbf{R}^{i}(\mathbf{r}_{\mathbf{i-1}}) = \mathbf{R}^{i}_{ext}(\mathbf{r}_{\mathbf{i-1}}) + \mathbf{R}^{i-1}_{\text{int}}(\mathbf{r}_{\mathbf{i-1}}) = \mathbf{K}^{i-1}_{t}\Delta\mathbf{r} \tag{9.16}$$

where $\Delta\mathbf{K}^{i-1}_{t}$ is the tangential stiffness matrix at configuration *i-1.* The eternal loads are calculated based on the configuration of the structure at *t-1*. This gives a prediction of a new set of displacements (j=1). Based on eq. (9.16), a prediction for the total displacement $\bar{\mathbf{r}}_{j=\mathbf{1}}$, is found as;

$$\bar{\mathbf{r}}_{j=\mathbf{1}} = \mathbf{r}_{\mathbf{i-1}} + \Delta\mathbf{r} \tag{9.17}$$

Based on this estimate for new displacement, both external and internal forces are derived based on new structural geometry, and the residual force is put into the equation of equilibrium as follows;

$$\Delta\mathbf{R}^{i}(\bar{\mathbf{r}}_{j}) = \mathbf{R}^{i}_{ext}(\bar{\mathbf{r}}_{j}) + \mathbf{R}^{i}_{\text{int}}(\bar{\mathbf{r}}_{j}) = \mathbf{K}^{i}_{t}\Delta\mathbf{r} \tag{9.18}$$

Note that both the external and internal forces will vary for each iteration, *j,* due to the strongly hydroelastic and position dependent nature of the fluid structure interaction.

Equation (9.18) is solved for the displacement $\Delta\mathbf{r}$. Incrementing *j* with one the total displacement is now updated as;

$$\bar{\mathbf{r}}_{j} = \bar{\mathbf{r}}_{j-\mathbf{1}} + \Delta\mathbf{r} \tag{9.19}$$

Now if $\Delta\mathbf{r}$ found from equation (9.19) is larger than the tolerated error in the displacements, equation (9.17) is updated *(j=j+1)* and eq. (9.18) is solved based on the new prediction for displacement. This iteration process is repeated until $\Delta\mathbf{r}$ is smaller than a tolerated error, then;

$$\mathbf{r}_{i} = \mathbf{r}_{j} \tag{9.20}$$

i is increased with one and eq. (9.17) is carried out for the new load increment. The Newmark-Beta scheme is frequently used for the dynamic time domain integration.

11.2.6 Approach time integration of net structure dynamic

A simple numerical model for calculation of response of a flexible netting panel is described in the following. The method is based on known top point motions of the net panel (fixed or with prescribed motions). The method is described in more detail by Lader at al (2003) and Lader and Enerhaug (2006).

The net is assumed modeled by single elements and nodes as shown in Fig. 9.5. The hydrodynamic forces acting on the nets structure are given by eq. (9.1) and (9.2) above.

The twines of a flexible net are subjected to an elasticity effect when the external forces are applied. The structural modeling of the net elements is shown in Fig 9.8. Each node is assumed connected to the other nodes through a non-linear spring. Each spring is assumed to have the following force –elongation relationship;

$$F_S = C_2\varepsilon^2 + C_1\varepsilon \qquad \text{for} \quad \varepsilon \geq 0 \tag{9.21}$$
$$F_S = 0 \qquad \text{for} \quad \varepsilon < 0$$

where F_S is the structural force and ε is the global elongation. The global elongation is given by $\varepsilon = (l - l_0)/l_0$ where l_0 is the un-deformed length and l is deformed length of the panel. C_1 and C_2 are constants describing the stiffness characteristics of each spring. For each element there is 6 springs which gives a total of 12 force contributions, 3 in each node as shown in Fig. 9.9.

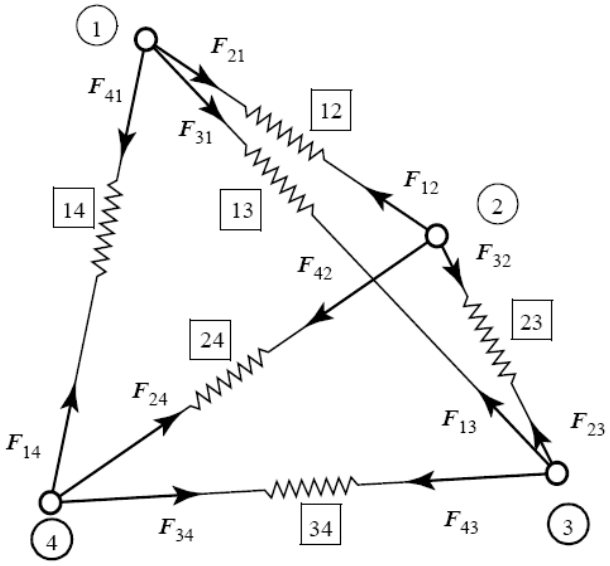

Figure 9.9 *Structural modeling of net elements. Node numbers are given in circles and spring number in squares.*

The force in the spring between node *n* and *m*, $\mathbf{F}_{S,nm}$ is now calculated using eq. (9.21) as follow;

$$\mathbf{F}^N_{S,nm} = (C_2\varepsilon_{nm}{}^2 + C_1\varepsilon_{nm})\mathbf{n}_{nm} \qquad \text{for} \quad \varepsilon \geq 0 \tag{9.22}$$
$$\mathbf{F}^N_{S,nm} = 0 \qquad \text{for} \quad \varepsilon < 0$$

where and ε_{nm} is the elongation given by;

$$\varepsilon_{nm} = \frac{l_{nm} - l_{0nm}}{l_{0nm}} = \frac{\left|\mathbf{x}_n - \mathbf{x}_m\right| - \left|\mathbf{x}_{0n} - \mathbf{x}_{0m}\right|}{\left|\mathbf{x}_{0n} - \mathbf{x}_{0m}\right|} \tag{9.23}$$

and $\mathbf{n}_{nm}$ is the unit directional vector for the force given by;

$$\mathbf{n}_{nm} = \frac{\mathbf{x}_n - \mathbf{x}_m}{\left|\mathbf{x}_n - \mathbf{x}_m\right|} \tag{9.24}$$

The total net system is divided into elements which are exposed to external forces as outlined above. The forces are distributed to the nodes to form a system of equation of motions. The hydrodynamic and structural forces are calculated in each element and the forces are then distributed to each node. The equation of motion is evaluated for the nodes. For one node surrounded by the four elements e_1 , e_2 , e_3 and e_4 the total structural and hydrodynamic forces from the nets in the node, see Fig. 9.10 for details, is given by;

$$\mathbf{F}_{Struct} = \mathbf{F}_{13}^{e1} + \mathbf{F}_{23}^{e1} + \mathbf{F}_{43}^{e1} + \mathbf{F}_{14}^{e2} + \mathbf{F}_{24}^{e2} + \mathbf{F}_{34}^{e2} + \mathbf{F}_{21}^{e3} + \mathbf{F}_{31}^{e3} + \mathbf{F}_{41}^{e3} + \mathbf{F}_{12}^{e4} + \mathbf{F}_{32}^{e4} + \mathbf{F}_{42}^{e4} \qquad (9.25)$$

$$\mathbf{F}_{Hyd} = \frac{1}{4}(\mathbf{F}_L^{e1} + \mathbf{F}_D^{e1} + \mathbf{F}_L^{e2} + \mathbf{F}_D^{e2} + \mathbf{F}_L^{e3} + \mathbf{F}_D^{e3} + \mathbf{F}_L^{e4} + \mathbf{F}_D^{e4}) \qquad (9.26)$$

The equation of motion, $\mathbf{F} = m\mathbf{a}$, are then evaluated in each node as;

$$\mathbf{F}_{Struct} + \mathbf{F}_{Hyd} + wg\mathbf{n}_g = m\mathbf{a} \qquad (9.27)$$

where w and m is the weight and mass respectively associated with the node, $\mathbf{n}_g$ is gravity unit vector [0, 0, -1], and $\mathbf{a}$ is the acceleration vector associated with the node.

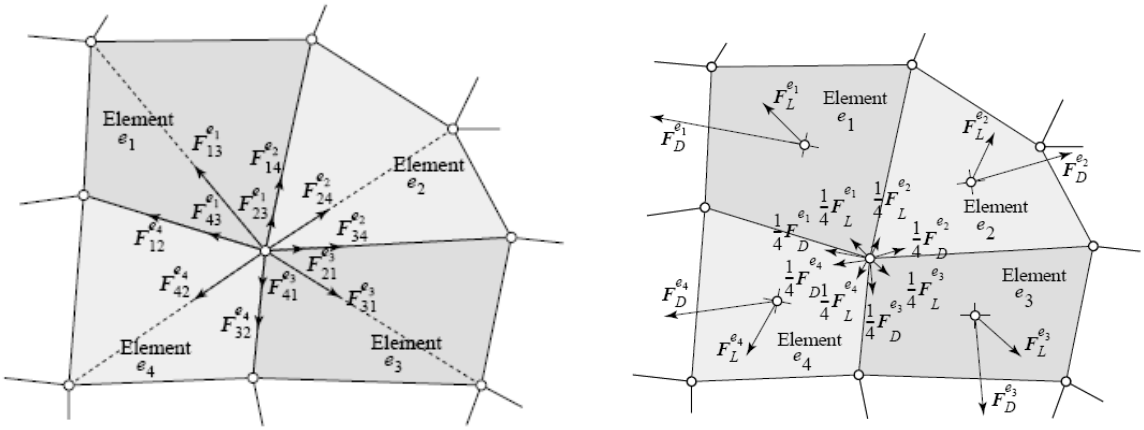

Figure 9.10 *Structural forces in one node (Left). Hydrodynamic forces in one node (Right)*

The acceleration of each element is found from the equation of motion, eq. (9.27). To calculate the movement of the node, the acceleration is integrated twice, i.e;

$$x = \int u \cdot dt = \int (\int a_x \cdot dt) dt \qquad (9.28)$$

A 4th order Runge-Kutta method can be used for the for the numerical integration solution of eq. (9.27).

11.3 Comparison with Model Test results

Two cases are considered, a net cage with fixed top frame in steady current and an elastic PEH cage with net exposed to waves and current.

11.3.1 Net cage in uniform Current

Model tests with a circular net in steady current have been carried out by Lader and Enerhaug (2005), see also Lader et.al. (2003). The Test set up is shown in Fig 9.11. Different size weights were attached to the bottom of the net. The tests were carried out in a flume tank. The deformation of the nets and the total drag and lift forces were measured. The netting is knotless with a mesh size of *d=32* mm and twine thickness of *t=1.8* mm. This gives a solidity ratio, $S_n = 0.225$.

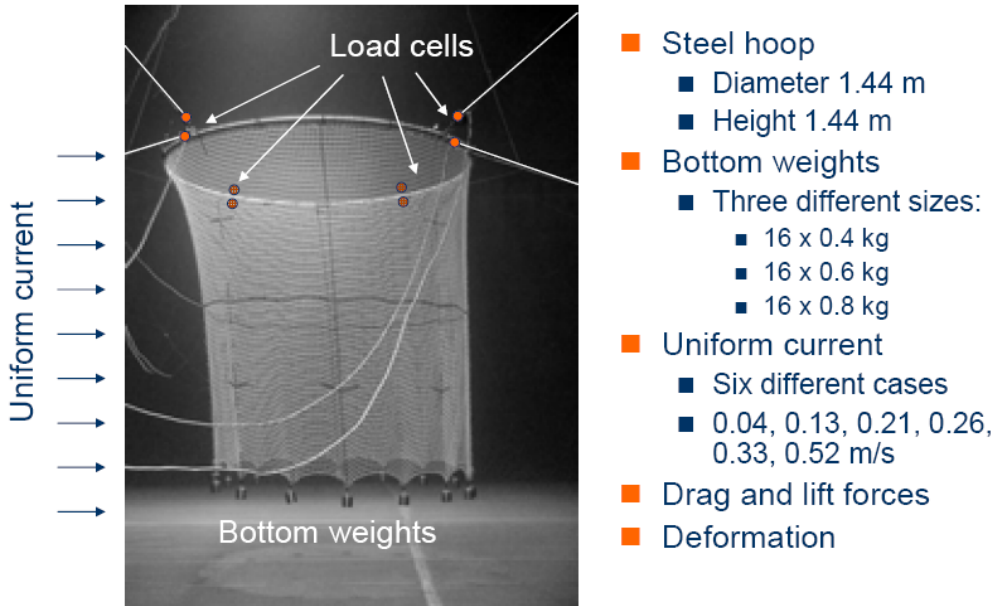

Figure 9.11 *Model tests with net cylinder in steady current. Test set up and test condition.*

In fig 9.12 measured and calculated deformation of the net structure are shown for the 5 different current speeds U=0.13 m/s - 0.52 m/s. Bottom weights equal to 16*0.4 kg were used. It is seen from the figure that the net deformation is reasonable well reproduced by the numerical model.

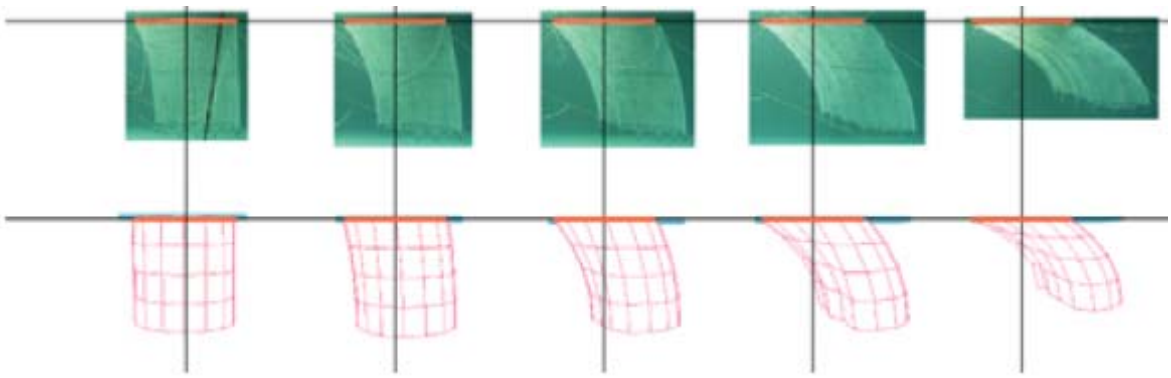

Figure 9.12 *Deformation of Net pen in current. U=0.13m/s, 0.21m/s, 0.26 m/s, 0.33m/s and 0.52 m/s. Top view; measured in tests. Bottom view; Simulated shape*

In Fig. 9.13 examples of measured time history for drag forces are shown for different current speed. The figure (left view) shows the development of drag force during the transient start-up phase of the flow to a steady state condition is reached. This phase is used for validation of the numerical model and it is seen that the agreement is good except for the lowest speed where the numerical model underestimate then drag force. In the same figure (right view) the steady state drag force is shown for the different cases tested. Both measured and simulated results are shown. For the velocity range 0.2-0.4 m/s good agreement is found, while for higher current speed the numerical simulations overpredict the drag force.

The deviations found for the lowest and highest current speed were explained by Reynolds number dependency of the drag coefficient. As can be seen from eq. (9.8) the drag coefficient was assumed to be independent of Reynolds number, but the above results shows that this may not be the case.

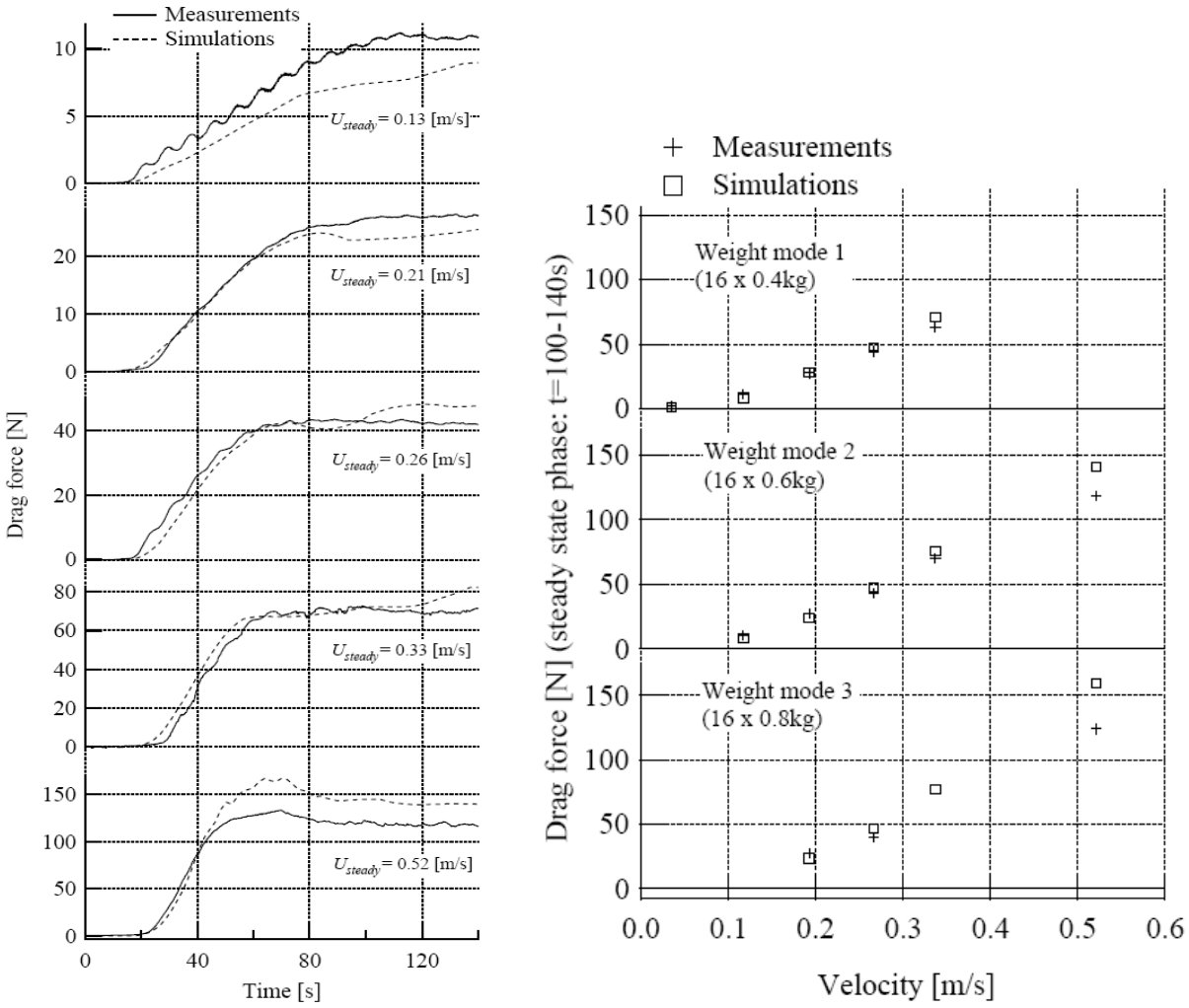

Figure 9.13 *Comparison between calculated and measured drag forces.*
*Left; Time histories for drag force for different velocities for weight 16*0.6kg*
Right; Steady state drag force as function of current speed for the different weight cases.

11.3.2 Flexible PEH cage with net in wave and current.

Model test with a flexible PEH Cage with net, see Fig. 9.2, in waves and current have been carried out. The tests were carried out in the Ocean Basin at MARINTEK. A description of the tests and comparison with nonlinear numerical simulations have been presented by Ormberg and Slaattelid (1993) and Ormberg (1991).

In the model tests the floating, flexible PEH collar, the nets and the mooring system were modeled based on correctly scaled stiffness and geometry of the floating collar as well as solidity ratio for the nets. The full scale dimensions of the cage were Diameter, D=22.3m and depths of nets equal to draft=20 m. The measurements included tension in mooring lines, bending moment in floating collar at 4 positions and displacement at different positions around the collar. The tests were carried out in current and in combine current and regular waves. The numerical simulations were carried out using a version of the non-linear f.e.m. program RIFLEX developed to handle elements in the free surface zone and net elements, see Ormberg (1991) for details. The wave force model used for collar and nets were as outlined above.

In Fig 9.14 the measured and calculated response of the floating collar in current are shown. The top view shows the bending moment around the collar including the measured bending moment in the 4 positions used. The lower view shows the shape and offset of the collar. For the bending moment the agreement is seen to be very good between calculated and measured results. For the shape also reasonable agreement is obtained when taking into account the nonlinear behavior and the large deformations observed.

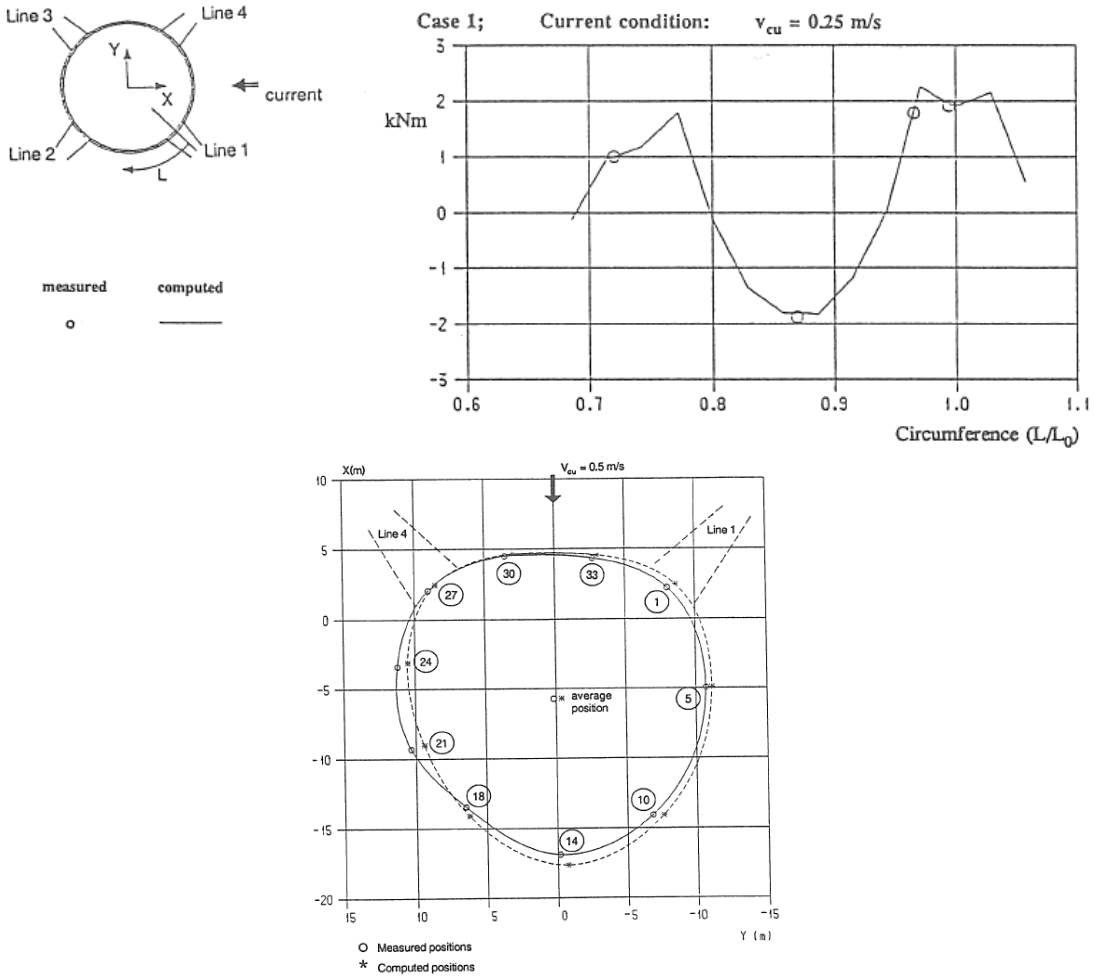

Figure 9.14 *Comparison between calculated and measured response of floating collar in current. Current velocity 0.5 m/. Top view; bending moment in floating collar. Bottom view; shape and offset of floating collar*

In Fig. 9.15 the comparison of bending moment in the floating collar in combined current and regular waves is shown. In the figure the mean value as well as maximum and minimum bending moment values are shown as function of position along the circumference of the collar. Some small deviations between computed and experimental results can be found, but taking into account all uncertainties involved, it can be concluded that the overall agreement is satisfactory.

Both the applied hydrodynamic load models for net / collar and the structural formulation will therefore give a realistic prediction of the behavior of an elastic cage system with nets in wave and current.

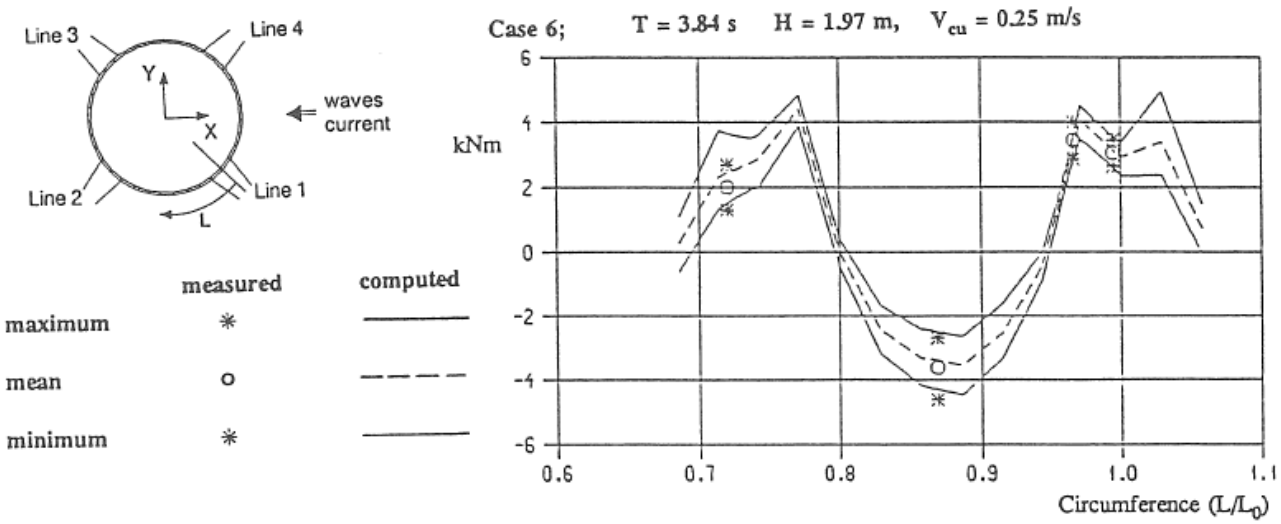

Figure 9.15 *Comparison between calculated and measured shape and offset of floating collar in current. Current velocity 0.5 m/s*

12 REFERENCES

Aarsnes, J.V. (1994). "An experimental investigation of the effect of structural elasticity on slamming loads and structural response", MARINTEK report MT60 A95-0053.

Aarsnes, J.V, Løland, G and Rudi, H. (1990). "Current Forces on Cage, Net deflection", in Engineering for Offshore Fish Farming, Glasgow, U.K., pp 137-152

Berstad, A. J., Trodstad, H. and Ytterland, A. (2004). "Calculation of the structural response of such flexible structures to verify structural integrity". Proc. OMAE, Vancouver, Canada

Campbell, I.M.C. and Weynberg, P.A. (1980). "Measurement of parameters affecting slamming". Report No 440, Technology Report Center No OT-R-8042, Southampton University.

Clough, R.W and Penzien, J. (1975). "Dynamic of Structures". McGaw-Hill. ISBN 0-07-011392-0

Drummen, I., Wu, M.K., and Moan, T. (2008). "Experimental and Numerical study of containership response in severe head seas", Submitted to Elsevier

Drummen, I., Moan, T., Storhaug, G. and Moe, E. (2006). "Experimental and Full scale investigation of the importance of fatigue damage due to wave induced vibration stress in a container vessel", Design and Operation of Container Ships. RINA, London UK.

Drummen, I. (2008). "Experimental and Numerical investigation of Nonlinear Wave Induced load effects in Container Ships considering Hydroelasticity", Phd thesis, NTNU, Trondheim

Faltinsen, O.M. (1990). "Sea Loads of Ships and Offshore Stryctures, Cambridge, Cambridge University Press.

Faltinsen, O.M and Zhao, R. (1991). "Numerical predictions of Ship Motions at High Forward Speed", Phil. Trans. R. Soc. Lond. A 334, pp 241-252.

Faltinsen, O.M. (1997). "The effect of Hydroelasticity on slamming", Phil Trans R Soc London, Ser. A 355: 575-591

Faltinsen, O.M. (1999). "Water entry of a wedge by hydroelastic orthotropic plate theory", J. Ship Res. 43, pp 180-193.

Faltinsen, O.M. (2000). "Hydroelastic Slamming", Journal of Marine Science and Technology, Vol 5, pp 49-65.

Faltinsen, O.M, Kvålsvold, J and Aarsnes J.V. (1997). " Wave Impact on a horizontal elastic plate", Journal of Marine Science and Technology, Vol 2. pp 87-100.

Fu, S., Moan, T., Chen, X. and Cui, W. (2006). **"**Hydroelastic analysis of flexible floating interconnected structures". 4th International Conference on Hydroelasticity in Marine Technology, Shanghai, 2006.

Greco, M., Colicchio, G. and Faltinsen, O. M. " Local and Global Hydroelastic Analysis of a VLFS". 4th International Conference on Hydroelasticity in Marine Technology, Shanghai, 2006.

Greenhow, M and Lin, ".M. (1983). " Non-linear free surface effects: experiments and theory. Report No83-19. Dept. Ocean Engineering, Cambridge Mass: Mass. Inst. Technology.

Hawthorne, W.R. (1961). "The early development of the Dracone Flexible Barge". Proceedings of the institution of Mechanical Engineers, 175, pp 52-83

Haugen, E. M. (1997). "Slamming on Wetdecks. Phd thesis, NTNU, Trondheim

Hermundstad, O.A, Aarsnes, J.V. and Moan, T. (1995), "Hydroelastic Analysis of a Flexible Catamaran and Comparison with Experiments", FAST '95, Lybeck, Germany, Vol I, pp 487-500

Hermundstad, O.A, Aarsnes, J.V. and Moan, T. (1995), "Linear Hydroelastic Analysis of High-Speed Catamaran and Monohulls", Journal of Ship Research. Vol 43. pp 48-63.

Hermundstad, O.A, and Moan, T. (2005), "Numerical and Experimental analysis of bow flare slamming on ro-ro vessel in regular oblique waves". Journal of Marine Science and Technology. 10: 105-122

Huang, C.C and Tang, H.J. and Liu, J.Y. (2006). " Dynamical analysis of net cage structures for marine aquaculture: Numerical simulation and model testing". Aquaculture Engineering.

Jeffferys, E.R. and Rainey, R.C.T (1994), "Slender Body Models of TLP and GBS Ringing", Pros. BOSS'94, pp 587-605

Lee, C.H. and Newman, J.N. (2000), "An Assessment of Hydroelasticity for very large hinged vessels". Journal of Fluid and Structure, Vol 14, pp957-970.

Leonard, J.W. (1988). "Tension Structures", McGraw-Hill Book Company. ISBN 0 07 037226 8 E. N.

Lader, P.F., Enerhaug, B. et.al. (2003). "Modelling of 3D net structures exposed to waves and current". Proc. 3rd int. conf. Hydroelasticity in Marin Technology, Oxford, UK.

Lader, P.F and Fredheim, A. (2006). "Dynamic properties of a flexible net sheet in waves and Current – A numerical Approach", Aquaculture Engineering, 35, pp 228-238

Løland, G and Aarsnes, J.V. (1994). "Fabric as construction material for marine applications.". Proceedings of International Conference on Hydroelasticity in Marine Technology. Pp 275-286. Trondheim, Norway.

Kvålsvold, J (1994). " Hydroelastic modeling of wetdeck slamming on multihull vessels. Phd thesis, NTNU, Trondheim.

Kvålsvold, J and Faltinsen, O.M. (1995). "Hydroelastic modeling of wetdeck slamming on multihull vessels". J. Ship Res. 39: 225-239.

Kvålsvold, J, Faltinsen, O.M. and Aarsnes, J.V. (1995). "Effect of structural elasticity on slamming against wetdeck of Multihull vessels". In 6th Int. Symp. On the Practical Design of Ships and Mobile Units (PRADS), Seoul, South Korea pp 1684-1699.

Maeda, H. (1991). "Modelling techniques for dynamic of ships", Phil. Trans R. Soc. London, Vol 334, pp 339-355.

Miyamoto, T and Tanizawa K. (1985). "A study of the impact on ship bow". J. Soc. Naval Arch. Japan, 158, pp 270-279.

Newman, N. (1977). ”Marine Hydrodynamics”. The MIT press Cambridge.

Newman, N. (1994). ”Wave Effects on Deformable Bodies”, Applied Ocean research, Vol. 16 No. 1, pp 47-59.

Ormberg, H. and Slaattelid, O.H. (1993). ”Response analysis of floating fish farms: Calculation and Verification”, First int. Conf. in Fish farming Technology, Trondheim Norway.

Ormberg, H. (1991). ”Non-linear response analysis of floating fish farm systems”, Phd thesis, Trondheim, Norway

Salvesen, N, Tuck, E.O and Faltinsen, O.M. (1970). ” Ship Motions and Sea Loads”, Trans. SNAME 78, 250-287

Stansberg, C.T, Huse, E., Krogstad, J. and Lehn, E. (1995), ” Experimental study of Non-linear loads on vertical Cylinders in steep random waves”, Proc. ISOPE, Vol 1, pp 75-82

Storhaug, G and Moan, T. ”Springing/Whipping response of a large oceangoing vessel – investigated by an experimental method”, In Proceedings Hydroelasticity in Marine Technology, Wuxi, China.

Thomson, W.T. (1993). ” Theory of Vibration with Applications”, Chapman & Hall, ISBN - 412-54620-5

Taghipour, R., Fu, S. and Moan, T. Validated two and three dimensional linear hydroelastic analysis using standard software. Paper No. 2006-JSC-478. Proceedings 16th Int. Offshore and Polar Engineering Conference & Exhibition ISOPE, San Francisco, California, USA. May 28-June 2, 2006.

Triantafyllou, M.S. (1990). ”Cable mechanics with marine applications”, Lecture notes, Dep. Ocean Engineering, MIT, Cambridge, Massachusetts, USA

Wagner, H. (1932)

Wu, M.K. Aarsnes, J.V. Hermundstad, O and Moan T. (1997). ”A practical Prediction of Wave-Induced Structural Responses in Ships with Large Amplitude Motion”. 21st Symp. Naval Hydrodynamics, Trondheim, Norway.

Yago, K. and Endo, H. (1996). ”On the hydroelastic response of Box-Shaped floating structure with shallow draft”. Journal of the Society of Navalø Architects of Japan, Vol 180, pp. 341-352

Zhao, R. and Faltinsen, O.M. (1988). ”Interaction between waves and Current on a two-dimensional body in the free surface”. Applied Ocean Research, Vol 10, No 2. pp 87-99.

Zhao, R and Triantafyllou, M.S. (1994). ”Hydroelastic analysis of a long flexible tube in waves”. Proceedings of International Conference on Hydroelasticity in Marine Technology. Pp 287-300. Trondheim, Norway.

Zhao, R. (1995). ”A complete linear theory for a two-dimensional floating and liquid filled membrane structure in waves”, Journal of Fluids and Structures, 9, pp 937-956.

Zhao, R, Faltinsen, O.M and Aarsnes J.V. (1996). ”Water entry of arbitary two-dimensional sections with and without flow separation”, Proc. Of the 21st Symp. On Naval Hydrodynamics, Trondheim Norway.

Zhao, R. and Aarsnes, J.V. (1998). "Numerical and experimental studies of a floating and liquid-filled membrane structure in waves", Ocean Engineering, Vol. 25, No 9, pp 753-765.

Zou, J., Yu, Y. and Kim, C.H. (1998), "Ringing of ISSC TLP due to laboratory Storm sea", Int. Journal of Offshore and Polar Eng., Vol. 8, No 2pp 81-89.

Økland, O. D. (2002). " Numerical and Experimental investigation of whipping in twin hull vessels exposed to sevre wetdeck slamming". Phd thesis, NTNU, Trondheim.

Appendix A

Dynamic analysis
1 Degree of Freedom System

A1 General

As the response of a dynamic system due to an arbitrary loading is a key issue in hydroelastic analysis, a short summary of methods for dynamic analysis relevant for hydroelastic response calculation is presented in this Appendix.

Good references for a general description of dynamic analysis are Thomsen (1993) and Clough and Penzien (1975)

A2 General formulation

A simple 1 degree of freedom dynamic system is considered;

$$m\ddot{x} + b\dot{x} + kx = F(t) \tag{A.1}$$

where *m, b* and *c* are the mass, damping and stiffness respectively. *F(t)* is the excited load.

The general solution of eq. (A.1) consist of two parts, the homogeneous and the particular solution, i.e;

$$x(t) = x_H(t) + x_P(t) \tag{A.2}$$

The particular solution is determined by the excitation force *F(t).*

A3 Free Oscillation

A3.1 Undamped Case

Free oscillations is the case with zero excitation load, ie *F(t)=0* in eq. (A.1). The solution to the equation of motion for this case is given by the homogeneous solution, $x_H(t)$.

For the undamped case the equation of free oscillation can be written as a homogeneous second-order linear differential equation;

$$\ddot{x} + \omega_N{}^2 x = 0 \tag{A.3}$$

The natural circular frequency of this system is given from:

$$\omega_N = \sqrt{\frac{k}{m}} \tag{A.4}$$

The natural period is given from the circular frequency as;

$$T_N = \frac{2\pi}{\omega_N} \tag{A.5}$$

The motion is harmonic and the general solution of eq. (A.3) is;

$$x_H(t) = A\sin\omega_N t + B\cos\omega_N t \tag{A.6}$$

where the coefficients *A* and *B* is determined from the initial conditions. Introducing the initial conditions for position and velocity the solution can be shown to reduce to ;

$$x_H(t) = \frac{\dot{x}(0)}{\omega_N}\sin\omega_N t + x(0)\cos\omega_N t \tag{A.7}$$

Where $x(0)$ and $\dot{x}(0)$ is the initial position and velocity respectively.

A3.2 Damped Case

For the case the equation of free oscillation can be written as;

$$m\ddot{x} + c\dot{x} + kx = 0 \tag{A.8}$$

The solution of this equation depends on the damping ration. Here we will only consider underdamped systems which means that the damping is less than the *critical damping* defined from;

$$c_{cr} = 2m\omega_N = 2\sqrt{km} \tag{A.9}$$

The damping ratio is defined as;

$$\varsigma = \frac{c}{c_{cr}} = \frac{c}{2m\omega_N}$$

The solution for the under critical damped system, $c/c_{cr} = \varsigma < 1$ is given on the form;

$$x_H(t) = e^{-\varsigma\omega_N t}\left(A\sin\omega_D t + B\cos\omega_D t\right) \tag{A.10}$$

where the coefficients *A* and *B* is determined from the initial conditions. ω_D is the damped natural frequency given by;

$$\omega_D = \omega_N\sqrt{1-(c/c_{cr})^2}$$

Introducing the initial boundary conditions for position and velocity the solution can be shown to reduce to;

$$x_H(t) = e^{-\varsigma\omega_N t}\left(\frac{\dot{x}(0)-x(0)}{\omega_D}\sin\omega_D t + x(0)\cos\omega_D t\right) \tag{A.11}$$

where $x(0)$ and $\dot{x}(0)$ is the initial position and velocity respectively.

It should be noted that due to damping the homogeneous solution will be a transient. In Fig. A.1 an example of damped transient response is shown.

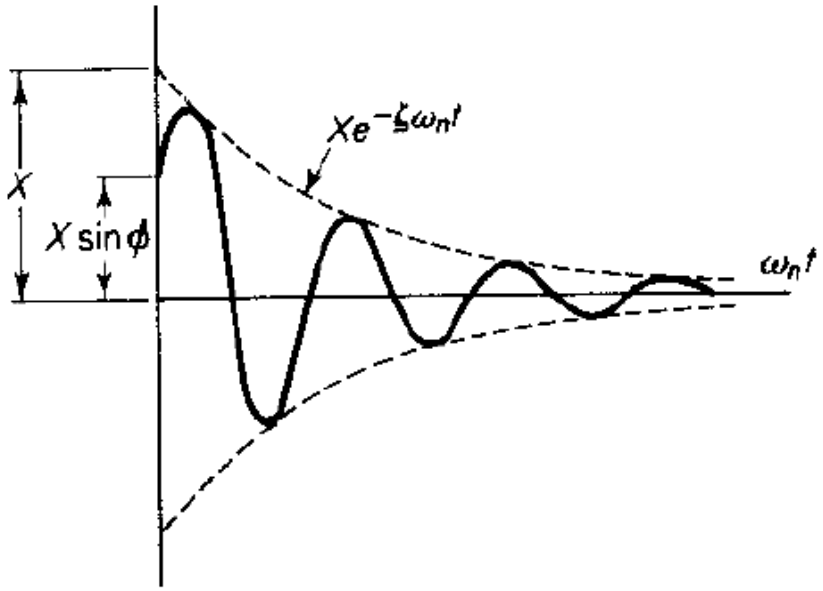

Figure A.1 *Damped transient response. Undercritical damping case*

A4 Linear, harmonic excitation case

For a linear, harmonic excitation i.e exciting force can be written as;

$$F(t) = F_0(\omega)\sin(\omega t) \tag{A.12}$$

where $F_0(\omega)$ is the force amplitude and ω is the frequency of excitation. The particular solution of this equation is a steady state oscillation with the same frequency as the excitation given on the form;

$$x_P(t) = X_0(\omega)\sin(\omega t - \varepsilon) \tag{A.13}$$

where $X_0(\omega)$ is the amplitude of oscillation and ε is the phase of the displacement relative to the excitation. Inserting eq. (A.13) into (A.1) we get the following solutions;

$$X_0(\omega) = \frac{F_0(\omega)}{\sqrt{(k - m\omega^2)^2 + (c\omega)^2}} \tag{A.14}$$

and

$$\varepsilon = \tan^{-1}\left(\frac{c\omega}{k - m\omega^2}\right)$$

Using complex notation we can write the harmonic loading as;

$$F(\omega) = F_0(\omega)e^{i\omega t} \tag{A.15}$$

Where F_0 is the complex load vector. The particular solution of eq. (A.1) with the load given by eq. (A.15) will also be a harmonic response on the form;

$$x_P(\omega) = X_0(\omega)e^{i\omega t} = H(\omega)F_0(\omega)e^{i\omega t} \tag{A.16}$$

$H(\omega)$ is the complex *frequency response function*. Inserting eq. (A.16) into (A.1) we get the following solutions;

$$H(\omega) = \frac{1}{-m\omega^2 + i\omega c + k} \tag{A.17}$$

$H(\omega)$ gives the same result as equation (A.14)

The results given by eq. (A.14) (or similar equation (A.17)) are presented in Fig. A.2. The ratio between the dynamic response and the static response can be expressed as a Dynamic Amplification Factor (DAF);

$$DAF = \frac{X}{F_0/k} = \frac{Xk}{F_0} = \frac{|H(\omega)|}{H(0)}$$

This factor is shown in Fig. A.2. The results are shown as function of damping ratio.

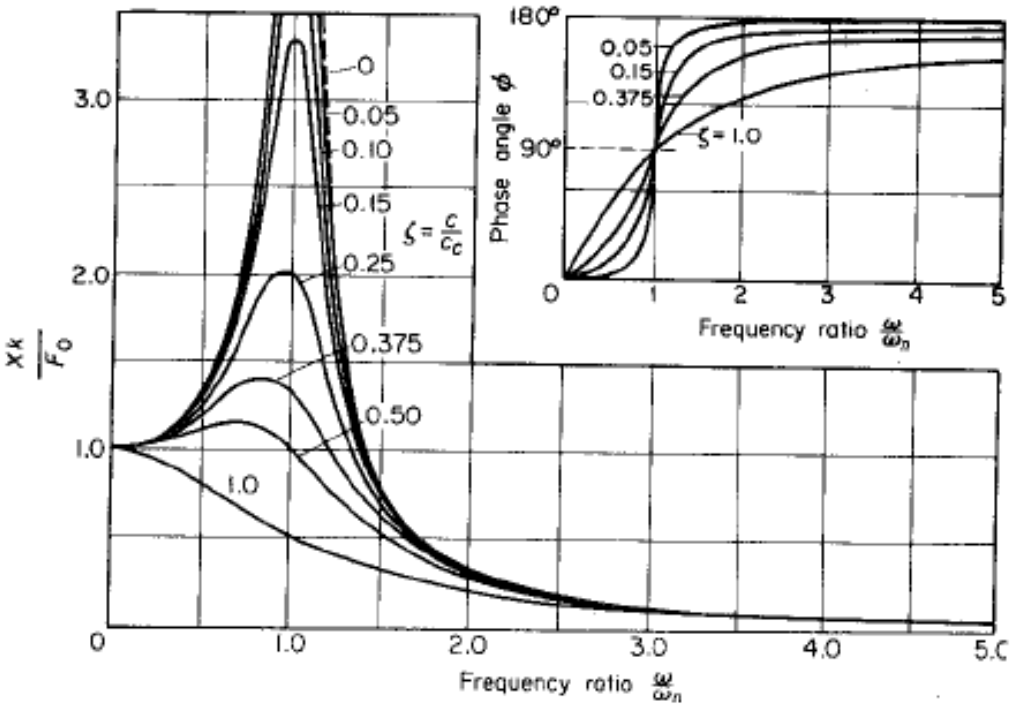

Figure A.2 *Dynamic response of 1 degree of freedom system excited by a harmonic load.*

The solution in time domain can be obtained from the frequency domain solution given by (A.16) by superposing the contribution from all frequencies (alternatively by direct use of the Fourier transformation) as;

$$x(t) = \frac{1}{2\pi}\int_{-\infty}^{\infty} H(\omega)F_0(\omega)e^{i\omega t}d\omega \tag{A.18}$$

A5 Non-harmonic loading - Transient Response

When a dynamic system is excited by a general nonperiodic excitation *F(t),* the response will be a transient response. For a general time dependent force the equation can be solved with numerical time integration. The particular solution can also be found using Fourier theory by representing the general nonperiodic excitation as a sum of harmonic components or by the impulse-response method. The later is discussed below.

An arbitrary excitation *F(t),* is assumed represented by a superposition of very short impulse excitations. From solution from each of these pulses the total response of a linear dynamic system will be given by superposition of the solutions for each of the pulses.

Impulse is the time integration of the force;

$$I = \int F(t)dt \tag{A.19}$$

A unit impulse or delta function, $\delta(t)$, is defined from the following requirements;

$$\delta(t-a) = 0 \quad \text{for} \quad t \neq a$$

$$\int_{-\infty}^{\infty} \delta(t-a)dt = 1 \tag{A.20}$$

The response of the dynamic system given by eq. (A.1) caused by this unit impulse, i.e;

$$m\ddot{x} + b\dot{x} + cx = F(t) = \delta(t) \tag{A.21}$$

The response of the system due to the unit pulse is denoted h(t) and often called the *impulse-response function*;

$$x(t) = h(t) \tag{A.22}$$

For a random pulse I, at time τ, with force $F(t) = I\delta(t-\tau)$ the response will be;

$$x(t) = I \cdot h(t-\tau)$$

The response due to pulse I, at time τ, is illustrated in Fig. A.3.

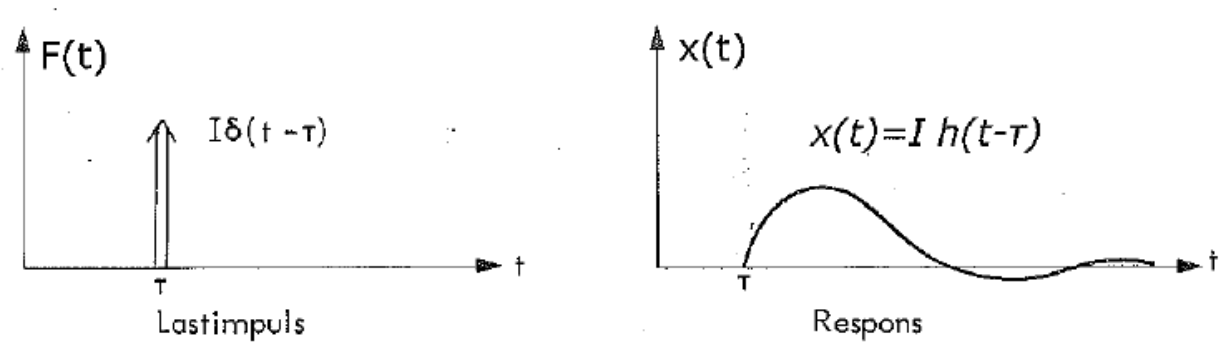

Figure A.3 *Illustration of response due to unit impulse.*

The impulse-response function can now be used to calculate the total response for an arbitrary excitation *F(t)*. The load is divided into a series of impulses which acts at

different time steps and different impulse values. This is illustrated in Fig A.4. The impulse shown act at time $t = \tau$ with impulse equal to $F(\tau)\Delta\tau$.

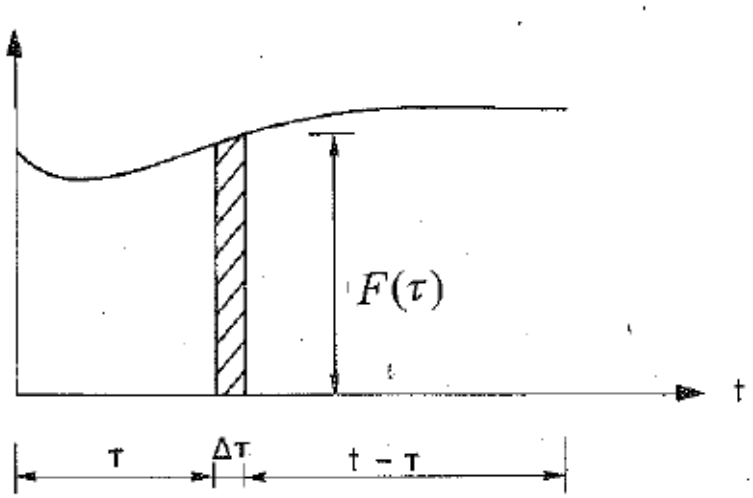

Figure A.4 *Arbitrary force represented by series of impulses.*

Using equation (A.19) this impulse gives a response;

$$x(t,\tau) = F(\tau)\cdot\Delta\tau\cdot h(t-\tau) \tag{A.23}$$

By integration over all pulses we obtain;

$$x(t) = \int_0^t h(t-\tau)\cdot F(\tau)\cdot d\tau \tag{A.24}$$

This integral is known as the *convolution integral* or as the *superposition integral*.

The impulse-response function can be obtained by using equation (A.21). After the duration of the unit impulse free oscillations of the system will take place.

For an undamped system the impulse-response function h(t) can be obtained from eq. (A.7) assuming a system initially at rest and excited by an impulse, i.e $x(0) = 0$ and $\dot{x}(0) = I/m$. This gives;

$$h(t) = \frac{1}{m\omega_N}\sin\omega_N t \tag{A.25}$$

Inserting into eq. (A.24) gives;

$$x(t) = \frac{1}{m\omega_N}\int_0^t \sin\omega_N(t-\tau)\cdot F(\tau)\cdot d\tau \tag{A.26}$$

For a damped system the impulse-response function h(t) can be obtained from eq. (A.10) assuming a system initially at rest and excited by an impulse. For the damped case this gives;

$$h(t) = \frac{1}{m\omega_D}e^{-\zeta\omega_N t}\sin\omega_D t \tag{A.27}$$

Inserting into eq. (A.24) gives for the damped case;

$$x(t) = \frac{1}{m\omega_D} \int_0^t e^{-\xi\omega_N (t-\tau)} \sin \omega_D (t-\tau) \cdot F(\tau) \cdot d\tau \tag{A.28}$$

This expression is known as the *Duhamel Integral* and give the particular solution for a general excitation.

The solution to the impulse-response function h(t) can also be obtained from the frequency domain solution for harmonic response given by eq. (A.17). By use of Laplace Transformation it can be shown that relation between the impulse-response function and the frequency response function eq. (A.17), can be written as;

$$h(t) = \frac{1}{2\pi} \int_{-\infty}^{\infty} H(\omega) \cdot e^{i\omega t} d\omega \tag{A.29}$$

Equation (A.29) shows that the impulse response function can be determined from the frequency response function. Similar we obtain the inverse relation;

$$H(\omega) = \int_{-\infty}^{\infty} h(t) \cdot e^{-i\omega t} dt \tag{A.30}$$

Results for response to different types of nonperiodic loadings will be discussed in chap 4 and 6 as part of evaluation of dynamic response to slamming loads.